Quantum Dash Multi-Wavelength Lasers for Next Generation High Capacity Multi-Gb/s Millimeter-Wave Radio-over-Fiber Wireless Communication Networks

Khan Zeb

A Thesis

In the Department

of

Electrical and Computer Engineering

Presented in Partial Fulfillment of the Requirements

For the Degree of

Doctor of Philosophy (Electrical and Computer Engineering) at

Concordia University

Montréal, Quebec, Canada

March 2023

CONCORDIA UNIVERSITY

SCHOOL OF GRADUATE STUDIES

This is to certify that the thesis prepared

By: Khan Zeb

Entitled: Quantum Dash Multi-Wavelength Lasers for Next Generation High Capacity Multi-Gb/s Millimeter-Wave Radio-over-Fiber Wireless Communication Networks

and submitted in partial fulfillment of the requirements for the degree of

Doctor of Philosophy (Electrical and Computer Engineering)

complies with the regulations of the University and meets the accepted standards with respect to originality and quality.

Examining committee:

_____	Chair
Dr. Gregory Butler	
_____	External Examiner
Dr. Odile Liboiron-Ladouceur	
_____	External to Program
Dr. Chadi Assi	
_____	Examiner
Dr. M. Reza Soleymani	
_____	Examiner
Dr. Dongyu Qiu	
_____	Supervisor
Dr. John Xiupu Zhang	
_____	Co-Supervisor
Dr. Zhenguo Lu	

Approved by: _____
Dr. Jun Cai
Graduate Program Director

March 15, 2023   _____
Dr. Mourad Debbabi
Dean of the Gina Cody School of Engineering and Computer Science

Abstract

Quantum Dash Multi-Wavelength Lasers for Next Generation High Capacity Multi-Gb/s Millimeter-Wave Radio-over-Fiber Wireless Communication Networks

Khan Zeb, Ph.D.
Concordia University, 2023

The ever-increasing proliferation of mobile users and new technologies with different applications and features, and the demand for reliable high-speed high capacity, pervasive connectivity and low latency have initiated a roadmap for the next generation wireless networks, fifth generation (5G), which is set to revolutionize the existing wireless communications. 5G will use heterogeneous higher carrier frequencies from the plentifully available spectra in the higher microwave and millimeter-wave (MMW) bands, including licensed and unlicensed spectra, for achieving multi-Gb/s wireless connectivity and overcoming the existing wireless spectrum crunch in the sub-6 GHz bands, resulting from the tremendous growth of data-intensive technologies and applications. The use of MMW when complemented by multiple-input-multiple-output (MIMO) technology can significantly increase data capacity through spatial multiplexing, and improve coverage and system reliability through spatial diversity. However, high-frequency MMW signals are prone to extreme propagation path loss and are challenging to generate and process with conventional bandwidth-limiting electronics. In addition, the existing digitized fronthaul for centralized radio access network (C-RAN) architecture is considered inefficient for 5G and beyond. Thus, to fully exploit the promising MMW 5G new radio (NR) resource and to alleviate the electronics and fronthaul bottleneck, microwave photonics with analog radio-over-fiber (A-RoF) technology becomes instrumental for optically synthesizing and processing broadband RF MMW wireless signals over optical links. The generation and distribution of high-frequency MMW signals in the optical domain over A-RoF links facilitate the seamless integration of high-capacity, reliable and transparent optical networks with flexible, mobile and pervasive wireless networks, extending the reach and coverage of high-speed broadband MMW wireless communications. Consequently, this fiber-wireless integration not only overcomes the

problem of high bandwidth requirements, transmission capacity and span limitation but also significantly reduces system complexity considering the deployment of ultra-dense small cells with large numbers of 5G remote radio units (RRUs) having massive MIMO antennas with beamforming capabilities connected to the baseband units (BBU) in a C-RAN environment through an optical fiber-based fronthaul network. Nevertheless, photonic generation of spectrally pure RF MMW signals either involves complex circuitry or suffers from frequency fluctuation and phase noise due to uncorrelated optical sources, which can degrade system performance. Thus simple highly integrated and cost-efficient low-noise optical sources are required for next-generation MMW RoF wireless transmission systems.

More recently, well-designed quantum confined nanostructures such as semiconductor quantum dash/dot multi-wavelength lasers (QD-MWLs) have attracted more interest in the photonic generation of RF MMW signals due to their simple compact and integrated design with highly coherent and correlated optical signals having a very low phase and intensity noise attributed to the inherent properties of QD materials. The main theme of this thesis revolves around the experimental investigation of such nanostructures on the device and system level for applications in high-speed high-capacity broadband MMW RoF-based fronthaul and wireless access networks. Several photonic-aided high-capacity long-reach MMW RoF wireless transmission systems are proposed and experimentally demonstrated based on QD-MWLs with the remote distribution and photonic generation of broadband multi-Gb/s MMW wireless signals at 5G NR (FR2) in the K-band, Ka-band and V-band in simplex, full-duplex and MIMO configurations over 10 to 50 km optical fiber and subsequent wireless transmission and detection. The QD-MWLs-based photonic MMW RoF wireless transmission systems' designs and experimental demonstrations could usher in a new era of ultra-high-speed broadband multi-Gb/s wireless communications at the MMW frequency bands for next-generation wireless networks.

The QD-MWLs investigated in this thesis include a simple monolithically integrated and highly coherent low-noise single-section semiconductor InAs/InP QD buried heterostructure passively mode-locked (PML) laser-based optical coherent frequency comb (CFC) and a novel monolithic highly correlated low-noise semiconductor InAs/InP

buried heterostructure common-cavity QD dual-wavelength distributed feedback laser (QD-DW-DFBL). The performance of each device is thoroughly characterized experimentally in terms of optical phase noise, relative intensity noise (RIN), timing jitter and RF phase noise exhibiting promising results. Based on these devices, different long-reach photonic MMW RoF wireless transmission systems, including simplex single-input-single-output (SISO) and multiple-input-multiple-output (MIMO) and bidirectional configurations, are proposed and experimentally demonstrated with real-time remote electrical RF synthesizer-free all-optical frequency up-conversion, wireless transmission and successful reception of wide-bandwidth multi-level quadrature amplitude modulated (M-QAM) RF MMW wireless signals having bit rates ranging from 4 Gb/s to 36 Gb/s over different hybrid fiber-wireless links comprising of standard single mode fiber (SSMF) and indoor wireless channel. The end-to-end links are thoroughly investigated in terms of error-vector-magnitude (EVM), bit-error-rat (BER), constellations and eye diagrams, realizing successful error-free transmission. Finally, novel high-capacity spectrally efficient MIMO and optical beamforming enabled photonic MMW RoF wireless transceivers design and methods based on QD-MWLs with wavelength division multiplexing (WDM) and space division multiplexing (SDM) are proposed and discussed. A proof-of-concept implementation of the proposed photonic MMW RoF wireless transmission system is also simulated in a simple WDM-based configuration with bidirectional 4×4 MIMO MMW carrier streams.

Acknowledgment

I would like to begin by thanking my supervisor Professor John X. Zhang for his consistent guidance, immense support and encouragement throughout my Ph.D. program, and for providing me with the opportunity to visit the AEP-NRC Canada Laboratories in Ottawa for my research. I am very grateful to my co-supervisor, Dr. Zhenguo Lu, for the opportunity to work and complete my thesis research at the AEP-NRC Labs. I also thank his encouraging leadership, valuable advice, constructive feedback, and constant support during my stay at the AEP-NRC Labs. The availability, helpful suggestions, encouragement and continuous support of my Ph.D. supervisors made this thesis possible.

I would also like to thank my committee members, Dr. Odile Liboiron-Ladouceur, Dr. Chadi Assi, Dr. Dongyu Qiu, Dr. Yousef R. Shayan, and Dr. M. Reza Soleymani, for their valuable feedback, suggestions, and comments.

I would like to express my genuine gratitude to Dr. Jiaren Liu for his mentorship, motivation, and long hours of discussions on research ideas and experiments at the AEP-NRC Labs. I am also grateful to Dr. Linda Mao, Dr. Chun Y. Song and Martin Vachon from the AEP-NRC group for their help and guidance in testing and experimentation in the Lab. Besides, my sincere thanks to all the AEP-NRC team members for the laser devices, and the co-authors of my papers, Dr. Mohamed Rahim, Dr. Philip J. Poole, Dr. Greg Pakulski, Dr. Pedro Barrios, Dr. Daniel Poitras, John Weber, Nicaulas Sabourin, Craig Storey, Dr. Shurui Wang, Dr. Eric Liu, and Dr. Muhammad Mohsin, for their help, feedback, and fruitful research discussions, and for making my stay at the AEP-NRC Labs memorable.

I am indebted to the NRC HTSN's program for supporting this research. I am also grateful for support from the Gina Cody School of Engineering and Computer Science and the PERSWADE program.

Last but not least, I cannot be thankful enough to my family and siblings for their endless support, motivation, love and patience; without their help and support, I would not be where I am today. I am grateful to my parents for their continuous support, prayers, encouragement, and unwavering belief in me. I thank my supportive wife and adorable kids for patiently sticking with me through the thick and thin of my Ph.D. journey. I may never have completed this thesis without the support of my wife.

Dedicated to my family, mentors and teachers

Table of Contents

List of Figures

List of Tables

List of Acronyms

Acronym	Definition
5G	Fifth Generation
3GPP	3rd generation partnership project
A-RoF	Analog radio-over-fiber
AWG	Arrayed waveguide grating
BBU	Baseband unit
BH	Buried heterostructure
BER	Bit error
BB-oF	Baseband-over-fiber
CFC	Coherent frequency comb
C-RAN	Centralized/Cloud radio access network
CoC	Chip on carrier
CO	Central office
DFB	Distributed feed back
D-RoF	Digital radio-over-fiber
DEMUX	De-multiplexer
eMBB	Enhanced mobile broadband
EDFA	Erbium-doped fiber amplifier
FMF	Few mode fiber
F-P	Fabry-perot
FR2	Frequency range 2
FWA	Fixed wireless access
FSL	Free-space loss
FEC	Forward error correction
HA	Horn antenna
IFoF	Intermediate frequency-over-fiber
IF	Intermediate frequency
I & Q	In-phase and quadrature
LNA	Low noise amplifier
LO	Local oscillator
LOS	Line-of-sight
LDC	Laser driver controller
mMTC	Massive machine type communications
MMWoF	Millometer-wave-over fiber
MLL	Mode-locked laser
MMW	Millimeter wave
MZM	Mach-Zehnder modulator
MDM	Mode division multiplexing

MIMO	Multiple input multiple output
MUX	Multiplexer
NR	New radio
OBF	Optical beamforming
OBFN	Optical beamforming network
OBPF	Optical band pass filter
OC	Optical coupler
OSA	Optical spectrum analyzer
OFDM	Orthogonal division multiplexing
PA	Power amplifier
PD	Photodetector
QD-MWL	Quantum dot/dash multi-wavelength laser
QD-DW-DFBL	Quantum dot/dash dual-wavelength laser
QAM	Quadrature amplitude modulation
QW	Quantum well
QD	Quantum dot/dash
RRH	Remote radio head
RF	Radio Frequency
RRU	Remote radio unit
FR2	Frequency range 2
ROP	Received optical power
RoF	Radio over fiber
RAU	Remote antenna unit
RIN	relative intensity noise
RTO	realtime oscilloscope
SEM	Scanning-electron-microscopy
SSMF	Standard single mode fiber
SDM	Space division multiplexing
TEM	Transmission electron microscopy
TDM	Time-division multiplexing
TTDL	True time delay line
URLLC	Ultra-reliable low latency communications
UE	User equipment
VOA	Variable optical attenuator
WDM	Wavelength division multiplexing
WSS	Wavelength selective switch

Chapter 1

Introduction

1.1   Problem Statement and Motivation

TO meet the ever-increasing demand for high bandwidth, high speed, low latency, and to overcome the global shortage of RF spectrum, frequency bands above 24 GHz in the millimeter-wave (MMW) spectrum with plentiful available bandwidths are envisioned for 5G wireless networks [1]. This paradigm shift in the RF spectrum for wireless carriers is inevitable in order to support the bandwidth hungry services and applications that urge the need for Gb/s wireless connectivity, such as ultra-high definition video streaming, gaming, virtual and augmented reality (VR/AR), Internet of Things (IoTs), artificial intelligence (AI), smart home/building, autonomous vehicles, and work and play in the cloud. In addition, we are becoming more and more dependent on online services, which is evident from the massive increase in Internet users and traffic growth in general and mobile users in particular as can be seen in Fig. 1.1. According to Ericsson mobility report June 2022, the global mobile network data traffic including fixed wireless access (FWA) reached to 84 Exabyte (EB) per month by the end of 2021 and is projected to grow and reach to 368 EB per month by the end of 2027 as shown in Figure 1.1 [2].
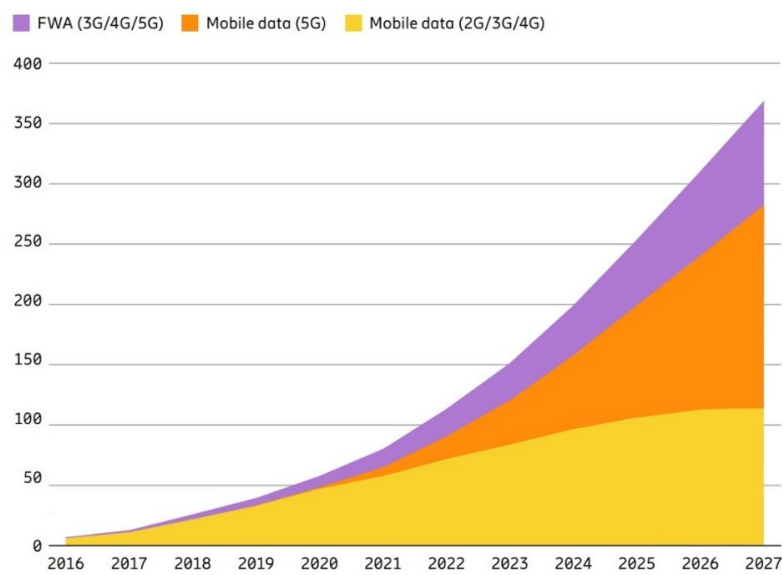
Figure 1.1: Global mobile network data traffic (EB per month) [2].

Moreover, the global monthly average usage per smartphone is expected to exceed 15 Gigabyte (GB) in 2022 and to reach 40GB by the end of 2027 [2]. It has also been realized during the pandemic that broadband ubiquitous connectivity matters more than ever before and wireless technology played a crucial role. Not only helped people to stay connected around the globe but also enabled telehealth, remote learning and education, and especially remote work that kept businesses, essential services and government operations running to meet daily needs [3]. This highlights the need and importance of the next-generation wireless communication networks, i.e., 5G wireless networks, which aims to virtually connect everyone and everything together, including person-to-person communication, devices, objects, and machine interaction. This will require 5G networks to provide ultra-high data rates, low latency, high reliability and massive connectivity pervasively.

To fulfill the 5G diverse requirements, the International Telecommunication Union Recommendation Sector (ITU-R) specifies 5G standards in International Mobile Telecommunications 2020 (IMT-2020) that identify three different usage scenarios including enhanced mobile broadband (eMBB), massive machine type communication (mMTC) and ultra-reliable low latency communication (URLLC) as shown in Fig. 1.2 (a) [4]. The eMBB features high speed broadband services with peak data download speed of up to 20-Gb/s and seamless user experience data rates of 100-Mb/s in wider coverage area as shown in Fig. 1.2 (b) with the expected speed of Gb/s in hotspot scenarios [4]. These ultra-high speed broadband and low latency services cannot be realized and supported by the already depleted sub-6GHz RF spectrum. Therefore, 5G wireless networks require high
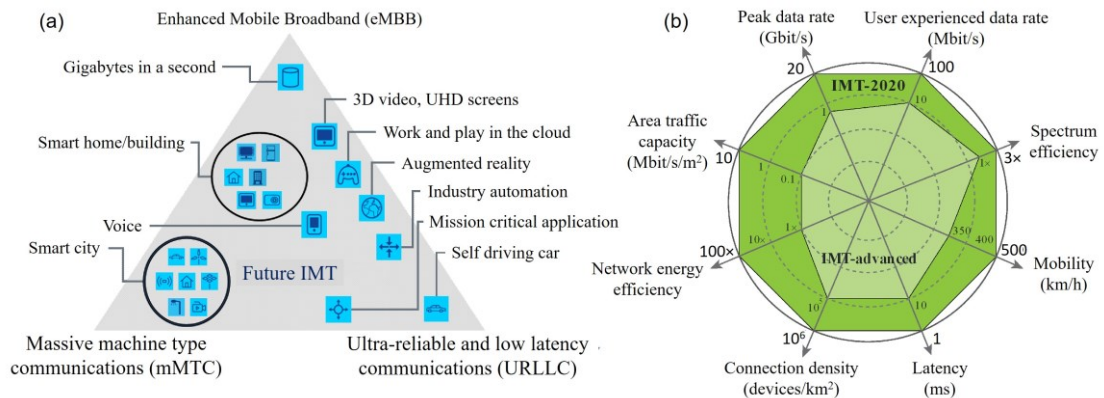
Figure 1.2: IMT-2020 (a) usage scenarios and (b) key capabilities [4].

frequency bands in the higher microwave and MMW spectrum (30 GHz – 300 GHz) with plentiful available bandwidths for the realization of ultra-high speed and high-capacity broadband wireless communications [5]. To this end, 3GPP has standardized higher frequency bands covering spectrum from 24.25 GHz to 52.6 GHz designated as frequency range 2 (FR2) in Release 15 for the development of 5G new radio (NR) (a global 5G standard for wireless air interface) systems [6]. More recently, 3GPP has extended FR2 operation in the MMW spectrum from 52.6 GHz to 71 GHz designated as FR2-2 in Release 17 [7]. Thus by using these higher frequency bands complemented by the massive multiple input multiple output (M-MIMO) and beamforming technologies, 5G and beyond wireless networks promise to achieve ultrahigh speed and extremely large capacity, very low latency, and better coverage with wideband operation for wireless applications. The M-MIMO technology can significantly increase the data throughput through spatial multiplexing and improve coverage and system reliability through spatial diversity, whereas the beamforming technology can help in mitigating losses, improving signal quality and eliminating undesirable interferences by directing several independent MMW wireless beams to specific locations/users.

However, the generation and distribution of ultra-high frequency broad bandwidth MMW signals with traditional methods is limited by the electronic bottleneck [8] and associated complexity and cost. In addition, these high frequency signals are highly susceptible to propagation path loss. Consequently, broad bandwidth, simple, efficient, and cost-effective photonic-aided MMW solutions in the form of microwave-photonics for the generation, processing, control and distribution of MMW signals in the optical domain in a fiber-wireless configuration with analog radio-over-fiber (A-RoF) is considered a viable alternative for application in broadband wireless access networks [8]–[10], especially in the fronthaul of 5G and beyond wireless networks having centralize cloud radio access network (C-RAN) architecture. Moreover, the existing fronthaul links between the remote radio units/heads (RRUs/RRHs) and baseband units (BBUs) are based on digital RoF (D-RoF) with a common public radio interface (CPRI) as the main interface protocol, which poses major challenges in terms of extremely high capacity requirements for 5G and beyond wireless networks. Therefore, A-RoF fronthaul is considered as one the promising solutions to CPRI based D-RoF for 5G and beyond C-RAN due to its bandwidth efficiency,

3

low latency, and cost-effectiveness [11]–[13]. Furthermore, considering the 5G ultra-dense and heterogeneous networks (HetNets) with a large number of remote RRUs/RRHs and the use of MMW spectrum along with M-MIMO and beamforming technology, the required bandwidth in RoF links, in particular fronthaul links, would scale up to an extent that would exceed the huge bandwidth offered by a single optical fiber link. Therefore, this expected rise in the bandwidth requirements of optical links calls for novel multiplexing dimensions, such as space division multiplexing (SDM) tailored with wavelength division multiplexing (WDM) and polarization multiplexing (Pol-Mux).

The basic notion of photonic-aided MMW signal generation and distribution in the optical domain through fiber-optic links is based on the remote optical mixing of two optical signals having different wavelengths spaced at the desired RF MMW signal on a high speed photodetector (PD) after running over several tens of kilometers of optical fiber [14]. Thus, photonic-aided techniques can be used to generate RF carrier signals with frequencies ranging from microwave and MMW to THz range, limited only by the frequency response of the PD. In this way, seamless fiber-wireless integration can be achieved [15] through generating RF MMW carriers optically, which is inevitable for 5G and beyond ultra-broadband wireless communication networks. Since in addition to being immune to electromagnetic interference, optical fiber offers high capacity, low latency and large transmission distance but limited mobility. On the other hand, wireless networks provide high mobility and seamless coverage but limited bandwidth and transmission distance. Therefore, seamless fiber-wireless convergence is necessary for ubiquitous and multi-gigabit wireless connectivity [15]. Accordingly, photonic MMW signals generation over fiber-optic links can significantly simplify the overall fronthaul architecture compared to the traditional architecture, especially the RF front-end in the C-RAN environment of 5G. Because digital or analog data can be modulated onto at least one of the optical signals in the baseband units (BBUs) located in the central office (CO) and the desired RF MMW carrier signal can be remotely generated optically right at the antenna eliminating the need for expensive components, such as digital to analog and analog to digital converters (DACs/ADCs) in the case of conventional digital RoF or electrical local oscillators and mixers in the case of conventional A-RoF. Thus, the optical devices and techniques that are used for MMW signals generation and processing in conjunction with the bandwidth

efficient A-RoF technology not only overcome the problem of high bandwidth requirements, transmission capacity and span limitation but also significantly reduce system complexity [9], [10], [16], [17], footprint, capital expenditure (CAPEX) and operating expenses (OPEX).

Nevertheless, photonic-aided generation of RF MMW signals through uncorrelated optical sources results in frequency fluctuation and phase noise, which degrades system performance [16], [18]. Thus, the phase fluctuations of the optical signals need to be highly correlated to ensure spectrally pure MMW carrier signal generation. Because if the optical signals are not phase correlated, for instance in the case of two different free running lasers, then the resulting MMW signal ends up with high phase noise, thus limiting the system performance [16], [18]. Conversely, if the phase noise of the two optical signals is correlated then the common noise of the two signals cancels out and a low phase noise MMW signal is generated. This entails either the elimination or correlation of phase noise of the corresponding optical signals for the generation of spectrally pure and phase stable MMW carrier signals. Thus low noise, highly correlated and integrated optical sources are required for 5G photonic-aided MMW RoF wireless transmission systems.

Various techniques have been developed and demonstrated under the umbrella of microwave photonics for photonic-aided RF MMW signals generation over optical links, ranging from optical heterodyne beating of two single wavelength individual laser sources [19] and external modulation of a single mode laser [20], [21] to picking pairs of modes from optical frequency combs [18], [22], [23], sources based on colorless laser diode [24], [25] and dual-wavelength optical sources [26], [27]. Similarly, several techniques have been reported for the phase locking and stabilization between the optical signals, including optical injection locking [28], optical-phase-locked-loop (OPLL) [29] and their combination [30]. The MMW optical sources with phase locking and stabilization offer better frequency correlation and stabilization than any two free-running lasers based schemes. Nonetheless, most of the MMW signal generation techniques utilizing phase locking and stabilization approaches rely on complex and expensive devices, such as modulators, microwave reference sources and other related components that add to the complexity and cost of the system. In addition, the bias drift associated with some of the

aforementioned schemes involving external modulators that can cause instability, hence limiting system performance. Consequently, besides attaining spectral purity and stability, the complexity and cost are the two key factors that need to be considered in the design of next generation wireless communications systems

In recent years, semiconductor quantum dash (QDash/Dot) multi-wavelength lasers (QD-MWL) have gathered considerable attention for photonic MMW signal generation and applications in optical MMW RoF transmission systems [16], [31]–[38]. Compared with other technologies, well-designed quantum confined nanostructures, such as semiconductor InAs/InP QD lasers have the distinctive advantage of achieving highly coherent and correlated optical signals with very low phase and intensity noise [36], [39]–[41], together with chip-scale integration viability. Owing to their inherent superior characteristics, such as reduced amplified spontaneous emission, large effective gain bandwidth, ultra-fast carrier dynamics, and improved temperature stability, QD materials based lasers are capable of achieving very narrow optical spectral linewidth and low relative intensity noise (RIN) as compared to quantum-well (QWs) based lasers, which are currently being used in most of the commercially available optical sources. Consequently, the generated RF MMW signals based on QD devices show better spectral purity due to high correlation of phase noise between the optical lines. Moreover, for further spectral purity and phase stabilization in QD-MWLs, a simple feedback mechanism of self-injection locking can be used [16], [39], [42], [43], which eliminates the need for comparatively more complex and expensive components making them a suitable candidate as an optical MMW source for 5G MMW RoF wireless communication systems. Thus, due to compact design and multiple highly coherent and low noise optical channels, QD-MWLs promise a low cost and flexible solution for 5G and beyond wireless communication networks, particularly in the application of fronthaul with M-MIMO RRUs/RRHs.

A single QD-MWL can be used as a common optical source for different RRUs/RRHs to provide optical local oscillator (LO) and data channels as well as to replace many individual laser sources in the central office (CO) and RRU/RRH offering low noise and cost-efficient solution for photonic-aided RF MMW RoF fronthaul systems of 5G and beyond wireless communication networks as shown in Fig. 1.3 (a). A simplified photonic-
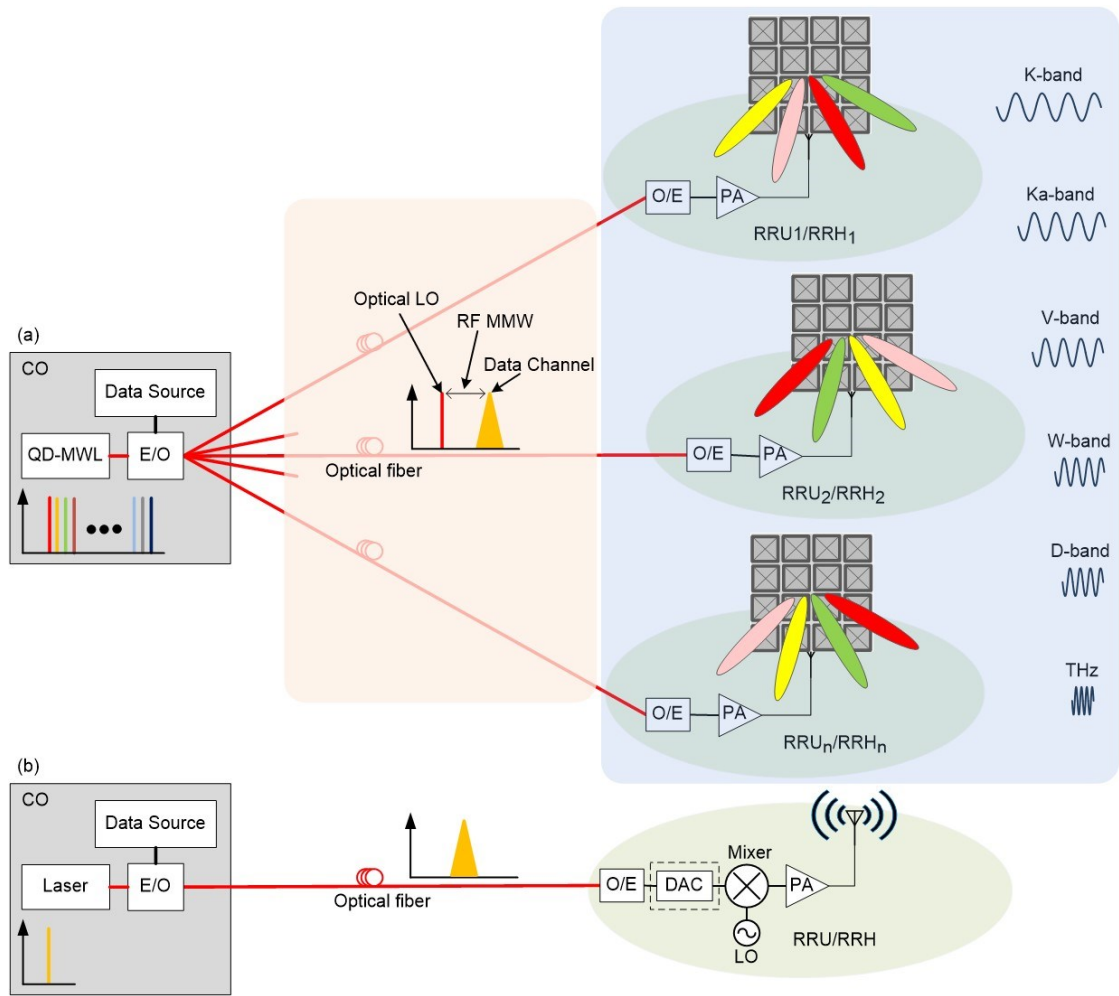
Figure 1.3: (a) Conceptual illustration of a photonic-aided MMW RoF architecture with a common optical source based on QD-MWL (b) Conventional digital/analog RoF architecture. E/O: electrical/optical conversion, PA: power amplifier, LO: local oscillator.

aided RF MMW RoF architecture (downlink) is illustrated in Fig. 1.3 (a) where multi-Gb/s wireless signal delivery is achieved through remote mixing of coherent common optical LOs and data channels based on a single QD-MWL source. In contrast, Fig. 1.3(b) shows the conventional and comparatively complex RoF architecture. In both cases, a fiber-optic receiver (photoreceiver) is required in the RRU/RRH for optical to electrical (O/E) conversion. However, in the former case, RF signals are up-converted photonically to the desired RF carrier frequency using a coherent common optical source i.e., QD-MWL, shared by different RRUs/RRHs resulting in reduce complexity by eliminating expensive components, such as electrical LOs and DACs/ADCs, compared to the latter case where

RF signals are up-converted by the conventional electronics. In addition, a single QD-MWL device can be used to generate RF carrier signals in multiple RF frequency bands in the microwave and MMW (30 GH – 300 GHz) spectrum, such as K-band, Ka-band, V-band, W-band, D-band etc., including 3GPP 5G NRs FR2-1 (24.25 GHz – 52.6 GHz) [6] and FR2-2 (52.6 GHz – 71 GHz) [7] bands, and even up to THz by selecting appropriate optical channels. Moreover, photonics-eneabled MMW M-MIMO and optical beamforming (OBF) can be efficiently realized by employing QD-MWL with phased array antennas (PAAs). Compared with the conventional electrical beamforming where a dedicated RF chain or phase/amplitude control is required for each radiating antenna element that adds up to the size, complexity and hardware cost in addition to bandwidth limitations, electromagnetic interference and high power consumption, OBF with higher available bandwidth can significantly reduce the complexity, cost and power consumption using photonic true time delay lines (TTDLs). The OBF with photonic TTDLs can also help in alleviating the problem of beam squint in wide-band applications. Since in the case of OBF with TTDLs, the beam pointing direction is a function of the optical delay line where all frequency components have the same delay times, whereas in the case of beamforming with electrical phase shifters, it is dependent on the signal frequency leading to beam squint in wide-bandwidth applications.

Thus motivated by the fact that photonic-aided RF MMW signals generation, processing and distribution over fiber-optic links using highly coherent and correlated low noise optical sources with A-RoF transport solutions leveraging SDM and wavelength division multiplexing (WDM) technologies can achieve high bandwidth, high-capacity, high centralization, long-reach, low-complexity, low latency and cost-effectiveness, in this thesis, long-reach high capacity multi-Gb/s photonic MMW RoF wireless transmission systems are proposed and experimentally demonstrated based QD-MWLs for the next generation of wireless communication networks.

1.2 Objectives

This thesis aims to investigate and characterize different nanostructure-based semiconductor QD-MWLs, which can operate at room temperature and cover an RF frequency range from tens of GHz to THz depending on the laser design, for application in the next generation of wireless communication networks. The thesis focuses on the experimental investigation of such nanostructure-based devices as compact and interated optical sources for the generation and transmission of RF millimeter-wave (MMW) signals, which can pave the way for the development of microwave photonic integrated circuits for applications in fiber-wireless integrated systems of 5G and beyond fronthaul and access networks. The QD-MWLs with high spectral purity, compact size, low cost, low power consumption, simple fabrication and integration feasibility have great potential as an efficient chip-scale candidate for deployment in fiber-wireless integrated 5G NR RoF-based fronthaul systems. Nevertheless, the application of QD-MWLs in broadband RoF wireless transmission systems with end-to-end RF MMW RoF wireless links is not yet fully explored and experimented with. Consequently, it is worth investigating to fully exploit the superior characteristics of QD-MWLs for the MMW RoF wireless transmission systems of 5G and beyond wireless communication networks. Thus, by considering the exceptional attributes of the semiconductor QD nanostructures based lasers, in this thesis, different highly coherent and correlated low-noise compact monolithic QD-MWLs, including a single-section semiconductor BH PML InAs/InP QD-MWL-based CFC and a novel semiconductor InAs/InP BH common cavity QD QD-DW-DFB are experimentally investigated for spectrally-pure MMW signals generation and data transmission over hybrid fiber-wireless links. This includes discussion on the lasers' design, fabrication, characterization and experimental demonstration in the proposed end-to-end proof-of-concept RF synthesizer-free MMW RoF wireless transmission systems. The demonstration includes real-time broadband high capacity photonics-assisted long-reach RF MMW RoF wireless links in single input and single output (SISO) and MIMO configurations with simplex and duplex transmission at 5G NR in the K-band, Ka-band, and V-band with data throughputs of multi-Gb/s over different spans of tens of kilometer of standard single mode fiber (SSMF) and several meters free-space indoor wireless transmission distances. Finally,

to simplify the overall C-RAN architecture and to alleviate the capacity bottleneck, especially the RRUs/RRUs and fronthaul capacity, respectively, the aim of the thesis is to thoroughly investigate and propose novel comprehensive system designs and methods for achieving flexible and scalable high-capacity spectrally efficient M-MIMO and optical beamforming (OBF) enabled all-optical photonic MMW RoF wireless transceiver systems for 5G and beyond wireless communication networks based on QD-MWL source with WDM and SDM technologies.

1.3 Contributions and Outline

A brief overview of the research contributions of the thesis is shown in Fig. 1.4. The different chapters include research work from the author's published articles. Note that the material growth and laser design and fabrication were provided by the Advanced Electronics and Photonics Research Centre, National Research Council of Canada (AEP-
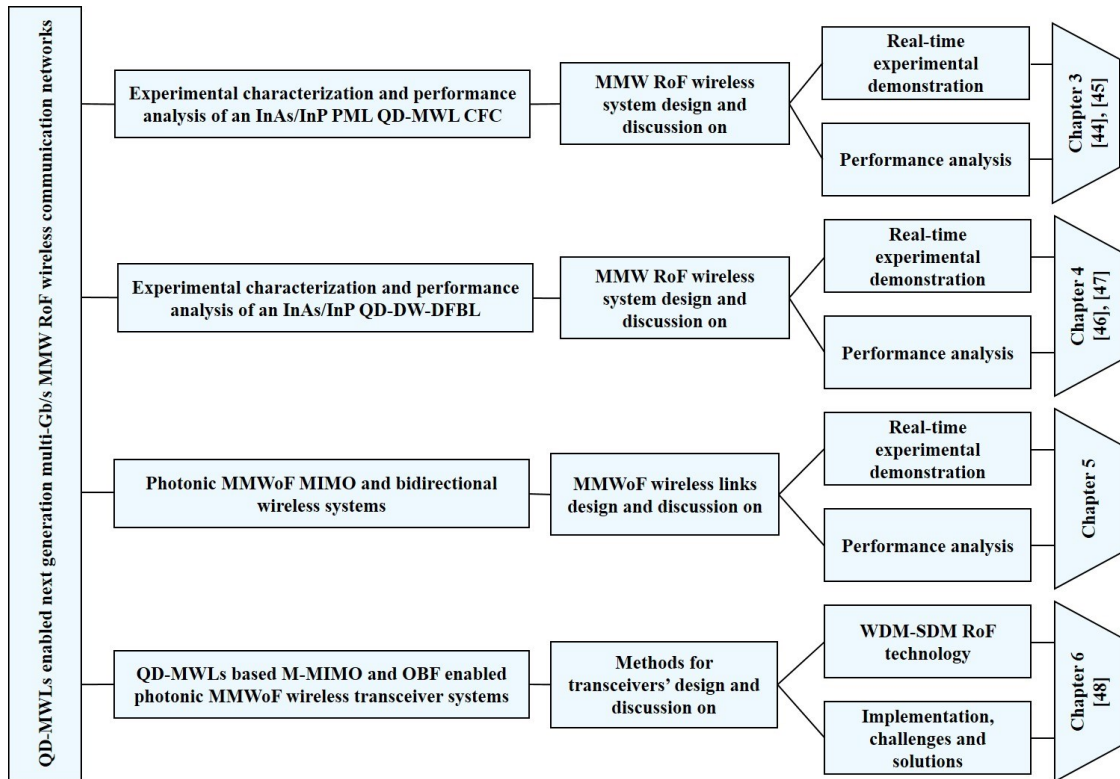
Figure 1.4: Overview of the thesis contributions.

NRC) Labs. The experimental setup was also established at the AEP-NRC Labs. The body of the thesis is structured as follows.

Chapter 1 presents the problem statement and motivation to this work. It highlights the next generation wireless communication networks, i.e., 5G and beyond wireless networks, requirements, key enabling technologies such as MMW, RoF, M-MIMO, and beamforming, and potential challenges and solutions with a brief description of the recent related works. Finally, the objectives and a brief summary of the contributions of this thesis are presented.

Chapter 2 provides a thorough background and literature review related to this work, which includes introduction to semiconductor lasers, QD-MWLs and mode-locking; MMW wireless communication and challenges; the basic concept of photonic MMW signals generation and related comprehensive state-of-the-art techniques, key challeneges and proposed solutions; radio access network with focus on fronthaul architecture challenges and key enabling solution for the next generation fronthaul; comprehensive discussion on RoF with state-of-the-art techniques and architectures; and comprehensive recent state-of-the-art related work on QD-MWL MMW RoF system.

Chapter 3 presents the experimental investigation of a compact, monolithic, highly coherent and low noise single-section buried heterostructure PML InAs/InP QD-MWL CFC with a free spectral range of 25 GHz. This includes the design, fabrication, experimental characterization and demonstration in the proposed end-to-end proof-of-concept multi-Gb/s A-RoF systems with RF wireless links at the 3GPP 5G NR frequency range 2 (FR2) band n258 (24.25 – 27.5 GHz) [44], [45].

Chapter 4 presents a highly correlated monolithic InAs/InP quantum dash buried heterostructure QD-DW-DFBL having ultra-low noise common cavity modes at different wavelengths with a tunable free-spectral range between 46 GHz and 48 GHz within the 5G NR FR2 standard band n262 (47.20 – 48.20 GHz) for MMWoF transmission systems. A thorough experimental characterization of the device is presented. Based on the device, broadband photonic MMWoF systems are proposed and experimentally demonstrated in real-time with the photonic generation, wireless transmission and detection of wide-

bandwidth multi-Gb/s RF synthesizer-free MMW M-QAM modulated (16-QAM, 32-QAM and 64-QAM) signals having symbol rate of 4- and 6-GBaud with a maximum bit rate of 36 Gb/s over hybrid fiber-wireless links comprising of back-to-back (BtB), 25 km and 50-km SSMF and 2-m to 9-m free-space wireless channel. The end-to-end MMW-over-fiber (MMWoF) wireless links are thoroughly characterized exhibiting promising EVM and BER values [46], [47].

Chapter 5 presents our proposed multi-Gb/s photonic MMW MIMO and duplex bidirectional systems based on QD-MWLs. This includes experimental demonstration of photonic-assisted MMWoF 2×2 MIMO and bidirectional wireless transmission systems at around 47 GHz in the V-band using a single low noise InAs/InP quantum dash dual-wavelength DFB laser (QD-DW-DFBL), and bidirectional wireless transmission system at around 28 GHz in the Ka-band employing a single low noise InAs/InP passively mode-locked (PML) QD-MWL-based coherent frequency comb (CFC).

Chapter 6 presents our proposed novel high capacity spectrally efficient MIMO and OBF enabled photonic MMWoF wireless transceiver system design and methods for 5G and beyond wireless networks based on QD-MWLs with WDM and SDM. Different potential implementation scenarios of the proposed system's design are discussed in detail, along with a proof-of-concept system simulation in a simple and basic configuration [48].

Chapter 7 concludes the thesis. This chapter gives concluding remarks, summary of the accomplished results and possible further research directions.

Related Publications

The author's Ph.D. research work contributed to the following journal publications, conference papers and a patent application denoted by J, C, and P, respectively.

J1: **K. Zeb**, Z. Lu, J. Liu, Y. Mao, G. Liu, P, J. Poole, M. Rahim, G. Pakulski, P. Barrios, M. Vachon, D. Poitras, W. Jiang, J. Weber, X. Zhang, and J. Yao*, "Broadband optical heterodyne millimeter wave-over-fiber wireless links based on a quantum dash dual-wavelength DFB laser," IEEE/Optica *Journal of Lightwave Technology*, Vol. 40, no. 12, pp. 3698 – 3708, Feb. 2022.

J2: **K. Zeb**, Z. Lu, J. Liu, Y. Mao, G. Liu, P. J. Poole, M. Rahim, G. Pakulski, P. Barrios, W. Jiang, and X. Zhang, "InAs/InP quantum dash buried heterostructure mode-locked laser for high capacity fiber-wireless integrated 5G new radio fronthaul systems," *Opt. Express*, vol. 29, no. 11, pp. 16164–16174, May 2021.

J3: **Khan Zeb**, X. Zhang, and Z. Lu, "High capacity mode division multiplexing based MIMO enabled all-optical analog millimeter-wave over fiber fronthaul architecture for 5G and beyond," *IEEE Access*, vol. 7, pp. 89522–89533, July 2019.

J4 Y. Mao, **K. Zeb**, Z. Lu, J. Liu, G. Liu, P. J. Poole, M. Rahim, G. Pakulski, P. Barrios, W. Jiang, and J. Zhang, "High performance InAs/InP quantum dash frequency comb laser for high capacity RoF wireless networks," *Sensors & Transducers*, vol. 255, no. 1, pp. 24-34, Jan. 2022.

J5: M. Rahim, **K. Zeb**, Z. Lu, G. Pakulski, J. Liu, P. J. Poole, C. Song, P. Barrios, W. Jiang, and X. Zhang, "Monolithic InAs/InP quantum dash dual-wavelength DFB laser with ultra-low noise common cavity modes for millimeter-wave applications," *Opt. Express*, vol. 27, no. 23, pp. 35368-35375, Nov. 2019.

P1: **K. Zeb**, Z. Lu, J. Liu, and X. Zhang, "Methods and apparatus for high capacity spectrally efficient MIMO and optical beamforming enabled photonic millimeter-wave over fiber (MMWoF) wireless transceiver systems based on quantum dot multi-wavelength lasers with wavelength division multiplexing and space division multiplexing," *patent application filed by the National Research Council Canada*, Oc. 2022.

C1: **K. Zeb**, Z. Lu, J. Liu, Y. Mao, M. Rahim, P. J. Poole, P. Barrios, G. Liu, G. Pakulski, W. Jiang, M. Vachon, D. Poitras, and X. Zhang, "A quantum-dash dual-wavelength DFB laser for optical millimeter-wave radio-over-fiber systems," *in Proc. Optical Fiber Communication Conference (OFC)*, June 2021, pp. 1-3.

C2: **K. Zeb**, Z. Lu, J. Liu, Y. Mao, G. Liu, P. J. Poole, C. Song, M. Rahim, G. Pakulski, P. Barrios, and X. Zhang, "A quantum dash mode-locked laser based photonic aided broadband multi-Gb/s wireless signal delivery system at 5G NR," *in Proc. SPIE 11711, Photonics West conference, Broadband Access Communication Technologies XV*, 117110I, Mar. 2021, pp. 65-70.

C3: **K. Zeb**, Z. Lu, J. Liu, Y. Mao, P. J. Poole, G. Liu, P. Barrios, M. Rahim, M. Vachon, D. Poitras, X. Zhang, and J. Yao, "Photonic Millimeter-Wave-over-Fiber MIMO Wireless System Based on a QDash Laser," *in Proc. IEEE Photonics North*, May 2022, pp. 1-1.

C4: Y. Huang, **K. Zeb,** G. Liu, P. Poole, X. Zhang, Z. Lu, K. Wu, and J. Yao, "Duplex Millimeter-Wave Over Fiber Link Using an InAs/InP Quantum-Dash Mode-Locked Laser," *in Proc. IEEE International Topical Meeting on Microwave Photonics (MWP), Oct. 4–6, 2022*, pp. 1-4.

C5: **K. Zeb**, Z. Lu, J. Liu, M. Rahim, G. Pakulski, P. J, Poole, Y. Mao, C. Song, P. Barrios, W. Jiang, and X. Zhang, "Photonic generation of spectrally pure millimeter-wave signal for 5G applications," *in Proc. IEEE International Topical Meeting on Microwave Photonics (MWP)*, Oct. 2019, pp. 1-4.

C6: **K. Zeb,** Z. Lu, J. Liu, Y. Mao, M. Rahim, P. J. Poole, P. Barrios, G. Liu, G. Pakulski, W. Jiang, M. Vachon, and X. Zhang, "Photonic wireless links for 5G broadband access networks," *in Proc. IEEE Photonics North*, June 2021, pp. 1-1.

C7: **K. Zeb**, Z. Lu, J. Liu, Y. Mao, G. Liu, P. J. Poole, M. Rahim, G. Pakulski, P. Barrios, W. Jiang, D. Poitras, and X. Zhang, "Ultra-Low intensity and phase noise quantum-dash dual-wavelength DFB laser for 5G millimeter-wave signals," *in Optica Laser Congress 2020 (Laser Application Conference)*, Oct. 2020, paper JTu5A.13.

C8: **K. Zeb**, Z. Lu, J. Liu, P. J. Poole, M. Rahim, G. Pakulski, Y. Mao, C. Song, and X. Zhang, "Experimental demonstration of photonic MMW-over fiber system for next generation access networks," *in Proc. IEEE Photonics North*, May 2019, pp.1-1.

In addition to the above articles, which contribute to the main content of this thesis, the author co-authored the following relevant publications.

J6: Y. Mao, G. Liu, **K. Zeb**, Z. Lu, J. Liu, P. J. Poole, C.-Y. Song, and P. Barrios, "Ultralow Noise and Timing Jitter Semiconductor Quantum-Dot Passively Mode-Locked Laser for Terabit/s Optical Networks," *Photonics*, Vol. 9, no. 10, pp. 695, Sep. 2022.

J7: Z. Lu, J. Liu, Y. Mao, **K. Zeb**, G. Liu, P. J. Poole, J. Weber, M. Rahim, G. Pakulski, C. Song, M. Vachon, P. Barrios, D. Poitras, S. Wang, and W. Jiang, "Quantum dash multi-wavelength lasers for Tbit/s coherent communications and 5G wireless networks," *Journal of the European Optical Society-Rapid Publication*, vol. 17, no. 9, pp. 1-7, June 2021.

C9: Z. Lu, **K. Zeb,** J. Liu, Y. Mao, G. Liu, P. J. Poole, P. Barrios, and X. Zhang, "Quantum dot multi-wavelength for high capacity 5G fiber-wireless integrated mobile fronthaul and access links," *in Proc. SPIE 11775, Photonics West conference, integrated Optics: Design, Devices, Systems and Applications VI*, 117750M, Mar. 2021, pp. 64-74.

C10: G. Liu, Z. Lu, J. Liu, Y. Mao, **K. Zeb**, M. Vachon, P. J Poole, P. Barrios, M. Rahim, G. Pakulski, and W. Jiang, "Static Characteristics of InAs/InP Buried Heterostructure Quantum Dash Mode-locked Lasers," *in Proc. IEEE Photonics North*, June. 2021, pp. 1-1.

C11: Z. Lu, J. Liu, Y. Mao, G. Liu, P. J. Poole, P. Barrios, M. Rahim, G. Pakulski, W. Jiang, D. Poitras, C. Song, M. Vachon, J. Weber, S. Wang, P. Zhao, C. Storey, **K. Zeb**, X. Zhang, J. Yao, and K. Wu, "Quantum-dot multi-wavelength lasers for millimeter wave generation and transmission," *in Proc. IEEE Photonics North* (invited talk), June 2021, pp. 1-1.

C12: Z. Lu, **K. Zeb**, J. Liu, G. Liu, Y. Mao, P. J. Poole, M. Rahim, G. Pakulski, P. Barrios, W. Jiang, and D. Poitras, "Quantum Dot Semiconductor Lasers for 5G & Beyond Wireless Networks," *(Invited paper) in Proc. SPIE 11690, Photonics West conference*, Smart Photonic and Optoelectronic Integrated Circuits XXIII, 116900N, March 2021, pp. 68-75.

Chapter 2

Background

2.1 Introduction to Semiconductor Lasers

2.1.1 A Brief Developmental History

THE journey of semiconductor lasers started in 1962 with the invention of the first gallium arsenide (GaAs) p-n junction based lasers [49]. It was followed by remarkable achievements, such as the formulation of the concept of double-heterostructure (DHS) based lasers in 1963 [50] replacing the simple p-n junction with different multiple semiconductor layers for better carriers and photons confinement, and subsequently, the development of first bulk semiconductor double-heterostructure lasers with reduced threshold continuous wave (CW) operation at room temperature in the early 1970s [51]. This triggered an immense interest in the physics and technology of the semiconductor hetrostructures based on III-V compounds and transformed the semiconductor laser technology from the research laboratories to the industries. Thus DHS lasers laid the foundation for quantum confined nanostructures, such as quantum well (QW), quantum dash (QD) and quantum dot (QD) semiconductor lasers. The first lasing using thin active region QWs was realized in 1975 [52] and the construction of first standard QW laser was demonstrated in 1978 [53] with superior characteristics, such as lower threshold currents, compared to its predecessor bulk DHS lasers. This is because the density of states (DOS) in QW structures were modified by confining the carriers to one dimension improving the performance. QW lasers have narrow-gap middle layer made of a thin semiconductor film with thickness of a few tens of nanometers (nm) < 50 nm, hence splitting the energy band of bulk semiconductors into discrete energy levels due to QW effects [54]. These and the subsequent achievements in the field of semiconductor lasers would not have been possible without the development of thin film deposition and crystal growth technology for the growth of heterostructures from III-V compounds, which gave access to a wide-range of optical spectrum by changing the lasing wavelength with the variation in composition of QW layer [55]. Thus the development of QW lasers has been considered a remarkable achievement in the history of semiconductor lasers, which have been used in real-systems

till this day and playing a crucial role in various applications, such as optical storage and data communications. However, the advancements in semiconductor laser technology continued looking for more confined devices with better performance that led to the development of systems with even lower dimensionality in the form QDots.

2.1.2 Quantum Dot/Dash Semiconductor Lasers: A Technology Overview

The concept of size quantization effects in heterostructurs semiconductor lasers was first introduced in 1976 [54] followed by the first theoretical investigation of quantum confinement of electrical carriers in such structures [56] and the experimental work on their realization and investigation [57] in 1982. However, it was not until 1994 that the first QDot laser was experimentally realized by *Hirayama et al* [58], which was fabricated by metal-organic chemical vapor deposition (MOCVD) growth technique with e-beam and wet etching of QW structures with lasing via excited states; still, exhibiting relatively high threshold current density due to the complex processing. At about the same time, the first self-assembled QDots based laser was reported by *Kirstaedter et al* [59] exhibiting lasing via the ground states with comparatively low threshold current density and large temperature. This motivated several studies in the field of QDots lasers on the optimization of device structures and materials growth quality with rapid improvements in the threshold current density exceeding the best values of QW lasers in merely a span of few years as shown in Fig. 2.1 [60]. The lowest threshold current density of below 10 A/cm^2 with the lowest internal losses of 0.25cm^{-1} for QD laser on GaAs platform was reported by *Deppe et al* in 2009 [61]. The low threshold current density and temperature sensitivity of QD-based material relative to QWs demonstrate their potential for minimizing the power consumption in addition to reducing the cost and avoiding overheating of the lasers and other adjacent electronic components in the circuits [60], [62]. Moreover, different self-assembled growth methods have been used and improved to grow the QD materials, such as metalorganic vapor phase epitaxy (MOVPE) [63], solid-state molecular beam epitaxy (MBE) [64], gas source MBE [65], and chemical-beam epitaxy (CBE) [66].

The quantum confinement of electrical carriers in nanostructures occur when one or more spatial dimensions reach to the de Broglie wavelength of the carrier, i.e., on the order
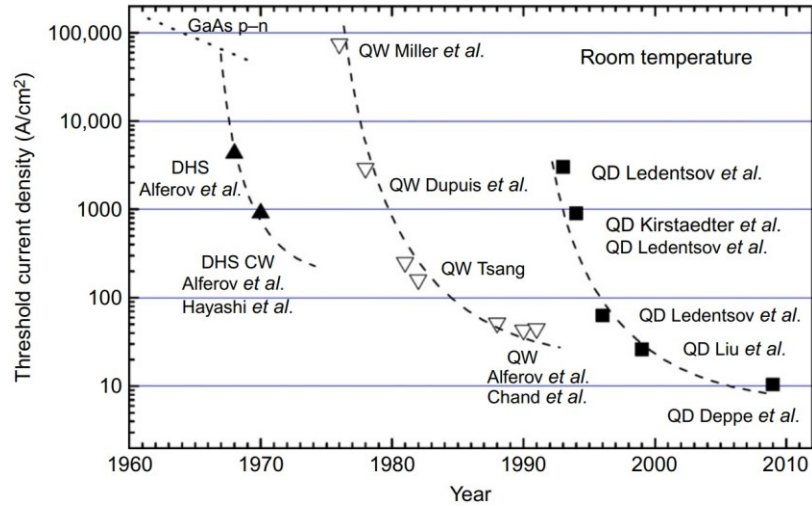
Figure 2.1: Chronological history of the heterostructure lasers showing the recorded threshold current densities at the time of publication for DHS, QW, and QD lasers (■ QD laser on GaAs; CW indicates threshold current values obtained under continuous mode operation) [60].

of 10 nm [67]. Such confinement results in carriers localization with a complete breakdown of the band structure leading to the quantification of DOS i.e., energy levels [54], which has been evolved from contentious to discreet in the conventional 3 dimensions (3D) Bulk and 2D QW to 0D QD structures as shown in Fig. 2.2. This quantum confinement helps in achieving larger optical gain even at low pump currents, which significantly improves the laser efficiency. As compared to Bulk and QW heterostructures where carriers are free in three and two dimensional space, respectively, carriers are confined in two dimensions in the case of QWires/QDashes with one direction freedom and in all three dimensions in the
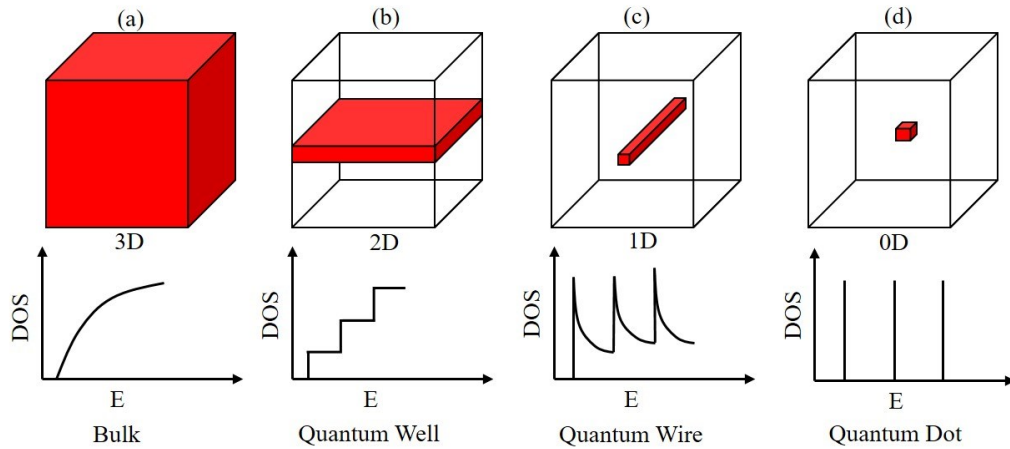
Figure 2.2: Evolution of the density of states for (a) bulk, (b) quantum well (QW), (c) quantum wire (same as QDashes), and (d) quantum dots (QD) materials.

17

case of QDots with zero-degree freedom as shown in Fig. 2.2 (d). This quantum confinement in QDash/Dot nanostructures results in unique optoelectronic properties [68] such as high material gain, high differential gain, low linewidth enhancement factor [69], ultra-fast carrier dynamics [70], ultra-low threshold current density [61], improved temperature stability [71], wide wavelength tuning range [72], and high spectral purity [73]. Due to these inherent properties, QDash/Dot materials based lasers are capable of achieving very narrow spectral linewidths (phase noise) and low relative intensity noise (RIN) compared with bulk and QWs [73]. Thus by reducing the active region dimensions, the carriers' confinement increases resulting in sharp increase in the DOS, which helps in reducing the threshold current and offering the aforementioned exceptional advantages compared with bulk and QW lasers. In addition, due to carriers' localization, QD lasers show less sensitivity to the crystalline defects compared with QW making them suitable candidates for silicon integration in photonics integrated circuits (PICs) [74]. These are some of the unique electrical and optical properties that make these devices promising optical sources for the next generation telecommunication networks in general and MMW wireless communications, such as 5G and beyond, in particular.

The light in QW lasers is generated by thin uniform layers (quantum wells) as shown in Fig. 2.3 (a), whereas in QD, it is generated by millions of semiconductor dots/dashes less than 50 nm in diameter as shown in Fig. 2.3 (b)-(c), respectively. Figures 2.3 (d)-(e) show plan-view scanning electron microscope (SEM) image of QDashes and QDots layers respectively. Each QD acts like an isolated light source, as shown in the zoom-in SEM image of Fig. 2.3 (f), interacting independently of its neighbors and emits light at its own unique wavelength. In other words, the QD gain medium is inhomogeneously broadened, unlike the uniform semiconductor layers in QW lasers shown in Fig. 2.3 (a), which are widely deployed in telecommunications networks today.

Usually the gain region of the QDots lasers consist of self-assembled Indium Arsenide (InAs) QDots layers either on GaAs substrate or Indium phosphide (InP) substrate emitting light in the O-band window (1260-1360 nm) or C-band window (1530-1565 nm) and longer wavelengths, respectively. Semiconductor lasers emitting at these two wavelength ranges have been gathered considerable attention over the past decades in the optical
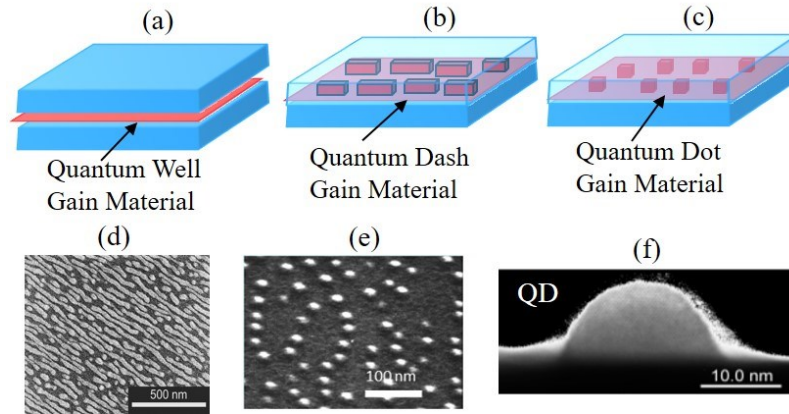
Figure 2.3: Schematics of material structures: (a) QW, (b) QDash, and (c) QDot, and plan-view scanning-electron-microscope (SEM) images of (d) QDashes layer [47] and (e) QDots layer with zoomed-in version of (f) a single InAs QD (courtesy of Dr. P.J. Poole National Research Council Canada) grown at the NRC Canada labs.

communications due to low loss and low chromatic dispersion in the standard optical fibers. The majority of studies on QDot lasers have investigated InAs/GaAs materials system with particular achievements in the 1.0–1.3 μm wavelength range [60]. The first QDots laser on GaAs substrate emitting at 1310 nm at room temperature was demonstrated by Huffaker *et al* in 1998 [75]. On the other hand, the first InP-based QDots laser emitting at ~1840 nm at 77 K was demonstrated by Ustinov *et al* [76] with the subsequent realization at room temperature by Nishi *et al* [77] during the same year. The emission of GaAs-substrate based lasers in the shorter wavelength range and the difficulty to reach longer wavelength range is due to the large lattice mismatch (7%) between InAs and GaAs compared with InAs/InP (3%). Consequently, this hinders fabrication of such lasers to operate in the telecommunication wavelength range of around 1.55 μm in the C-band and longer in contrast to the InP-based lasers [78]. Therefore, the interest of growing QDot lasers on InP-based material systems dominated in order to fully utilize the predicted performance improvements associated with QDots operating at longer wavelengths that cannot be achieved on GaAs-based material systems.

The design of InP-based QDot/Dash lasers is very similar to that of the conventional InP-based QW structures with the main difference of QDots/Dashes instead of QWs in the active region. A typical design of such structures is shown in a schematic in Fig. 2.4 (a) [60]. The structure usually consists of an InGaAsP or InGaAlAs waveguiding core,
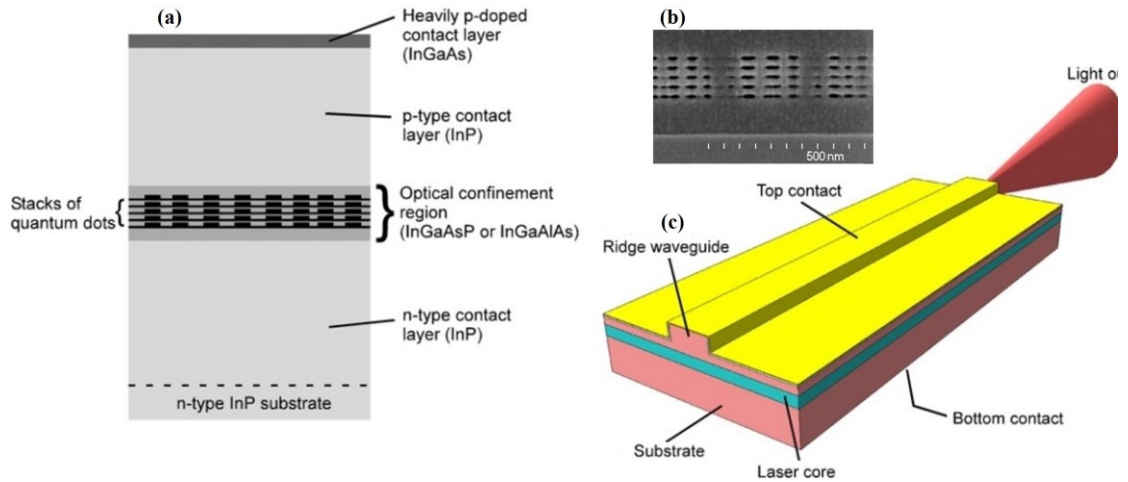
Figure 2.4: (a) Schematic of a typical InP-based laser layers structures, (b) Cross-sectional SEM image of a selectively etched stacked five layers of InAs QDots in an InGaAsP matrix showing vertically well aligned QDots, and (c) Schematic diagram of a simplest single-mode ridge waveguide Fabry–Perot laser with cleaved facets and no wavelength selecting elements [60].

typically between 200-400 nm thick, which encloses the InAs QDots/Dashes layers and providing both electrical and optical confinement for the injected carriers (electrons and holes) and lasing mode, respectively. These quaternary alloys are usually grown either on InP (100) or InP (311) B substrates. To prevent defects or dislocations due to strain-mismatch, the lattice parameters of the barriers are matched to the substrates by adjusting the relative ratio of Ga and As or Ga and Al. To obtain enough gain for lasing, multiple stacks of QDots/Dashes are used in the active region of the laser to achieve high density of QDots/Dashes as shown in Fig. 2.4 (a)-(b) [60]. In the SEM image of Fig, 2.4 (b), it can be seen that dots are perfectly aligned vertically in the different layers. This is due to the generated stain field in the layers that cap the dots and form nucleation sites for dot formation [60]. The core of the laser is surrounded by the n- and p-type doped InP cladding regions establishing the p–n diode for electrical injection. Typically, these structures are grown on an n-type InP substrate and capped with a heavily p-doped InGaAs layer for good ohmic contacts. By using these structures, different semiconductor lasers can be obtained, for instance, a schematic diagram in Fig. 2.4 (c) shows a simplest form of a semiconductor single mode ridge waveguide Fabry–Perot laser [60].

The name "dash" in QDash lasers was first originated from the growth of elongated QDots structures of Indium Antimonide (InSb) grown on semi-insulating InP (001)

substrates in 1996 [79] and the growth of InAs QDashes on GaAs (211)B substrates was first reported in 1997 [80]. Nevertheless, it was not until 2001 that the first self-assembled InAs QDash lasers grown by MBE on InP (001) substrates were reported in [78]. The elongated quantum wire-like structures as shown in Fig. 2.3 (d) tend to result from the small lattice mismatch and subsequent complex strain distribution during the self-assembly growth of QDots. The QDashes exhibit mixed intermediate characteristics in-between the QW and QDots and due to the broadband gain profile, they can emit in the wavelength range between > 1.4 μm and > 2.0 μm [72]. Figure 2.5 shows the progress in the lasing wavelength of InAs/InP QDot and QDash lasers at room temperature with tuning ranges of approximately 0.4 μm and 0.6 μm, respectively, and with the lasing wavelength beyond 2 μm covering the entire optical communication spectrum of C, L and U bands [72]. Similar to QWires, the carriers in QDashes are confined in two dimensions and are free to move only along the elongated direction. The QDashes have generally 10 to 20 nm widths, 1 to 4 nm heights, and lengths in the range of ~30 to hundreds of nm. In addition, QDashes tend to achieve higher material and model gain compared to QDots due to large volume of material coverage [72].

After the first demonstration of InAs/InP QDash laser [78], numerous research works have been reported exploring and investigating the exceptional characteristics of QDashes, including different material systems, such as InAs/InGaAlAs/InP [81] and InAs/InGaAsP/InP [82], different types of lasers, such as single mode lasers [83], dual-mode lasers [36], and mode-locked multi-wavelength lasers [39], [40], [84]–[87], and optical injection locking [88]–[90].

2.1.3 Quantum Dot/Dash Multi-Wavelength Lasers (QD-MWLs)

The QDot and QDash gain media can be used to realize semiconductor QDot/Dash multi-wavelength lasers (QD-MWLs) that operate over wider wavelength range, thanks to the broadband gain profile of QDot/Dash materials. The gain profile of QDot/Dash materials is significantly broader than their conventional QW counterparts due the large inhomogeneous broadening linked with Dot/Dash size variations, which is very useful for making tunable and broadband lasers with wider wavelength range [60] as shown in Fig.
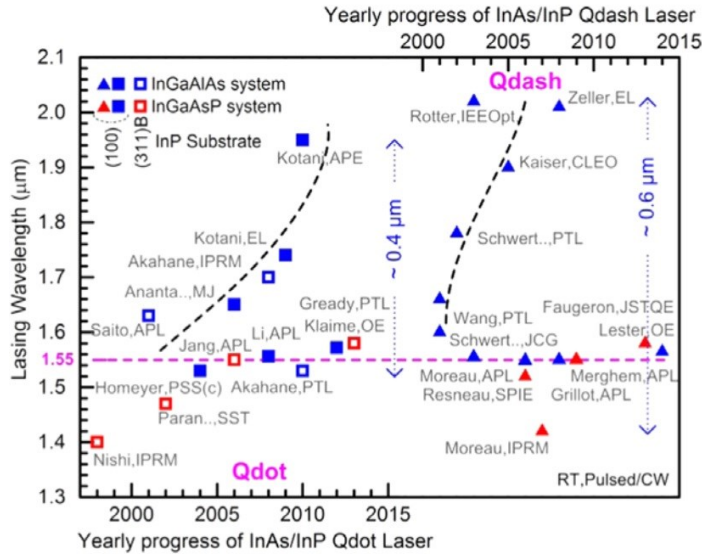
Figure 2.5: Chronological progress of heterostructure lasers showing the recorded lasing wavelength range at room temperature (RT) for InAs/InP QDot (squares) and QDash (triangles) lasers at the time of publication [72].

2.5 and Fig. 2.6 (a), respectively [72]. Figure 2.6 (a) summarizes the demonstrated broadband InAs/InP QDots/Dashes laser diodes along with superluminescent diodes (SLD) [72]. Thus in the case of Fabry–Perot (F-P) lasers, the combination of large gain bandwidth and gain saturation in QDot/Dash medium can result in broadband optical spectra having multiple optical lines with flat-topped at different wavelengths (multi-wavelength) as the drive current is increased, as shown in Fig. 2.7 for a 860 μm long F-P laser with a 3 μm
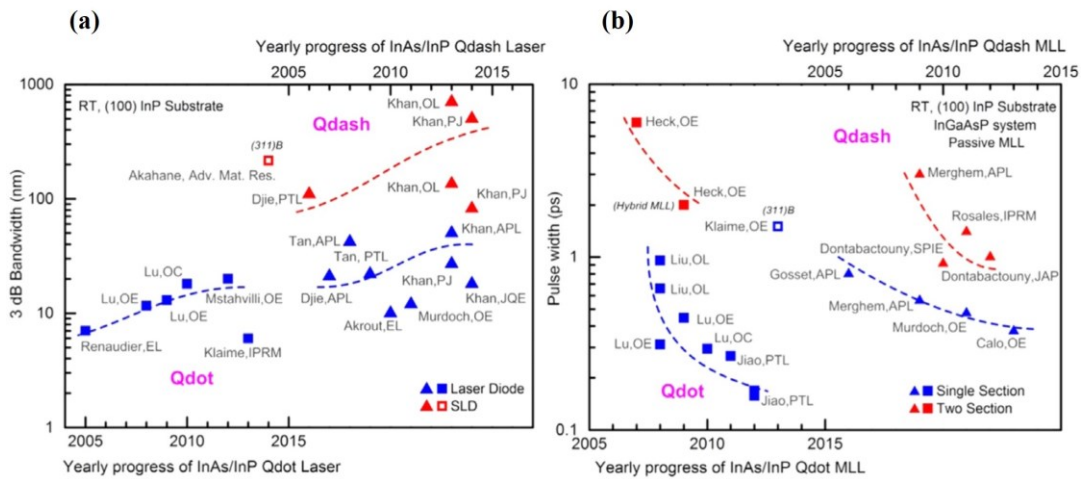
Figure 2.6: Chronological progress reported for InAs/InP QDot (squares) and QDash (triangles) lasers and MLLs achieving (a) broadband emission, and (b) reduced pulse width, respectively [72].

22
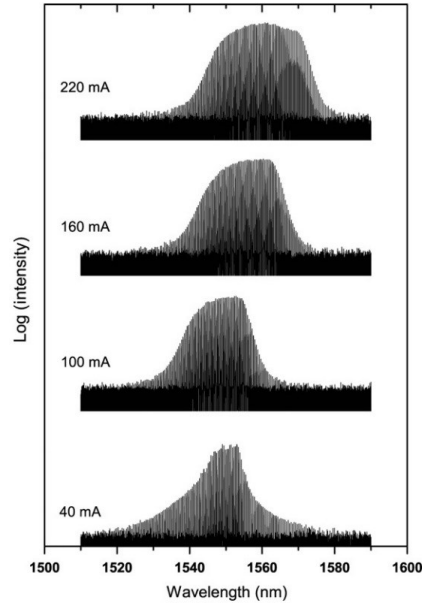
Figure 2.7: Lasing spectra of an InAs/InP QD-MWL as a function of injection current at room temperature [60], [66].

wide waveguide in CW operation mode at room temperature[60], [66]. The spectrum of this laser at 240 mA is comprised of multi- wavelength F-P modes with 3dB bandwidth, signal-to-noise ratio (SNR), and total optical power of greater than 15 nm, 62 dB, and 40 mW, respectively.

This shows that the broad gain spectrum of QDot/Dash gain media make them ideal candidates for realizing coherent QD-MWL sources using mode-locking schemes to generate simultaneous phase locked multi-wavelength channels where the spacing between the adjacent channels is determined by the cavity length. Such laser sources are ideal contenders for the high capacity next generation communication networks, especially 5G and beyond MMW wireless communication networks, where a single such device can be used to replace many individual laser sources. In addition, the channel spacing of the device can be tuned to acquire the desired RF MMW signals range by either controlling the cavity length or modulating the device with an external source.

Furthermore, another simple approach of realizing RF MMW signals with high spectral purity is the design QD dual-wavelength optical sources with high correlation between the modes, particularly in the C-band, for next generation of broadband MMW wireless communication networks. Multi-wavelengths including dual-wavelength can also be

achieved in QD DFB/DBR cavity arrangements by using specialized gratings or/and multi-sections including external cavities. However, the dual-wavelength modes obtained in such arrangements are usually not coherent and may not be correlated compared to F-P mode-locked lasers (MLLs), except in the case where optical modes are from common cavity gain medium. In the case of DFB/DBR QD-MWLs (mostly dual-wavelength) [36], [91], desired modes (may be common cavity modes) are enhanced to oscillate in the cavity and unwanted spectral features are suppressed either through different specialized gratings or the combination of gratings and multi-sections. This means that these modes experience lower losses and stronger amplification as they travel back and forth in the cavity. They can achieve relatively high phase correlation in the case of common cavity modes.

2.1.3.1 Mode-Locking in QD-MWLs

Typically, coherent multi-wavelength channels in semiconductor QDot/Dash heterostructures are achieved by virtue of mode-locking in F-P cavity given the broad gain spectrum and fast dynamics offered by the QDot/Dash materials [92], [93]. Mode-locking in QD-MWLs locks/synchronizes the phase of longitudinal modes in the F-P cavity of the laser. This results in a regular train of very short optical pulses spaced by the repetition period or the cavity round-trip time, T_r, in time domain, ranging from few tens of picoseconds (ps) to femtoseconds (fs), which correspond to a broadband coherent frequency comb with free spectral range (FSR), $F_r = \frac{1}{T_r}$, ranging from few GHz to 100s of GHz in the frequency domain. This means that the different longitudinal modes simultaneously oscillate in the laser cavity with synchronized stable phase and amplitude relationship that results in coherent low noise multi-wavelength broadband optical frequency comb. Different techniques are used to achieve mode-locking in semiconductor QD-MWLs, which can be broadly classified into three main categories including active mode-locking, passive mode-locking, and hybrid mode-locking. Among them, passive mode-locking technique has been widely used to generate ultra-short optical pulses. In active mode-locking, an external source is used to modulate the gain section of the laser with frequency equal to the mode spacing or repetition frequency of the cavity [94], [95]. On the other hand, passive mode-locking is achieved without using any external source by either incorporating a saturable absorber together with the gain section within the laser

cavity of a two-section device [96], [97] or through self-pulsation due to strong non-linear effects in the laser cavity of a single-section device [92], which is explained later in this section. Hybrid mode-locking is the combination of both active and passive mode-locking [94], [98].

After the first demonstration of passive mod-locking in two-section GaAs-based 1.3 μm QD laser in 2001 with pulse repetition rate of 7.4 GHz and a duration of 17 ps [96], several studies have been reported on InP-based passively mode-locked QD-MWLs based on two-section [85], [97], [99], [100] and single-section [40]–[42], [82], [85], [86], [92], [93], [99], [101]–[103] cavities. The first self-pulsating monolithic single-section InP-based F-P semiconductor QD-MWL was demonstrated by *Renaudier et al* in 2005 with a repetition rate of 45 GHz at 1.5 μm and a 3dB beat-note linewidth of 70 kHz showing mode-locking [101]. On the other hand, passive mode-locking in two-section InP-based QDash-MWL was first studied by *Gosset et al* in 2006 in conjunction with single-section devices [99], whereas the first two-section InP-based QDot-MWL was demonstrated by *Heck et al* [97] in 2006 with pulse generation at 4.6 GHz and pulse durations of 6 ps to 11 ps at around 1.53 μm. Thus by manipulating the broadband nature of the QDot/Dash materials, ultra-short pulses are generated based on passive mode-locking techniques with the reported values of pulse duration progressively reaching to the fs range with time, as shown in Fig. 2.6 (b).

In the case of a self-pulsating single-section QD lasers, the device is usually comprised of only a gain section where mode-locking/phase-locking between the longitudinal modes of the F-P cavity is attributed to the stronger non-linear effects of self-phase modulation (SPM), cross-phase modulation (XPM) and the resultant enhanced four-wave-mixing (FWM) non-linear phenomenon within the QD laser structure [86], [92], [99]. This process of FWM form a strong correlation between the phases of the longitudinal modes of the F-P cavity where more modes are locked together and brought above the lasing threshold, eventually leading to ultra-short pulses train with a repetition rate corresponding to the cavity round-trip time [92]. This also helps to reduce the mode partition noise, and hence the relative intensity noise (RIN) of the individual modes [86]. Thus owing to the inhomogeneous gain in QD materials, the mode competition is dramatically suppressed
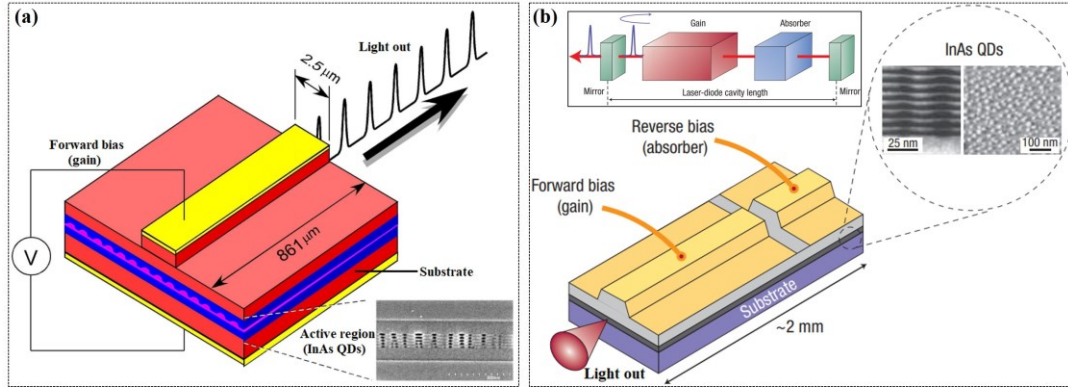
Figure 2.8: Schematic of a self-pulsating single-section monolithic InAs/InP QD-MWL (Inset, plan-view SEM image of QD layers) [93]. (b) Schematic of a monolithic two-section QD (Insets, main components that form the laser diode and transmission electron microscopy (TEM) photographs of QD layers) [94].

leading to very stable QD-MWLs with tens or hundreds of longitudinal lasing modes [93]. Figure 2.8 (a) shows an example of a self-pulsating passively mode-locked monolithic single-section InAs/InP QD-MWL which can generate ultra-short pulses with repetition rates of 10 to 100 GHz depending on the active length of F–P cavity [93]. On the other hand, in the case of passively mode-locked two-section devices, there is a gain section as well as a saturable absorber incorporated into the laser cavity constituting two-section F–P device as shown in Fig. 2.8 (b) [94]. The gain section is forward biased to provide optical amplification while the saturable absorber section is reversed biased to achieve mode-locking condition. Thus the passive self-mode-locking in the two-section devices is achieved through interplay between gain and absorption sections where the absorption also helps in shortening the circulating pulses.

In both single and two-section laser structures, the device generally takes the form of a typical QD p-i-n-doped semiconductor laser diode where the gain medium is comprising of multiple stacks of QDs layers sandwiched between multiple confinement layers of III-V materials including 3D barriers, 2D wetting layers and spacers on a substrate of InP or GaAs. The wetting layers interconnect the 0D QDs while the barriers are for better confinement and modal gain. The spacers are used for uniform growth of QDs, which separates each QD layer. After electrical injection, the carriers are transported from the top-layer to the barrier and then into the wetting layer before being captured into the QDs [67]. Furthermore, mode-locking requires inhomogeneously broad gain medium, which is

provided by the QD materials along with the aforementioned mechanisms, in order the different longitudinal modes to simultaneously oscillate in the laser cavity with a stable phase relationship. Thus due to small carriers' confinement factor and discrete delta-function like density of states, QD materials achieve broad gain bandwidth, ultra-fast carrier dynamics, small linewidth enhancement factor and high saturation powers, which lead to better mode-locking compared to Bulk and QW materials.

Passively mode-locked QD-MWLs are considered cost-efficient due to simple and monolithic design with better stability and performance. Specifically, self-pulsating single-section InAs/InP based semiconductor QD-MWLs emitting light over a large wavelength range covering the C- and L-bands with a channel spacing from few GHz to THz and a total output power of ≥50 mW at room temperature are reported [92], [93], [104]–[106]. These QD-MWLs exhibit a frequency comb nature with a broad spectrum of equally spaced optical phase-locked modes with correlated phase noise and generate ultra-short pulses train having a repetition rate that corresponds to a specific frequency depending on the laser cavity length design. For instance, the optical spectrum, pulses train, and pulse width for one of such devices with a cavity length of 456 μm are shown in Fig. 2.9 (a), Fig. 2.9 (b) and Fig. 2.9 (c), respectively [135].

Moreover, QD materials exhibit more stable mode-locking with stable pulse train having low phase and amplitude fluctuations compared to Bulk and QW [86], [98]. Therefore, QD-MWL devices have ultra-low intensity and ultra-low phase noise, which are desirable for spectrally pure MMW signals generation for 5G wireless communications. Due to the high correlation and phase matching between the longitudinal modes of the passively mode-locked QD-MWLs, the resultant RF beat note linewidth is much narrower than the spectral linewidth of individual modes. This shows that better mode-locking results in low phase noise, which in turn results in narrow spectral linewidth. Since phase noise translates to the spectral linewidth. Owing to the small confinement factor in QD materials, less spontaneous emission is coupled to the lasing modes in QD-MWLs leading to reduced phase and amplitude noise and consequently to narrow RF spectral linewidth as compared to Bulk and QW as can be seen in Fig. 2.10 [41], [86], [103]. Figure 2.10 (a) shows RF beat-note linewidth for mode-locked lasers based on Bulk, QW, and QD
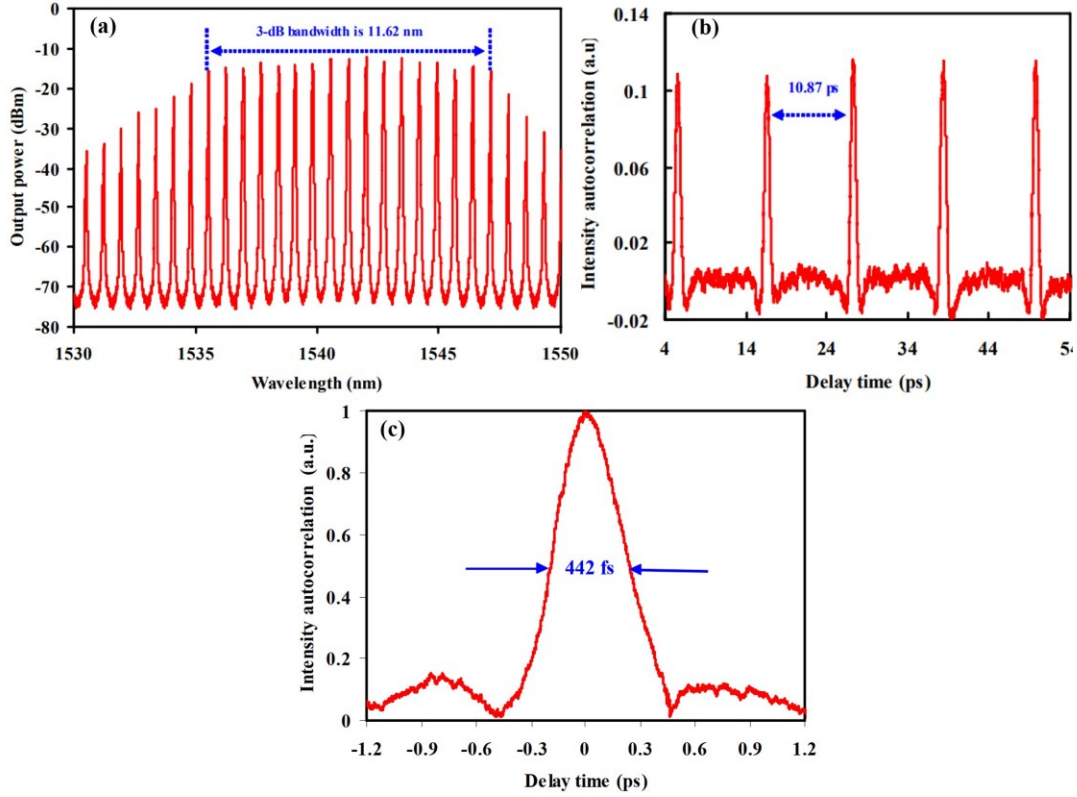
Figure 2.9: (a) Optical spectrum of a passive mode-locked single-section InAs/InP QD-MWL with an active cavity length of 456 μm and ridge width of 2.5 μm at an injection current of 45 mA with (b) its optical intensity autocorrelation pulse trains with the periodic time of 10.87 ps, which corresponds to a repetition rate of 92 GHz when the injection current is 60 mA, and (c) recorded pulse width corresponds to 312-fs at the injection current of 45 mA [92].

materials [41], [103], whereas Fig. 2.10 (b) shows mod-beating measured spectrum for QW and QD-MWLs with identical designs which were grown and processed at the same time [86]. The reported RF beat-note linewidth is typically between few hundreds of hertz (Hz) to few tens of kilohertz (kHz) for QD-MWLs as compared to hundreds of kHz and on the order of MHz for QW and Bulk lasers, respectively [41], [103]. This consequently leads to a reduced timing jitter in such devices [87], [88], [98], [102], [103]. Both low phase noise and timing jitter are crucial performance elements considering the optical sources for MMW signals generation.

Similarly, the intensity noise performance of QD-MWLs is shown to be better than QW, especially at low frequencies, which is very important for data communication. It is reported that below 2 GHz, the RIN for individual modes from a QW laser was much higher than that for the QD-MWL, reaching to as high as −95 dB/Hz for QW compared to −118
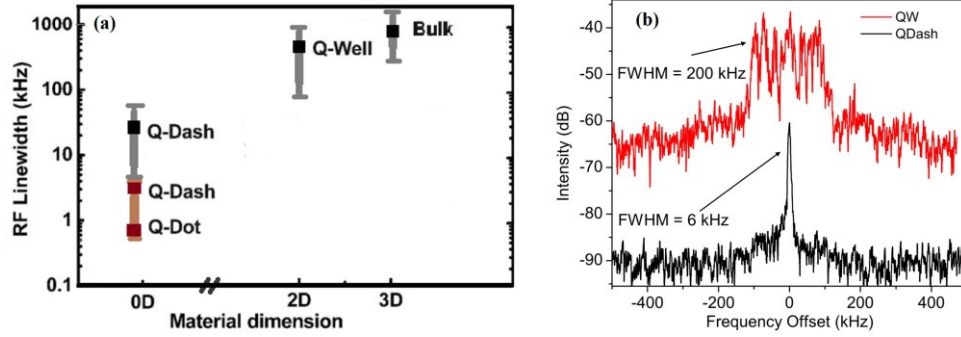
Figure 2.10: An RF beat-note linewidth comparison between Bulk, QW, and QDot/QDash material structures [41], [103]. (b) Comparison of the measured mode-beating spectrum for identical designs of QW and QD-MWLs with RF linewidth of 200 kHz and 6 kHz, respectively (FWHM: full width at half maximum) [86].

dB/Hz for QD at 10MHz [86]. The average RIN for individual channels of QD-MWL devices is reported to be typically less than – 130 dB/Hz [39], [103], [106]. In summary, self-pulsating single-section passively mode-locked QD-MWLs are simple coherent monolithic integrated low-cost chip-scale frequency comb sources which operate with a single DC power supply and having flat broadband spectra with good noise performance.

It is due to the aforementioned inherent properties of QD material that single-section passively mode-locked InAs/InP QD-MWLs have recently attracted more attention for generating RF MMW signals with high spectral purity and accuracy. The focus of this work is on the experimental investigation of such QD-MWLs along with a class of novel synthesized grating based monolithic semiconductor InAs/InP QD dual-wavelength DW-DFBLs with common cavity modes.

2.2   Millimeter-Wave Wireless Communications

Millimeter-wave (MMW) is the band of extremely high frequency spectrum between 30 GHz and 300 GHz with enormous amount of available bandwidth, which corresponds to a wavelength range between 1 and 10 millimeters. The study of millimeter-wave dates back to more than 100 years with the experimental demonstrations by Bose and Lebedew at wavelength range as short as 5 and 6 mm in 1890s [107]. However, the application of MMW in radio mobile communications was originally conceived in the early 1990s and 2000s with the design of wireless system and channel propagation model, characterization
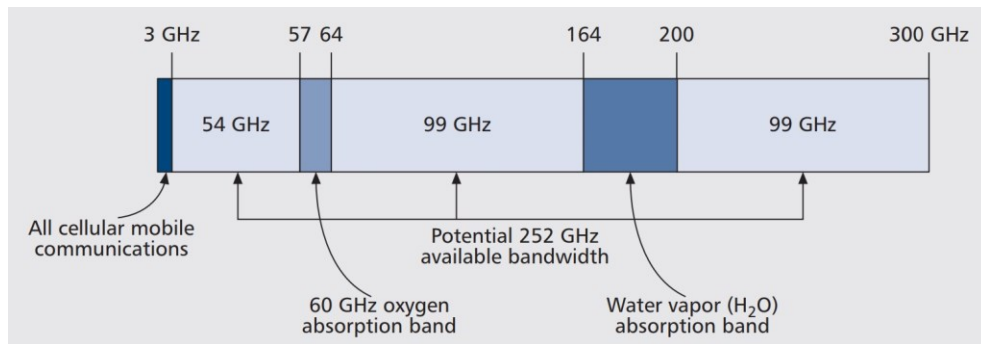
Figure 2.11: MMW spectrum [109]

and measurements [108]. Afterward, the feasibility of MMW for next generation mobile broadband wireless communications with Gb/s data rates was demonstrated in 2011 [109]. It was shown that between 3 and 300 GHz spectrum, about 252 GHz can potentially be exploited for mobile broadband wireless communications as can be seen in Fig. 2.11 [109]. Because of the availability of continuous broad bandwidth globally unlicensed spectrum, the 57–64 GHz oxygen absorption band can also be used for short range wireless communications with fiber-like connectivity. Thus, MMW wireless communications opens up new opportunities for achieving higher data rates to bridge the capacity gap between the high capacity fiber optical links and lower frequency wireless links. In addition, a variety of measurements have been demonstrated at 28, 38, 60, and 73 GHz showing the feasibility of MMW for next generation of wireless communications [1], [110], [111].

Thus, due to the increasing demand for high bandwidth and faster data speed, and the congestion in sub-6 GHz spectrum where current wireless communication systems operate, more recently, there has been growing interest in exploiting the under-utilized MMW spectrum for 5G and beyond wireless communications networks. 5G is aimed to make use of the plentiful available spectrum in the higher RF bands including higher microwave and MMW frequency bands to deliver multi-Gb/s data speeds. Towards this, frequency bands between 24.25 GHz and 71 GHz are specified by the 3GPP for 5G NRs, which are expanded from 24.25-52.6 GHz in Release 15 [6] to 52.6-71 GHz in 17 [7] as shown in Fig. 2.12 [112]. These higher frequency bands in the MMW spectrum both licensed and unlicensed with abundant available bandwidths are inevitable in order to support the enhanced diverse requirements of the 5G envisioned various usage scenarios and
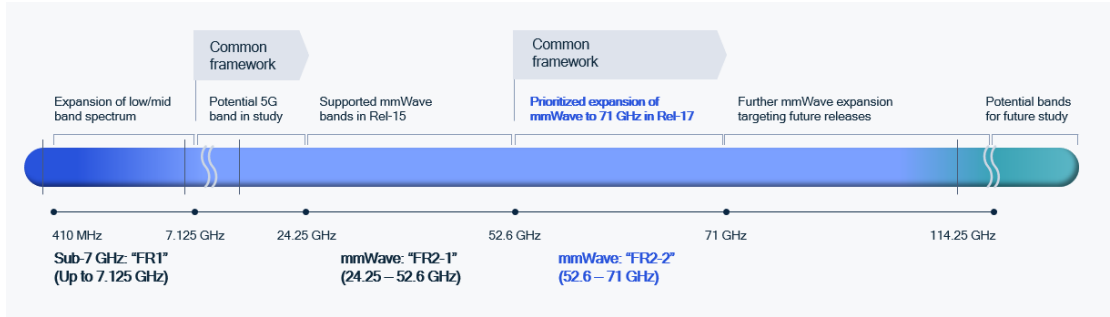
Figure 2.12: 3GPP 5G MMW frequency bands with potential future expansion [112]

applications, such as eMBB communication that features 20Gb/s peak data rates with 100 Mb/s reliable user experience in wide coverage area and expected Gb/s in hotspot cases [4]. Moreover, the use of such spectrum at the untapped MMW frequency bands is considered one of the main differences between 5G and its predecessors, i.e., 4G [1]. Thus, MMW communications offer many advantages, such as large bandwidth with the possibility of achieving optical fiber-like data rates, miniaturized components, narrow beams with better immunity to interference, low latency, high security, and efficient spectrum reuse.

2.2.1 Millimeter-Wave Key Challenges

Despite the potential superior characteristics of MWW compared to lower frequency bands, there are several challenges associated with using MMW in the next generation of wireless communications. Some of the critical challenges are briefly described in the following sub-sections.

2.2.1.1 Millimeter-Wave Propagation Characteristics

All radio signals usually experience some form of loss or attenuation while propagating from the transmitter to the receiver, mainly due to absorption or scattering. However, due to the significantly shorter wavelength compared with the lower portion of the spectrum, for instance, the sub-6-GHz spectrum, MMW has distinctive propagation characteristics in terms of propagation path loss and other environmental effects, such as atmospheric gaseous attenuation (water vapor and oxygen absorption), precipitation attenuation (rain), scattering effects, diffraction, and foliage and solid objects blockage [113], [114].

31

Consequently, MMW wireless communication is highly dependent on the propagation environment.

2.2.1.1(a) Free-Space Path Loss

MMW frequency signals are highly susceptible to propagation path loss compared with longer wavelength microwave or other lower frequency bands, i.e., below 6-GHz. The propagation path loss essentially refers to the reduction in the signal strength (power density) as it travels from the transmitter to the receiver. The received power in the case of free-space transmission can be described by Friis transmission formula as follows [108];

$$P_r = P_t G_t G_r \left(\frac{\lambda}{4\pi}\right)^2 d^{-n}, \qquad (2.1)$$

where P_t, G_t, G_r, d, and λ represent the transmitted power, transmitter's antenna gain, receiver's antenna gain, transmission distance between transmit and receive antennas, and the operating wavelength, respectively. Besides, n is the path loss exponent, equal to 2 in free space. The expression in (2.1) can also be used to approximately describe the received power in the case of non-free-space propagation by altering the value of path loss exponent according to the channel measurements. The value of path loss exponent n usually varies between 2 and 6 for different propagation conditions. Thus, the frequency and distance dependent free-space path loss (FSL) or spreading loss, which is described as the ratio of the transmitted power to the received power, between two isotropic antennas with unity gain and unobstructed path can be derived from equation (2.1) as follows;

$$FSL = \frac{P_t}{P_r} = \left(\frac{4\pi d}{\lambda}\right)^2. \qquad (2.2)$$

After changing the units in equation (2.2), the FSL in line-of-sight (LOS) configuration can be expressed in the decibels as follows [114];

$$FSL_{dB} = 92.4 + 20\log f + 20\log d, \qquad (2.3)$$

where frequency f and distance d are in gigahertz and kilometers, respectively. Thus, at higher frequencies, the FSL significantly increases, which limits the range of MMW

wireless communications links to shorter distances. For instance, the FSLs at 28 GHz and 70 GHz are 22.9 dB and 30.9 dB, respectively, more than at 2 GHz [113]. Moreover, non-LOS propagations experience additional losses compared with LOS. Therefore, the excessive propagation path loss of MMW signals in the wireless channel requires some sort of compensation to make MMW wireless communications practical, which can be achieved by employing high-gain phased array antennas with multiple-input-multiple-output (MIMO) and beamforming technologies.

2.2.1.1(b) Atmospheric and Rain Losses

MMW wireless communication links are also highly prone to atmospheric transmission losses, especially losses due to absorption and rainfall attenuation, given the shorter wavelength of the MMW signals. This results in additional path loss for MMW propagation. The gaseous particles usually absorb the MMW signal in the air when propagating through the atmosphere, which results in transmission losses. The atmospheric absorption is mainly dominated by the resonances of oxygen (O_2) and water vapor (H_2O) molecules. Moreover, the absorption is frequency dependent and different frequency signals experience different losses with the greater losses occur at certain frequencies that coincide with the mechanical resonance frequencies of the gas molecules as shown in Fig. 2.13 [114]. The atmospheric absorption (mainly oxygen and water vapor) is dominant in
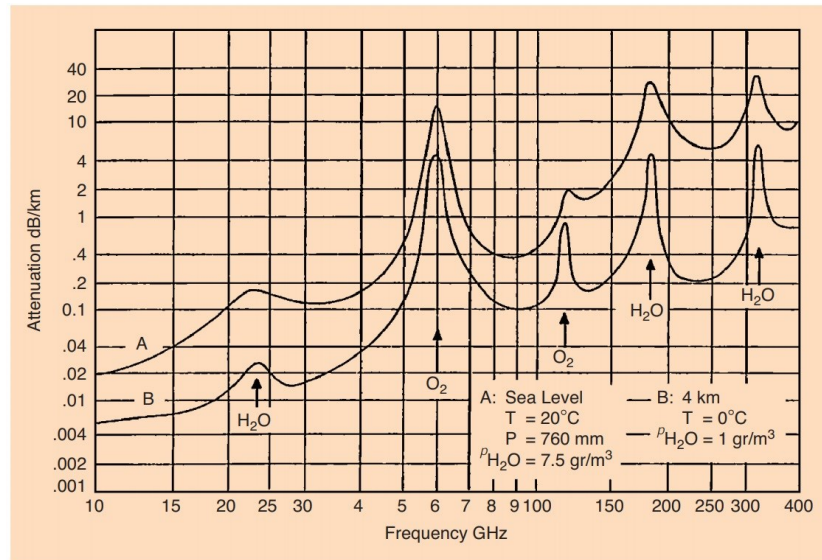
Figure 2.13: MMW average atmospheric absorption, taken from [114].

33

the vicinity of 23, 60, 120, and 180 GHz as can be seen in Fig. 2.13. At these frequencies, the absorption of radio signals is relatively high resulting in higher attenuation, hence leading to shorter MMW wireless communication links.

Furthermore, rain is the dominant propagation impairment for wireless communication links above 10 GHz. Rain attenuation is both due to absorption and scattering, depending on the size of the raindrops and carrier wavelength. Because the size of the raindrops is approximately identical to radio wavelengths at the MMW frequencies, consequently inducing a scattering effect in the radio signals [114]. The rain attenuation is dominant across all the frequency spectrum above 10 GHz except at 60 GHz, 120 GHz, and 180 GHz, where the atmospheric attenuation is still prevalent even in the presence of a rainfall rate above 20 mm/h, as shown in Fig 2.14 [115]. Besides, snow, hail, and fog have a relatively minor effect on the MMW propagation in the lower portion of the spectrum [113]; nevertheless, the impact of snow accumulation on the antenna surface or antenna radome cannot be ignored [116]. Thus, MMW communication links can be drastically affected by atmospheric and rain attenuation, with rain being the dominant impairment factor. However, considering the small cell size on the order of 200 meters in the urban environment, MMW wireless communication is still feasible in the presence of atmospheric and rain attenuation [1]. It has demonstrated that the effect of rain will be minimal on the propagation of MMW at 28 GHz and 38 GHz for a distance of less than 1 km. For example, the rain attenuation is expected to be about 1.4 dB under heavy rainfall of about 1 inch/h for cellular propagation at 28 GHz over a 200 m distance [1].
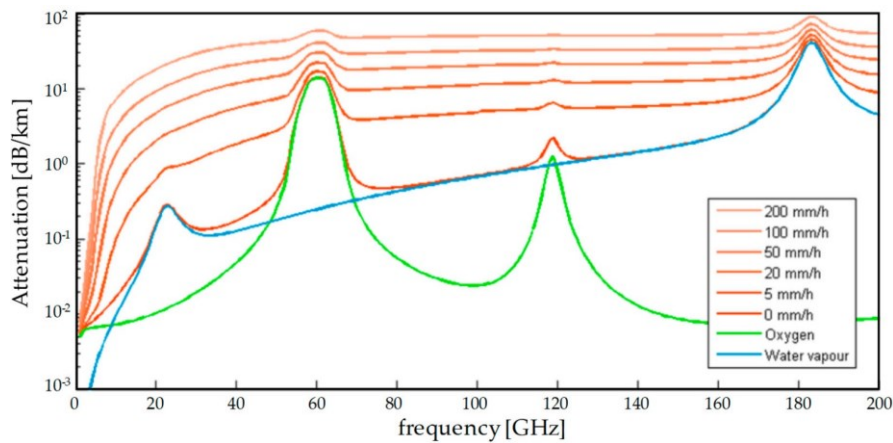
Figure 2.14: Combined atmospheric and rain attenuation, taken from [115].

34

2.2.1.1(c) Foliage and Penetration losses

Foliage losses and solid object blockages are other critical challenges that impair radio signals at the MMW frequencies. Foliage losses are non-negligible for MMW and can be a limiting factor for MMW wireless communication links in some cases, as shown in Fig. 2.15 [109]. For instance, for a penetration of 10 m, the foliage loss at 80 GHz can be about 23.5 dB compared to about 8.5 dB at 3 GHz. Moreover, unlike lower frequency radio signals, MMW signals cannot penetrate well through most solid materials due to their shorter wavelength nature. For example, there is about 28 dB and 40 dB penetration loss for bricks and tinted glass, respectively, at 28 GHz, which is significantly higher than the losses at microwave frequency bands [117]. In addition, based on penetration loss measurements for building materials in an outdoor urban environment at 9.6, 28.8 and 57.6 GHz, it was found in [118] that loss was slight for clear glass in a LOS path configuration. However, it increased by 25 to 50 dB for coated materials on the glass wall with no detection in most cases through steel-reinforced concrete or brick buildings. Similarly, in the case of the non-LOS path between buildings of several common materials, the loss was found to be in access of 100 dB [118]. Although the penetration losses for dry walls and clear glass are relatively lower, the enormous propagation path loss, combined with the penetration loss, makes it nearly impossible to provide coverage from an outdoor base station to an indoor area and vice versa. Radio-over-fiber (RoF) technology can mitigate
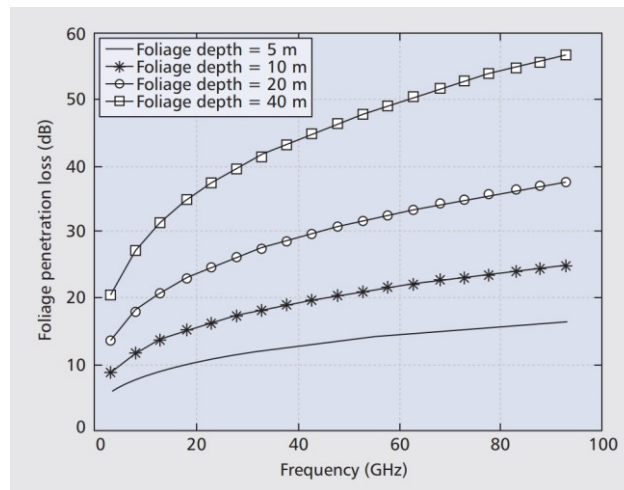
Figure 2.15: Foliage loss, taken from [109]

this problem by distributing the high-frequency MMW signals in the optical domain to indoor and longer distances.

Besides the already discussed propagation factors, MMW wireless communication links are also subject to additional propagation effects caused by other processes, such as scattering effects (defused and specular reflections), multi-path effects, Doppler effect, diffraction, refraction, cross-polarization, and antennas' misalignment.

2.2.1.2 Millimeter-Wave Signals Generation

Apart from the peculiar characteristics of MMW signals, operation at such high frequencies with wide bandwidth impose significant challenges on the performance, design and implementation of electronic hardware components and systems [111], [119]. Among them, generating high performance carrier signals at the MMW frequencies is a critical challenge for electronic systems due to diverse requirements, such as large bandwidth, low phase noise, high accuracy, high efficiency, low power consumption, low complexity, and low cost. Therefore, radio signals at MMW frequencies are very challenging to generate with the traditional bandwidth-limiting electronics. The MMW carrier signals in wireless communication transceiver systems are usually realized through mixers, local oscillators (LOs), and other essential electronics by up-converting a low-frequency signal to the desired MMW frequency. The LO frequencies are commonly generated either through direct oscillators [120], [121] or based on frequency multiplication of relatively low-frequency sources [122], with the multiplier being a nonlinear device. The former has the limitation of maximum oscillation frequency, whereas the latter introduces more complexity to the system. Although various approaches have been demonstrated to realize high-frequency MMW signals generation electronically, they still suffer from the significantly increased complexity due to multi-stage frequency multiplication and associated cost to operate at higher frequencies > 30 GHz. In addition, the hardware performance decreases and the impairments, for instance, phase noise and frequency error, increase with frequency. Furthermore, it is impractical to distribute such high-frequency MMW signals in the electrical domain due to high losses.

Thus, compared with electronic systems that are subject to bandwidth limitations in addition to complexity, cost, and performance degradation at high-frequency operations, photonic MMW signals generation is considered a viable alternative with pronounced advantages including large bandwidth, high speed, high isolation, strong immunity to electromagnetic interference, low system complexity, small footprint, long transmission distance, and improved performance [8]–[10].

2.3   Photonic Millimeter-Wave Signals Generation and Transmission

Microwave photonics has been envisioned as a disruptive technology to generate, process, control, and distribute MMW signals. Therefore, over the past decades, photonic generation of radio signals at the MMW frequencies (30 GHz – 300 GHz) have attracted greater interest from both academia and industry [8], [9], [26]–[28], [123]–[125], particularly for applications in future seamless fiber-wireless integrated access networks, such as fronthaul of 5G and beyond mobile wireless communication networks [18], [27], [28], [123].

2.3.1   Principle of photonic MMW Signal Generation

The core concept of photonic MMW signals generation is based on the heterodyne beating of two optical signals having different wavelengths (λ_1 and λ_2) spaced at the desired MMW frequency together on a high-speed photodetector (PD), as shown in Fig.2.16 [14]. The frequency of the resultant MMW signal at the output of PD corresponds to the wavelength difference between the two optical signals. In the simplest form, the two optical signals can be stated by their respective electrical fields;
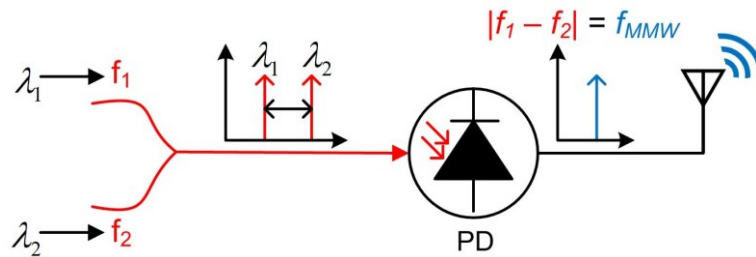
Figure 2.16: Basic principle of photonic MMW signal generation and transmission.

$$e_1(t) = A_1 \cos(2\pi f_1 t + \phi_1), \tag{2.4}$$

$$e_2(t) = A_2 \cos(2\pi f_2 t + \phi_2), \tag{2.5}$$

where A_1 and A_2 represent the amplitude, f_1 and f_2 the frequency, and ϕ_1 and ϕ_2 the phase of the two optical signals, respectively. The corresponding optical signal at the input of PD can be expressed by adding equations (2.4) and (2.5),

$$e_1(t) + e_2(t) = A_1 \cos(2\pi f_1 t + \phi_1) + A_2 \cos(2\pi f_2 t + \phi_2). \tag{2.6}$$

With the PD response being proportional to the optical intensity, its electrical signal can be evaluated from equation (2.6) as;

$$|e_1(t) + e_2(t)|^2 = |A_1|^2 + |A_2|^2 + 2A_1 A_2 \cos\big(2\pi(f_1 - f_2)t + (\phi_1 - \phi_2)\big). \tag{2.7}$$

The last term in (2.7) represents the corresponding MMW signal with its total resultant phase. Given the limited bandwidth of the PD and co-polarized optical signals, the consequent photocurrent of the generated MMW signal at the output of PD is given by;

$$I_{ph-MMW} = A\cos\big(2\pi(f_1 - f_2)t + (\phi_1 - \phi_2)\big), \tag{2.8}$$

where A is a constant term determined by the amplitudes of the optical signals and the responsivity of the PD. The term $(f_1 - f_2)$ represents the electrical frequency separation of the two optical signals generating the corresponding MMW signal. Thus photonic techniques can be used to generate RF signals of up to THz range, limited only by the frequency response of the PD. In this way, seamless fiber-wireless integration can be achieved [15] by generating MMW carriers optically, which is inevitable for 5G broadband wireless communication networks, given the enormous requirements for large bandwidth and the susceptibility of MMW signals to high transmission and propagation losses.

2.3.2   Remote Optical Heterodyne MMW RoF System Architecture

The remote heterodyning of two optical signals with data modulated on one or both of them after running over several tens of kilometers of optical fiber is the simplest and most promising approach to MMW signals generation and efficient distribution in the optical

domain. Since the remote generation of high frequency RF MMW signals not only overcomes the problem of transmission span limitation due to optical fiber dispersion [126] but also considerably reduces system and network complexity, footprint, CAPEX and OPEX. Particularly in the case of 5G wireless networks where many RRUs/RRH are expected to be connected to the CO through an optical fiber-based fronthaul network. In addition, any modulated data is preserved on the optical signals and translated to the corresponding MMW carrier signal. Figure 2.17 shows typical optical heterodyning
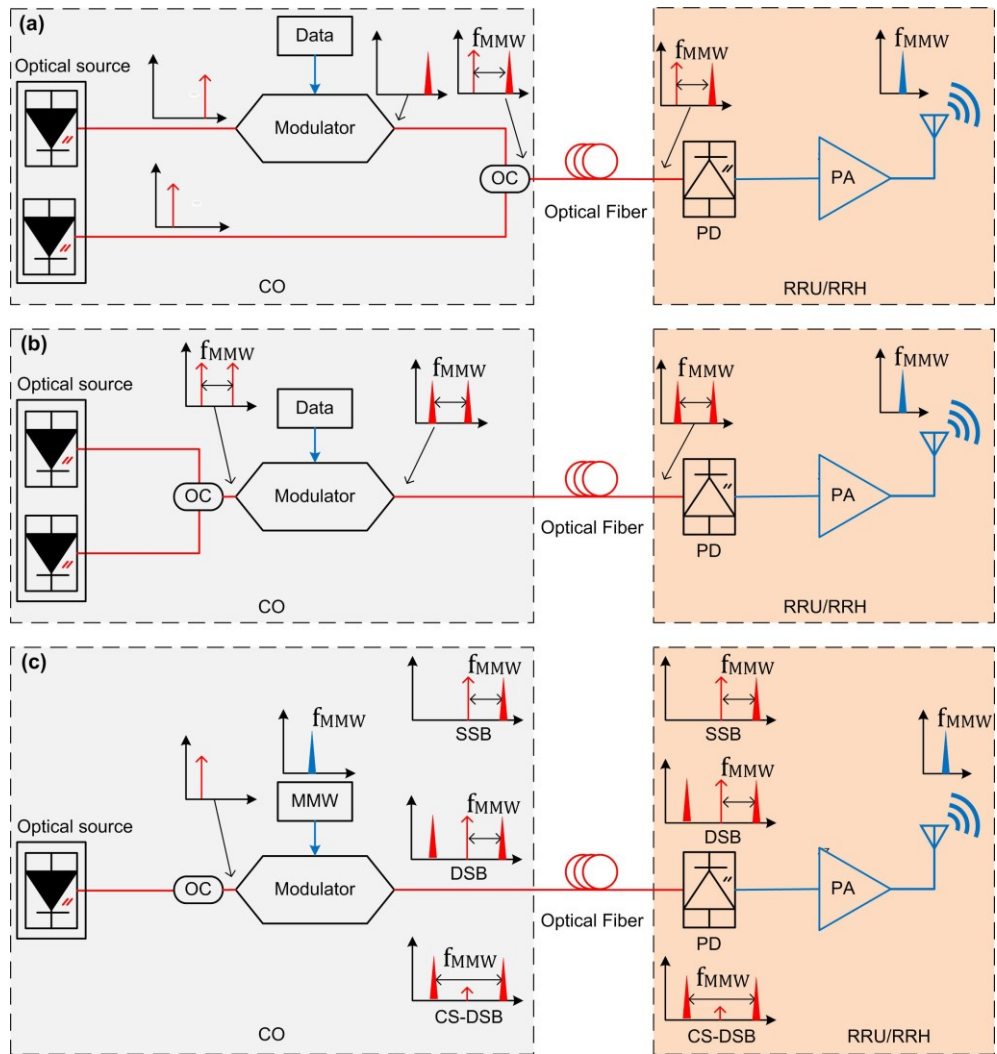
Figure 2.17: Photonic MMW signal generation and data transmission using optical heterodyning: (a) with one data modulated and one unmodulated optical signals, (b) with two data modulated optical signals, and (c) with single sideband (SSB), double sideband (DSB) or carrier suppressed double sideband (SC-DSB) MMW modulated optical signals in the transmission fiber. Insets showing figurative illustration of optical and electrical spectral components at different stages. OC: optical coupler, PD: photodetector, PA: power amplifier, CO: central office, RRU/RRH: remote radio unit/head.

schemes for generating MMW signals and data transmission in the downlink where digital or analog data can be modulated onto the optical signals in the baseband unit (BBU) located in the central office (CO). The desired MMW signal can be remotely generated optically right at the antenna in the RRU/RRH. In the first scheme shown in Fig. 2.17 (a), data is encoded onto one of the two optical modes via an optical modulator using advanced modulation formats. The optical modes could be from a common optical source or individual lasers.

In contrast, both modes are modulated with the data in the second case, as shown in Fig. 2.17 (b). The latter case might not be suitable for transmitting closely spaced signals with complex modulation formats because of the in-band beat noise resulting from the direct beating of multiple sidebands that can degrade system performance [127]. Comparatively, the former scheme is robust to in-band beating noise and chromatic dispersion. Similarly, the down-conversion of the received uplink MMW data modulated wireless signals in the duplex systems (not shown here) at the RRU/RRH to an intermediate frequency (IF) or baseband can also be achieved by employing optical channels with appropriate spacing. Depending on the implementation scenario, the uplink MMW can also be translated to the IF range or baseband at the RRU/RRH without using any additional LO source by mixing it with a bandpass-filtered downlink-generated MMW carrier [128]. Direct down-conversion of high frequency MMW signals can significantly reduce the cost and complexity of RRU/RRH, and the power budget and impairments of the fiber-optic link.

On the other hand, in the last option shown in Fig. 2.17 (c), the MMW signal is realized by directly modulating an optical carrier with the desired MMW signal either in single sideband (SSB), double sideband (DSB) or carrier suppressed double sideband (CS-DSB) configuration, with the first and last ones relatively more robust to chromatic dispersion. Nonetheless, these methods require expensive high-speed optoelectronic devices. Also, in addition to low conversion efficiency, they are comparatively more susceptible to transmission impairments [17], which degrade the system's performance and reach.

2.3.3 State-of-the-art Photonic MMW Generation Techniques

Photonics MMW signal generation has been widely studied, and many techniques have been developed. The photonic MMW signals generation techniques can be broadly classified into six main categories having further sub-categories based on the underline technology, as shown in Fig. 2.18. These techniques are summarized in Table 2.1 with their brief description and common advantages and disadvantages. Among these technologies and techniques, the most promising and flexible are OFCs based on single-section passively mode-locked (PML) semiconductor QD multi-wavelength lasers (QD-MWLs), as discussed in section 2.1.3. The PML semiconductor QD-MWL CFCs are advantageous due to their simple and compact design with a broad bandwidth spectrum providing an equally spaced large number of highly correlated and coherent optical channels with low noise. In addition, low-noise monolithic dual-wavelength lasers, especially common cavity semiconductor lasers, are considered attractive optical sources to generate RF MMW signals due to their cost-effectiveness, relatively high power, compact size, correlated and
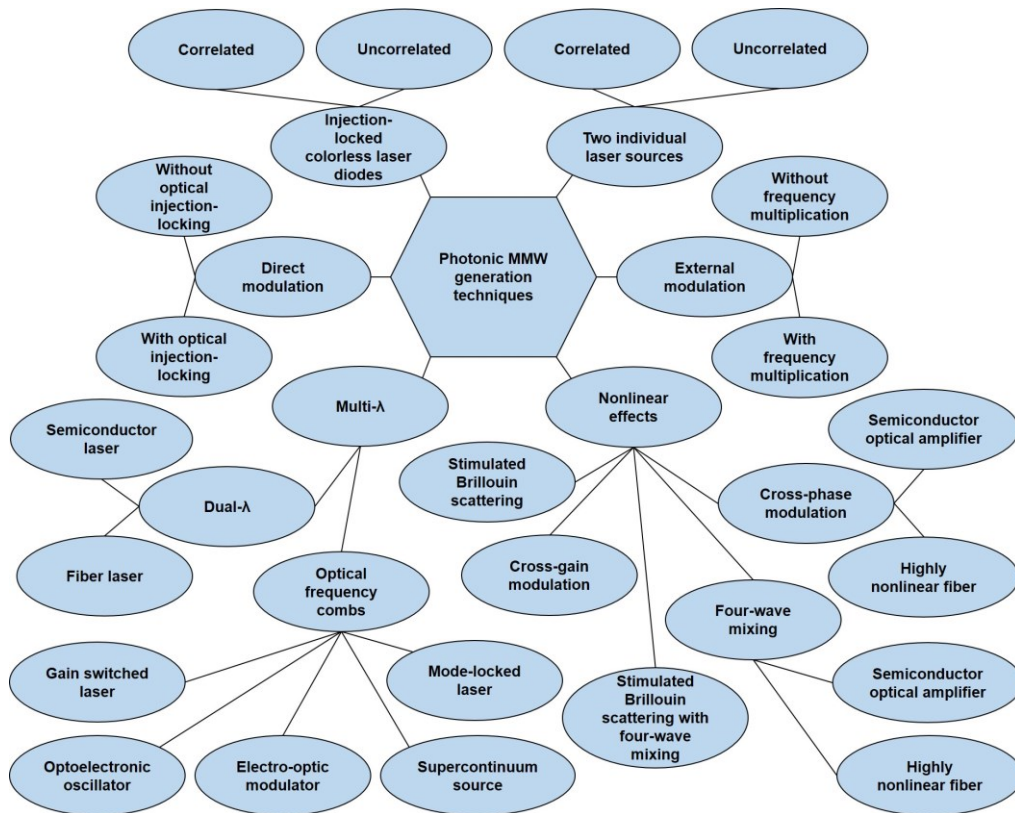
Figure 2.18: Classification of photonic MMW signals generations' techniques/sources.

low-noise modes. The semiconductor PML QD-MWL CFCs and dual-wavelength lasers have the possibility of monolithic integration with other components. In this thesis, we experimentally investigate PML QD-MWL CFC and a novel monolithic common cavity QD-DW-DFB laser for MMW signals generation and transmission by proposing high-capacity MMW RoF wireless transmission systems.

Table 2.1: Classification of photonic-aided MMW signals generation techniques based on the underline technology and in light of a thorough literature review, a brief description and some of the common advantages and disadvantages of each category. FPLD: Fabry-Perot laser diode; OIL: optical injection-locking; PD: photodetector; BW: bandwidth; CS-DSB: carrier suppressed double sideband; HNLF: highly nonlinear fibers; FWM: four-wave-mixing; XPM: cross-phase-modulation; XGM: cross-gain-modulation; SBS: Stimulated Brillouin scattering; SOA: semiconductor optical amplifier; OFC: optical frequency comb; GSL: gain switched laser; OEO: optoelectronic oscillator; EOM: electro-optic modulator; SCS: Supercontinuum source; MLL: mode-locked laser; FPLD: Fabry-Perot laser diode; LO: local oscillator; CLD: colorless laser diode; NL: non-linearity; IM: intensity modulator; MZM: Mach-Zhender modulator; PM: phase modulator; EAM: electro absorption modulator; MZI: Mach-Zhender interferometer; WDM: wavelength division multiplexing; ASE: amplified spontaneous emission; VCSEL: vertical cavity surface emitting lasers; WGMR: whispering gallery mode resonator; NOLM: nonlinear optical loop mirror; IF: intermediate frequency, PML: passively mode-locked, PMLLs: passively mode-locked lasers.

	Technique	Description	Advantages	Disadvantages
Two individual laser sources	**Uncorrelated** [19], [129]	Using two independent lasers spaced at the desired MMW frequency	• Very high MMW frequencies • Low-frequency electronics and optical devices	• MMW with low spectral purity and accuracy • Require narrow linewidth lasers
	Correlated [130], [131]	Locking two independent lasers with the modulated side-band injection-locking for the desired MMW signals generation	• Relatively high MMW spectral purity and frequency accuracy • High MMW frequencies • Low-frequency electronics and optical devices	• Complexity and cost • Require additional external sources for mode-locking
Injection-locked colorless laser diodes	**Correlated** [24], [123], [132]	Using CLDs (FPLDs with weak-cavity effect due to low end-facet reflectance) for direct data encoding and dual-mode selection and amplification with external optical source(s) for MMW generation	• Eliminating large BW optical modulator and high-frequency electronics • Flexible multi-modes selection • Correlated phase noise	• Complexity and cost • Require longer cavities • CLD narrow analog BW
	Uncorrelated [25]	Using the directly modulated selected mode and another independent optical source for MMW generation	• Eliminating large BW optical modulator and high-frequency electronics • Flexible multi-modes selection • Large tunability	• Complexity and cost • Random phase noise • Additional optical LO • CLD narrow analog BW

Table 2.1: (continued).

	Technique	Description	Advantages	Disadvantages
Direct modulation	**Without OIL** [133]	Directly modulating lasers with high RF sources for the desired RF MMW signals	• Simple and cost-effective	• Modulation BW limitation • Impairments (RIN, chirp, NLs) • Require high RF source • Unsuitable for MMW due to limited frequency (<30 GHz) • Low capacity
	With OIL [134], [135]	Injection-locking of a directly modulated laser with an external high-power master laser source for enhancing the laser's performance	• Improved modulation BW and impairment characteristics • Relatively improved capacity	• Complexity and cost • Require high RF and extra optical sources • Inadequate for MMW > 60 GHz • Sensitive to temperature fluctuation
External modulation	**Without frequency multiplication** [136], [137]	Externally modulating laser's light with a high frequency RF MMW source using a large BW optical modulator (IM (MZM), PM, EAM) for converting high frequency MMW signals to optical frequencies for transmission	• Better BW than direct modulation • Simple configuration and flexible to modulation schemes • Good spectral purity	• Require broad BW modulator and high-frequency MMW source • Impairments at high frequencies • Complex electronics • High insertion loss, high power consumption • Modulator's bias drift
	With frequency multiplication [20], [21], [138]	Using a low-frequency RF source with frequency multiplication achieved through exciting higher order harmonics or CS-DSB or different arrangements of multiple modulators in cascade, parallel, dual-polarization or combination	• Stable MMW with high frequencies using low frequency electronics and small BW modulators • Highly flexible and scalable configurations • High spectral purity	• Complexity and Cost • Require filtering of undesired harmonics • High insertion loss, high power consumption • Modulator's bias drift

Table 2.1: (continued).

Technique			Description	Advantages	Disadvantages
Nonlinear effects	**FWM**	**SOA** [139]–[141]	Exploiting the non-linear effect of FWM in SOAs for optical up-conversion through generating phase-correlated idlers by pump wavelengths	• Simple, low cost, and easy integration of SOA • Immunity to SBS • Transparent to data-rates and modulation formats	• Narrow modulation BW, inherent carrier saturation, and polarization sensitivity • Low conversion efficiency
		HNLF [124], [142]	Exploiting the non-linear effect of FWM in HNLF for optical up-conversion through generating phase-correlated idlers by pump wavelengths	• Extremely high mixing BW with multiple channels up-conversion in a WDM configuration • Transparent to data-rates and modulation formats	• Large fiber length and high input power requirements (bulky and expensive) • High power triggers SBS and low power limits FWM
	XPM	**SOA** [143]	Exploiting the non-linear effect of XPM through the interaction of optical LO and optical IF in SOA-MZI for optical up-conversion	• Better linearity, conversion efficiency, low input power requirement and insensitivity to polarization	• SOA's Limited XPM BW, channels cross-talk and complex structure • Dependency on data-rates and modulation format
		HNLF [8]	Exploiting the non-linear effect of XPM through the interaction of optical LO and optical probe signals in HNLF with NOLM or straight pass configurations for optical up-conversion	• Large mixing BW in HNLF with multiple channels up-conversion in a WDM configuration • High conversion than FWM	• Polarization sensitivity • Require power optimization for better conversion efficiency • Conversion efficiency dependency on data-rates and modulation format
	XGM [144], [145]		Exploiting the non-linear effect of XGM through interaction of optical LO and optical IF signals in SOAs for optical up-conversion	• High conversion efficiency and polarization insensitivity • High conversion than FWM	• Limited XGM BW • Need high input power • Channels' cross-talk and carrier saturation • Dependency on data-rates and modulation
	SBS [146], [147]		Exploiting the non-linear effect of SBS in optical fiber through counter propagation of pump wavelengths for selective sidebands Brillouin amplification for optical up-conversion	• Inherent transmission and amplification capabilities with easy control of the generated RF MMW signal through the injected pumps	• Complexity and cost • Large fiber length, high ASE noise and limited gain BW • Inadequate for very high-frequency • Effect of drift in pump frequency on operation
	FWM with SBS [148]		Combining the non-linear effects of FWM and SBS in SOA and optical fiber for generating and amplifying the desired optical sidebands and suppressing undesired ones for optical up-conversion	• Inherent optical frequency multiplication and selected amplification	• Complexity and cost • Large fiber length, high ASE noise and limited gain BW of SBS • Narrow modulation BW, inherent carrier saturation • Polarization sensitivity of SOA

Table 2.1: (continued).

			Technique	Description	Advantages	Disadvantages
Multi-wavelength sources	OFCs		**GSL** [18], [149]	Driving semiconductor laser (DFB or VCSEL) with a large electrical sinusoidal signal generating OFC with equally spaced multi-wavelengths	• Highly correlated channels and low phase noise MMW • Easy tunability by varying the modulation frequency	• Complexity and cost • Require high power RF source • Comb lines are limited by the laser's BW and RF source
			OEO [22], [23], [150]	Driving an OFC with the OEO either directly or in self-oscillating mode where the OFC generated tone drives the OFC in a closed feedback loop with optical storage element of long optical fiber or high-Q WGMR in different configurations resulting in multi-wavelengths	• Typically, no requirement for RF reference source in OEO • Very low phase noise	• Low power per mode • Require high-Q electrical/optical filter and combination of OEO fiber loops increasing bulkiness and complexity • Temperature stability control • High power consumption
			EOM [151], [152]	Externally modulating CW light source by a microwave signal obtaining sidebands and multiplying them by different configurations of the modulator (s) resulting in equally spaced multi-wavelengths	• Highly correlated optical channels • Stable low phase noise MMW • Tunable and adjustable FSR • Scalable and flexible	• Complexity and cost • Modulator's bias drift and high insertion loss • Require RF source • Low power per mode
			SCS [153], [154]	Exploiting optical non-linearity by injecting ultra-short optical pulses into highly NL optical waveguides or HNLFs generating equally spaced multi-wavelengths	• Require no MMW electronics and large BW modulator • Broad BW and scalability • Correlated phase	• High insertion and propagation losses • Complexity and cost • FSR is limited by the input optical source • Low power per mode
			MLL [16], [35], [37], [85], [151], [155], [156]	Locking/synchronizing the phase of longitudinal modes in the laser cavity results in a regular train of very short optical pulses with the different longitudinal modes simultaneously oscillating with synchronized stable phase and amplitude relationship leading to coherent broadband equally spaced multi-wavelength OFC	• Simple, low-cost, small size, low power consumption, broad BW, highly coherent and correlated modes, and monolithic integration, especially in the case of PML QD-MWLs • Spectrally pure RF MMW generation • No requirement for RF reference source in PMLLs	• Low power per mode • Fixed FSR • Spectral purity and frequency accuracy depend on the laser design

45

Table 2.1: (continued).

		Technique	Description	Advantages	Disadvantages
Multi-wavelength sources	Dual-wavelength sources	**Semiconductor lasers** [36], [157]–[163]	Dual-wavelengths are typically achieved either based on external cavities, separate multi-section structures with independent bias control or common cavities with different gratings configurations	• No requirement for RF reference source • Low phase noise and spectrally pure MMW, especially in the case of common cavity optical modes • Low power consumption, and monolithic integration capability • Reduce cost and complexity	• Temperature and current control for spectral purity and accuracy • Limited tunability
		Fiber lasers [27], [164], [165]	Dual-wavelengths are typically achieved in a ring or linear cavity configurations with various gain mechanisms, including EDFA, SOA and SBS, and filtering techniques within the cavity to filter and amplify the desired selected two modes and suppress all other modes	• No requirement for RF reference source • Low phase noise, especially in SBS case • Spectrally pure MMW	• Relatively complex • Require sophisticated filtering mechanism due to densely-spaced longitudinal modes • Limited tunability

2.3.4 Key Challenges of Photonic MMW Signal Generation and Potential Solutions

MMW signals in the optical domain are commonly generated using commercially available single-frequency laser sources, which might not achieve high spectral purity and accuracy due to their lack of coherence and correlation. Relative phase noise between the individual optical sources will result in noise in the generated MMW signal, degrading the system performance [166]. This can be an issue for 5G and beyond wireless communication systems, where high-order modulation techniques will be in place [18], which are sensitive to phase noise. Hence low-phase noise MMW signals are considered instrumental in facilitating the use of complex modulation formats for future MMW wireless

communication systems [167]. Besides, RIN also transfers to the generated MMW signals, consequently, impairing the performance of MMW communication systems [168]. Accordingly, the characteristics of the resultant MMW signals heavily rely on the spectral purity and stability of the laser sources. Thus, as discussed earlier, in the optical heterodyne MMW RoF configuration, the phase fluctuations of the two optical signals must be highly correlated to ensure spectrally pure MMW carrier signal generation. Since the phase noise of the two optical signals transfers directly to the generated MMW signal [9], [14] as can be seen from equation (2.8). Therefore, if the two optical signals are not phase correlated, for instance, in the case of two different free-running lasers, then the resulting MMW signal ends up with high phase noise- thus limiting the system performance [16], [18]. Conversely, if the phase of the two optical signals is correlated, i.e., an optical source where ϕ_1 and ϕ_2 vary together, then the common noise of the two optical signals cancels out and a low phase noise MMW signal is generated. This entails either the elimination or correlation of phase noise of the corresponding optical signals for the generation of spectrally pure and phase-stable MMW carrier signals. Thus, the optical MMW source lies at the heart of optical heterodyne MMW RoF technology and highly correlated and integrated optical sources are desirable for 5G and beyond MMW RoF wireless communication systems.

To this end, several schemes have been reported for the phase locking and stabilization between the optical signals, including optical injection locking [28], optical-phase-locked-loop (OPLL) [29] and a combination of them [30]. MMW generation by employing these schemes offers better frequency correlation and stabilization than based on any two free-running lasers. Nevertheless, most phase locking and stabilization approaches rely on complex and expensive devices, such as modulators, microwave reference sources and other related components that add to the complexity and cost of the system. In addition, the bias drift associated with some of the methods discussed above involves external modulators that can cause instability, limiting system performance. In addition, most techniques described in Table 2.1 are either complex and costly, not fully mature for practical applications or result in relatively broad beat-note linewidth. The most straightforward approach to attaining high spectral purity is considered to be the design of dual-mode optical sources [157] with high coherence, particularly in the C band.

Nonetheless, most of the reported dual-mode lasers are based on either external cavity [161] or separate multi-section structures with independent bias control for each section [157], [159], [162]. Therefore, such optical laser sources either involve complex control circuitry or result in a relatively broad linewidth beat-note due to the uncorrelated phase noise of the two optical modes. Instead, the generation of concurrent dual-modes from a single cavity sharing a single-gain medium is appealing due to device compactness, cost-effectiveness, high temperature stability and high spectral purity [158]. Although simultaneous two-wavelength lasing has been demonstrated in QW lasers using a single cavity structure [158], [160], relatively high spectral linewidths were achieved. Recently, quantum dot/dash (QD) based lasers have been shown to have great potential as efficient optical beat sources due to the inherent characteristics of QD materials [16], [31]–[39]. Compared to bulk and QW semiconductor materials, QD materials have superior characteristics due to their compactness, ultra-low threshold current density, ultra-fast carrier dynamics, improved temperature stability, and high spectral purity [80]. Owing to the inherent characteristics, QD materials-based lasers can achieve very narrow spectral linewidths and low RIN compared to QWs [86], [103]. Therefore, QD-MWLs are attractive sources for generating MMW signals with high spectral purity.

Several passively mode-locked InAs/InP QD-MWLs emitting light over an extensive wavelength range covering the C- and L-bands with a channel spacing from 10 GHz to 1000 GHz and a total output power of up to 50 mW at room temperature are reported [35], [39], [42], [43], [85], [87], [88], [93], [104]–[106], [169], [170]. The QD-MWL provide a simple multi-wavelength coherent comb source with the channel spacing determined by the laser cavity length, as discussed in section 2.1.3. The unique properties of these QD lasers arise from the gain medium, which is composed of millions of InAs semiconductor dots less than 50 nm in diameter. Each QD acts like a sole light source interacting independently of its neighbors and emits light at its unique wavelength. In other words, the InAs QD gain medium is inhomogeneously broadened, unlike the uniform semiconductor layers in QW lasers deployed in telecommunications today. The combination of inhomogeneous broadening and passive mode-locking results in a coherent multi-wavelength laser source where each channel is inherently stable with lower intensity noise and optical phase noise than comparable QW-based semiconductor lasers [39], [41], [42],
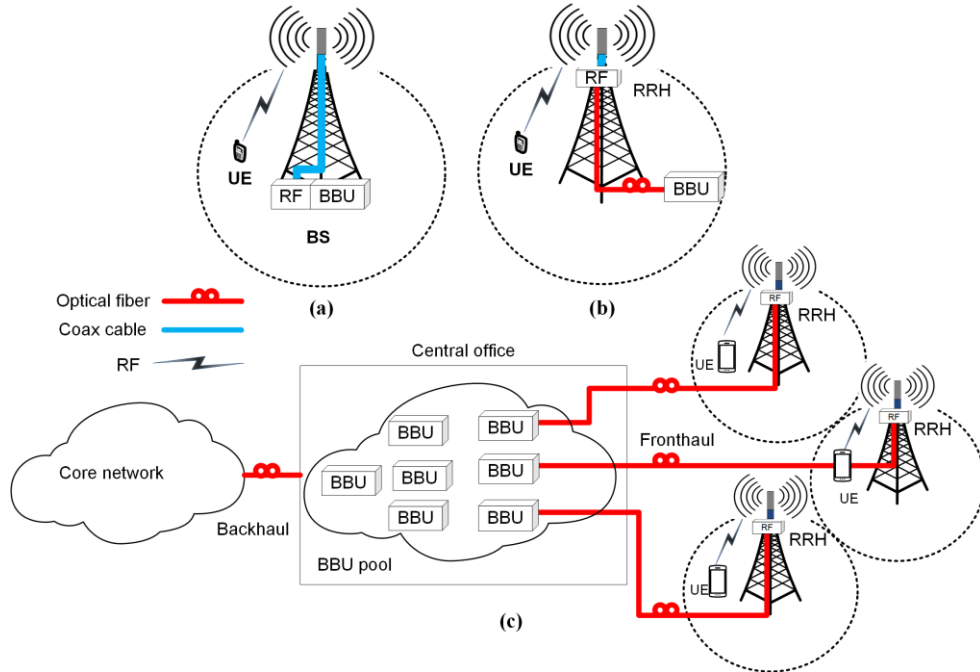
Figure 2.19: The RAN architecture evolution: (a) Conventional macro base station, (b) Conventional D-RAN, and (c) C-RAN architecture. UE: user equipment [48].

[86], [87], [98], [102], [106], [170]. Consequently, the generated MMW signals based on coherent semiconductor QD-MWL devices can achieve better spectral purity and frequency accuracy because of the high correlation of phase noise between the optical lines [16]. Thus, by considering the exceptional characteristics of QD materials, in this thesis, we investigate monolithic InAs/InP QD-MWLs, including dual-wavelength DFB laser and passively mode-locked Fabry-Perot (FP) frequency comb as an optical beat source for MMW signals generation and transmission.

2.4   Radio Access Network

The cellular radio access network (RAN) has evolved from the conventional macro base station to the centralized RAN (C-RAN) and small-size cell architecture with exponential growth in mobile users and bandwidth-hungry applications and services, as shown in Fig. 2.19. Small cells offer more coverage, capacity and spectral efficiency and C-RAN architecture is considered cost-effective, efficient, scalable, flexible, and hence influential in exploiting the full competencies of 5G [11]. Thus, the C-RAN with small cells is progressively replacing the legacy distributed RAN (D-RAN) architecture [171].

49

A traditional macro base station architecture is typically comprised of a radio equipment control (REC), aka baseband unit (BBU), and a radio equipment (RE), aka radio unit (RU), located at the premises of the mast, where RU is connected to the antennas at the top of the mast via coaxial cables, as shown in Fig. 2.19 (a). RU usually performs functions such as amplification, filtering, modulation/demodulation, digital-to-analog/analog-to-digital conversion (DAC/ADC), and frequency conversion of RF signals where the BBU is typically responsible for baseband signal processing, control and management etc. In the case of classical D-RAN, the BBUs and RUs, known as remote radio heads/units (RRHs/RRUs), are split where RRHs are moved to the top of the mast connected to the antennas via small coaxial jumpers, as shown in Fig. 2.19 (b). Each tower has a dedicated BBU connected to the RRHs visa optical fiber. In C-RAN architecture, in contrast with the conventional macro base station, as shown in Fig. 2.19 (a) and D-RAN, as depicted in Fig. 2.19 (b), the BBUs are moved to the central office (CO) and can be shared among sites in a virtualized BBU pool in a cloud environment. In contrast, the RRHs remain at the cell sites, which are connected to the BBUs through a network segment called fronthaul [172], as shown in Fig. 2.19 (c). Usually, the transport medium in the fronthaul network is optical fiber, which carries radio frequency (RF) signals in between the BBUs and RRHs. The BBUs are further connected to the core network through the backhaul network. The RRHs transmit and receive the RF signals over the air interface, whereas the BBUs perform the baseband and packet processing in a cloud environment, as shown in Fig. 2.19 (c).

2.4.1 Fronthaul Architecture and Key Challenges

The centralization of RAN imposes stringent requirements on the fronthaul capacity and latency [11]. Therefore, designing an efficient fronthaul for 5G and beyond is inevitable to achieve low latency and avoid the capacity crunch. A high-capacity fronthaul for realizing centralized processing can be achieved using seamless fiber-wireless integration. Gigabit wireless connectivity is also one of the drivers behind such integration. Therefore, optical fiber is a transport medium in the fronthaul links [173]. RoF-based fronthauling has already been used in the existing wireless infrastructure, which will also be the future of wireless communication networks [174]. Since such networks can enable the reduction of bandwidth requirements, latency and complexity.

RoF-based fronthaul links can be mainly categorized into digital RoF (D-RoF) and A-RoF, as shown in Fig. 2.20 (a) and Fig. 2.20 (b), respectively. The existing fronthaul links are based on the former category where the industry standard interface protocols such as common public radio interface (CPRI), open base station architecture initiative (OBSAI), and open radio equipment interface (ORI) have been defined to transport radio signals between the BBU and RRH. Among them, CPRI is the most widely implemented interface between BBU and RRH/RRU in the fronthaul. Nevertheless, CPRI is foreseen to be impractical considering the high bandwidth requirements of the next generation fronthaul [11]. Because CPRI is digitized serial bandwidth inefficient interface and has a constant bit rate. CPRI digitizes the wireless signals into in-phase and quadrature (I/Q) waveforms and transports them along with control words (CWs), which are used for equipment control and management and synchronization information, using time division multiplexing (TDM) and on-off keying modulation format as depicted in Fig. 2.20 (a). Consequently, the CPRI interface has a constant bit rate for transporting antenna samples between a BBU and RRH/RRU ranging from 614.4 Mbit/s (option 1) to 24.33024 Gbit/s (option 10) over several kilometer distances between the RRHs/RRUs and the BBU, which depends on the
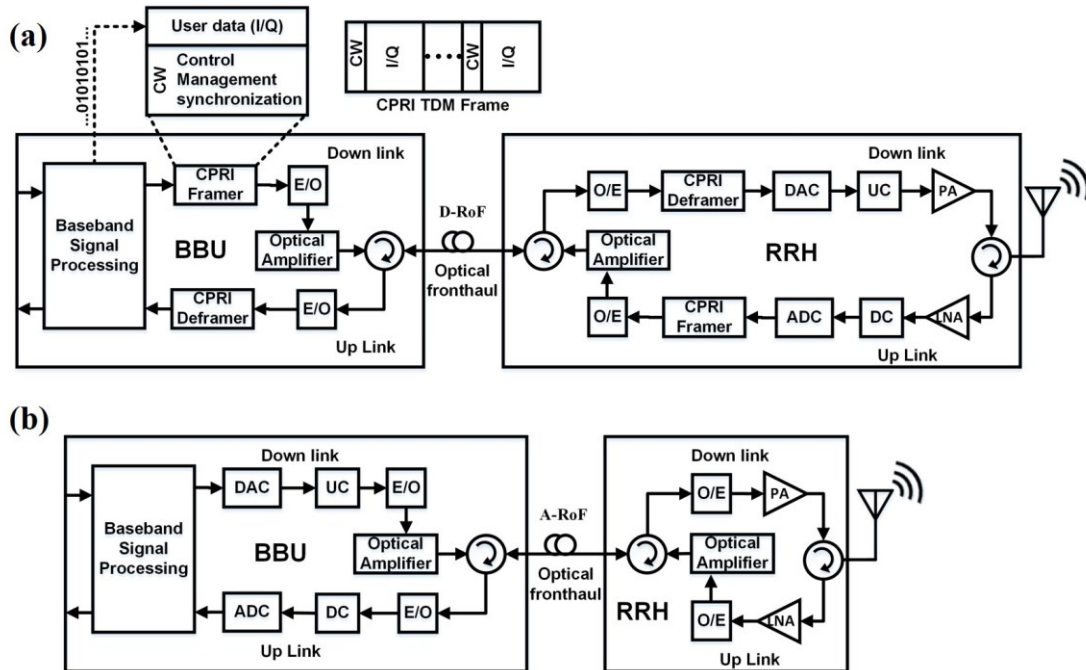
Figure 2.20: Schematic of a generic fronthaul architecture (a) CPRI-based D-RoF fronthaul, and (b) A-RoF fronthaul. E/O: electrical to optical, O/E: optical to electrical, PA: power amplifier, LNA: low noise amplifier, UP/DC: up/down conversion [48].

radio access technology, sampling rate, carrier bandwidth, and MIMO implementation [11], [172]. Thus, CPRI interface requires higher rates to carry small volume of users' data. The CPRI data rate is evaluated as [172];

$$(Data\ rate)_{CPRI} = S \times M \times SR \times N \times 2(I/Q) \times CW \times C, \qquad (2.9)$$

where S, M, SR, N, 2(I/Q), CW, and C represent the number of sectors, the number of antennas per sector, sampling rate (sample/s/carrier), sample width (bits/sample), multiplicative factor for I and Q data, control word factor, and codding factor (10/8 for 8B/10B code or 66/64 for 64B/66B code), respectively. Thus, besides the strict requirements of signal synchronization, jitter, latency and complexity issues, CPRI poses significant challenges regarding extremely high capacity for 5G and beyond mobile networks. For instance, based on (2.9), the data rate requirement of a CPRI-based fronthaul link can be as high as 590 Gbit/s if a 5G system utilizes wireless signals with aggregated bandwidth of 200 MHz, 16×16 MIMO antennas and three sectors [175]. Moreover, when the network is further extended with massive MIMO systems, as expected in 5G and beyond, the transmission capacities of fronthaul would scale to the range of Tb/s per cell, which questions the capability of the current CPRI-based D-RoF fronthaul [176].

2.4.2   Key Enabling Technologies and Solutions for Next Generation Fronthaul

Research efforts are intensely focused, both from industry and the research community, on designing novel fronthaul technologies and systems to overcome the bandwidth, flexibility, and scalability limitations of the existing CPRI-based digitized fronthaul architecture. Several approaches have been proposed to overcome the limitations of the current D-RoF fronthaul for achieving efficient C-RAN, ranging from CPRI bandwidth compression [177] and functional splits [178]–[180] to radio-over-Ethernet (RoE) [181] and a fully A-RoF-based fronthual [17], [174], [182], [183].

Different wireless data compression techniques are used in bandwidth compression to reduce the CPRI-based fronhaul link load [171], [177]. Similarly, in functional split, different functions can be moved to the RRH from the BBU and vice versa depending on the requirements and system configuration to ease the burden on the fronthaul transport

link. In the traditional C-RAN architecture, most processing functions reside in the BBU, for instance, resource block mapping, channel coding, modulation, fast Fourier transform (FFT), medium access control, wireless resource control and management etc., where RRH/RRU mainly transmits/receives the wireless signals over the air interface. Thus, considering CPRI, which requires substantial optical bandwidth compared to the actual transported radio data, the functional split point between the BBU and RRH/RRU can be redefined to reduce the transport bandwidth overhead over the fronthaul network. Towards this, various split options (from option 1 to option 8) between central and distributed units are considered by the 3GPP in Release 14, as seen in Fig. 2.21 [184]. The last three options are for the split points at the physical layer, where option 8 represents the existing conventional fronthaul with CPRI interface protocol. The details about these functional splits and related functions are out of scope of this thesis and can be found in [184].

On the other hand, in RoE, the CPRI digitized radio I/Q payload, potential vendor-specific and control data channels/flows are encapsulated and mapped into the Ethernet frame based on IEEE 1914.3 standard for transporting over Ethernet and Internet Protocol (IP) packet network. More details about RoE can be found in [181]. In addition, several organizations have been developing new fronthaul standards and interface technologies to tackle the challenges imposed by the 5G, which include enhanced CPRI (eCPRI) [185], Ethernet-based time-sensitive networking (TSN) [186], next-generation frontal interface (NGFI) [187], 5G-XHual [188], and 5G-Crosshaul [189], [190]. Besides, mobile data offloading schemes using complementary networks and technologies, such as Wi-Fi,
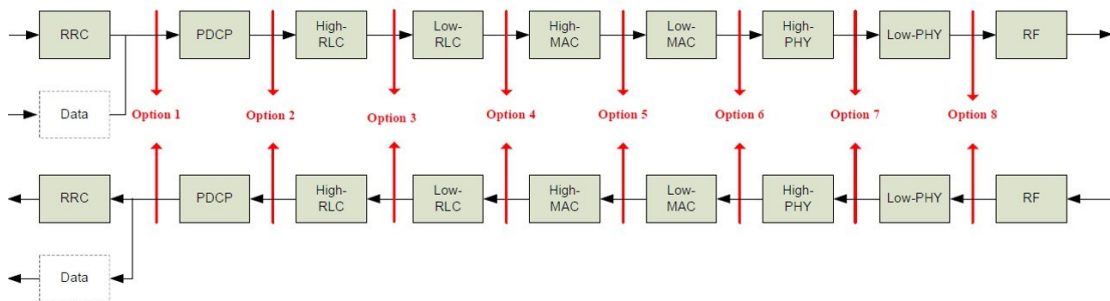
Figure 2.21: Function split between central, i.e., BBU, and distributed, i.e., RRH/RRU, units [184]. RRC: radio resource control; PDCP: packet data convergence protocol; RLC: radio link control; MAC: medium access control; PHY: physical layer.

femtocells etc., are proposed to lower the congestion on the mobile access network [191]. Additionally, various delta-sigma modulation schemes are investigated to alleviate the inadequacies of the existing fronthaul by reducing the capacity requirement while keeping the advantages of the digitized signal transport [192]–[195].

Among the above described fronthaul solutions, A-RoF fronthaul approach has been considered one of the best potential candidates for 5G and beyond C-RAN due to its low bandwidth requirement, low latency, cost-effectiveness, and energy efficiency [11], [174], [176], [182], [183]. Thus, to overcome the shortcomings of the current digitized mobile fronthaul, a fully A-RoF mobile fronthaul is proposed to be one of the promising solutions for 5G and beyond in the literature [11], [174], [176], [182], [183]. A-RoF fronthaul can be achieved by directly modulating the optical carrier with RF signals and transmitting them as analog waveforms over the optical link from the BBUs to RRHs, and vice versa, as shown in Figure 2.20 (b). In such systems, different types of multiple analog RF signals are directly converted to the optical domain and transported simultaneously over optical fiber links. In this way, the analog-to-digital converter (ADC) and digital-to-analog converter (DAC) are kept in the BBU; hence achieving high centralization and reducing the complexity of RRH. Furthermore, with analog mobile fronthaul, the large overhead required for digitization of wireless signals to the CPRI format can be avoided, which achieves high bandwidth efficiency. For instance, if we consider the same link configuration for A-RoF fronthaul link, as described above for D-RoF with CPRI, with aggregated bandwidth of 200 MHz, 16×16 MIMO antennas and three sectors, the bandwidth requirement significantly reduces to around 10 GHz [175]. In addition, the extra latency that comes from the format conversion of wireless signals can also be reduced.

Moreover, the fronthaul networks initially relied on a dedicated dark fiber. However, considering the enormous capacity and cost of the next-generation fronthaul network, other complementary and enhanced transport solutions such as microwave/MMW [196], [197], space division multiplexing (SDM) in few-mode fiber (FMF) [198] and multicore fiber (MCF) [199], wavelength-division multiplexing (WDM) [200], time division multiplexed passive optical network (TDM-PON) [178], WDM-PON [201], TWDM-PON [202], and Ethernet-based fronthaul networks [203] are under consideration.

54

Thus, the key challenges in designing fronthaul architecture for next-generation wireless networks are to avoid the capacity bottleneck and to achieve low latency and high centralization. A-RoF technology is introduced as an enabler to overcome the capacity limitations and to simplify the fronthaul design by achieving C-RAN as highlighted in the literature review. Since A-RoF fronthaul supports simultaneous transmission of various RF signals ranging from low frequency to MMW and multiple radio access services, such as 4G, 5G, and WiMAX. Moreover, the A-RoF fronthaul becomes more scalable and flexible when tailored with SDM technology along with WDM, which can be achieved by leveraging mode-division multiplexing (MDM) in FMF, MCF, ring-core fiber (RCF) or the combination of them. This increases the capacity and reduces the latency, cost and complexity. In conclusion, a high-bandwidth, low-latency, cost-effective, flexible, and scalable fronthaul is essential for the next generation of wireless comminutions, which the optical fiber connections with A-RoF technologies can efficiently accomplish. In this thesis, we propose and experimentally demonstrate photonic-enabled high capacity flexible and scalable A-RoF based fronthaul transmission systems for next generation MMW wireless communication networks.

2.5 Introduction to Radio-over-Fiber

Radio-over-fiber refers to a technology where the light wave is modulated with an RF signal and transmitted over a low-loss and high-bandwidth optical fiber, as shown in Fig. 2.22. RoF enables seamless fiber-wireless integration (optical fiber and RF integration),
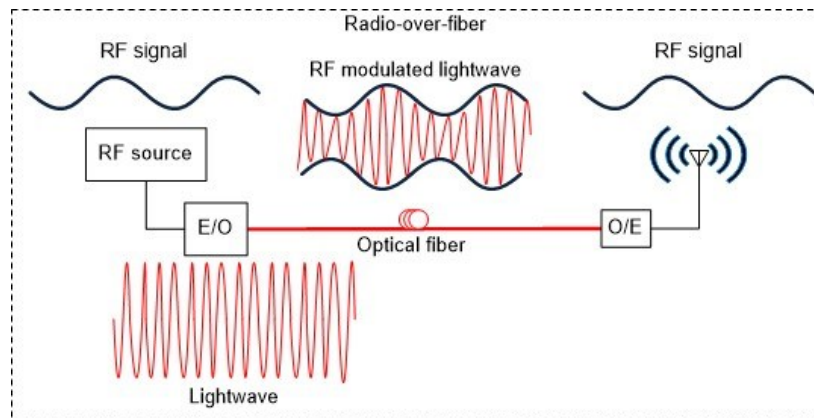
Figure 2.22: Basic principle of RoF. E/O: electrical to optical; O/E: optical to electrical.

i.e., integrating high capacity, reliable and transparent optical networks with flexible, mobile and pervasive wireless networks. Fiber-wireless convergence is inevitable for the next-generation high-capacity, high-speed wireless communication networks to achieve ubiquitous and multi-gigabit connectivity [15]. In addition, owing to its enormous bandwidth, multiple services can share the same optical link. Besides, RoF enables antenna remoting with centralized control that allows easy maintenance, upgrades, and resource sharing [204].

2.5.1 Key Radio-Over-Fiber Technologies

The fiber-wireless transport technology for RF wireless signal distribution can be mainly classified into digital and analog. The former includes digital-radio-over fiber (D-RoF) and digital-intermediate-frequency-over fiber (D-IFoF). On the other hand, the latter can further be categorized into analog-radio-over fiber (A-RoF), aka RoF, A-IFoF, analog-baseband-over fiber (A-BBoF), and digital signal processing assisted analog RoF (DSP-ARoF) [204]–[206].

Figure 2.23 (a) shows a simplified schematic of the D-RoF for downstream transmission. The radio signal is digitized before modulating the optical carrier, and the sampled digital signal is transported over the fiber-based fronthaul link in a serial form. In this case, the sampled signal can directly modulate the laser. This also alleviates the intermodulation distortion (IMD) arising from the electrical to optical conversion, improving the links dynamics range. The dynamic range of the D-RoF is independent of the fiber length until the power level goes below the receiver sensitivity [207]. However, the radio signal needs to be converted back to an analog RF form at the RRH/RRU, requiring signal processing, which adds to the cost and complexity. In addition, D-RoF is very demanding in terms of bandwidth. The DAC functions are performed at the RRH/RRU to translate the incoming digitized RF signal from BBU to analog prior to transmission over the air interface. Similarly, the uplink signal requires ADC to digitize the RF signal. Thus, D-RoF scheme necessitates high-speed ADC/DAC with a bandwidth larger than the RF carrier frequency with enough sampling rate and resolution. Considering MMW wireless signals in the next generation of wireless communications, this
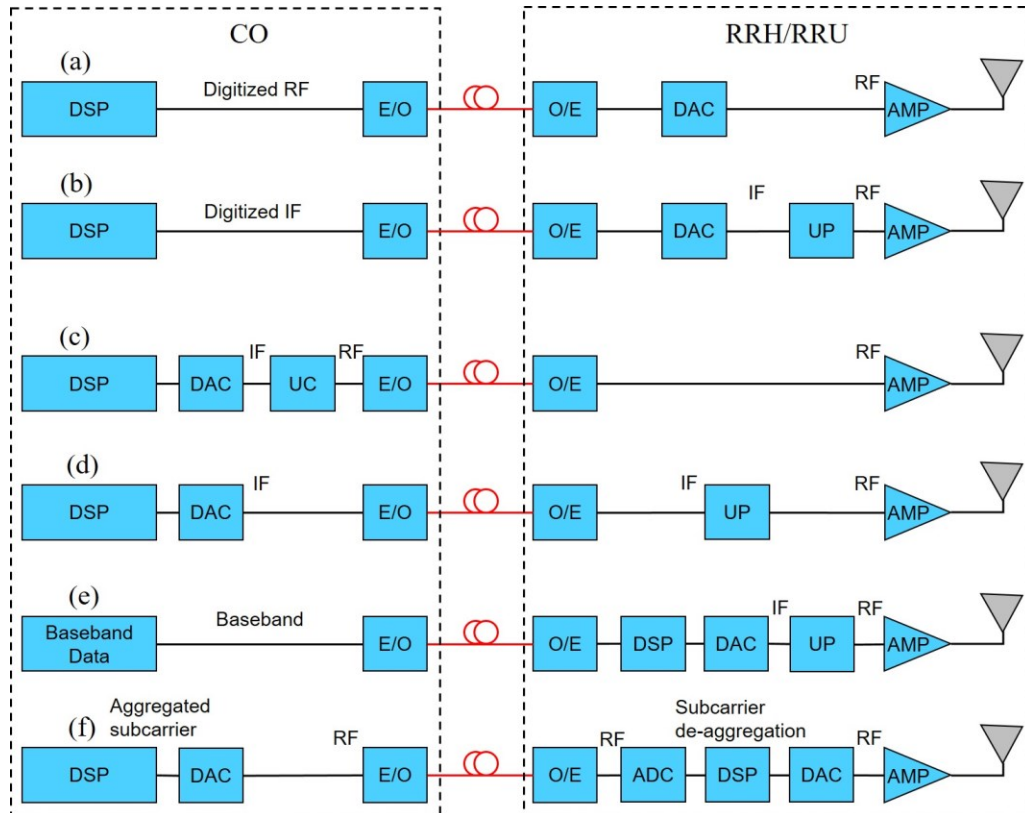
Figure 2.23: High level schematic of downstream (a) D-RoF, (b) D-IFoF, (c) A-RoF, aka RoF, (d) A-IFoF, (e) A-BBoF, and (f) DSP-ARoF transport architectures. DSP: digital signal processing; O/E: optical to electrical conversion; E/O: electrical to optical conversion; DAC: digital to analog converter; ADC: analog to digital converter; UP: up-conversion; AMP: amplifier; CO: central office.

requirement even becomes more stringent. To overcome this problem, D-IFoF can be used, as shown in Fig. 2.23 (b), where wireless signals located at the IF are digitized and transported over the fiber fronthaul link in a serial form, as in the case of D-RoF CPRI fronthaul interface. Furthermore, considering that the information bandwidth in most applications is a fraction of the carrier frequency, bandpass sampling can be used to directly digitize high-frequency analog bandpass radio signals to baseband or IF with a lower processing rate [208]. Since in such methods, the sampling rate no longer depends on the carrier frequency but rather on the information bandwidth. For MMW frequencies, the signal needs to be translated to an intermediate frequency (IF) before digitizing it with the bandpass sampling technique. This technique is mainly beneficial in the uplink. However, besides the hardware's complexity and cost, this method also produces an excessively high

data rate on the optical link. Thus, implementing D-RoF is challenging for wireless signals operating at higher frequencies in the MMW frequency bands [207].

In contrast, A-RoF, aka RoF, uses a microwave signal to directly modulate the optical carrier and transmit it over the optical fiber fronthaul link in an analog form, as shown in Fig. 2.23 (C). This can be achieved by directly modulating the laser in the case of a low-frequency radio signal or using an external optical modulator, such as MZM, in the case of radio signals at higher microwave or MMW frequencies and preferably in single sideband modulation mode to avoid dispersion induce power penalty [209]. A-RoF is the simplest architecture because it directly transports the RF signal without any need for frequency translation at the RRH/RRU, which significantly simplifies the RRHs/RRU architecture by relocating all the signal processing and DAC functions to the central office. In addition, A-RoF achieves high centralized control and processing with support for multi-band and multiple RF wireless signals. Moreover, A-RoF exhibits higher bandwidth efficiency than D-RoF because the bandwidth of modulating RF signal is unchanged. Yet, it is low because it requires one optical carrier per radio signal [206]. Additionally, the electrical to optical conversion and vice versa needs to be low loss and highly linear to avoid IMD. Furthermore, in A-RoF, the dynamic range of the optical fiber linearly decreases with the length of the fiber due to attenuation. Besides, the link's bandwidth should be substantially large than the highest microwave signal's frequency regardless of the information bandwidth. Also, A-RoF requires high-speed optoelectronic devices, especially at higher frequencies such as MMW.

Some of the A-RoF requirements and impairments can be significantly reduced by using a modulating wireless signal located in the IF frequency to modulate optical career and transmit over the optical fiber link in the form of A-IFoF, as shown in Fig. 2.23 (d). Nevertheless, this is at the expense of the complexity of RRH/RRU where stable local oscillators (LOs) and mixers are required for frequency up-conversion. Still, A-IFoF is more economical because multiple radio channels in the form of subcarriers aggregation with frequency division multiplexing (FDM) can be transported simultaneously to the RRH/RRU. Various signals can be combined/split and up/down converted using analog signal processing. However, multiple signals in an A-RoF link are prone to IMDs, which

can be compensated by implementing specialized techniques [209], but this can increase the complexity and cost of the system.

In the case of A-BBoF, the radio signal located in the baseband is used to modulate the optical carrier and transport over the fiber link as an analog baseband data signal, as shown in Fig. 2.23 (e). Consequently, the wireless signal processing is moved to the RRH/RRU. A-BBoF scheme is more efficient regarding the optical bandwidth [210] and chromatic dispersion. This scheme also requires low-speed optoelectronic devices. Moreover, A-BBoF is compatible with the existing optical communication networks. A-BBoF can be very cost-effective and more feasible if the baseband wireless data signals are up-converted photonically at the RRH/RRU, as discussed in Section 2.3 of this thesis., therwise it results in RRH/RRU complexity. More hardware is required to process and transform the baseband wireless data into RF wireless signals electronically, in addition to the requirements of separate optical resources for each channel.

Furthermore, in the case of DSP-ARoF, the radio signal is processed digitally using digital signal processing techniques before being modulated onto the optical carrier. Different subcarriers or multiple wireless signals are aggregated in the digital domain using DSP in the central office (CO). Then the aggregated signals are transmitted in the analog form in the optical domain over the fiber-based fronthaul link using a single wavelength channel link, as shown in Fig. 2.23 (f). DSP-based subcarrier aggregation can typically be achieved either in the frequency domain [211], time domain [212] or code domain [213]. Thus, DSP-RoF helps in increasing the spectral efficiency of wireless channels. Like A-IFoF, this scheme is also bandwidth-efficient, scalable and flexible. DSP-ARoF can also address the A-RoF inherent susceptibility to impairments by using advanced mitigation techniques at the expense of added latency [206]. Nevertheless, due to the high-speed DAC/ADC and DSP requirements, DSP-ARoF architecture is subject to relatively high power consumption, complex design and high cost.

2.5.2   Discussion on A-RoF Key Challenges

As discussed earlier, A-RoF is considered one of the promising candidate technologies for realizing high speed, high capacity, low complexity, and flexibility and scalability

requirements of the next generation of wireless communication networks, especially fronthaul networks. However, A-RoF fronthaul is prone to various impairments such as poor E/O and O/E conversion efficiency, nonlinear impairments, chromatic dispersion and other noises, which deteriorate the performance of A-RoF transmission. With multiple higher RF signals, the A-RoF link is prone to IMD due to nonlinearity caused by RF electrical and optical components in the link. Since A-RoF transmission faces non-linear characteristics, which induce power penalties and IMD, thus limiting the transmission distance. Therefore, linearization is required either through the components design or other techniques, such as pre-distortion and post-distortion techniques. In the case of direct modulation, a rationally low modulation depth at the laser is required in order to gain operation in the linear region. Moreover, A-RoF transmission has length-dependent issues for high RF signals. Since chromatic dispersion at RF frequencies >10 GHz is a real problem because it severely limits the propagation of high RF or MMW signals. Chromatic dispersion can be significantly reduced by using A-IFoF, which also relaxes the demand for high-speed optoelectronic components associated with the A-RoF link. However, this will increase the complexity of the RRH/RRU where stable local oscillators and mixers will be required for frequency translation. This shortcoming can be overcome by generating and distributing the RF/MMW signals in the optical domain, as discussed in Section 2.3 of this thesis. The RF/MMW signals are generated remotely through optical heterodyning. Nevertheless, generating MMW signals in the optical domain with high spectral purity and accuracy is a challenging issue due to the high dependence of wireless transmission performance on the linewidth and phase noise attributes of the generated MMW signals, which in turn depend on the spectral purity and coherence of the optical sources generating them [123]. Thus, optical MMW generation requires stable optical sources with narrow spectral linewidth and low-intensity noise, such as QD-MWLs [42], which is the focus of this thesis.

2.6   State-of-the-art in QD-MWLs based MMW RoF systems

Since the inception of semiconductor QD-MWLs based MMW RoF systems [214], a number of InP-based QD-MWLs are demonstrated over the past decade for optical MMW sources in both C-band [16], [33], [35]–[38], [155], [156] and L-band [31], [32], [34], [38],

[214]–[218] widows of optical communications, summarized in Table 2.2. With the advent of MMW for the next generation wireless communication networks, i.e., 5G and beyond, QD-MWLs are getting more attention for photonic MMW signals generation and applications in optical heterodyne MMW RoF systems due to the technology maturity and exceptional characteristics, such as highly coherent and correlated optical signals with very low phase and intensity noise.

Table 2.2: Comprehensive summary of the state-of-the-art QD-MWLs based MMW RoF systems.

Ref.	Optical Source	λ Band	MMW Frequency (GHz)	Data Rate (Gb/s)	Mod. Format	MMW RoF Link	
						SMF (km)	WL (m)
[155], [214], [219]	PML-QD-MWL	C	~60	3.03	QPSK (OFDM)	0.05	-
[155], [156], [219]	PML-QD-MWL	C	~60	1.25 to 5	OOK	~ 0.054	25
[35]	PML-QD-MWL	C	25	0.08	16-QAM	20	2
[16]/[220]	SIL-PML-QD-MWL	C	60	1.12/~1.17	64-QAM (OFDM)	25	-
[221]/[37]	SIL-QD-MWL	C	100	10	OOK	50	10/15
[33]	SIL-QD-MWL	C	40/80	10	16-QAM (OFDM)	50/25	20
[38]	HIL-QD-MWL	C & L	60	10	32-QAM (OFDM)	50	-
[31]/[34]	EIL/SIL-QD-MWL	L	28	2	QPSK	20	4/6
[34], [216]/[217]	SIL/SIL&EIL-QD-MWL	L	30	2	QPSK	20	2
[32]	SIL-QD-MWL	L	28/25	8	QPSK/16-QAM	10	4/2
[36]	QD-DW-DFBL	C	146	1	OOK	-	0.025

Mod. Format: modulation format; PML: passively mode-locked; SIL: self-injection-locked; EIL: external-injection-locked; HIL: hybrid-injection-locked; WL: wireless link

A 774 µm long FP cavity buried ridge structure InP-based passively mode-locked (PML) QD-MWL with free spectral range (FSR) of 54.8 GHz and 3dB beat note linewidth of 18 kHz was first demonstrated for 58.9 GHz MMW indoor bidirectional RoF transmission with 3.03 Gb/s data rate over 50 m SMF [155], [214], [219]. The active region of the device was comprised of 6 QDash layers. In the downlink, the 3.03 Gb/s RoF system was realized by directly modulating the QD-MWL with a 1.87 GHz bandwidth QPSK orthogonal frequency-division multiplexing (OFDM) format based on IEEE 802.15.3c group standard signal at IF of 4.5 GHz. Similarly, by employing the same optical source, a

58.8 GHz MMW QPSK OFDM signal in the uplink was down-converted to around 4.5 GHz. In addition, the same device with a different cavity length of 710 µm having an FSR of 58.8 GHz was demonstrated in broadband RoF wireless system for HDTV applications. The transmission of non-return-to-zero ON–OFF keying (NRZ-OOK) modulated signal at 60 GHz MMW was realized by employing an electro-absorption modulator (EAM). The RoF links having a data rate between 1.25 to 5 Gb/s were directly detected with envelops detection method using GaAs Schottky detector over 2.5 m and 25 m wireless links through 50 m SMF [155], [156], [219].

Recently, in [35], a highly integrated PML QD-MML without any controlled optical feedback or injection locking was demonstrated in a converged optical-wireless WDM access network scenario, including simultaneous transmission of 32-GBaud dual-polarization QPSK (DP-QPSK) coherent and 20 MHz bandwidth 16-QAM MMW and 64-QAM citizens broadband radio service (CBRS) signals over 50-km and 20 km fiber links, respectively. In the converged system, the 80 Mb/s MMW RoF link at 25 GHz over a 2-m wireless distance through 20 km fiber was realized by selecting equally spaced comb lines and externally modulating them with 20 MHz 16-QAM data signal before transmission. The 20 MHz and 2 m wireless distances were limited by the available resources and space in the Lab, respectively. Furthermore, in [16], [220], an integrated single-section F-P cavity PML QD-MWL with FSR of 32.5 GHz under free space optical feedback was demonstrated for the optical heterodyne generation and transmission of 60 GHz OFDM 64-QAM MMW signals over 25 km SMF with an aggregated data rate of around 1.12/~1.17 Gb/s. The laser's optical and beat note linewidths were around 4 MHz and several 10's kHz, respectively. Two comb lines spaced at about 65 GHz were selected. One of them was externally modulated with 195 MHz bandwidth 64-QAM OFDM data signal at IF of 5 GHz with different subcarriers' bandwidth resulting in 1.12/~1.17 Gb/s link data rates. The free space optical feedback was incorporated for self-injection-locking (SIL) through a ~30-cm external cavity. The cavity was comprised of a mirror, free space attenuator and collimating lens to reduce the phase noise of the optical lines and beat note by tuning the position of the mirror with a piezo controller.

On the other hand, in [221], a WDM hybrid system including fiber, fiber-wireless, and fiber-free-space-optic (fiber-FSO) links was demonstrated based on a SIL 50 GHz ML QD-MWL frequency comb. Five high-quality optical carriers out of the total eight ML comb lines were used for 10 Gb/s OOK modulated hybrid links, including baseband fiber link, 50 GHz and 100 GHz MMW RoF links over 50-km SMF with the subsequent wireless transmission of 100 GHz signal over 10-m RF link and 50 GHz over 40-m FSO link. An uplink was also emulated by re-modulating one of the downlink optical carriers using a reflective semiconductor amplifier (RSOA) with 2.5 Gb/s baseband data. This data was transmitted over a 10-m free-space visible light communication (VLC) link through a different 50 km SMF using a multimode VCSEL-based VLC system. This work was extended in [37] with 10 Gb/s OOK and 32-QAM OFDM RoF links at 100 GHz and 100 MHz over 15-m and 10-m, respectively, through 50-km SSMF along with the Rayleigh backscattering noise elimination technique by employing different carrier wavelengths for the up/down bidirectional streams in a single fiber. Likewise, in another demonstration in [33], the same device was used for optical heterodyne MMW RoF links with 10-Gb/s 16-QAM OFDM data signals at 40 GHz and 80 GHz over 50 km and 25 km SMF, respectively, followed by 20-m wireless transmission in a hybrid MMW-FSO configuration. These links were established by first modulating WDM four optical channels of the comb with 100 GHz spacing using the 10-Gb/s 16-QAM OFDM data signal and then passed through 50-km SSMF for decorrelation before modulating by another 20-GHz RF signal via phase modulator for harmonic sidebands generation. The corresponding 40/80 GHz MMW signals are then realized by selecting the even and odd sidebands using an optical interleaver. The self-injection locking in [33], [37], [221] was employed through a feedback loop incorporating an optical circulator (OC), an erbium-doped fiber amplifier (EDFA), a 3-dB coupler and a tuneable band pass filter (TBPF). In the same way, in [38], a bidirectional MMW/THz RoF system with 32-QAM OFDM 10/12.5 G/s and 6.5/10 Gb/s in the downlink and uplink was demonstrated employing hybrid injection locked (HIL) L-band and C-band QD-MWLs, respectively, with subsequent transmission over 100 m FSO link. The C-band MMW/THz optical channels were also transmitted in the downlink, which was then used for uplink data transmission on a different SMF of 50km/25km to alleviate Raleigh backscattering. The injection locking of both optical sources involved

HIL, i.e., passive and external injection locking (EIL), by employing an external tunable optical source.

Moreover, optical heterodyne MMW RoF links at 28 GHz were demonstrated using dual-comb lines from an injection-locked InAs/InP L-band QD-MWL based comb [31]. The demonstration included 2-Gb/s quadrature phase-shift keying (QPSK) data transmission in the downlink over 4-m [31] to 6-m [34] wireless distances through 20 km SSMF. The two comb lines were externally modulated with QPSK 2-Gb/s signals at IF of 5 GHz using an MZM. The dual-comb lines were generated using EIL through an external commercial master tunable laser source in [31] and SIL in [34] to first lock one longitudinal mode of the L-band InAs/InP QD-MWL. Then, feeding this longitudinal locked mode to a phase modulator (PM) driven by a 33 GHz RF source to generate an optical comb with an FSR of 33 GHz followed by a tunable optical filter to filter the corresponding two comb lines. In [34], [216] a QPSK 2 Gb/s 30 GHz MMW link over a 2-m wireless distance through 20 km SMF and 5-m FSO link was also demonstrated by altering the FSR of the comb to 35 GHz. This work was further extended in [217] by analyzing both SIL and EIL QD-MWL for 30 GHz MMW links, including a ~1-m FSO link under dusty weather conditions with a 1-m wireless link through 20- km SSMF. Additionally, in another work [32], bidirectional RoF links at 28 GHz downlink and 25-GHz uplink were demonstrated using dual-comb lines from the same SIL L-band InAs/InP QD-MWL-based comb in [34]. A maximum of 4-Gbaud 8-Gb/s QPSK and 2 Gbaud 8 Gb/s 16-QAM data transmission in the downlink and uplink over up to 4-m and 2-m wireless links, respectively, through 20-km SMF, was demonstrated. In the uplink, a 25-GHz signal with QPSK/16-QAM data was first generated using Keysight VSG (E8267D) and transmitted over the wireless link before modulating the two downlink optical carriers for uplink fiber transmission [32]. In a further study, a frequency comb based on the modulation of the SIL longitudinal mode of the L-band QD-MWL was generated by a tunable RF source through a phase modulator. The comb was used to generate, wirelessly transmit and characterize unmodulated MMW signals at 28, 38, and 60 GHz MMW over 2-m and 6-m wireless links [218].

Furthermore, a 780 μm long QD dual-wavelength DFB laser (QD-DQ-DFBL) was demonstrated in [36] for the transmission of 1-Gb/s NRZ-OOK externally modulated data using MZM at 146 GHz over 2.5-cm optical heterodyne RF link in a back-to-back fiber configuration with a packaged high-speed antenna-integrated traveling-wave uni-traveling carrier photodiode (TW-UTC-PD). In this device, two monolithically integrated DFB lasers separated about 20 μm apart on InGaAsP in QD in a well structure with six QDash layers were combined in a Y-coupler. The two wavelengths from each DFB having individual bias control were thus combined into a single passive waveguide with a tuning range between 70 and 146 GHz. This device's 3dB optical linewidth was measured to be less than 700 kHz [91].

2.7   Summary

This chapter provides extensive background, a thorough literature review, and fundamental concepts about the work in this thesis. This includes a developmental background of semiconductor lasers in general and QD-MWLs in particular, MMW wireless communications and challenges along with potential solutions, the concept of photonic MMW signals generation and transmission and classification of the state-of-the-art photonic MMW signals generation techniques, introduction to radio access and fronthaul networks and next generation fronthaul challenges and key solutions, and introduction to RoF and key enabling technologies. Finally, a comprehensive related literature review of state-of-the-art QD-MWL-based RoF systems is presented, which is used to compare our work in this thesis. Thus, this chapter lays the foundation for the rest of the chapters, which are based on our published work, and where the background and principles discussed in this chapter are used to design and experimentally demonstrate QD-MWL laser based RoF wireless communication systems for next-generation networks.

Chapter 3

Low-Noise InAs/InP Buried Heterostructure PML QD-MWL for High Capacity Fiber-Wireless Integrated Systems

3.1 Introduction

THE demand for high bandwidth, reliable and faster data speed, and the congestion in the sub-6 GHz spectrum have initiated the adoption of higher frequencies (>24.25GHz) in the MMW spectrum for 5G wireless communication networks [1]. These higher frequencies with abundantly available bandwidths are inevitable for wireless carriers to support the enhanced heterogeneous requirements of the 5G envisioned diverse usage scenarios with bandwidth-hungry services and applications, such as Gb/s wireless connectivity, ultra-high definition video streaming, Internet of Thing (IoT), smart home/building, virtual and augmented reality (VR/AR), autonomous vehicles, and work and play in the cloud. Enhanced mobile broadband (eMBB) is one of the three 5G standard usage scenarios set by the International Telecommunication Union Recommendation Sector (ITU-R) in the International Mobile Telecommunications 2020 (IMT-2020). eMBB features a peak data download speed of more than 20-Gb/s and seamless 100-Mb/s user experience data rates in wider coverage areas with the expected speed of Gb/s in hotspot cases [4]. Such ultra-high speed and broadband wireless signals cannot be realized and supported by the already depleted sub-6 GHz RF spectrum. Therefore, to fulfill the requirements of IMT-2020, 3GPP has identified and standardized the underutilized high-frequency bands (24.25 GHz to 52.6 GHz) in the MMW spectrum for the development of 5G NR (a global standard for 5G wireless interface) systems [6]. Nevertheless, generating, processing, controlling and distributing such ultra-high speed and wideband wireless signals in the electrical domain may not be feasible due to the electronics bottleneck [10], [15], [222]. Microwave photonics with RoF is identified as one of the keys enabling technologies for generation and distribution of high bandwidth and ultra-high speed MMW RF signals in the optical domain [10], [15], [222], [223]. Moreover, to satisfy the 5G requirements, fiber-wireless integration is indispensable. The photonic-aided frequency up-conversion through remote heterodyne mixing of two coherent optical signals is the

simplest approach to generate wideband high-speed RF wireless signals and to achieve fiber-wireless convergence. In this way, the two optical signals after running over several tens of kilometers of optical fiber, with the modulated data onto either one or both of them, and spaced at the desired MMW RF carrier signal, are mixed on a high speed photodetector [26], [125]. This not only overcomes the problem of electronics bottleneck, and transmission span limitation and provides seamless fiber-wireless conversion but also substantially reduces system and network complexity, footprint, as well as Capital Expenditures (CAPEX) and Operating Expenses (OPEX) considering the expected deployment of ultra-dense small cells with large number of 5G remote radio units (RRUs) having massive multiple-input-multiple-output (MIMO) antennas connected to the baseband units (BBUs) in a centralized cloud environment through an optical fiber-based fronthaul network.

Numerous techniques have been developed and demonstrated under the umbrella of microwave photonics for MMW RF signals generation over the optical links, ranging from optical heterodyne beating of two single wavelength individual laser sources [19] and dual wavelength lasers [26], [27] to employing optical modulator (s) [20], [21] and optical frequency combs based on various schemes [16], [18], [22], [23], [35], [218], [220], [222], [224], [225]. Among them, optical coherent frequency combs (CFCs) based on integrated monolithic semiconductor passively mode-locked lasers (PML) quantum dash (QDash) or quantum dot (QD) multi-wavelength lasers (QD-MWLs) [16], [35], [218], [220], [225] are very attractive due to simple and compact design and broadband flat spectra having multiple highly coherent and low noise optical channels. This promises a low-cost and flexible solution for 5G and beyond wireless networks, particularly in the application of fronthaul with massive MIMO RRHs/RRUs. Because a single CFC can replace not only many individual laser sources in the central office (CO), but also provide common coherent optical local oscillators (LOs) for photonic up-conversion of RF signals in the RRUs. This significantly simplifies the overall system and network complexity. In addition, the noise performance (phase noise and RIN) of the optical sources directly affect the frequency instability and phase noise of the photonically generated RF carrier signals, which in turn impairs the performance of RoF wireless transmission systems [18], [166], [168]. Therefore, highly coherent low-noise optical sources are considered instrumental in

facilitating future photonic MMW RF wireless communication systems. Owing to their inherent superior characteristics, such as reduced amplified spontaneous emission, large effective gain bandwidth, ultra-fast carrier dynamics, and improved temperature stability [138], QDash/QD materials-based lasers can achieving stable mode-locking with multi wavelengths having very narrow optical spectral.

3.2   Related Work

InAs QDash lasers grown on InP substrates have been studied for many years [78], with many mode-locked devices reported operating in the C-band [39], [43], [66], [82], [85], [87], [88], [169] and L-band [82], [84], [100], [226], [227]. These include devices based on single section [39], [43], [66], [82], [84], [85], [87], [88], [169], [226] and two section [85], [100], [227] configurations, with the single-section self-pulsating or PML laser devices being considered advantageous due to better pulse generation with increase average output power [40]. Recent demonstrations show the potential of these InP-based ML QD-MWLs for MMW applications. These include the demonstration of RF MMW signal generation [215] and wireless transmission [218] using injection-locked L-band QD-MWLs, and Gb/s RoF wireless communication systems with [33], [221] and without RF wireless links [16], [220] using injection-locked C-band QD-MWLs.

However, most of the reported QD-MWL devices in the literature demonstrate relatively broad free-running spectral linewidths. It is believed that the buried heterostructure (BH) configuration with blocking layers has superior characteristics compared to the typical ridge configuration in terms of linewidth, frequency noise, threshold current, and efficiency. BH also improves the mode symmetry with a lower divergence angle resulting in better coupling to optical fibers. Nevertheless, BH PML QD-MWL devices and their application in end-to-end RoF systems with RF wireless links have not yet been fully explored. Consequently, it is worth investigating to fully exploit the superior characteristics of BH PML QD-MWL for RoF systems of 5G and beyond wireless communication networks.

In this chapter, we report a low noise monolithically integrated BH PML QD-MWL-based coherent frequency comb (CFC), with a free spectral range of 25 GHz, its design,

fabrication, through experimental characterization, and demonstration in an end-to-end proof-of concept RoF system with RF wireless links. Broadband photonics-assisted wireless links at 5G NR (FR2-1) with data throughputs of 16-Gb/s (4Gbaud 16-QAM) over 25.22 km SSMF and 0.5-m to 2-m free-space wireless transmission distance are experimentally demonstrated employing the BH PML QD-MWL based CFC with EVM well below the standard limit of 12.5% [6] and BER under the 7% overhead forward error correction (FEC) requirement of 3.8×10^{-3}.

This chapter is based on the published articles in [44], [45], [228]. The rest of the chapter is organized as follows. The theoretical background of phase noise and timing jitter estimation in ML lasers is presented in Section 3.3. Section 3.4 presents QD-MWL design and fabrication. The experimental characterization with comparative analysis results, and a discussion are presented in Section 3.5. In Section 3.6, the proposed QD-MWL-based end-to-end RoF wireless communication system and experimental results based on real-time demonstration are presented. Lastly, Section 3.7 present the summary of this Chapter.

3.3   Theory of Timing Jitter

Generally, the noise effects in a semiconductor ML laser are mainly from the amplitude, the central optical frequency, the pulse frequency spacing, and the optical phase. Still, the broadening of the mode line-shape in the PML laser is dominated by the contributions of optical phase noise and pulse timing fluctuations [229], [230]. Each mode's phase and timing fluctuations are affected by amplified spontaneous emission noise going through a random walk process [102]. Therefore, the timing jitter exhibits a diffusion-like behavior. Suppose $\Delta t_r (t)$ expresses the timing fluctuations in the mode position at time t; a Gaussian random process can describe the timing jitter σ with mean = 0 and total variance $\sigma = <|\Delta t_r (t)|^2> = Dt$, where D is the timing jitter diffusion constant. Then phase fluctuation follows the behavior $\Delta\theta(t) = 2\pi f_0 \Delta t_r(t)$, where f_0 is the center frequency or repetition rate. From analyzing the complex electric field of a semiconductor PML laser, considering only the effects of phase and timing fluctuations, the complex optical field is given by [231].

$$E(t) = \sum_{n=-\infty}^{\infty} A[t - n\Delta t(n)]e^{-j[2\pi f_0(t-nT_0)+\Delta\theta(n)+\phi(n)]}, \qquad (3.1)$$

where $A(n)$, $\Delta t(n)$, $f_0(n)$, $\Delta\theta(n)$, and $\phi(n)$ are the mode envelope, timing fluctuations, the center frequency, phase noise, and static phase of the n_{th} longitudinal mode respectively. T_0 represents the repetition period where $f_0 = 1/T_0$. Following [231], the optical spectrum can be calculated by taking the electric field autocorrelation function and Fourier transform. A set of Lorentzian modes with frequencies f_n and the full width at half maximum (FWHM) linewidths Δf_n compose the optical spectrum as follow,

$$S(v) \sim \frac{|\hat{A}(f-f_0)|^2}{\pi} \sum_{n=-\infty}^{\infty} \frac{\Delta f_n}{(f-f_n)^2 + \Delta f_n^2},$$ (3.2)

where $\hat{A}$ is the Fourier transform of the mode envelope. The quantum-limited optical phase noise and timing jitter random walk fluctuations induce the Lorentzian mode shape in all the longitudinal modes [229]. The FWHM optical mode linewidth is given by [232],

$$\Delta f_n = \Delta f_{min} + 2\pi f_0^2 D(n - n_{min})^2,$$ (3.3)

where n_{min} is the mode number corresponding to the minimum linewidth Δf_{min}. In an ideal situation, Δf_{min} would be the linewidth for all the modes if there were no timing fluctuations.

In the same way, the RF spectrum of beating note based on the laser's optical spectrum can be calculated as a set of Lorentzian modes with FWHM linewidth of m_{th} harmonic, Δf_{RFm}, as follows [231],

$$S_{RF}(v) \sim \frac{1}{\pi} \sum_{n=-\infty}^{\infty} \frac{\Delta f_{RFm}}{(f-mf_0)^2 + \Delta f_{RFm}^2}.$$ (3.4)

The RF spectrum is found to consist of a sum of Lorentzian modes centered at mf_0 with each harmonic corresponding to the beating between a pair of modes separated by m-1 modes in the optical spectrum. At any given value of m, each harmonic will have an integer m^2 proportional multiple to the 1st harmonic linewidth and related to D provided by [232];

$$\Delta f_{RFm} = \Delta f_{RF1} m^2 = 2\pi f_0^2 D m^2$$ (3.5)

From the coefficients of Eq. (3.5), the relationship between the first harmonic RF spectrum linewidth and timing jitter diffusion constant D can be extracted and is given by,

$$\Delta f_{RF1} = 2\pi \, f_0^2 D. \tag{3.6}$$

The amplitude noise could perturb RF spectrum as in the case of an actively mode-locked laser [233]. Higher harmonics of the photocurrent could be used to distinguish between phase noise and amplitude noise. However, in PML laser, the amplitude noise is dominated by the phase; consequently, using any different order of the harmonics does not influence on the RF linewidth [234], as seen from Eq. 3.5.

Moreover, from Eq. (3.3) and (3.6), for a PML laser, the optical mode linewidth Δf_n and the 1st RF harmonic linewidth Δf_{RF1} are related by as follows;

$$\Delta f_n = \Delta f_{min} + \Delta f_{RF1}(n - n_{min})^2. \tag{3.7}$$

Eq. (3.7) shows that the first harmonic RF linewidth Δf_{RF1} of the semiconductor PML laser can be estimated by measuring the optical linewidth, i.e., optical phase noise, of each longitudinal mode and performing a parabolic fit as a function of the mode number.

Furthermore, from the well-known method developed by Linde [233] or active ML lasers, phase noise spectrum $L(f)$ is equal to the normalized RF power spectral density (PSD) $P(f)$, as shown in Fig. 3.1(a) [45] in one Hz bandwidth, and is given by,

$$L(f) = \frac{P(f - f_0)}{RBW * P_{tot}} \tag{3.8}$$

where, f_0 and P_{tot} are the carrier peak frequency and the total integrated power of the RF PSD, respectively, and RBW is the resolution bandwidth used in the RF spectrum analyzer. Drzewietzki et al. [235] verified that this phase noise estimation method is only valid for PML lasers at frequency offsets well above the carrier peak linewidth. Fig. 3.1(b) shows a typical phase noise spectrum $L(f)$ for a PML laser, where f_1, f_2, f_3, and f_4 indicate the frequency boundaries of the different noise mechanisms with various slopes, such as flicker frequency modulation ($1/f^3$), white flicker frequency noise ($1/f^2$), flicker phase modulation ($1/f^1$), and white phase noise ($1/f^0$), respectively [236]. The A_{12}, A_{23}, A_{34}, and A_{45} represent the corresponding noise areas of the different noise mechanisms.
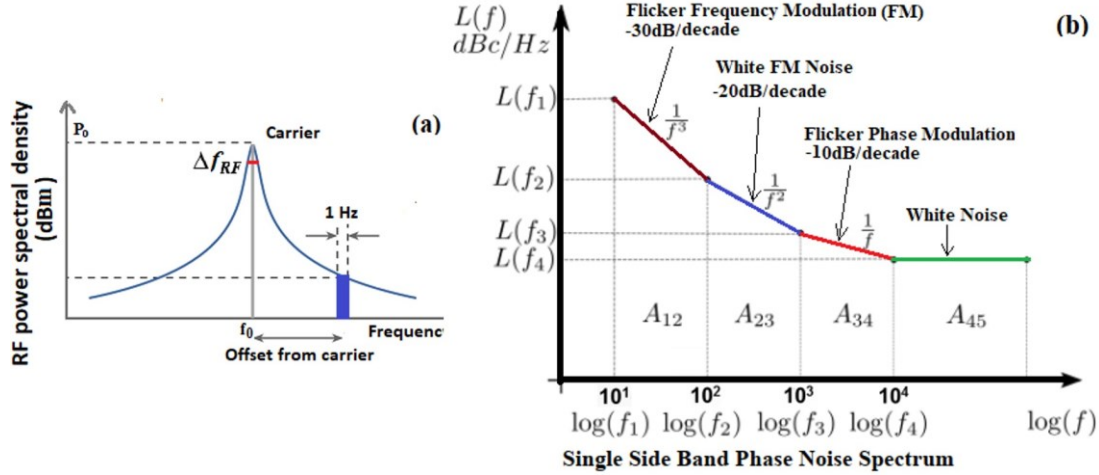
Figure 3.1: The 1st harmonic RF PSD showing FWHM bandwidth, peak power and central frequency. (b) A single sideband phase noise spectrum, $L(f)$, obtained from normalized RF PSD in one Hz bandwidth by Eq. (3.8) at a frequency offsets well above Δf_{RF1} showing regions and areas of different noise mechanisms with a frequency related various slopes and frequency boundaries [45].

The integrated (pulse-to-clock) time jitter from phase noise spectrum in the case of an F-P semiconductor PML laser, especially with the active region in a laser diode that consists of QD structures investigated in this work. Due to material nonlinearities and saturated absorber in the gain area, the phase correlation of the optical longitudinal modes can occur, resulting in a four-wave mixing process and, consequently, passively mode-locking [66], as discussed in Section 2.1.3.1 of this thesis. Thus, the commonly integrated root-mean-square (RMS) time jitter, also known as pulse-to-clock timing jitter, can be obtained from the integration of the single sideband (SSB) phase noise spectrum as shown in Fig. 3.1 (b) and Eq. (3.8) as follows;

$$\sigma_{int} = \frac{1}{2\pi f_0}\sqrt{2\int_{f_{low}}^{f_{high}} L(f)df} = \frac{1}{2\pi f_0}\sqrt{2(A12 + A23 + A34 + A45)}, \qquad (3.9)$$

where f_{high} and f_{low} are the upper and lower integration frequencies, respectively, in the interested range, and A_{12}, A_{23}, A_{34}, and A_{45} correspond to the areas of flicker frequency modulation, white flicker frequency noise, flicker phase modulation, and white phase noise, respectively [236], as shown in Fig. 3.1 (b). As pointed out in [235], this phase noise estimation method is only valid for PML lasers at frequency offsets well above the carrier peak linewidth.

72

For the time jitter estimation from RF PSD, a time jitter estimation method was explicitly proposed for semiconductor PML lasers [234]. The properties of intrinsic phase noise from relatively broadband spontaneous emission in the PML laser lead to a Lorentzian-shaped PSD of photocurrent RF phase noise. A study of the linewidth of the first harmonic of photocurrent RF can provide a simple and appropriate way to characterize the timing jitter of a semiconductor PML laser. According to the ref. [234], for a high repetition rate PML laser, as expressed in f_0, the pulse-to-pulse RMS timing jitter σ_{ptp} can be described as;

$$\sigma_{ptp} = \frac{1}{f_0} \sqrt{\frac{\Delta f_{RF}}{2\pi f_0}}, \tag{3.10}$$

where Δf_{RF} is the FWHM Lorentzian linewidth of the first harmonic of RF PSD. Timing jitter can be estimated by measuring the first harmonic photocurrent RF PSD of a semiconductor PML laser, and fitting the peak with a Lorentzian function. From equation (10), it is noticed that for a certain repetition rate f_0, the pulse-to-pulse timing jitter of a semiconductor PML laser is proportional to the square root of the Lorentzian linewidth of the RF PSD of the laser. Therefore, the FWHM of the RF beat note from a semiconductor PML laser determines the level of phase coherence between the modes of the optical frequency comb.

Timing jitter can also be estimated from the optical linewidth (phase noise) measurements. From Eq. (3.7), the first harmonic RF linewidth Δf_{RF1} can be estimated by measuring the optical phase noise of each longitudinal mode and performing a parabolic fit as a function of mode number. Therefore, the pulse-to-pulse jitter can be estimated from optical phase noise measurements by parabolic curve fitting, as shown in Eq. (3.10). This method does not require direct measurement of the RF PSD for a high repetition rate laser that necessitates the use of a high-speed photodetector. Therefore, this method is not restricted to measuring lasers with repetition rates below ~100 GHz.

3.4   Laser Design and Fabrication

The device presented in this paper is an InP-based p-n blocked buried heterostructure (BH) Fabry-Perot (FP) laser. Figure 3.2 (a) shows a schematic of the cross-section of the laser. The laser structure is comprised of a 170 nm thick InGaAsP waveguide core with 10 nm $In_{0.816}Ga_{0.184}As_{0.392}P_{0.608}$ (1.15Q) barriers embedding five stacked layers of InAs QDashes as the active gain region surrounded by n- and p- type InP cladding layers. A scanning electron microscope (SEM) image of the five stacked layers of QDs along the waveguide core of the laser is shown in Fig. 3.2 (b). The 10 nm barriers are thick enough to avoid electronic coupling between QDash layers, but correlated vertical stacking of the dashes is observed due to the strain fields. The lower n-type InP cladding contains 1.03Q ballast layers to pull the optical mode into the n-type region. This reduces cavity loss, increases efficiency, and reduces the coupling of spontaneous emission to the optical mode. Chemical beam epitaxy (CBE) was used to grow the InAs QDash material in a manner similar to that in [66], with further growth steps required for creating a buried heterostructure being performed by MOCVD. The average QDash density in each active
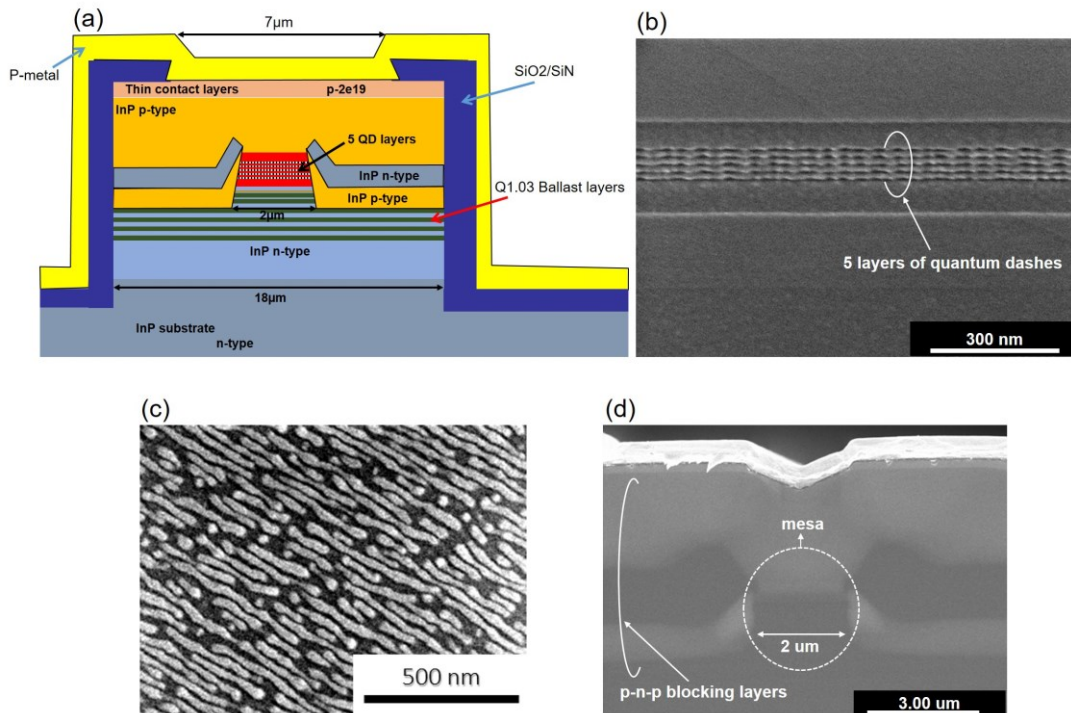
Figure 3.2: (a) Schematic of the cross-section of the laser. SEM images of (b) 5 stacked layers of quantum dashes, (c) the top view of the quantum dashes layer, and (d) front cross-section of the fully processed BH PML QD-MWL.

layer was around $3.5 \times 10^{10} cm^{-2}$. A scanning electron microscope (SEM) image of a typical QDash layer used in the fabrication is shown in Fig. 3.2(c).

The 1735 µm long laser waveguide was fabricated via standard photolithography in a combination of dry-, wet-etching and contact metallization techniques. After growing the laser core, a 2 um wide waveguide mesa was created by etching through the 1.15Q waveguide core followed by the selective overgrowing of pnp blocking layer structure to confine current to the waveguide mesa. Then after removing the selective area dielectric mask, the final p-type InP cladding and contact layers were grown. Both facets of the laser were left uncoated. A SEM image of the front cross-section of a fully fabricated BH PML QD-MWL is shown in Fig. 3.2(d).

3.5   Experimental Characterization

3.5.1   Laser Mounting and Test Station

The cleaved 1735 µm long laser chip is mounted on a commercially available Aluminum Nitride (AlN) carrier with two gold (Au) electroplated contacts to provide mechanical support and electrical connection to the laser chip, respectively. The bottom contact of the BH PML QD-MWL chip-on-carrier (CoC) provides a cathode connection through Eutectic Gold Tin (AuSn). In contrast, the top contact through wire-bonding provides the corresponding anode connection. For experimental characterization of the QD-MWL, the CoC is placed on a copper block with a thermoelectric cooler (TEC) underneath, as shown in Fig. 3.3.

A laser diode controller (LDC) (ILX Lightwave, Model LDC-3722) is used to DC bias the CoC through a pair of probes and drive the corresponding TEC to control its temperature. The laser output light is collected from its front facet using a collimated lensed polarization maintaining (PM) fiber attached to a two-stage PM optical isolator. The position of this fiber is adjustable in three dimensions for coupling the light from the laser cavity. A tunable optical bandpass filter (OBPF) is used to filter out individual light channels for analysis.
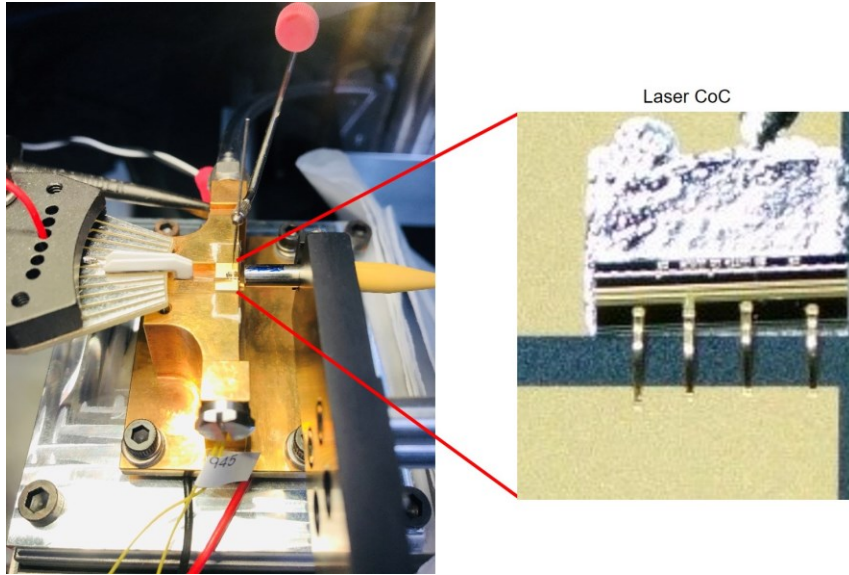
Figure 3.3: Laser testing setup with zoomed-in version showing PML BH QD-MWL CoC device.

3.5.2 Experimental Results and Performance Evaluation

The free running PML QD-MWL without any controlled feedback is characterized by measuring its light – current (L-I) curve, optical spectrum, phase noise, RIN and RF beat note. Figure 3.4 (a) shows a typical L-I characteristic curve of the BH PML QD-MWL measured at 19 °C. It can be seen that the laser starts lasing at around 50 mA and provides a maximum average output power of ~50 mW. The laser output spectrum is characterized using an optical spectrum analyzer (Anritsu, Model AQ6317B) with a spectral resolution of 0.01 nm. Figure 3.4 (b) shows the optical spectrum of the laser at 423 mA. Moreover, the device's typical RF beating frequency spectrum of about 25 GHz measured at 440 mA is shown in Fig. 3.4 (c). The laser operates in the shorter part of the C band with its central wavelength of around 1531 nm and 6-dB optical bandwidth of around 9 nm providing ~ 47 highly coherent optical channels with an optical signal-to-noise ratio of better than 40 dB as shown in Fig 3.4 (b).

Moreover, to characterize the device's noise performance, selected optical channels covering the spectrum of the BH PML QD-MWL-based CFC in the C-band are filtered out using an optical band pass filter (EXFO XTM-50-SCL-S-M) for optical phase noise and RIN analysis. The optical frequency noise of the selected individual channels is measured
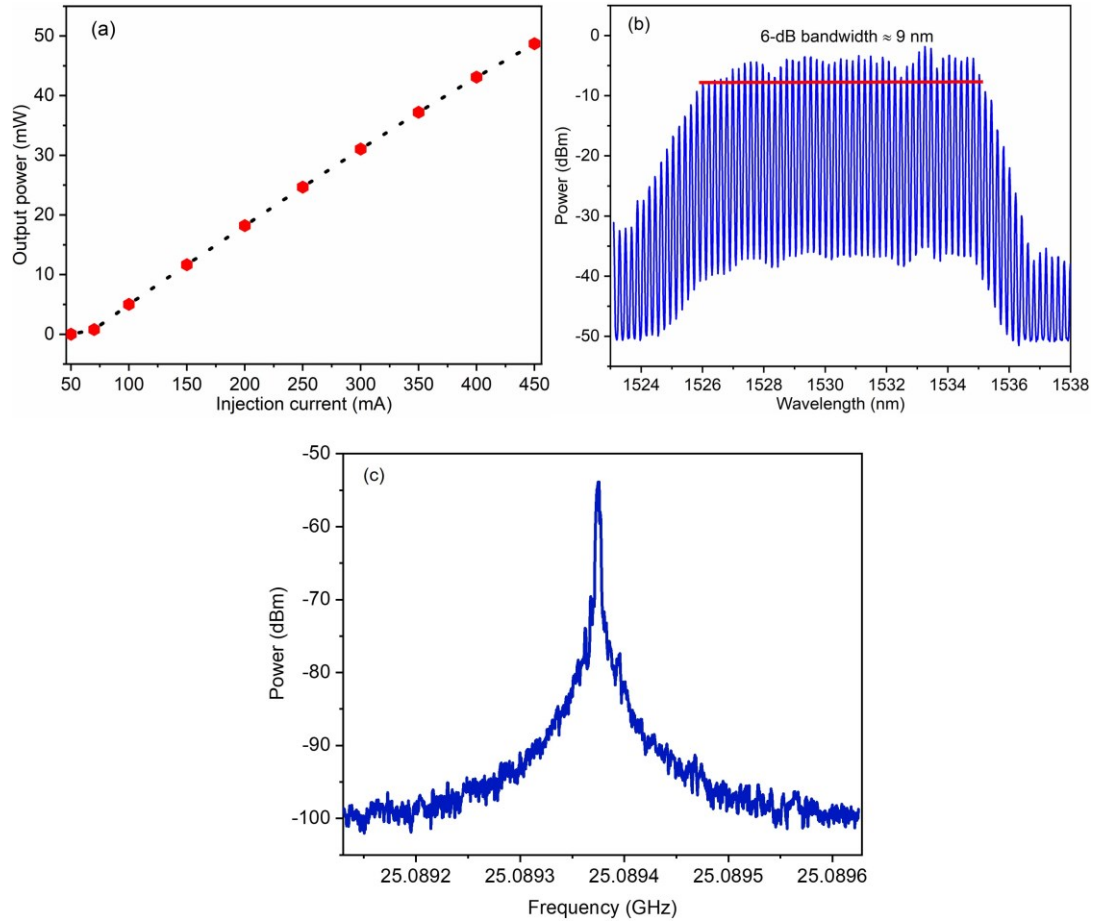
Figure 3.4: Measured (a) L-I characteristics, (b) optical spectrum, and (c) RF beat note spectrum (resolution bandwidth 5 kHz and video bandwidth 100 Hz), of the BH PML QD-MWL.

using an automated laser linewidth/phase noise measurement system (OE4000 OEWaves Inc.). The corresponding optical spectral linewidth is estimated from the selected channels' measured optical frequency noise spectrum, which is between 133.6 kHz to 306.2 kHz, as shown in Fig 3.5 (a). Similarly, the RIN is measured using a RIN measurement system (Agilent N4371A) and the integrated RIN for the selected individual channels over a frequency range of 10 MHz to 20 GHz is calculated between -130.7 dB/Hz and -136.6 dB/Hz, as shown in Fig 3.5 (b). It is observed that the BH PML QD-MWL achieves RIN and optical linewidth for each individual optical channel, typically less than -130 dB/Hz and 466.5 kHz, respectively. Furthermore, a 50 GHz signal analyzer (Keysight, Model N9030A) with a high-speed IR photodetector (New Focus, Model 1014) is used to investigate the RF phase noise and timing jitter performance of the BH PML QD-MWL between any two of its adjacent optical channels. It is observed that the device exhibits RF
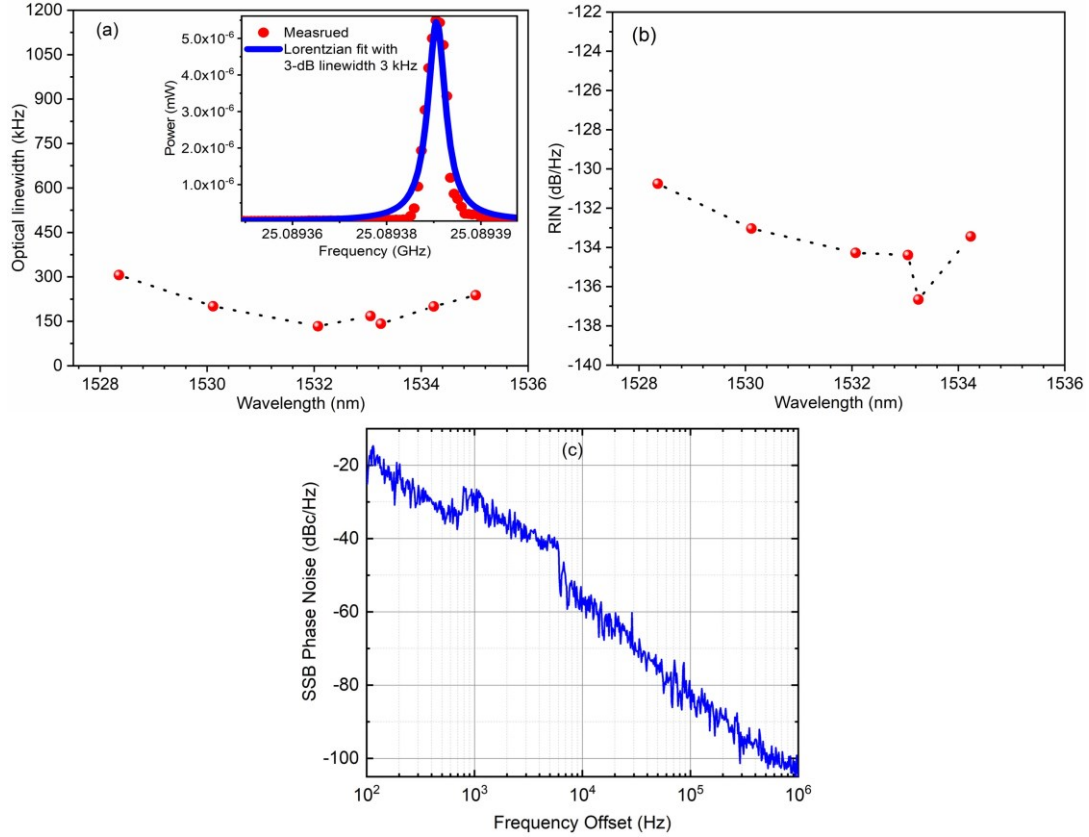
Figure 3.5: Measured (a) optical spectral linewidth for individual selected channels (inset showing RF beat-note of around 25.089 between any two adjacent channels with 3-dB linewidth ≤ 3 kHz measured at the resolution bandwidth (RBW) of 5.1 kHz and video bandwidth (VBW) of 100 Hz), (b) integrated RIN for individual selected channels over a frequency range of 10 MHz to 20 GHz, and (c) RF beat note SSB phase noise.

3-dB linewidth as low as 3 kHz to 0.512 kHz and timing jitter as low as 5.53 fs to 2.28 fs under stable operating conditions. The 3-dB RF linewidth is estimated from the measured RF spectrum of the beat-note signal at around 25.89 GHz using Lorentzian fit as shown in the inset of Fig 3.5 (a). The corresponding timing jitter is calculated from the obtained 3-dB RF linewidth [87], [235]. In addition, Fig. 3.5 (c) depicts the RF beat note SSB phase noise in the range from 100 Hz to 1 MHz, which is around -86 dBc/Hz at a 100 kHz offset and -106 dBc/Hz at a 1 MHz. Note that the SSB phase noise of a bared CoC device was measured in a crowded open Lab environment in its free-running operation using a phase noise measurement application on a 50 GHz signal analyzer (Keysight Technologies Model N9030A). Besides the simple design and fabrication as well as good optical noise performance of the laser, this narrow beat-note linewidth and low timing jitter not only shows high coherence between the optical channels of the laser but are of paramount
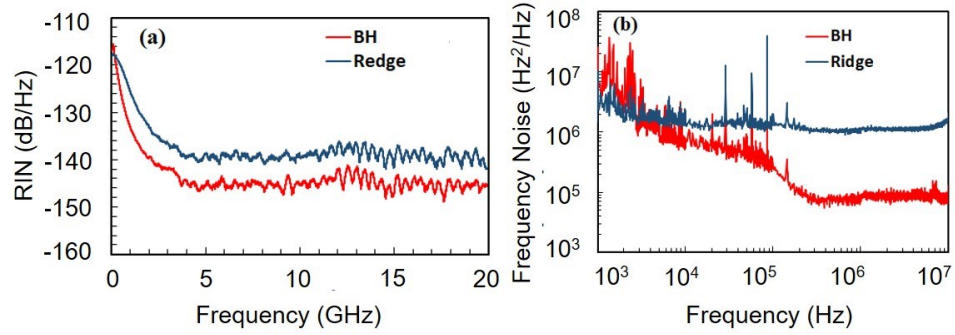
Figure 3.6: Measured (a) single channel RIN and (b) frequency noise spectra for a 25 GHz BH PML QD-MWL compared with a ridge structure-based PML QD-MWL having the same repetition rate and under the same measurement conditions.

importance for the spectrally pure mm-wave RF signals generation and data transmission in 5G optical heterodyne RoF systems.

Moreover, the noise performance of the 25 GHz BH PML QD-MWL is compared with a similar 25 GHz PML QD-MWL based on the surface ridge structure presented in [87]. To verify the superior noise performance characteristics of the 25 GHz BH PML QD-MWL, firstly RIN and frequency noise spectra of both devices are compared under the same experimental conditions, as shown in Fig. 3.6 (a) and Fig. 3.6 (b), respectively.

Although RIN has no adverse effect on coherent communications since balanced receivers suppress the RIN influence of both the carrier and the LO; however, due to the comb modes constantly exchange energy amongst each other caused by mode partition noise, the RIN of individual comb lines is usually high [237] and cannot be neglected. Particularly in the application of optical heterodyne-based RoF wireless fronthaul networks where a single optical receiver is used. It can be seen from Fig. 3.6 that the RIN and frequency noise significantly reduce in the case of BH QD-MWL-based CFC compared to a similar ridge structure device. This reduction is about 6 dB in the frequency range from 4 GHz to 20 GHz for RIN and at least 10 times lower in the high-frequency range from 0.1 MHz to 10 MHz for frequency noise compared with ridge structure laser. The low RIN values are attributed to the characteristics of QD material inside the laser cavity with very low mode partition noise in the BH waveguide active region.
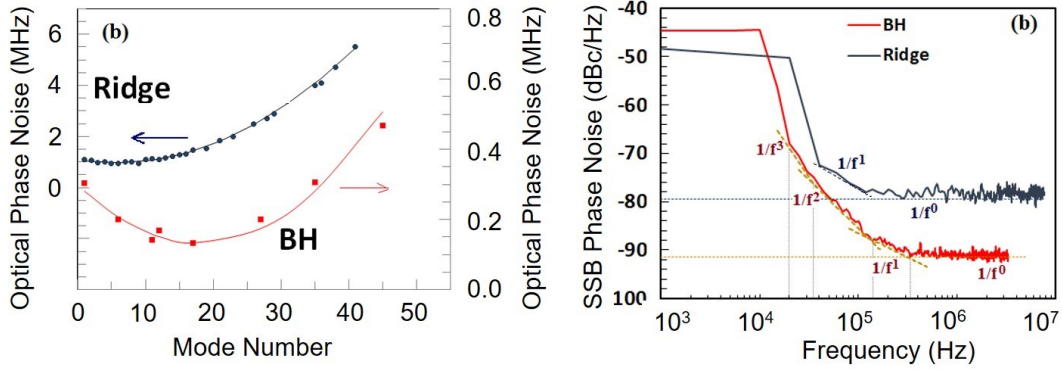
Figure 3.7: Measured (a) optical phase noise vs. laser mode number and (b) single sideband (SSB) phase noise spectrum obtained from a 25 GHz BH QD-MWL compared with a ridge structure-based PML QD-MWL having the same repetition rate and under the same measurement conditions.

To characterize the phase noise performance of the BH QD-MWL, selected optical channels covering the spectrum of the laser in the C-band are filtered out using an OBPF. The optical spectral linewidth, i.e., optical phase noise, for some of the selected Channels from 1526.4 nm to 1535.8 nm (covering 47 modes) is estimated from the measured optical frequency noise spectrum as shown in Fig. 3.7 (a). The performance is characterized for ridge structure-based CFC under the same measurement conditions. The phase noise measured for the 25 GHz BH QD-MWL in between ~0.133 MHz to ~0.460 MHz, as shown in Fig. 3.7 (a), which is much lower than the measured phase noise for ridge structure between ~0.97 MHz to ~5.5 MHz.

For analysis of the timing jitter from optical phase noise, the measured curves of phase noise vs. Mode channel number are parabolic fitted using the expression in Eq. (3.7). The fitting results of Δf_{nim}, n_{nim}, and Δf_{RF1} for both PML QD-MWL-based CFCs are listed in Table 3.1 for comparison. The minimum phase noise $\Delta f_{min} = 0.133$ MHz and the first harmonic RF linewidths $\Delta f_{RF1} = 0.512$ kHz are extracted for the BH QD-MWL, which are both about 7 times smaller than that obtained from the laser with ridge structure. The pulse-to-pulse timing jitter $\sigma_{ptp} = 2.28$ fs for the laser with BH is estimated from Δf_{RF1} using Eq. (3.10) as shown in Table 3.1, which is about 3 times lower than that from a laser with ridge structure.

Table 3.1: Estimated minimum optical linewidths, i.e., minimum optical phase noise, Δf_{nim}, minimum mode number n_{nim}, first harmonic RF spectrum linewidth Δf_{RF1}, estimated pulse-to-pulse timing jitter (PtPTJ), and integrated timing jitter (ITJ) for the 25 GHz QD-MWL with both BH and surface ridge structures.

QD-MWL Structure	Phase Noise vs. Mode Number Fitting			PtPTJ (fs)	ITJ (fs)
	Δf_{nim} *(MHz)*	n_{nim}	Δf_{RF1} *(kHz)*		
BH	0.133	18	0.512	2.28	0.48
Ridge	0.968	6	3.57	6.03	1.90

Furthermore, for integrated timing jitter performance analysis from RF phase noise, a single side-band (SSB) phase noise spectrum is obtained from measured RF PSD using a high speed IR photodetector and 50 GHz signal analyzer (Keysight Technologies Model N9030A). Figure 3.7(b) shows an SSB phase noise spectrum obtained from measured RF PSD by Eq. (3.8) for the 25GHz QD-MWLs both in the case of BH and surface ridge structures. The calculated integrated timing jitter of 1.90 and 0.48 ps are obtained for QD-MWLs with ridge and BH structures, respectively, using Eq. (3.9). The integrated timing jitter is reduced 4 times in the case of fabricated QD-MWL with BH structure compared to surface ridge structure. It can be seen from Fig. 3.7(b) that the in the case of QD-MWL with BH structure, the four typical noise types, i.e. flicker frequency modulation, white flicker frequency noise, flicker phase modulation, and white phase noise, exhibit predicted down tendency with slops of *$1/f^3$, $1/f^2$, $1/f$,* and *$1/f^0$*, respectively, as discussed in section 3.3. However, in the QD-MWL with surface ridge structure, flicker phase modulation is dominated, and the white phase noise covers the flicker frequency modulation and white flicker frequency noises, as shown in Fig 3.7(b). The white phase noise of the QD-MWL with BH structure is about 12 dB lower than that of the QD-MWL with surface ridge structure. This is perhaps why the performance of RIN, phase noise, and timing jitter of laser with BH structure is much better than that with surface ridge structure.

3.6 Multi-Gb/s Photonic-Aided RoF Wireless Communication System based on QD-MWL

3.6.1 System Experimental Setup

The BH PMWL QD-MWL-based CFC is evaluated in a system experiment by realizing photonics-assisted RoF wireless data transmission links. The schematic of experimental setup of the proposed system with the corresponding signals' spectra at different points along the transmission path is shown in Fig. 3.8 (a). Figure 3.8 (b) illustrates the corresponding experimental setup in the Lab with the RF MMW wireless link highlighted. In our experimental demonstration, we emulate a typical 5G fronthaul scenario with centralized radio access network (C-RAN) architecture. A remote optical heterodyne of two optical channels (data channel and optical-local oscillator (LO)) is employed to up-convert baseband data signals to the desired RF carrier signal in the optical domain at the RRU without using any RF electrical LO. Thus, an RF LO-free RRU is realized.
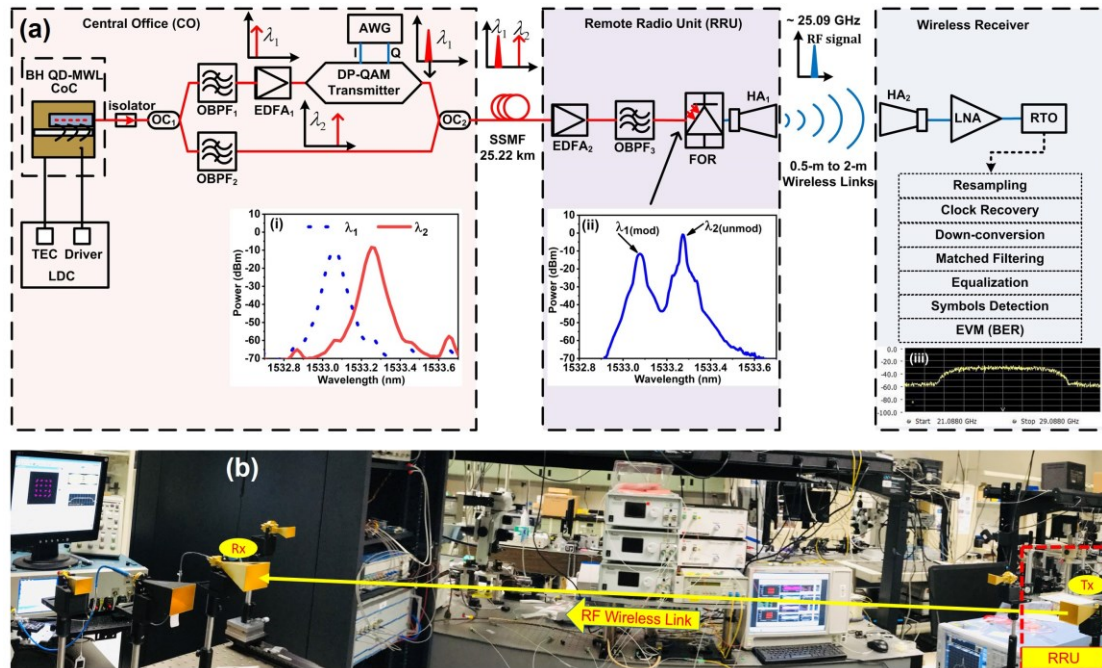
Figure 3.8: (a) Schematic of the experimental setup for photonics-assisted RoF RF signal generation, data transmission and detection using BH PML QD-MWL-based CFC with the insets showing optical spectra (i) of the selected two optical channels (data channel and optical LO) at the CO before modulation and (ii) after 25.22 km SSMF transmission (data channel modulated) at the RRU before the FOR, and (iii) electrical spectrum of the 4-Gbaud modulated 25 GHz RF wirelessly received signal at the wireless receiver. (b) A photo of the Laboratory testbed showing the RF wireless link.
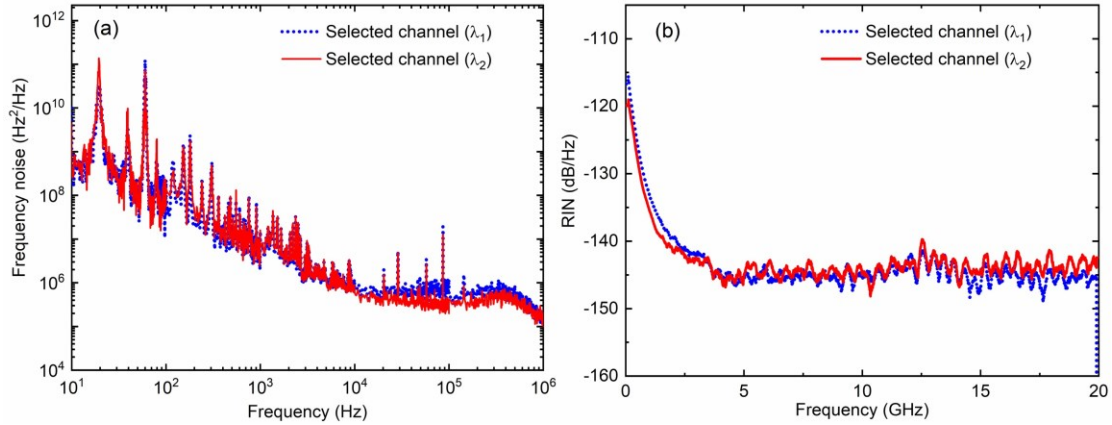
Figure 3.9: Measured (a) optical frequency noise and (b) RIN spectra for the selected modulated (λ_1) and unmodulated (λ_2) channels (data channel and optical LO) of the BH PML QD-MWL.

In the central office (CO), the BH PML QD-MWL device is used as a main optical source, which is biased at 422.78 mA and maintained at 19 °C using the LDC. The output of BH PML QD-MWL is connected to a 50/50 PM optical coupler (OC_1) through a two-stage PM isolator to avoid any back reflections, followed by two tunable optical bandpass filters ($OBPF_1$ and $OBPF_2$). The two OBPFs are used to select two adjacent optical channels; one for data transmission and another as an optical LO for photonic up-conversion at the RRU, spacing at the RF carrier frequency near the center of the standard 3GPP 5G NR frequency FR2-1 band n258 (24.25 to 27.5 GHz). The inset (i) in Fig. 3.8 (a) shows the optical spectra of the two selected optical channels at 1533.044 nm (λ_1) and 1533.240 nm (λ_2), respectively, that are filtered out from the free-running CFC spectrum obtained from the BH PML QD-MWL cavity without employing any controlled feedback mechanism. It is noteworthy that the selection of optical channels is flexible and scalable. The device can be used to generate RF signals in higher frequency bands of MMW spectrum including, K-band, K-band, V-band, W-band and even THz range depending on the channels spacing of the selected tones and modulating signals. The measured optical frequency noise and RIN spectra for the two selected optical channels are shown in Fig. 3.9 (a) and Fig. 3.9 (b), respectively. For these frequency noise spectra, the estimated optical spectral linewidths for λ_1 and λ_2 are 167.878 kHz and 141.828 kHz, respectively. Their integrated RIN calculated from the RIN spectra over a frequency range of 10 MHz to 20 GHz is -134.384 dB/Hz and -136.655 dB/Hz, respectively. After boosting the power

of optical data channel (λ_1) by an erbium-doped fiber amplifier (EDFA$_1$), it is modulated with 16-QAM digital baseband signals having a symbol rate of 4-GBaud by employing two channels (in-phase (I) and quadrature (Q)) of a dual polarization (DP) QAM optical transmitter system (SHF 46215B DP-QAM). The 4- GBaud 16-QAM baseband signals are generated electronically using an arbitrary waveform generator (AWG) (Keysight Technologies, Model M9502A) with a pseudo-random binary sequence (PRBS) pattern of $2^{11}-1$ bits. A root-raised cosine (RRC) filter with a roll-off factor of 0.35 is also employed for pulse shaping. The second optical tone (λ_2) is a supplementary channel to provide optical LO for heterodyne RF carrier signal generation at the RRU. The modulated and unmodulated optical signals are combined in a 50/50 OC2 and transmitted over a 25.22 km SSMF to the RRU.

In the RRU, the received optical signal is amplified by an EDFA$_2$ followed by OBPF$_3$ to filter out the effect of amplified spontaneous emission (ASE) noise and other optical components. The corresponding optical spectrum of the received 4-Gbaud modulated (λ_1) and unmodulated (λ_2) signals (data channel and optical LO) at the RRU is shown in the inset (ii) of Fig. 3.8 (a). These two optical signals are then beat together on a 38 GHz bandwidth fiber-optic receiver (FOR) (New Focus model 1474-A) to generate the 16 Gb/s (4-GBaud × 16-QAM) modulated RF carrier signal at ∼25.09 GHz. The FOR is directly attached to a 17/20 dBi Horn antenna (WR-34) with a 20-33 GHz bandwidth that transmits the generated 4-GBaud RF data signal over 0.5-m to 2-m free-space indoor wireless distance, as shown in Fig. 3.8 (b). The wireless link of up to 2-m is limited by the congested space in our Lab. The RF signal is then received by another identical Horn antenna and amplified by a low noise amplifier (LNA) before capturing into a real-time oscilloscope (RTO) for processing. The signal is captured and coherently detected in real-time by using a 33-GHz bandwidth and 100 GSa/s speed Tektronix DPO73304SX oscilloscope with vector signal analysis software (SignalVu). This process involves several digital signal processing (DSP) steps before the signal is demodulated. These steps include resampling, carrier and timing recovery, signal digital down conversion, RRC matched filtering to recover the baseband IQ data and to minimize inter-symbol interference (ISI), adaptive equalization to compensate for linear distortions, symbols detection, and data demodulation to calculate the EVM and BER. Finally, the system performance is evaluated

by analyzing EVM and BER of the received demodulated 16-QAM 4-GBaud (16-Gb/s) data signals. The BER is obtained from the EVM measurements [238], [239].

3.6.2 Experimental Results and Discussion

The performance of BH PM QD-MWL is evaluated in a proof-of-concept end-to-end fiber wireless integrated system experiment by generating, transmitting and detecting broadband RoF wireless signals in the downlink in real-time in terms of EVM and BER. In the experiments, photonics-assisted frequency up-conversion and detection of 4 GBaud 16 QAM baseband data signals are successfully demonstrated over 25.22 km SSMF and 0.5m to 2 m free-space indoor wireless RF links with EVM and BER below the standard limit of 12.5% and FEC requirement of 3.8×10^{-3}, respectively. A typical RF spectrum of the wirelessly received 25GHz 4GBaud 16QAM modulated data signals at the wireless receiver with 5.4 GHz transmission bandwidths can be seen in the inset of Fig. 3.8 (a) (iii). Moreover, Fig. 3.10 (a) and Fig. 3.10 (b) show the measured rms EVM (%) and
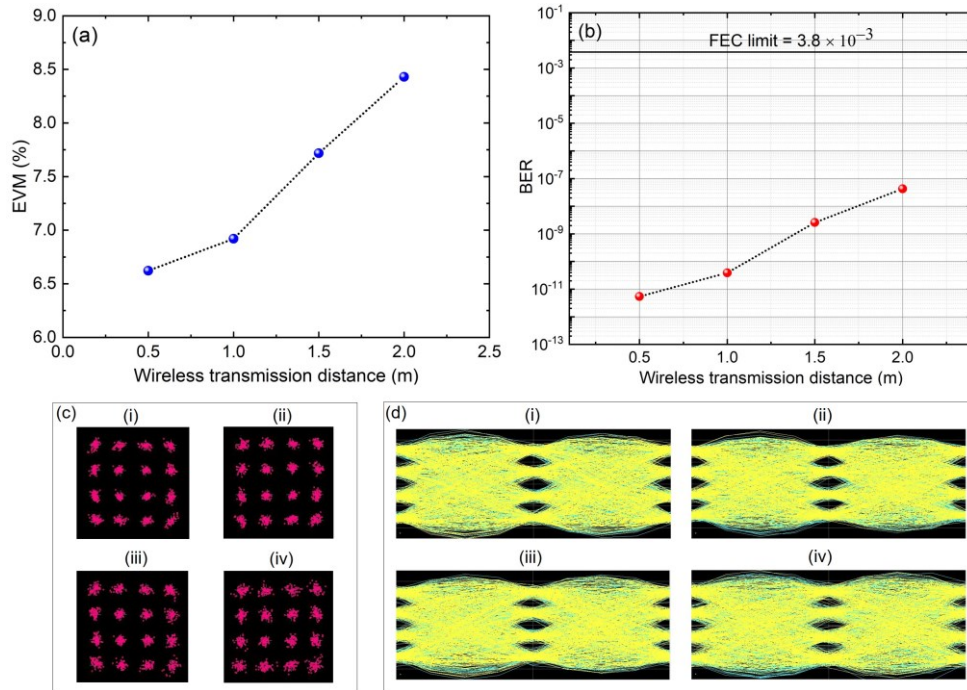
Figure 3.10: Experimental transmission performance of the BH PML QD-MWL in photonics-assisted 16Gb/s (4Gbaud × 16QAM) wireless links at ~25.09GHz 5G NR over 0.5m to 2m RF link distance through 25.22km SSMF with (a) rms EVM (%) and (b) calculated BER as a function of wireless link distance, (c) 16QAM constellations and (d) their corresponding eye diagrams observed for 4Gbaud signals after (i) 0.5m, (ii) 1m, (iii) 1.5m, and (iv) 2m, wireless links, respectively.

corresponding calculated BER as a function of RF link distance, respectively, at a fixed received optical power (ROP) of around 2dBm. It can be seen that for all the RoF wireless links, an EVM and BER of well below the standard FEC is achieved. Moreover, Fig. 3.10 (c) and Fig. 3.10 (d) shows the corresponding clear constellation and open eye diagrams for the received 4 Gbaud 16 QAM data signals over 25.22 km SSM RoF wireless links of (i) 0.5 m, (ii) 1 m, (ii) 1.5 m, and (iv) 2 m with the measured rms EVM of 6.62%, 6.92%, 7.72%, and 8.43%, respectively.

Moreover, Fig. 3.11 (a) and Fig. 3.11 (b) show the measured EVM and calculated BER at the wireless receiver as a function of the ROP. These results were obtained by employing a pair of 20 dBi Horn antennas in the RF wireless link. It can be seen from Fig.3.11 that the achieved BER performance is well below the standard FEC requirement of 3.8×10^{-3}, respectively, for all the cases. The clear constellation diagrams of the corresponding wirelessly received 16QAM signals are shown in the inset of Fig. 3.11 (a). Thus, a successful error-free RoF downlink wireless transmission of 16 Gb/s is achieved. The results show that decreasing the ROP degrades the EVM and BER performance as expected, considering the wireless channel path loss. In addition, it is noticed that slight variations in the link distance or ROP slightly varies the EVM and BER performance; however, this proportionality increases with a large increase in the link distance or significant drop in the ROP. It should also be noted that the experiments are run in a crowded Lab environment with the BH PML QD-MWL device unpackaged bared chip operating without any controlled feedback mechanism.
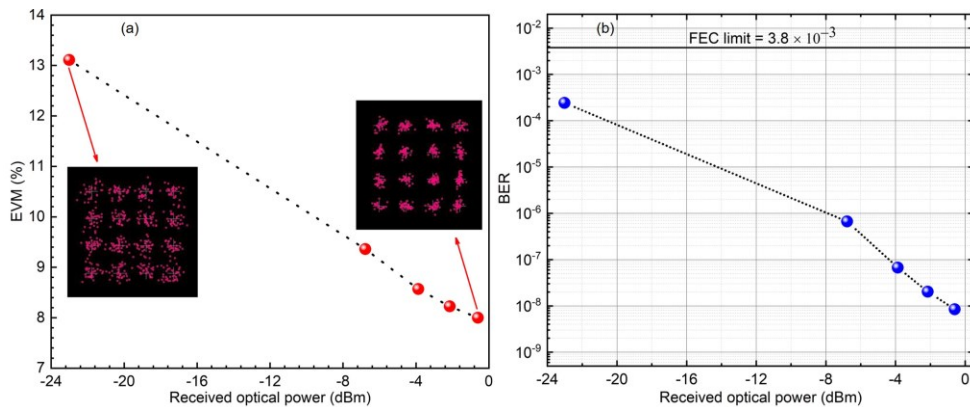
Figure 3.11: (a) Measured rms EVM and (b) calculcated BER versus ROP for 4Gbaud 16QAM signals detected over 2 m free space wireless channel through 25.22 km SSMF.

It can be seen that by using two optical channels of the BH PML QD-MWL-based CFC, an RF carrier signal of around 25 GHz with a total bit rate of 16 Gb/s (4Gbaud × 16QAM) is successfully delivered over 2 m wireless distance with an EVM and BER well below the forward error correction limit. As demonstrated, higher frequency broadband modulated radio carrier signals between 25 GHz and 1.15 THz can be remotely generated photonically by selecting the optical LO and data channel from the CFC spectrum spaced at the desired frequency. This shows that BH QD MLLs are equipped with the capability to handle the heterogeneous requirements of 5G and beyond fiber-wireless networks. Moreover, Table 3.2 compares our work in this chapter with state-of-the-art development discussed in Section 2.6, Chapter 2 of this thesis. Thus, the results indicate that the low noise monolithic integrated InAs/InP BH PML QD-MWL CFC with broadband flat spectra having multiple highly coherent optical channels is a promising optical source for applications in high-speed and high-capacity next generation fiber-wireless integrated communication systems.

Table 3.2: Comparison with state-of-the-art QD-MWLs based MMW RoF systems.

Ref.	Optical Source	λ Band	MMW Frequency (GHz)	Data Rate (Gb/s)	Mod. Format	MMW RoF Link	
						SMF (km)	WL (m)
[155], [214], [219]	PML-QD-MWL	C	~60	3.03	QPSK (OFDM)	0.05	-
[155], [156], [219]	PML-QD-MWL	C	~60	1.25 to 5	OOK	~ 0.054	25
[35]	PML-QD-MWL	C	25	0.08	16-QAM	20	2
[16]/[220]	SIL-PML-QD-MWL	C	60	1.12/~1.17	64-QAM (OFDM)	25	-
[221]/[37]	SIL-QD-MWL	C	100	10	OOK	50	10/15
[33]	SIL-QD-MWL	C	40/80	10	16-QAM (OFDM)	50/25	20
[38]	HIL-QD-MWL	C & L	60	10	32-QAM (OFDM)	50	-
[31]/[34]	EIL/SIL-QD-MWL	L	28	2	QPSK	20	4/6
[34], [216]/[217]	SIL/SIL&EIL-QD-MWL	L	30	2	QPSK	20	2
[32]	SIL-QD-MWL	L	28/25	8	QPSK/16-QAM	10	4/2
[36]	QD-DW-DFBL	C	146	1	OOK	-	0.025
This work	**PML-QD-MWL**	**C**	**25 GHz**	**16**	**16-QAM**	**25**	**2**

Mod. Format: modulation format; PML: passively mode-locked; SIL: self-injection-locked; EIL: external-injection-locked; HIL: hybrid-injection-locked; WL: wireless link

3.7   Summary

In this chapter, we present a highly coherent low-noise and monolithically integrated semiconductor BH PML InAs/InP QD-MWL-based CFC with simple and compact design providing a large number of highly correlated optical channels with low noise and high power performance with an FSR of around 25 GHz for broadband fiber-wireless integrated RoF-based 5G NR fronthaul systems. The CFC features low threshold current, high output power, and flat broadband spectrum with a 6-dB bandwidth of around 9 nm having ~47 equally spaced highly coherent and low noise optical channels. The device is experimentally characterized, and the results of RIN, phase noise, and timing jitter are compared with a similar PML QD-MWL CFC based on a ridge waveguide structure. It is shown that the QD-MWL with BH structure exhibits significantly reduced RIN, phase noise, and timing jitter compared to the surface ridge structure. For the timing jitter, a theoretic background is also presented including characterization methods from both the 1st harmonic RF power spectral density and optical phase noise. In addition, a proof-of-concept photonic-aided multi-Gb/s RoF wireless system based on the BH QD-MWL is proposed and experimentally demonstrated in end-to-end RoF wireless links. A comparison with state-of-the-art work is also presented. The noise performance of each filtered individual channel of the developed 25GHz BH PML QD-MWL is experimentally characterized as exhibiting an optical phase noise of less than 466.5 kHz and an integrated average RIN of typically less than -130 dB/Hz over the frequency range from 10MHz to 20GHz. Its RF beat note linewidth between two adjacent channels is measured to be ≤ 3 kHz with a calculated time jitter of ≤ 5.53 fs. Furthermore, by using the BH PML QD-MWL CFC, a successful demonstration of photonic generation, transmission, and detection of broadband wireless RF signals at around 25 GHz over 0.5m to 2-m free space indoor wireless links through a total of 25.22 km SSMF with a data rate of 16 Gb/s is presented. The demonstrated RoF wireless links achieve EVM and BER well below the standard requirements. The results indicate that the InAs/InP BH QD-MWL-based CFC has the potential to synthesize LO-free radio signals at frequencies of up to 1.15 THz with multi-Gb/s wireless signals delivery featuring low noise and cost-efficient solution for broadband RoF-based fronthaul systems of next generation wireless communication networks.

Chapter 4

InAs/InP QD DW-DFB Laser for High Capacity Broadband Optical Heterodyne MMWoF Wireless Systems

4.1 Introduction

IN recent years, optical generation of millimeter-wave (MMW) signals (30 GHz – 300 GHz) have been attracting considerable interest from both academia and industry due to its advantage of simple, flexible and scalable system design for achieving very high frequencies with very low noise. In particular, applications in future seamless fiber-wireless integrated access networks, such as fronthaul for 5G and beyond mobile wireless communication networks [18], [27], [123], are of interest. Since 3GPP has standardized higher frequency bands for 5G new radio (NR) between 24.25 GHz to 52.6 GHz designated as frequency range 2 (FR2) in Release 15 [6] and this range is extended from 52.6 GHz to 71 GHz in Release 17 named as FR2-2 [7].

Usually, radio frequency (RF) signals are generated in the electrical domain; however, considering the ultra-high speed MMW signals, photonic-based techniques are more suitable. Because of low system complexity, low cost, high tunability, high spectral purity, and long transmission distance, they are considered advantages over their conventional electrical counterparts [18], [240]. Thus, the generation and processing of high-speed and broadband MMW signals in an all-electrical setup are hindered by the bandwidth limitation of electronic devices in addition to cost and complexity. Besides, the transmission of MMW signals over long distances is a real challenge. Consequently, broad bandwidth, simple, efficient, and cost-effective photonic MMWoF solutions are viable alternatives for MMW signal generation, processing, control and distribution in the optical domain for application in broadband wireless access networks [9], [10]. The optical devices and techniques that are used for MMW signals in conjunction with the bandwidth-efficient analog radio-over-fiber (A-RoF) technology not only overcome the problem of high bandwidth requirements, transmission capacity and span limitation but also significantly reduce system complexity [9], [10], [16], [17] footprint, capital expenditure (CAPEX) and operating expenses (OPEX), as discussed in the previous Chapters.

The basic notion of MMW signal generation and distribution in the optical domain through MMWoF links is based on the remote optical heterodyne beating of two phase-correlated optical signals having different wavelengths on a high-speed photodetector (PD) after running over several tens of kilometers of optical fiber [14], as discussed in Section 2.3, Chapter 2 of this thesis. Consequently, photonic RF signal generation techniques can be used to generate RF signals of up to THz range, limited only by the frequency response of the PD. However, MMW signals in the optical domain are commonly generated using commercially available single-frequency laser sources, which might not achieve MMW signals with high spectral purity due to the lack of coherence and correlation between the laser sources themselves. Relative drift in emission wavelength between the sources will cause broadening/degeneration of the MMW signal, degrading the system performance. It has been recently shown that the performance of wireless transmission is strongly dependent on the intensity and phase noise attributes of the optically generated MMW signals, which heavily rely on the spectral purity and coherence of the optical sources generating them [123], [168]. Thus, it requires optical sources with ultra-narrow optical linewidth and low relative intensity noise (RIN).

4.2   Related Work

Various solutions have been proposed and demonstrated to obtain low phase and intensity noise in bulk / quantum-well (QW) based laser sources. This is done by either generating heterodyne signals from the same laser source with methods such as external modulation [20], [21], and gain-switched optical frequency combs [18] or individual laser sources with schemes such as optical injection locking [28], and optical-phase-locked-loop (OPLL) [29], as discussed in detail in Section 2.3, Chapter 2 of this thesis. Nevertheless, most of these methods are comparatively complex and not cost-effective. In contrast, the simplest and most cost-effective approach to attaining high spectral purity would be the design of dual-mode optical laser sources [157] with high coherence and correlation in the C-band. C-band allows access to commercial telecommunication components to modulate, control, and manipulate optical signals. Yet, most of the reported dual-mode lasers are based on either external cavity [161] or separate multi-section structures with independent bias control for each section [157], [162]. Therefore, such optical laser sources either involve

complex control circuitry or result in a relatively broad linewidth beat note due to the uncorrelated phase noise of the two optical modes. Instead, the generation of concurrent dual-modes from a single cavity structure sharing a single gain medium is appealing due to device compactness, cost-effectiveness, high-temperature stability and high spectral purity. Although simultaneous two-wavelength lasing has been demonstrated in QW lasers using a single cavity structure [158], [160], nonetheless, the two modes do not share exactly the same gain region, and relatively high optical spectral linewidths were achieved. Thus, such sources will most likely result in larger linewidth beat-note signals. On the other hand, quantum dot and quantum dash (QD) based lasers have been shown to have great potential as efficient optical beat sources due to the inherent characteristics of QD materials [73], [241]. QD materials have superior attributes due to their compactness, ultra-low threshold current density, ultra-fast carrier dynamics, improved temperature stability, and high spectral purity [68]. Owing to the inherent characteristics of QD materials, QD materials-based lasers are capable of achieving very narrow spectral linewidths and low RIN as compared to QWs [73], as discussed in Section 2.1.3.1, Chapter 2 of this thesis. These characteristics make the QD-based dual-wavelength lasers attractive sources for generating MMW signals with high spectral purity and coherence.

Compared with other optical sources, such as QD combs or QD injection locked laser diodes and dual-mode devices based on separate DFB cavities or individual DFB lasers, common-cavity QD DW-DFB laser (QD-DW-DFL) offers a compact and simple solution for MMWoF systems by generating two different wavelengths from within the same cavity featuring high output optical power and low noise. This results in high optical power per mode (significantly higher than for a QD comb laser) and high spectral purity with low phase and relative intensity noise. Importantly, this makes the device comparatively simple and compact. Consequently, the QD-DW-DFBL has the advantage of reducing system complexity and cost showing the potential to offer a simple and low cost solution for 5G optical heterodyne MMWoF systems.

Thus, by making use of the unique properties of QD materials, in this chapter, we present the design, growth, fabrication and experimentally investigation of a novel compact monolithic InAs/InP QD-DW-DFBL. The QD-DW-DFB lasers work at room temperature

and can cover an RF frequency range from 30 GHz to 300 GHz. Our experimental results show that this novel monolithic QD-DW-DFBL can achieve a very narrow optical linewidth down to 15.83 kHz and RIN as low as -158.3 dB/Hz in the frequency range from 10 MHz to 20 GHz. Using this laser, we can generate high-purity MMW signals between 46 GHz and 48 GHz with a record narrow linewidth of 26 kHz, which, as far as we know, is the best result reported so far for a single cavity-based free-running dual-wavelength semiconductor laser with common cavity modes. Moreover, using the InAs/InP QD-DW-DFBL for MMWoF systems, we present the experimental demonstration of broadband multi-Gb/s optical heterodyne MMWoF wireless links at 5G NR frequency of around 47.27 GHz. The demonstration includes electrical RF synthesizer-free real-time photonic generation, wireless transmission and detection of wide-bandwidth MMW M-QAM modulated (16-QAM, 32-QAM and 64-QAM) data signals having symbol rates of 4- and 6-GHz with bit rates ranging from 16 Gb/s (4-GBaud × 16-QAM) to 36 Gb/s (6-GBaud × 64-QAM) over hybrid fiber-wireless links comprising of a back-to-back (BtB), 25-km and 50-km SSMF and 2-m to 9-m free-space wireless channel. After long-reach transmission of baseband data modulated optical signal in 25-/50-km SSMF, the MMW carrier is optically-synthesized remotely through optical-heterodyning for free space wireless data transmission. This ensures the transmission and distribution of ultra-high frequency MMW signals over long distances with better performance. Moreover, a thorough end-to-end optical-MMW link analysis is performed with different M-QAM, fiber spans, MMW link distances and data transmission bandwidths to evaluate the transmission performance of the proposed QD-DW-DFL-based MMWoF system in terms of EVM, BER, constellations and eye diagrams. To the best of our knowledge, this is the first experimental demonstration to realize MMWoF wireless links at the potential 5G NR frequency band of around 47.27 GHz with real-time wireless transmission and detection of wideband MMW M-QAM (16-/32-/64-QAM) modulated data signals having a maximum bit rate of 36 Gb/s using a free-running InAs/InP QD-DW-DFBL. The generated MMW frequency range from 46 GHz to 48 GHz of the device falls within the potential 3GPP 5G NR standard band (n262) of frequency range 2 (FR2), offering a promising optical MMW source for 5G MMWoF systems.

The work in this chapter is based on the published articles in [46], [47], [242]–[244]. The remainder of this chapter is organized as follows. Section 4.3 presents the design, fabrication, and implementation of the QD-DW-DFBL. The device's experimental characterization is presented in Section 4.4. Section 4.5 presents the proposed QD-DW-DFBL-based MMWoF wireless system design and detailed implementation. It is followed by the experimental results and discussion in Section 4.6. Finally, section 4.7 summarizes this Chapter.

4.3   QD DW-DFB Laser Design and Fabrication

The device studied in this paper is an InP-based p-n blocked buried heterostructure (BH) common cavity quantum dash dual-wavelength distributed feedback laser (QD DW-DFBL). Figure 4.1 (a) shows a schematic of the cross-section of the laser. The undoped gain region of the device consists of five stacked layers of InAs QDs in a 170 nm thick
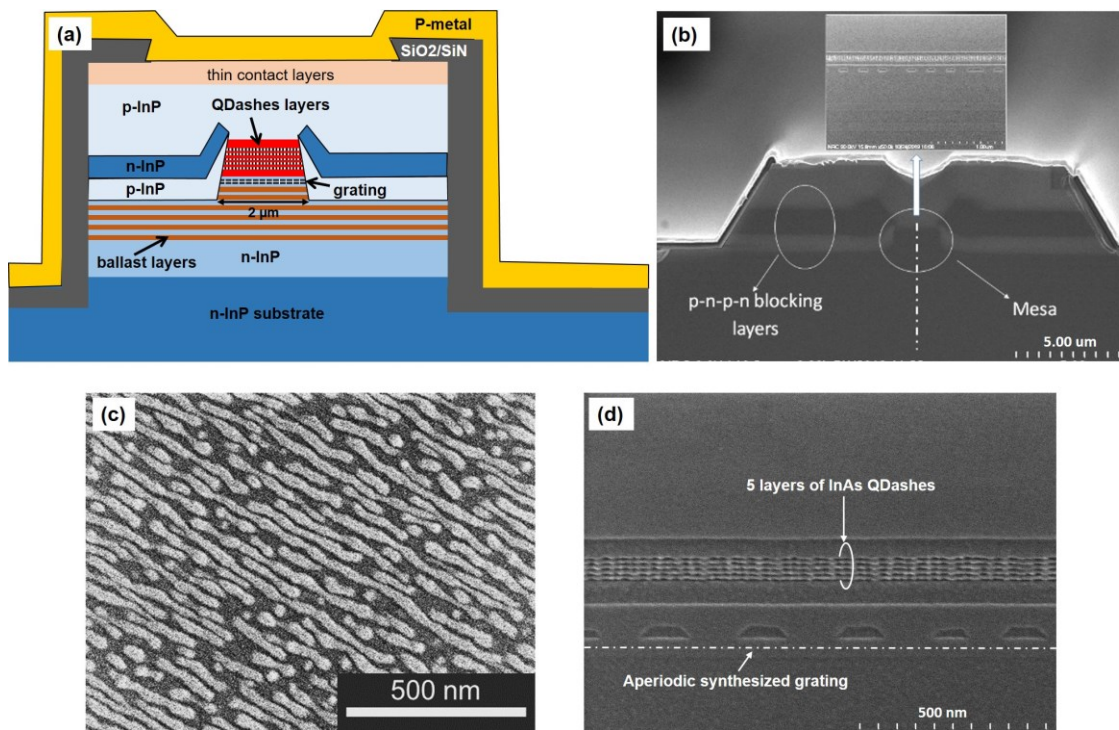
Figure 4.1: (a) Schematic of the cross-section of the QD-DW-DFBL. SEM images: (b) front cross section of the fully fabricated BH QD-DW-DFBL with inset showing lateral cross section of a portion of the synthesized grating at the middle of the mesa along the optical waveguide, (c) top view of quantum dashes layer, (d) the lateral cross-section through the middle of the mesa of the device showing synthesized aperiodic grating underneath 5 stack layers of QDs.

InGaAsP waveguiding core with 10 nm $In_{0.816}Ga_{0.184}As_{0.392}P_{0.608}$ (1.15Q) barriers. The waveguide core provides both carrier and optical confinement. The active region is surrounded by n-type and p-type InP cladding layers as shown in Fig. 4.1 (a). In the lower n-type InP cladding, 1.03Q ballast layers are employed to pull the mode into the n-type region, which helps in reducing cavity loss and increasing efficiency. This also reduces the spontaneous emission coupling to the optical mode. The InAs QD material was grown on (001)-oriented n-type InP substrate using chemical beam epitaxy (CBE) followed by further etch and regrowth steps using metal-organic chemical vapor deposition (MOCVD) to create the BH. The growth of the dashes was performed in a manner very similar to that in [66], where to encourage the growth of dashes rather than dots, a thin layer of GaAs rather than GaP was grown before the InAs was deposited. Fig. 4.1 (c) shows a plan view scanning electron microscope (SEM) image of a typical quantum dash layer used for laser fabrication. The 1800 µm long laser waveguide was fabricated through standard photolithography with dry- and wet-etching and contact metallization techniques. Following the growth of the laser core, a mesa is formed by etching through the 1.15Q core and grating layer using a dielectric mask and a combination of dry and wet etching. A pnp blocking layers' structure was then selectively overgrown to confine the carriers to the waveguide mesa. The dielectric mask was removed and followed immediately by a final growth that consisted of p-type InP cladding and contact layers. Fig. 4.1(b) shows an SEM image of the output front cross-section of a fully fabricated BH QD DW-DFB laser. The inset in Fig. 4.1 (b) is a lateral cross-section through the middle of the 2.0 µm mesa showing a portion of the synthesized grating. After cleaving, both facets of the device were AR coated.

A novel synthesized aperiodic non-uniform diffraction grating is incorporated below the QDs active layers underneath the waveguiding core in the n-type InP cladding, as shown in Fig. 4.1 (a), which was defined using e-beam lithography and wet etching. This can also be seen in the SEM image of the lateral cross-section of the device below the 5 stack layers of QDs in Fig 4.1 (d). The novel synthesized aperiodic diffraction grating layer was designed to provide distributed feedback such that two longitudinal modes would lase simultaneously. This generates two highly correlated longitudinal modes simultaneously at different wavelengths with a drive current and temperature-controlled tunable MMW
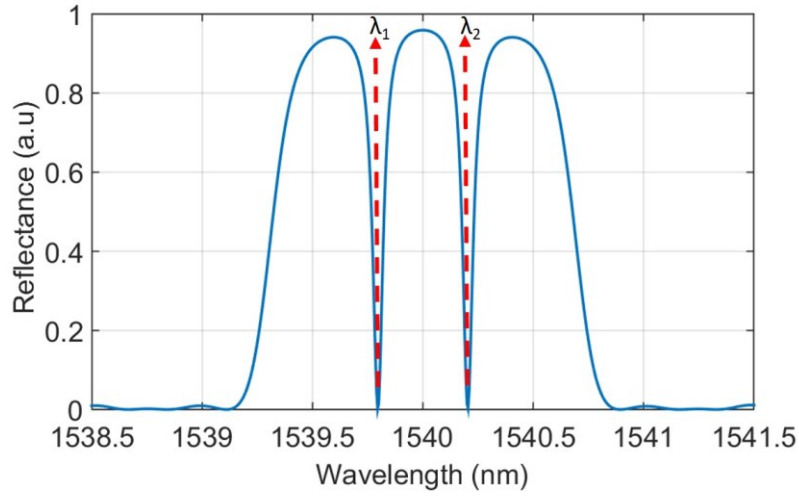
Figure 4.2: Reflection spectrum of the QD-DW-DFBL cavity.

frequency range between 46 and 48 GHz from within the single optical cavity of the device with QD active layers. The desired reflection spectrum of the diffraction grating was obtained through optimization [245] of the transfer matrix formulation of the laser cavity. This method consists of combining multiple stop-bands with various amplitudes to create the desired spectrum. Optimization involves maximization of the gain margin between the two desired modes and the Bragg side modes, as well as obtaining a uniform optical field distribution along the laser cavity. Particular attention was paid to obtaining almost identical threshold gain for both desired modes. The result of the optimization is a non-uniform and aperiodic grating spanning total length of the laser cavity. Fig. 1 (d) shows a cross section of the synthesized grating underneath the active region with five stacked layers of InAs QDs, and Fig. 4.2 shows the resulting reflection spectrum of the synthesized grating with location of the two optical modes highlighted. It consists of three stop-bands with two central dips and a flat frequency response on the edges of the outer stop-bands. The gain margin between the two dominant modes and the next lowest threshold mode is calculated to be 45 cm^{-1}, and the threshold gain difference between the dominant modes is less than 10^{-3} cm^{-1}. The spacing between the modes was designed to be around 47 GHz. Both facets of the 1.8 mm long device had antireflective coating (AR).

4.4 Experimental Characterization of the QD-DW-DFBL

4.4.1 Laser Mounting and Test Station

The cleaved 1800 µm long laser chip is mounted on a commercially available Aluminium Nitride (AlN) carrier to provide mechanical support to the device. The chip on carrier (CoC) is shown in the zoomed inset of Fig. 4.3. The QD-DW-DFBL chip is bonded to the carrier with Gold Tin (AuSn) providing the cathode connection, with the top contact being wire bonded for the anode connection as shown in the zoom-in of Fig. 4.3. For the experimental characterization of the QD-DW-DFBL, in the experiment, the CoC is placed on a copper block with a thermoelectric cooler (TEC) driven by a laser diode controller (LDC) (ILX Lightwave, Model LDC-3722) to reduce the power driving noise and environment temperature frustration. The LDC biases the laser through a pair of DC electrical probes, as shown in Fig. 4.3, and also drives the corresponding TEC to control its temperature. The output light of the laser was collected from the front facet through a collimator attached to a single mode polarization maintaining (PM) fiber. The position of this fiber is adjustable in three dimensions for optical coupling of the light from the laser cavity. A two-stage PM optical isolator was incorporated after the collimator in order to avoid any back reflection into the laser cavity from the measurement system.
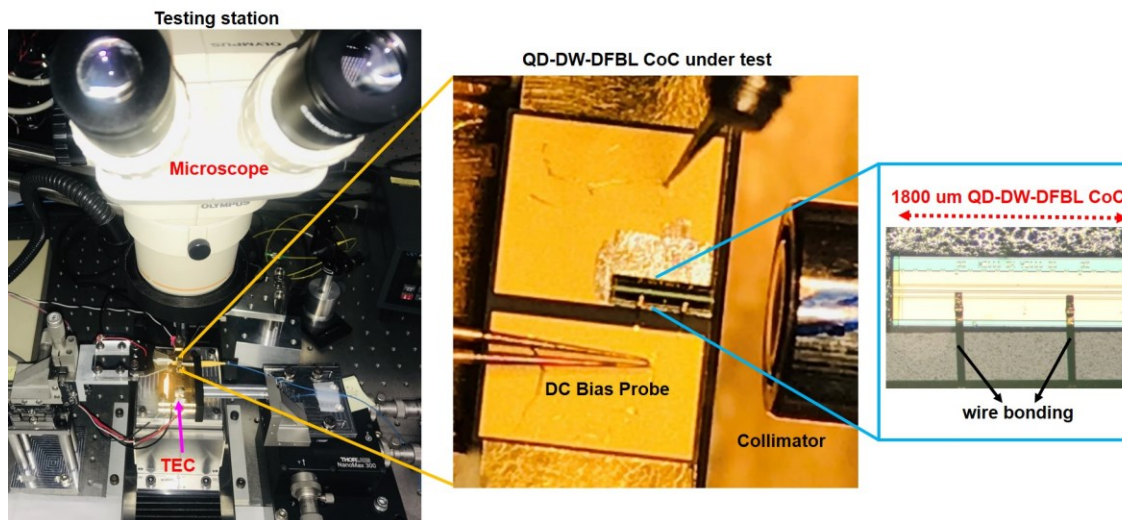
Figure 4.3: Laser testing station with zoomed-in version showing QD-DW-DFBL CoC under test.

Moreover, for the laser spectra measurements, an optical spectrum analyzer with a spectral resolution of 0.01 nm was used. The optical phase noise and RIN of the device were measured with a commercial OEwaves OE4000 automated laser linewidth/phase noise measurement system and Agilent N4371A RIN measurement systems, respectively. A tunable filter (Santec OTF-970) was also used for filtering individual modes for analysis. For the MMW signal generation, the two optical modes were mixed together on a Newport high-speed photodetector (Model-1014), and the corresponding results were measured through a Keysight 50 GHz PXA signal analyzer (Model N9030A).

4.4.2   Experimental Results and Performance Characterization

The free running BH QD-DW-DFBL without any controlled feedback is characterized by measuring its light – current (L-I) curve, optical spectrum, phase noise, RIN and RF beat note. The laser chip was tested by applying continuous wave injection current. All measurements are carried out at 18°C and 360 mA where it is not stated.

The characteristics of the laser and the generated MMW signals are analyzed in terms of spectral purity along with the dependency of the operating optical modes on the bias current applied to the device. We measured the light-current (L-I) characteristics, spectra, and behavior of the optical modes as a function of injection current. Fig. 4.4 (a) shows the typical L-I characteristics of the device. Lasing starts at a threshold current of around 70 mA and the device shows stable linear behavior in terms of output power as a function of injection current. Fig. 4.4 (c) shows the corresponding optical spectra of the device taken under different current biases ranging from 180 to 500 mA. Satellite modes are observed on either side of the two main modes due to four wave mixing (FWM) within the laser cavity. Fig. 4.4 (b) shows the power and emission wavelength of the four strongest lines. A redshift is observed with increasing drive current with the spacing between the two main modes increasing by 0.0158 nm when varying the current from 180 to 500 mA. The mode spacing corresponds to beat note frequencies between 46 and 48 GHz. This shows that by changing drive current and temperature the mode spacing can be tuned by around 0.0158 nm, which corresponds to tuning MMW frequency range from 46 GHz to 48 GHz. However, the RF beat note of the QDash DW-DFB laser can be adjusted from the GHz to
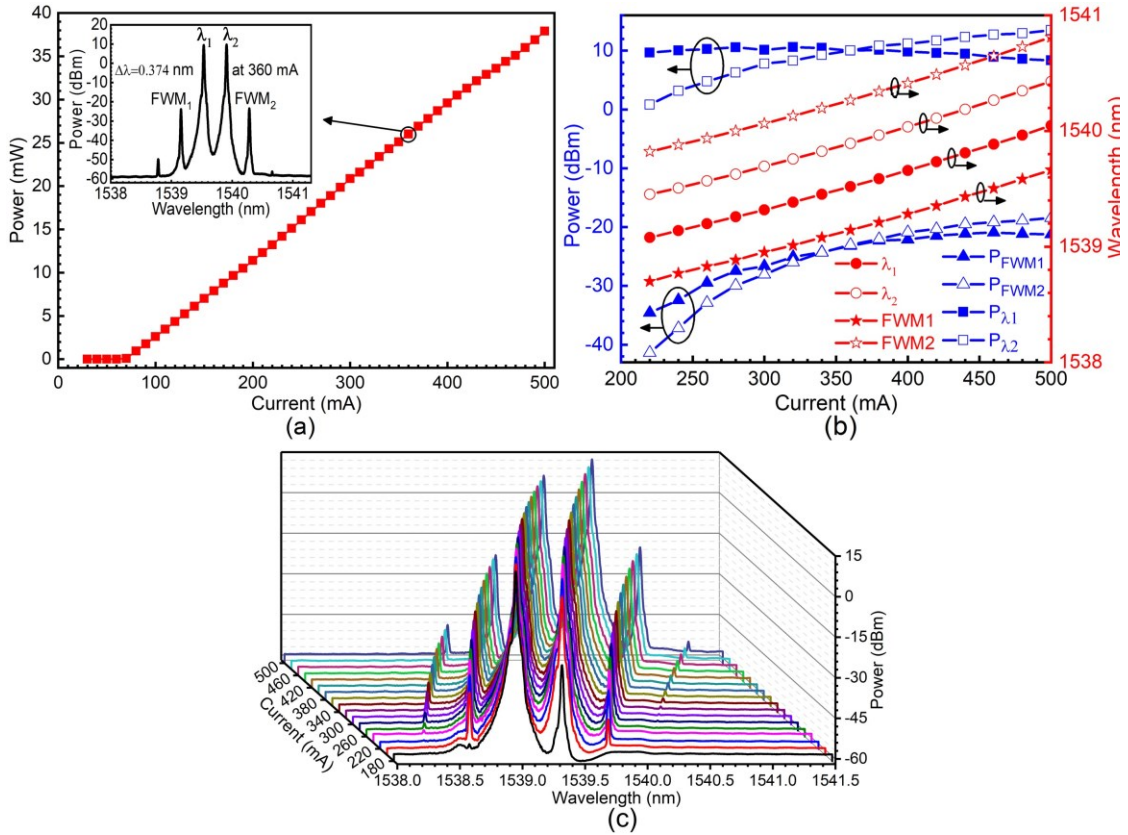
Figure 4.4: Measured (a) L-I characteristics (inset shows the optical spectrum at 360 mA), (b) variation of the emitted dual-modes, FWM and their corresponding output powers as a function of bias current, and (c) spectra at different bias currents of the QD-DW-DFBL.

the THz range by modifying the design of the synthesized aperiodic grating of the device for the desired spectrum.

Although the device exhibits stable dual-wavelength lasing in a large range of injection currents, the intensity of the two optical modes becomes equal around 360 mA with a wavelength spacing of 0.374 nm as depicted in the inset of Fig. 4.4 (a) and Fig. 4.4 (b). It should also be noted that at an injection current above 180 mA, the device starts exhibiting FWM signals at the shorter and longer wavelength sides of the two modes as shown in Fig. 4.4 (c). These FWM signals stem from the mixing process that occurs within the laser cavity itself, which shows the spectral and temporal stability of the corresponding two optical modes. This shows nonlinear effects of the cavity, which is believed to result in phase locking of the modes, hence reducing their relative amplitude and phase variation. This further stabilizes modal amplitudes and relative phase of the QD DW-DFBL. In
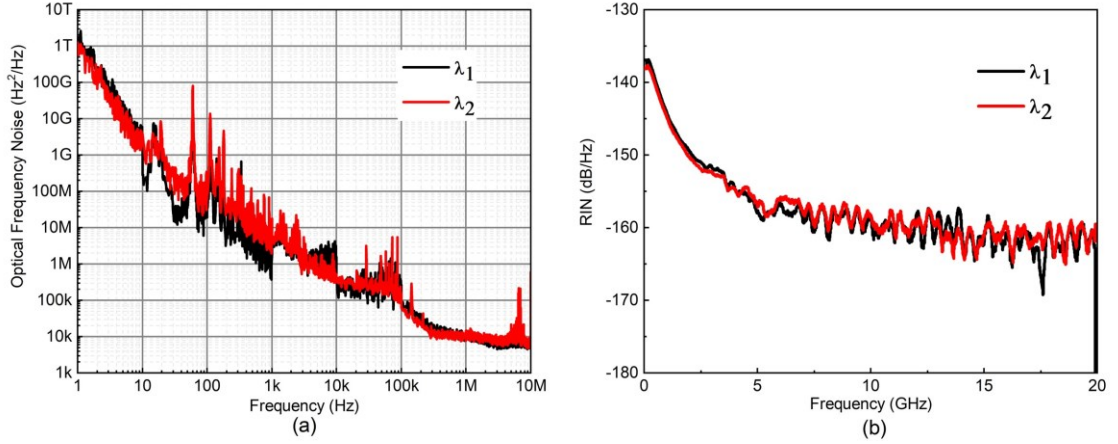
Figure 4.5: Measured (a) optical frequency noise spectra and (b) RIN spectra of the QD-DW-DFBL at a bias current of 360 mA.

addition, the FWM peaks follow the same trend, both in terms of intensity and wavelength, as that of the two optical modes as depicted in Fig. 4.4 (b). Thus, the output optical spectrum of the laser is comprised of two dominant optical modes with equal amplitudes at two different wavelengths around 0.374 nm apart as shown in the inset of Fig. 4.4 (a). Generating both frequencies in the same cavity significantly reduces noise and linewidth of the generated light.

The phase noise and RIN were measured experimentally for the two dominant optical modes. At a bias current of 360 mA, optical linewidths of 25.9 kHz and 29.4 kHz were measured for the two optical modes at λ_1 =1539.522 nm and λ_2=1539.896 nm, respectively. Their corresponding optical frequency noise spectra are shown in Fig. 4.5 (a). Average RIN was measured as -150.8 dB/Hz for the first optical mode (λ_1) and -151.4 dB/Hz for the second mode (λ_2) over the frequency range from 10 MHz to 20 GHz. Fig. 4.5 (b) shows the corresponding RIN of the two optical modes. At higher injection current, optical linewidth as narrow as 15.83 kHz and average RIN as low as -158.3 dB/Hz have been achieved. The corresponding optical frequency noise and RIN spectra for the lowest measured optical linewidth and RIN of the QD-DW-DFBL are shown in Fig. 4.6 (a) and Fig. 4.6 (b), respectively. Thus, the integrated RIN and optical linewidth for each individual channel are measured to be typically less than -150 dB/Hz in the frequency range from 10 MHz to 20 GHz and 30 kHz with the lowest recorded down to -158.3 dB/Hz and 15.83
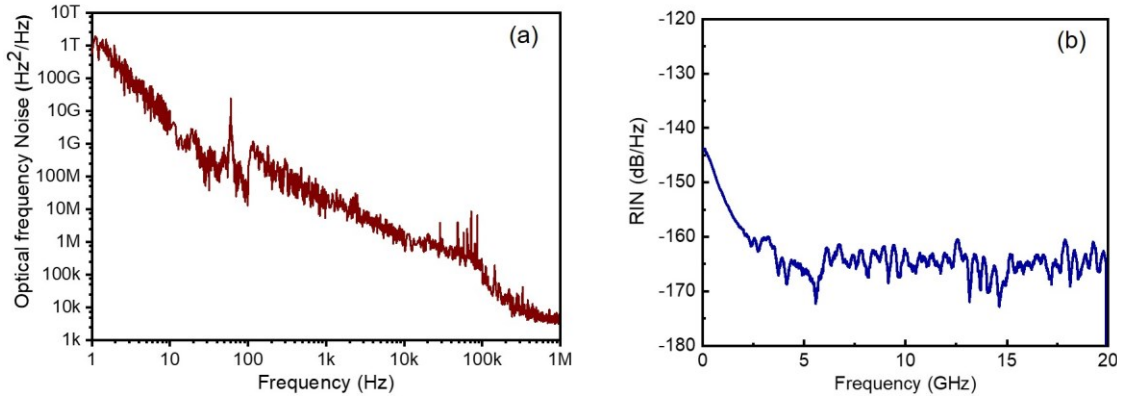
Figure 4.6: Measured spectra of (a) optical frequency noise at a bias current of 465 mA and (b) RIN at a bias current of 500 mA of the QD-DW-DFBL.

kHz, respectively, in free running operation. This subsequently results in generating a low phase noise optical heterodyne MMW carrier beat signal.

The MMW signals were generated between 46 and 48 GHz by heterodyne beating of the optical modes emitted from laser at different bias currents. Figure 4.7 (a) and Fig. 4.7 (b) show typical spectra of the corresponding beat note signals of 46.82639 GHz and 47.16556 GHz, respectively, which were generated at a bias current of 300 mA and 360 mA. For accurate measurement of the MMW spectral linewidths, the curves in Fig. 4.7 were smoothed (the black curves show smoothed results). The measured -3dB and -20dB
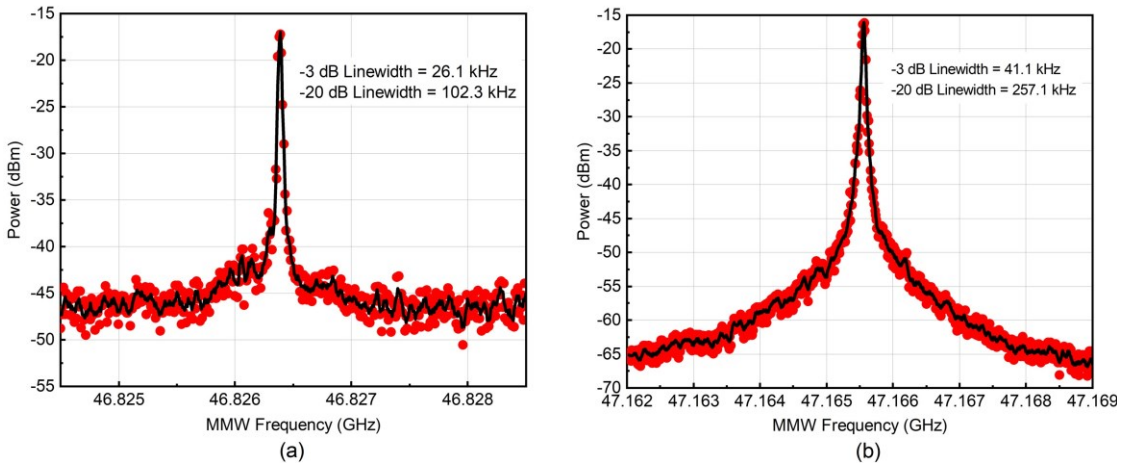
Figure 4.7: Measured spectra (in red) with smoothing version of the results (in black) for -3 dB and -20 dB linewidth measurements of (a) 46.82639 GHz MMW signal at 300 mA (resolution bandwidth (RBW) = 51 kHz, video bandwidth (VBW) = 1 kHz) and (b) 47.16556 GHz MMW signal at 360 mA (RBW = 51 kHz, VBW = 510 Hz).

spectral linewidths of the MMW signal at 46.82639 GHz are 26.1 kHz and 102.3 kHz, respectively. Similarly, for the MMW signal at 47.16556 GHz, the -3dB and -20dB spectral linewidths were measured to be 41.1 kHz and 257.1 kHz, respectively. To our knowledge, these are the best results reported so far for a common cavity based free running QD DW-DFB semiconductor laser operating in the 1550 nm wavelength range. These results are promising for applications as a compact MMW optical beat source in MMW Radar systems and heterodyne MMW communication systems for 5G and beyond mobile networks, particularly for achieving seamless fiber-wireless integrated fronthaul.

4.4.3 Optical Heterodyne MMW Signals Analysis and Comparison

The QD DW-DFBL-based generated MMW signals are compared in terms of spectral linewidth with MMW signals generated using commercial single-wavelength lasers as external optical sources in two different scenarios. In the first case, the MMW signal is generated by the heterodyne beating of the two common cavity optical modes (λ_1 = 1539.522 and λ_2 = 1539.896 nm) emitted from the free running QD-DW-DFBL biased at 360 mA, as shown in Fig. 4.8 (c). Figure 4.8 (a) shows a typical spectrum of the corresponding MMW signal at around 47.16556 GHz. For comparison purposes, an optical mode (λ_{SWL} = 1539.595) from a commercial single-wavelength (SW) external cavity tunable laser source (Agilent 8164B) was mixed with one of the two modes, i.e., λ_2 ($\lambda_{QD-DW-DFBL}$ = 1539.946) of the QD-DW-DFBL at an MMW frequency difference of around 47.2 GHz. The corresponding optical and MMW spectra are shown in Fig. 4.8 (c) and Fig. 4.8 (b), respectively. The measured -3dB and -20dB spectral linewidths of the generated MMW signal of around 47.16556 GHz obtained from the dual-modes of the common cavity are 41.1 kHz and 257.1 kHz, respectively. On the other hand, the measured -3dB and -20dB spectral linewidths of the MMW signal obtained from the beating of SW commercial external cavity laser with one of the two modes of the QD DW-DFBL are 317.4 kHz and 831.7 kHz, respectively. This shows that the spectral linewidth of the MMW signal generated with the QD DW-DFBL source is nearly eight times narrow than the latter case, as expected. This is because the two optical modes in the latter case are no more correlated when one of the modes is from a different cavity of a different laser.
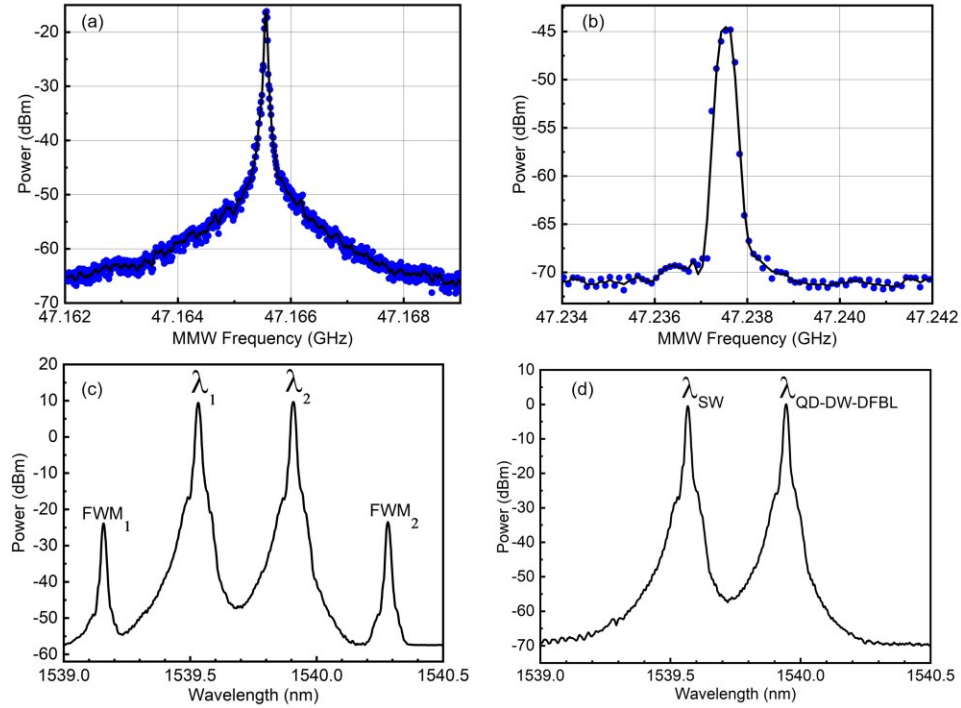
Figure 4.8: (a) The 47.16556 GHz MMW signal obtained from beating together the emitted optical modes of QD-DW-DFBL biased at 360 mA, RBW = 51 kHz, VBW = 510 Hz. (b) The 47.2 GHz MMW signal obtained by beating one of the emitted optical modes from QD-DW-DFBL biased at 360 mA with an external commercial tunable SWL laser, RBW = 51 kHz, VBW = 100 Hz. Optical spectra of (c) QD-DW-DFBL and (d) mode two of QD-DW-DFBL with an external commercial SWL laser's mode.

In the second case, the generated MMW signal using optical heterodyne of ultra-low noise common cavity optical modes from QD-DW-DFBL is compared with the MMW signal generated based on two individual commercial external cavity SWL tunable lasers. The measured estimated linewidth of each common-cavity optical mode of QD-DW-DFBL (λ_1 =1539.770 nm and λ_2 =1540.150 nm) biased at 430 mA was 23.7 kHz. Whereas for the two commercial SWL laser sources (λ_{SWL1} =1539.531 nm and λ_{SWL2}=1539.897 nm), the measured linewidth was 3.2 kHz and 5.4 kHz, respectively. Their corresponding frequency noise measurements are shown in Fig. 4.9 (a). The optical linewidths of the individual commercial laser sources are better than the common cavity optical modes due to the fact that commercial lasers have long external cavities with controlled circuitries, whereas the common-cavity modes are from a free running un-packaged device. However, despite the narrow optical spectral linewidth, the 3dB spectral linewidth of the generated MMW signal is observed to be broadened in the case of individual commercial SWL lasers compared to QD-DW-DFBL, as shown in Fig. 4.9 (c) and Fig. 4.9 (b), respectively. This
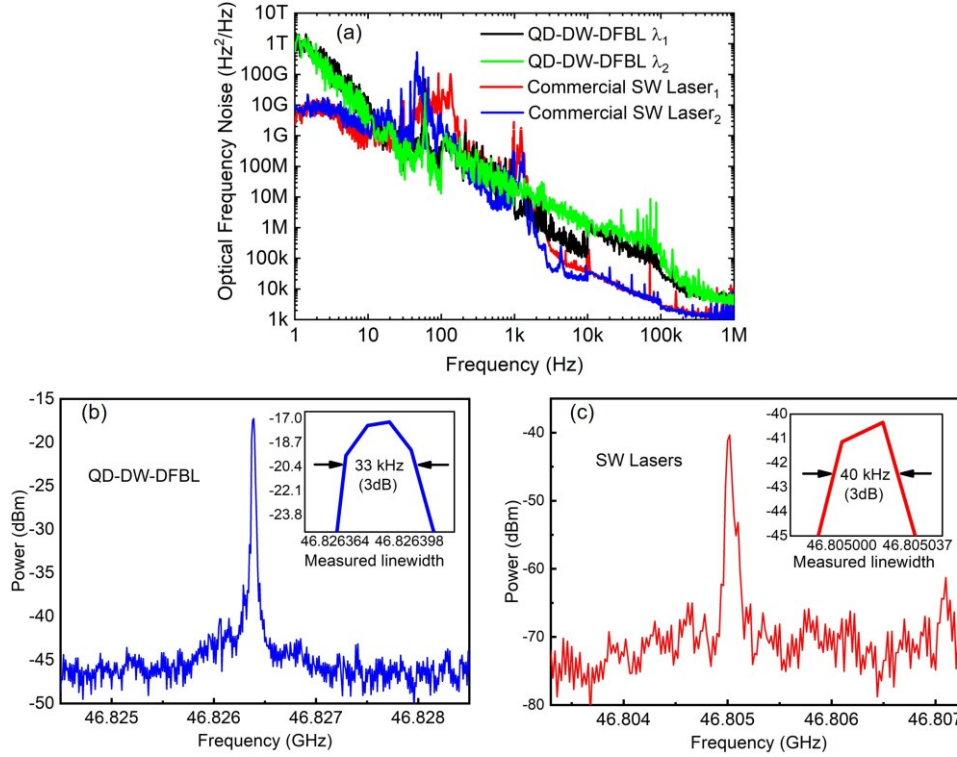
Figure 4.9: (a) Frequency noise spectrum of common-cavity modes and two external cavity tunable SWL commercial lasers (Agilent 8164B). Typical MMW signals spectra with inset showing measured 3dB linewidths of (b) common-cavity modes of QD-DW-DFBL biased at 300 mA (RBW = 51 KHz, VBW = 1 kHz) and (c) two commercial external cavity tunable SWL lasers (RBW = 100 KHz, VBW = 10 kHz).

is because the two optical modes in the former case are not from the same cavity gain medium and are emitted from different lightwave sources, whereas in the latter case, they are from the same cavity and gain medium, hence exhibit frequency correlation and results in narrow beat note linewidth. This agrees with the fact that for perfectly coherent optical modes, the beat note linewidth can be much narrow than the sum of the optical modes' linewidths.

4.5 Design and Experimental Configuration of QD-DW-DFBL Based Broadband Optical Heterodyne MMWoF Wireless System and Links

A schematic of the experimental configuration for the proposed optical heterodyne MMWoF wireless system is depicted in Fig. 4.10. In our demonstration, we emulate a typical 5G C-RAN fronthaul architecture where the experimental setup is comprised of a baseband unit (BBU) connected to an RF electrical LO-free optical heterodyne synthesizer
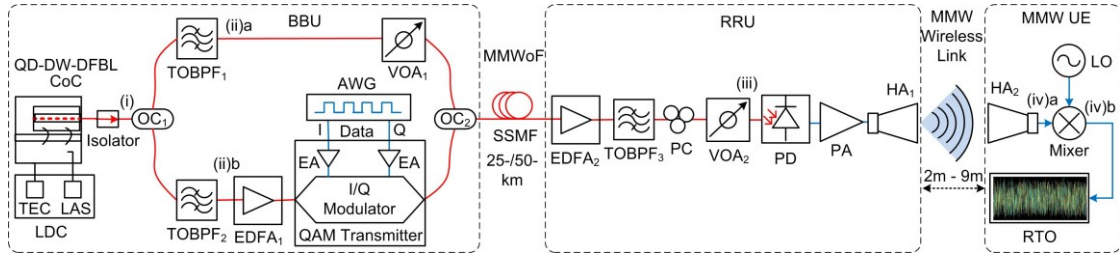
Figure 4.10: Schematic of the system experimental setup for the optical heterodyne MMWoF wireless links based on the QD-DW-DFBL. BBU: baseband unit; RRU: remote antenna unit: MMW UE: millimeter-wave user equipment; CoC: chip-on carrier; OC: optical coupler; TEC: thermoelectric cooler; LAS: laser; LDC: laser diode controller; TOBPF: tunable optical band pass filter; EDFA: erbium doped fiber amplifier; AWG: arbitrary waveform generator; EA: electrical amplifier; VOA: variable optical attenuator; PC: polarization controller; PA: power amplifier; HA: horn antenna; LO: local oscillator; RTO: real-time oscilloscope.

based remote radio unit (RRU) through a 25-km or 50-km SSMF link followed by 2-m to 9-m MMW free space indoor MMW wireless link connecting to the MMW user equipment (EU). Figure 4.11 shows a detailed component pictorial view of the experimental setup including the MMWoF wireless transmission link. In the BBU, the InAs/InP common cavity QD-DW-DFBL is employed as the main optical source. Its output optical spectrum is shown in Fig. 4.12 (i). In our experiments the QD-DW-DFBL CoC is placed on a copper block with a TEC underneath for temperature control. The temperature of the CoC and the laser bias current are controlled through a LDC (ILX Lightwave, Model LDC-3722) where the laser is biased through a pair of DC electrical probes, as shown in Fig. 4.10 and the
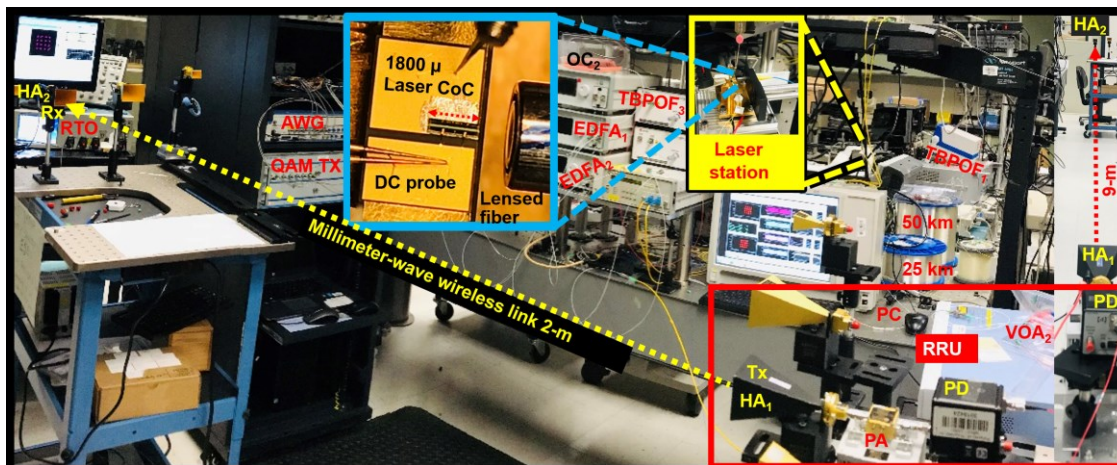
Figure 4.11: Photos of the Laboratory experimental setup of QD-DW-DFBL based optical heterodyne MMWoF system with insets showing the QD-DW-DFBL CoC on a laser testing station, MMW wireless transmission links (2-m to 9-m), SSMFs (25 & 50-km), wireless transmitter (Tx) and receiver (Rx) and all the other key components of BBU, RRU and MMW UE.

inset of Fig. 4.11. Throughout our experiments, the temperature and injection current of the CoC are maintained at 18°C and 360 mA, respectively.

In the BBU, the laser output power is coupled from its front facet through a lensed single mode polarization maintaining fiber (SMPMF) followed by a two stage PM isolator to avoid back reflection into the laser cavity. The light is then split into two paths by employing a 10/90 PM optical coupler (OC_1) followed by two tunable optical band pass filters (TOBPFs). The two optical filters, $TOBPF_1$ and $TOBPF_2$, separate the two optical modes having a frequency spacing of around 47.27 GHz into channel 1 (1539.821 nm) and channel 2 (1540.195 nm) as shown in Fig. 4.12 (ii). Channel 2 is used as the optical modulated channel for long-reach data transmission whereas channel 1 is used as an un-modulated optical LO for remote optical heterodyning to optically synthesize the MMW carrier for free space wireless data transmission.
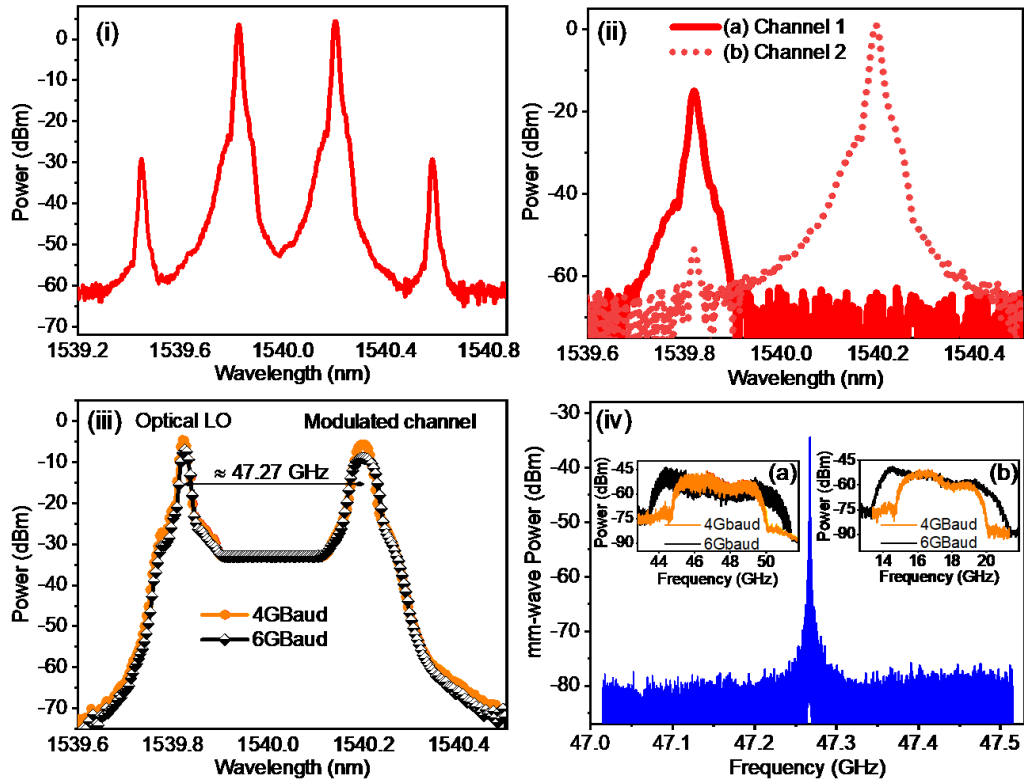
Figure 4.12: Measured (i) optical spectrum of the QD-DW-DFBL at the BBU after isolator (ii) optical spectrum of (a) channel 1 (optical LO) and (b) channel 2 (data channel) after TOBPF1 and TOBPF2, respectively, (iii) unmodulated (optical LO) and optical modulated data channel at the PD, and (iv) typical spectrum of the MMW carrier at the UE before down-conversion with insets showing the received 4-GBaud and 6-GBaud modulated 16-QAM data signals occupying 5.4 GHz and 8.1 GHz transmission bandwidth, respectively (a) before mixer and (b) after mixer by down-converting to IF.

As a proof of concept, a QAM optical transmitter having thermally stable in-phase/quadrature (I/Q) Lithium Niobate (LiNbO$_3$) Mach-Zehnder modulator (MZM) and linear data driver electrical amplifiers (EAs) is used in our experiments to realize the data modulated optical channel. Consequently, channel 2 is modulated with baseband 16-, 32-, and 64-QAM data signals having symbol rate of 4-GHz and 6-GHz that are generated electronically by a 65-GSa/s arbitrary waveform generator (AWG) (Keysight M8195A) with a pseudo-random binary sequence (PRBS) pattern of 2^{11}-1 bits where the bit sequence is mapped onto the I and Q components of the signals. The corresponding data signals are then passed through a root raised cosine (RRC) filter with a roll-off factor of 0.35 for Nyquist pulse shaping. After pulse shaping, the signals are resampled and channel corrections are applied for amplitude flatness before feeding them to the optical transmitter. The data signals are then amplified by two linear data EAs in the optical transmitter before they are fed to I/Q MZM for modulation. Before modulation, the data channel is boosted with an erbium-doped fiber amplifier (EDFA$_1$) to compensate for the insertion loss of the filter and optical modulation transmitter. A PM variable optical attenuator (VOA$_1$) is also employed in the un-modulated path to equalize its power level to that of modulated channel since the two paths have different losses.

The effective path length difference between the two arms of the transmitter can affect the degree of phase correlation between the two wavelength signals, potentially leading to relatively high phase noise in the generated mm-wave carrier [16], [18]. This decorrelation between the two channels can be avoided by incorporating an optical delay line in the unmodulated path to equalize the effective path lengths. In this way the QAM modulated 47.27 MMW carrier signal is realized in the optical domain with a maximum data rate of 36 Gb/s. Finally, the modulated and unmodulated optical channels are combined in a 50/50 OC$_2$ and transmitted over the optical fiber link to the RRU. The optical fiber link is comprised of 25-km or 50-km SSMF spool as highlighted in Fig. 4.11.

The received optical signal at the RRU is amplified through EDFA$_2$ followed by OBPF$_3$ to remove the amplified spontaneous emission (ASE) noise as shown in Fig. 3 and Fig. 4. The optical spectrum of the corresponding received modulated and un-modulated carriers before the PD is shown in Fig. 4.12 (iii). The photo-mixing output of these two optical

frequency signals on a high speed PD (Newport Model-1014), is directly attached to a 22-24 dBi Horn antenna (HA$_1$) (WR-22) through an RF Q-band power amplifier (PA) with a nominal gain of 45 dB. Thus, a MMW carrier of around 47.27 GHz is optically synthesized remotely without using any electrical LO and the optical data is translated to the corresponding MMW carrier. The data signal on the 47.27 GHz MMW carrier is subsequently transmitted over the 2-m to 9-m wireless link. A polarization controller (PC) is incorporated in the RRU to adjust the polarization direction of the incoming optical signal before photo-mixing to ensure maximum output power at the output of PD. A PM VOA$_2$ is also employed at the RRU before the PD to control the received incident power on the PD for different wireless link measurements. Note that similar to the transmitter system at the BBU, we use off-the-shelf components at the RRU to demonstrate our proof-of-concept broadband multi-Gb/s MMWoF system. Nevertheless, all of these components, where the EDFAs can be replaced by semiconductor optical amplifiers (SOAs), could be heterogeneously integrated to microwave photonic circuits making the BBU and the RRU more simple compared with the conventional RoF fronthaul systems.

The MMW data signal is received by another identical Horn antenna at the user equipment (UE) over the free space wireless link. This MMW signal is then down-converted to an intermediate frequency (IF) of around 17.3 GHz with an electrical LO before capturing into a real-time oscilloscope (RTO) for processing, as shown in Fig. 4.10. Figure 4.12 (iv) shows the corresponding received MMW carrier at around 47.27 GHz along with the 4-GBaud and 6-GBaud modulated 16 QAM data signals in the insets (a) before and (b) after down-conversion, occupying transmission bandwidth of 5.4 GHz and 8.1 GHz, respectively. After down-converting the received MMW signal to an IF, as shown in the inset (b) of Fig. 4.12 (iv), it is coherently detected and processed in real-time by employing vector signal analysis software (SignalVu) on a 100 GSa/s Tektronix DPO73304SX oscilloscope having 33-GHz analog bandwidth. The signal undergoes several digital signal processing (DSP) steps including resampling, clock recovery, digital down-conversion, match filtering, synchronization, and adaptive equalization before it is demodulated to measure the error vector magnitude (EVM) and calculate the bit error rate (BER). For match filtering, an RRC matched filter with roll-off factor of 0.35 is employed to recover the baseband IQ data and to minimize inter-symbol interference (ISI). Similarly,

a decision-directed, feed-forward (FIR) adaptive equalizer is used to compensate for linear distortions. Finally, the system integrity and communication performance is evaluated in terms of measured EVM and calculated BER [238].

4.5.1 Experimental Results and Discussion

The performance of the whole MMWoF wireless system is thoroughly analyzed in terms of EVM, BER, constellations, and eye diagrams. Multilevel QAM signals including 16-QAM, 32-QAM and 64-QAM are used to realize MMW wireless links with link capacities ranging from 16-Gb/s to 36-Gb/s. The system performance is then evaluated for different line rates over a fixed MMW wireless link through different fiber lengths by varying the received optical power (ROP), and for different wireless link lengths by changing the wireless transmission distance at a fixed ROP through a 25 km SSMF.

Figure 4.13 (a) and Fig. 4.13 (b) summarize the EVM performance results of 4-GBaud and 6-GBaud 16-QAM signals with data rates of 16 Gb/s and 24 Gb/s, respectively, over a
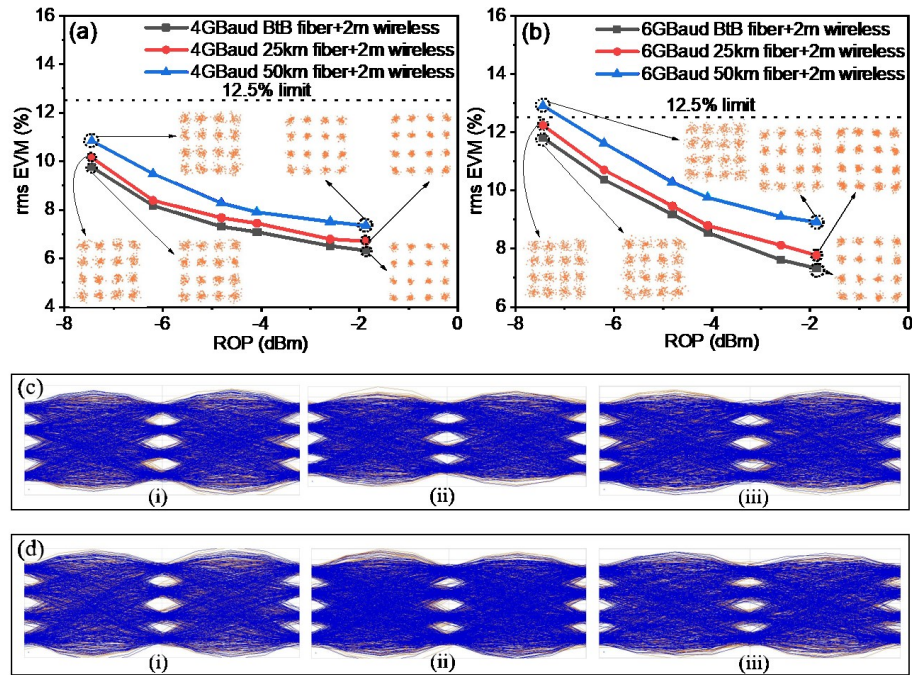
Figure 4.13: rms EVM measured at the UE versus ROP at the PD for 16-QAM modulated data signals with (a) 4-GBaud symbol rate occupying 5.4 GHz bandwidth and (b) 6-GBaud symbol rate occupying 8.1 GHz bandwidth. Eye diagrams recorded at the UE over 2-m wireless link at the ROP of ~ -1.9 dBm for 16-QAM (c) 4-GBaud and (d) 6-GBaud through (i) BtB, (ii) 25-km, and (iii) 50-km SSMF link, respectively.

2-m MMW wireless link through BtB, 25-km and 50 km SSMF. The different fiber lengths and signal bandwidths are employed to analyze and compare the fiber and signal bandwidth induced impact on the performance with BtB as a reference. In each case, the root mean square (rms) EVM of the 4-GBaud and 6-GBaud 16-QAM wirelessly received MMW signals is measured in real-time at the MMW UE shown in Fig. 4.10 for different ROPs at the PD. Note that in order to analyze the effect of the optical fiber transmission on the wireless link, the ROP for all of the three fiber lengths is kept identical at the PD by using VAO2 as shown in Fig. 4.10.

The results show that for all 16-QAM signals, the EVM is below the 3GPP standard requirement of 12.5%, except for the case of 6-GBaud transmission through a SSMF length of 50 km, where it is slightly over the limit at the ROP of around -7.5 dBm. The inset of Fig. 4.13 (a) and Fig. 4.13 (b) also include clear constellation diagrams showing the successful detection of the corresponding 4-GBaud and 6-GBaud 16-QAM MMW signals at the ROP of -1.9 dBm and -7.5 dBm, respectively. This is also evident from the open eye diagrams of the corresponding wirelessly received 4-GBaud and 6-GBaud 16-QAM signals as depicted in Fig. 4.13 (c) and Fig. 4.13 (d), respectively, at the ROP of -1.9 dBm for the (i) BtB, (ii) 25 km, and (iii) 50 km scenarios. Moreover, Fig. 4.14 depicts the rms EVM as function of the baud rate for the successful detection of 16-QAM modulated optical heterodyne MMW signals, centered at around 47.27 GHz, over 2-m wireless link through BtB, 25-km and 50-km SSMF at the ROP of -1.9 dBm.
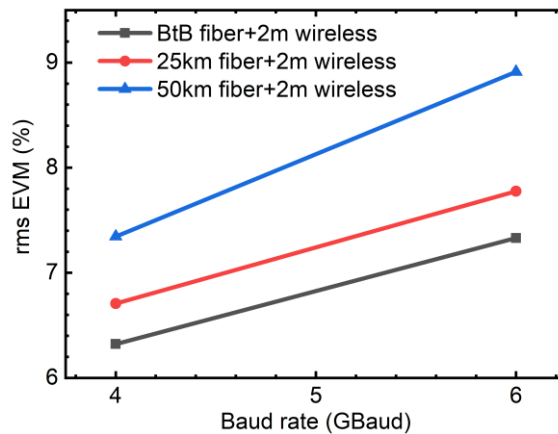
Figure 4.14: rms EVM as a function of the baud rate for 16-QAM MMWoF wireless links at the ROP of ~ -1.9 dBm.
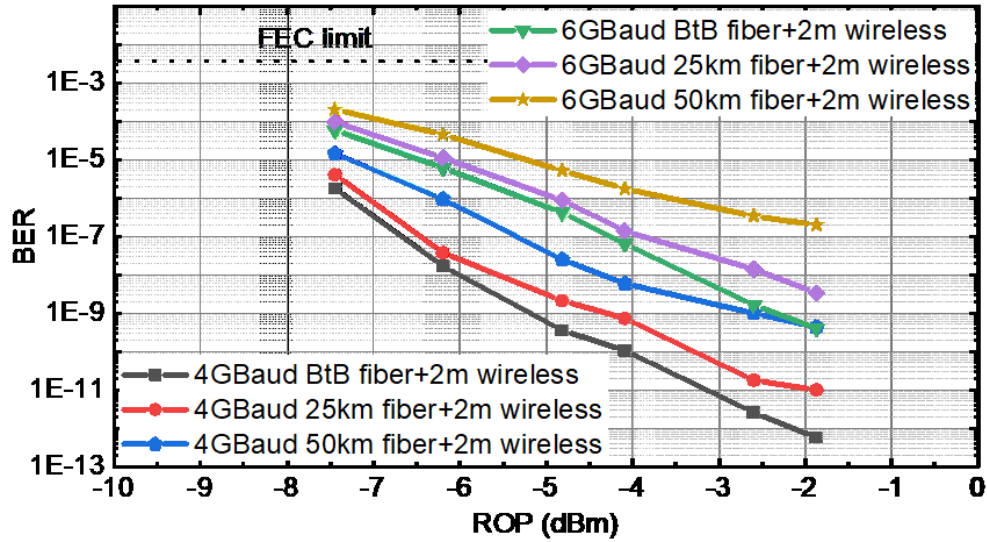
Figure 4.15: Calculated BER as a function of ROP for 4-GBaud and 6-GBaud 16-QAM data signals measured over 2-m MMW wireless link through BtB, 25-km and 50-km SSMF.

Figure 4.15 plots the calculated BER versus the ROP for both 4-GBaud and 6-GBaud 16-QAM MMW signals through BtB, 25 km and 50 km SSMF. The BER is calculated based on the measured rms EVM using the relationship between EVM and BER derived in [238]. It is noted that the BER increases with the increase in baud rate from 4-GBaud to 6-GBaud at the same ROP. A BER $< 10^{-9}$ is observed for 4-GBaud transmissions at the ROP of > -2.5 dBm for all of the three scenarios. However, for 6-GBaud transmissions, the same is only observed in the case of BtB scenario, as shown in Fig. 4.15. Overall, the BER performance for both 4-GBaud and 6-GBaud transmissions under all scenarios is below the standard FEC limit of 3.8×10^{-3}.

Generally, an increase in performance degradation is observed with an increase in bandwidth of the transmitted signals from 5.4 GHz to 8.1 GHz having baud rate of 4-GBaud and 6-GBaud, respectively, as can be seen from Fig. 4.14. This is attributed to the fact that the MMWoF system is more prone to noise and propagation loss at wideband signal operation. However, it is observed that on average, the fiber length of 25 km induces slight performance degradation with EVM penalty of around 0.4 dB for both 4-GBaud and 6-GBaud optical heterodyne MMW wireless transmissions with respect to their BtB scenarios. This degradation further increases to around 1.1 dB and 1.2 dB for 4-GBaud and 6-GBaud transmissions, respectively, in the case of 50-km fiber. Similarly, an average

penalty of around 0.7 dB and 0.8 dB is observed between 25-km and 50-km transmissions of 4-GBaud and 6-GBaud mm-wave signals, respectively. Nevertheless, an average degradation of about 1.7 dB is observed between the transmissions of 4-GBaud and 6-GBaud 16-QAM MMW signals through BtB, 25-km and 50-km SSMF, which corresponds to an average optical power penalty of around 2.8 dB. This is ascribed to the very nature of the wide bandwidth operation encountering relatively more noise, fiber dispersion and channel propagation loss at the MMW frequency. A typical spectrum of the received modulated MMW data signals at the UE with 5.4 GHz and 8.1 GHz transmission bandwidths both before and after down-conversion can be seen in the inset (a) and (b) of Fig. 4.12 (iv), respectively, for the ROP of around -1.9 dBm at the PD. The uneven envelop of the received modulated signals towards the high frequency end is due to the operating frequency range of the PD, PA and antennas.

Thus, the EVM and BER performance degradation with fiber length in the aforementioned cases is believed to be due to the accumulated dispersion encountered over the optical fiber link along with the effective path length difference between the two optical carriers at the transmitter [16] and the corresponding wireless propagation path loss. To further improve the results, an optical delay line can be incorporated in the un-modulated path at the transmitter side and dispersion compensation can be employed to further reduce the effect of optical carrier decorrelation at the PD [18]. Besides, it is observed that polarization misalignment impacts the results, which can be avoided by employing proper polarization control. In addition, based on the antennas configuration in our experiments, accurate direct line-of-sight (LOS) path is required from the transmitter antenna to the receiver antenna to establish a link with better performance.

The effect of the MMW wireless link length on the performance of the system is also investigated. Fig. 4.16 shows the BER performance at different wireless link distances through a 25-km SSMF at a fixed ROP of around -1.9 dBm for both 4-GBaud and 6-GBaud 16-QAM signals. Their corresponding constellation diagrams for a wireless link distance of 6-m are also shown in Fig. 4.16. The measured EVM values for these constellation diagrams of 4-Gbaud and 6-Gbaud received signals were 10.33% and 11.26% respectively. The results show that BER performance of under the FEC limit of 3.8×10^{-3} is achieved
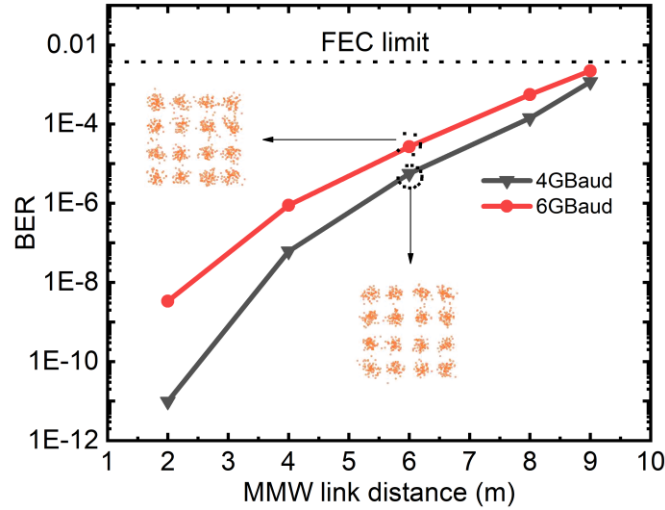
Figure 4.16: BER versus MMW wireless link distance at ROP of ~ -1.9 dBm for 4-GBaud and 6-GBaud 16-QAM received signals through 25-km SSMF.

for both 4- and 6-GBaud MMW signals wireless transmissions with a maximum MMW link distance of 9-m at the ROP of -1.9 dBm. It is apparent that the 4-GBaud 16-QAM signal achieves better BER performance as compared to 6-GBaud 16-QAM. However, in both cases, the performance deteriorates as the wireless distance increases. In general, it is observed that increase in the RF link distance or decrease in the ROP degrades the system performance. This is attributed to the wireless propagation path loss along with imprecise antenna alignment and increase in noise level at the received low MMW signal power that results in low electrical signal to noise ratio (ESNR) contributing to the performance degradation. Moreover, since we use directional antennas in our experiments their alignment becomes critical as the wireless distance increases and the lack of proper LOS impacts the link performance.

Finally, Fig. 4.17 (a) – (b) and Fig. 4.17 (c) – (d) show the constellation diagrams for 4- and 6-GBaud 32-QAM and 64-QAM MMWoF wireless links, respectively, with 25-km SSMF and 2-m wireless distance at the ROP of around -1.9 dBm at the PD. The rms EVM values for 4-/6-Gbaud 32-QAM and 64-QAM links with a transmission bandwidth of 5.4-/8.1-GHz were measured to be 5.56%/6.56% and 6.05%/6.62%, respectively. Figure 4.17 (a) and Fig. 4.17 (b) show the comparison between 4-GBaud and 6-GBaud 32-QAM MMW signals transmissions with the calculated BERs of 7.26×10^{-9} and 7.06×10^{-7}, respectively.
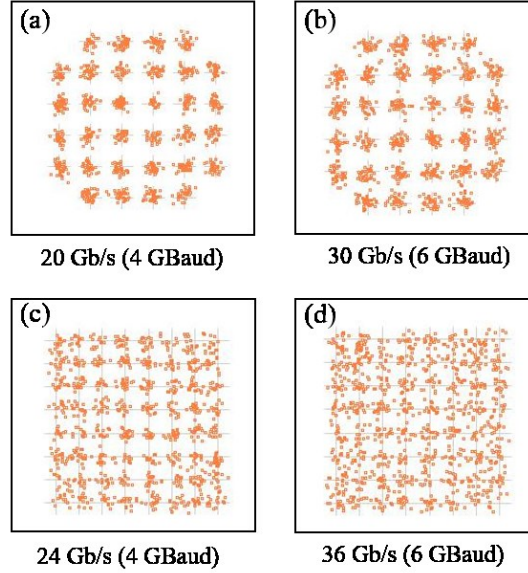
Figure 4.17: Wirelessly received signal constellations of (a) 4-GBaud 32-QAM (20 Gb/s), (b) 6-GBaud 32-QAM (30 Gb/s), (c) 4-GBaud 64-QAM (24 Gb/s), and (d) 6-GBaud 64-QAM (36 Gb/s).

Similarly, Fig. 4.17 (c) and Fig. 4.17 (d) show the comparison between the MMWoF wireless transmission of 4-GBaud and 6-GBaud 64-QAM MMW signals with the calculated BER of 8.94×10^{-5} and 2.84×10^{-4}, respectively. This constitutes a link data throughput of 20 Gb/s and 30 Gb/s in the case of 4- and 6-GBaud 32-QAM signals, and 24 Gb/s and 36 Gb/s in the case 64-QAM signals, respectively.

Furthermore, Table 4.1 compares our work in this chapter with state-of-the-art-work on the QD-MWL-based RoF system, as discussed in Section 2.6, Chapter 2 of this thesis. The results show that the QD-DW-DFBL-based optical heterodyne MMWoF wireless links achieve EVM and BER performance of under the FEC limit in all cases for both 4- and 6-GBaud wideband 47.27 GHz MMW wireless signals transmissions with a minimum BER of 5.7×10^{-13} and 4×10^{-10}, respectively, and a maximum bit rate of 36 Gb/s. These results demonstrate the capabilities of DQ-DW-DFBLs with the MMW frequency range within the 5G NR standard band (n262) of FR2 as a promising optical MMW source for 5G optical heterodyne synthesizer based MMWoF wireless systems.

Table 4.1: Comparison with state-of-the-art QD-MWL-based MMWoF systems.

Ref.	Optical Source	λ Band	MMW Frequency (GHz)	Data Rate (Gb/s)	Mod. Format	MMW RoF Link SMF (km)	WL (m)
[155], [214], [219]	PML-QD-MWL	C	~60	3.03	QPSK (OFDM)	0.05	-
[155], [156], [219]	PML-QD-MWL	C	~60	1.25 to 5	OOK	~ 0.054	25
[35]	PML-QD-MWL	C	25	0.08	16-QAM	20	2
[16]/[220]	SIL-PML-QD-MWL	C	60	1.12/~1.17	64-QAM (OFDM)	25	-
[221]/[37]	SIL-QD-MWL	C	100	10	OOK	50	10/15
[33]	SIL-QD-MWL	C	40/80	10	16-QAM (OFDM)	50/25	20
[38]	HIL-QD-MWL	C & L	60	10	32-QAM (OFDM)	50	-
[31]/[34]	EIL/SIL-QD-MWL	L	28	2	QPSK	20	4/6
[34], [216]/[217]	SIL/SIL&EIL-QD-MWL	L	30	2	QPSK	20	2
[32]	SIL-QD-MWL	L	28/25	8	QPSK/16-QAM	10	4/2
[36]	QD-DW-DFBL	C	146	1	OOK	-	0.025
This work	**QD-DW-DFBL**	**C**	**47.2 GHz**	**36**	**16/32/64-QAM**	**25/50**	**2 - 9**

Mod. Format: modulation format; PML: passively mode-locked; SIL: self-injection-locked; EIL: external-injection-locked; HIL: hybrid-injection-locked; WL: wireless link

4.6   Summary

In this chapter, we present a novel monolithic semiconductor buried heterostructure InAs/InP QD-DW-DFBL as a compact optical MMW source. The device uses a common gain medium in a single cavity structure for simultaneous correlated and stable dual-mode lasing in the 1550-nm wavelength range using. Simultaneous two highly correlated longitudinal modes lase from within the same cavity of the device due to the distributed feedback provided by a novel synthesized aperiodic non-uniform diffraction grating placed below the QDs active layer. The integrated RIN and optical linewidth for each individual mode are measured to be typically less than -150 dB/Hz in the frequency range from 10 MHz to 20 GHz and 30 kHz with the lowest recorded down to -158.3 dB/Hz and 15.83 kHz, respectively, in free running operation. This subsequently results in generating a low

phase noise optical heterodyne MMW carrier beat signal with a 3dB linewidth of typically ≤ 40 kHz. By changing drive current and temperature, the mode spacing of the device can be tuned by around 0.0158 nm, which corresponds to tuning MMW frequency range from 46 GHz to 48 GHz. Nevertheless, the RF beat note of the device can be adjusted from the GHz to the THz range by modifying the design of the synthesized aperiodic grating of the device for the desired spectrum.

Moreover, we successfully demonstrate various real-time broadband optical heterodyne synthesizer based MMWoF wireless links featuring multi-Gb/s data rates with a maximum data capacity of 36 Gb/s (64-QAM × 6-GBaud) having EVM and BER below the standard 7% overhead FEC limit of 3.8 x 10^{-3} using the QD-DW-DFBL in free running condition. We demonstrate real-time broadband multi-Gb/s electrical RF synthesizer-free millimeter-wave (MMW) signals generation and wireless transmission at the 5G new radio (NR) frequency band of around 47 GHz based on analog radio-over-fiber (A-RoF) fronthaul. One laser mode is encoded using 4-/6-GBaud multilevel quadrature amplitude modulation (M-QAM) (16-/32-/64-QAM) baseband data signals, the other lasing mode is used as an optical local oscillator for optical-heterodyne remote up-conversion to a MMW carrier of 47.27 GHz. Consequently, optical baseband modulated data signals with data capacity up to 36 Gb/s (6-GBaud × 64-QAM) are transmitted through back-to-back (BtB) and 25-/50-km of standard single mode fiber (SSMF) before the MMW carrier is optically synthesized remotely for free space wireless data transmission and detection over up to 9-m. The end-to-end MMW-over-fiber (MMWoF) wireless link is thoroughly characterized exhibiting promising error-vector-magnitude (EVM) and bit-error-rate (BER) values. The 4-/6-GBaud 16-QAM MMWoF wireless links achieve EVMs down to 6.32%/7.33%, 6.71%/7.78%, and 7.35%/8.91% through BtB, 25-km, and 50-km SSMF, respectively. Similarly, the EVM for 32-QAM and 64-QAM links is observed to be 5.56%/6.56% and 6.05%/6.62%, respectively. Moreover, in each case, the calculated BER is below the forward error correction (FEC) limit of 3.8 × 10^{-3}. The results indicate that the optical heterodyning of two highly correlated and low noise optical signals is an efficient method for transporting and distributing high frequency MMW data signals in the optical domain over long distances. After long-reach transmission of these basebands data modulated optical signals, the corresponding desired MMW modulated carrier signal can be optically-

synthesized remotely through photonic up-conversion in the MMW RoF systems for free space wireless data transmission. This greatly simplifies the overall system by preserving any modulated data format on the optical signals and translating it to the corresponding MMW carrier signal. This eliminates front end expensive components, such as electrical LOs and ADCs/DACs at the RRU. This highlights the potential of low noise, correlated and monolithically integrated InAs/InP QD-DW-DFBLs for deployment as an alternative to individual DFB lasers in 5G and beyond optical heterodyne MMWoF wireless communication systems.

Chapter 5

MIMO and Bidirectional Multi-Gb/s Photonic MMWoF Wireless Communication Systems Based on QD-MWLs

5.1   Introduction

T HE rapid increase in high-bandwidth multi-media services and novel applications, and the tremendous increase in the growth of internet traffic and mobile technology demand for high-speed broadband wireless communication systems with higher capacity and coverage. 5G new radio promises to achieve extremely large capacity, very low latency and better coverage with wideband operation for wireless applications. For this, due to the limited and overcrowded spectra of the current wireless systems, 5G is aimed to utilize higher radio frequency (RF) bands including higher microwave and millimeter-wave (MMW) bands with sufficient available spectra to deliver multi-Gb/s data speeds. This is complemented by MIMO technology, which can significantly increase data capacity through spatial multiplexing and improve coverage and system reliability through spatial diversity. However, MMW frequency signals are prone to extreme propagation path loss and challenging to generate with the conventional bandwidth-limiting electronics. Towards this, microwave photonics with radio-over-fiber (RoF) technology is considered instrumental for optically synthesizing MMW carrier signals remotely extending the reach and coverage of high speed broadband MMW wireless communication systems [9]. This is because of the photonics and RoF technology's capability to generate and distribute MMW signals through optical fibers, which is advantageous in terms of low loss, wide bandwidth, and immunity to electromagnetic interference [127]. In addition, it can seamlessly be integrated with the existing optical fiber infrastructure serving the first/last mile access networks, such as PON and WDM. Nevertheless, one limiting factor of the photonic MMW is the phase noise [18] resulting from uncorrelated optical signals of individual free-running optical sources, degrading system performance. Thus, highly correlated and low noise optical sources are required.

Moreover, photonic MMW signal generation techniques can be seamlessly integrated with multiple-input-multiple-output (MIMO) technology to increase the wireless transmission capacity [19], [246]. Thus, multiple antennas can simultaneously transmit various MMW wireless signals reducing the requirements for high bandwidth elect optic devices and increasing transmission capacity. The photonic MMW with MIMO in an RoF can be realized by employing optical polarization multiplexing, which can effectively double the transmission capacity [19]. Thus, various MMW MIMO RoF wireless transmission systems and techniques are presented in the literature for increasing the capacity of the next generation wireless communication networks, for instance [19], [176], [200]. Furthermore, bidirectional full-duplex communication links can be realized in the RoF networks, and extensive work has been done in this direction [24], [32], [37], [38], [128], [198], [214]. In duplex communications, a single optical source can be shared between the downlink and uplink by employing wavelength-reused schemes reducing the cost and complexity of the system.

In recent years, semiconductor QD-MWLs have shown to be promising optical sources for photonic MMW signals generation and applications in MMWoF systems [1[16], [31]–[38], [156], [214], [216], [217], [219]–[221]. QD-MWL technology offers cost-effective solution for MIMO and bidirectional system. A single QD-MWL offers low-noise optical channels that can be effectively utilized in the MIMO and bidirectional systems. However, until recently, not much research has been devoted to photonic MMW MIMO and bidirectional systems based on QD-MWL technology, which can be a promising optical source for the next generation of MMW RoF wireless communications networks.

In this chapter, we present Multi-Gb/s photonic MMWoF MIMO and duplex bidirectional wireless transmission systems based on QD-MWLs. This includes experimental demonstrations of photonic-assisted broadband MMWoF 2×2 MIMO and bidirectional wireless transmission systems at the 5G NR FR2-1 in the V-band and Ka-band based on a single low noise InAs/InP quantum dash dual-wavelength DFB laser (QD-DW-DFBL) and a single InAs/InP passively mode-locked (PML) QD-MWL-based coherent frequency comb (CFC). The demonstrations include successful real-time error-

free transmission and detection of wideband 16 QAM modulated vector MMW signals with a maximum bit rate of 16 Gb/s. This chapter includes results published in [247], [248].

The rest of this chapter is organized as follows. Section 5.2 presents the design, experimental demonstration, results and discussion of our proposed multi-Gb/s photonic MMWoF MIMO wireless transmission system based on QD-MWLs. It is followed by the duplex bidirectional photonic MMWoF wireless systems' designs, experimental configurations and experimental results in Section 5.3 and Section 5.4. Finally, Section 5.5 presents the summary of this Chapter.

5.2   Photonic MMWoF 2×2 MIMO Wireless Transmission System

Figure 5.1 shows a conceptual architecture of the proposed polarization multiplexing-based photonic MMWoF 2×2 MIMO wireless transmission system based on QD-MWL. In the proposed system architecture, a typical 5G C-RAN fronthaul is emulated where a single QD-MWL is shared between the CO and RRU. In the optical network, the MMW MIMO streams are realized using optical polarization multiplexing of a single QD-MWL together with the remote photonic MMW signals generation. On the other hand, in the wireless link, dual-polarized antenna elements of a phased array antenna (PAA) are employed for cross-polarization beams. This configuration alleviates the cross-talk between any two streams at a single carrier frequency reducing the transmitter and receiver digital-signal-processing
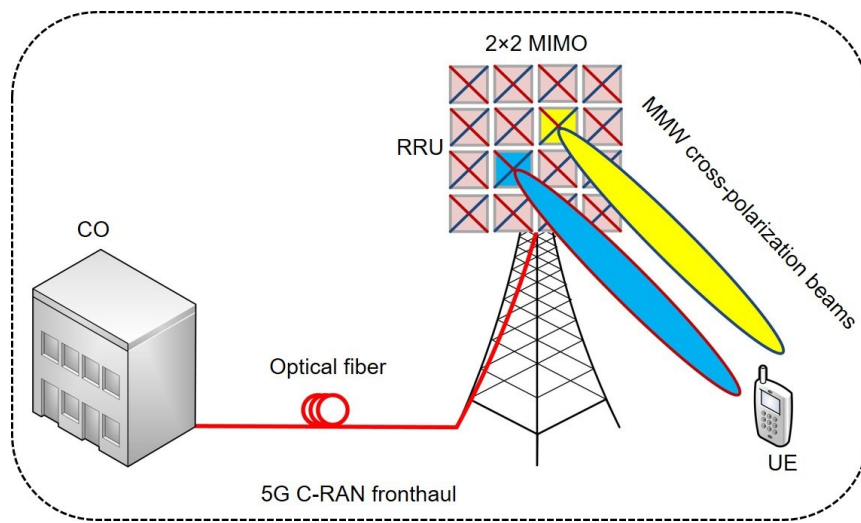
Figure 5.1: Photonic MMWoF 2×2 MIMO wireless communication system architecture.

(DSP) complexity. In addition, MIMO, combined with polarization multiplexing, doubles the wireless transmission capacity. In the proposed system, the based RF MIMO streams modulate the QD-MWL optical channel and are transported over the optical fiber link in the analog baseband form. The MIMO wireless streams can also be at the intermediate frequency (IF). The corresponding MIMO streams are then up-converted to the desired MMW carrier frequency optically at the remote radio unit (RRU). This significantly reduces the bandwidth requirements and complexity of optoelectronic devices. Additionally, the effect of chromatic dispersion is also reduced. The scheme can be scaled to M×M MIMO by employing multiple optical channels and multiple layers of the PAA along with MIMO DSP. In addition, analog optical beamforming can be easily incorporated into the proposed architecture using optical beamforming network based on true time delay elements. This will enable beam steering to steer the beam in the desired user direction. Thus, MMW wireless beam(s) can be directed to the desired user, and a null can be created in the path of the interference user. In this manner, single-user MIMO (Su-MIMO) or multi-user MIMO Mu-MIMO can be effectively achieved to efficiently share the time and frequency resources and increase user and network throughput. Thus, combining A-RoF with flexible MIMO and optical beamforming technologies in conjunction with the photonic generation and distribution of MMW MIMO streams in the optical domain helps in efficient resource utilization with more centralization and less complexity at the RRU. This centralized architecture helps in the implementation of software define network control (SDN) and network function virtualization (NFV) for efficient management of the resources with a central virtualized BBUs pool.

5.2.1 Design and Experimental Configuration of the Proposed Photonic MMWoF 2×2 MIMO Wireless Transmission System Based on QD DW-DFBL

The schematic of the proposed system is shown in Fig. 5.2 (a). In our experiment, a photonic MMWoF 2×2 MIMO architecture shown in Fig. 5.1 is realized with an optical LO and optical polarization multiplexed data channel to generate, transmit, and detect single carrier-based broadband wireless streams at 5G NR in the V-band over 2 m wireless channel through back-to-back (BtB), 10 km, and 25 km SMF using a common cavity InAs/InP QD-DW-DFBL. The MMWoF MIMO system configuration is mainly comprised

of three modules, namely the optical transmitter module, photonic MMW 2×2 MIMO RRU module, and MMW 2×2 MIMO receiver module, as shown in Fig. 5.2 (b)(i), 5.2 (b)(ii),
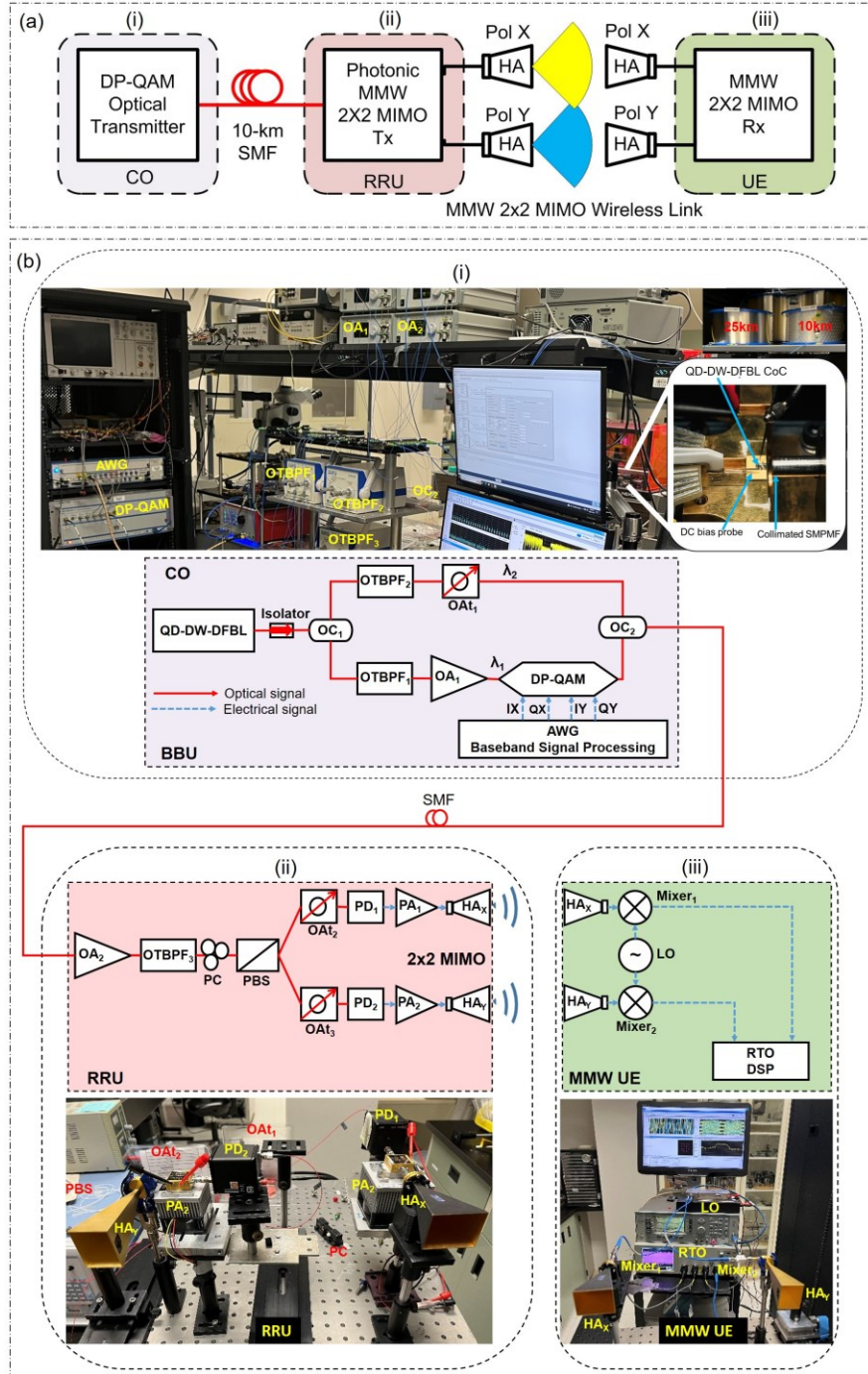
Figure 5.2: (a) Schematic of the proposed photonic MMW 2×2 MIMO RoF wireless transceiver system. (b) Detailed diagrams of each module along with photos of the experimental Lab setups: (i) optical transmitter module at the BBU, (ii) photonic MMW 2×2 MIMO wireless transmitter module at the RRU, and (ii) MMW 2×2 MIMO wireless receiver module at the user equipment (UE).

and 5.2 (b)(iii), respectively. The optical transmitter module encompassing dual-polarization QAM (DP-QAM) optical transmitter, QD-DW-DFBL optical source, arbitrary waveform generator (AWG), optical tunable bandpass filters (OTBPFs), optical amplifier (OA: EDFA), optical attenuator (OAt), and optical couplers (OC). The RRU module includes OA (EDFA), OTBPF, polarization controller (PC), polarization beam splitter (PBS), OAts, photodetectors (PDs), MMW power amplifiers (PAs), and a pair of Horn antennas (HAs). In contrast, the wireless receiver is comprised of a pair of Horn antennas identical to the transmitter ones, two identical double-balanced mixers, an electrical local oscillator, a 3dB electrical power splitter, an electrical PA, and a real-time oscilloscope (RTO).

The optical transmitter in the central office (CO) is connected to an RRU in a BtB configuration, 10 km, and 25 km SMF spool with an InAs/InP QD-DW-DFBL as the main optical source. The light is collected from the front facet of the device using a collimated single mode polarization maintaining fiber (SMPMF), as shown in the inset of Fig. 5.2 (b) (i). The output of laser is connected to a 10/90 polarization maintaining OC_1 through a two-stage PM isolator followed by two TOBPFs, i.e., $TOBPF_1$ and $TOBPF_1$. The OBPF1 and OBPF2 separate the two optical modes of the optical source into channel 1 (90%) and channel 2 (10%), respectively. Channel 1 and channel 2 are used as optical data and optical LO channels, respectively. The optical LO is used to remotely synthesize the corresponding MMW carriers without requiring the bulky electrical LOs, mixers, and other related electrical components. Consequently, an electrical RF LO free RRU is achieved.

After amplifying channel 1 through an OA_1, it is modulated with 2-Gbaud 16 QAM baseband data signals by DP-QAM optical transmitter. The DP-QAM optical transmitter encompasses two thermally stable in-phase/quadrature (I/Q) Lithium Niobate (LiNbO3) Mach-Zehnder modulators (MZMs) integrated into parallel (one modulator per polarization plane) branches. In other words, each branch of the DP-QAM optical transmitter includes one nested MZI structure per polarization plane. One of its branches also consists of a 90° polarization rotator to realize dual-polarization. Also, the QAM's four phase states are obtained by $\pi/2$ shift of the Q parts before the light streams are combined inside the respective nested MZI structures. Moreover, linear data driver electrical

amplifiers (EAs) are used for RF data signals amplification and driving the MZMs. Light at the input of the optical transmitter is split into two paths and directed to the two respective I/Q MZMs for modulation, with one being followed by the $90°$ polarization rotator. The two modulated optical paths are then combined at the optical transmitter's output. The 2-Gbaud 16 QAM baseband data signals are created using an AWG with a pseudo-random bit sequence (PRBS) pattern of $2^{15}-1$ bits. A pulse shaping with a root-raised cosine (RRC) filter and roll-off factor of 0.35 is also applied to the data streams. The corresponding baseband I/Q data signals are then applied to the four I/Q channels, i.e., IX, QX, IY, QY, connected to two I/Q MZMs of the DP-QAM optical transmitter through EAs, as shown in Fig. 5.2(b)(i). Thus, the four electrical baseband data streams, i.e., I and Q in the X and Y polarization plane, are converted into one optical polarization multiplexed modulated data signal. Consequently, the DP-QAM optical transmitter is employed to realize 2-Gbaud 16-QAM baseband modulated polarization multiplexed optical signals through channel one of the QD-DW-DFBL. Moreover, a variable OAt_1 is employed in the path of channel 2 to adjust its power level. The modulated and unmodulated optical channels are combined in a 50/50 OC2, transmitted in a BtB configuration and over 10 km and 25 km SMF to the RAU. This implies that the two MIMO wireless data streams are realized in two orthogonal polarization planes.

In the RRU, the received optical multiplexed signal is amplified by another OA_2 followed by $TOBPF_3$ to filter out its amplified spontaneous emission (ASE) noise, as shown in Fig. 5.2(b)(ii). The optical signal is then passed through a PC to adjust the polarization direction of the signals before splitting into their respective polarizations, i.e., X and Y, by a PBS. The corresponding two X and Y polarization optical channels having optical data and optical LO signals are then focused onto a pair of identical parallel PDs (New Focus 45 GHz IR PD Model 1014), i.e., PD_1 and PD_2, through two variable OAts, i.e., OAt1 and OAt_2, to generate the 2 Gbaud modulated MMW MIMO streams at around 47.3 GHz. The two OAts are used to adjust the optical power at the input of each PD. The two PDs are directly attached to a pair of HAs through a pair of identical Q-band (33-50 GHz) PAs with a nominal gain of about 45 dB. The two HAs are mounted in cross-polarization configuration, with one being at the vertical polarization state and the other at the horizontal polarization state. The HA_X and HA_Y are 22 to 24 dBi WR-22 and 25 dBi WR-19 antennas, respectively.

The corresponding MMW carrier signals at around 47.3 GHz having aggregated data speed of 16-Gb/s are then transmitted over 2 m free space wireless channel.

After receiving the two streams in the MMW user equipment (UE) by a pair of identical HAs, i.e., HA_X and HA_Y, having the same polarization states as that of the transmitter HAs, the signals are fed to two parallel double-balanced mixers directly attached to the HAs, as shown in Fig. 5.2 (b)(i). Thus, the RRU is connected to an MMW UE through a single carrier-based point-to-point 2×2 MIMO wireless links. The single carrier MMW 2×2 MIMO configuration is achieved through remote optical heterodyning of a single laser source with optical dual-polarization and two pairs of HAs in their cross-polarization arrangement making the system much simpler. In this way, the system capacity is doubled, and the crosstalk between the two wireless streams is averted, easing the complexity of MIMO signal processing at the receiver. The two received streams are first down-converted to an intermediate frequency (IF) by incorporating an electrical LO through electrical PA and power splitter into the mixers. The IF signals are then fed to two different ports of a real-time oscilloscope (RTO) and coherently detected and processed in real-time for EVM and BER analysis. The signals undergo several DSP steps, such as resampling, clock recovery, digital down-conversion, match filtering, synchronization, and adaptive equalization, before demodulation to measure the EVM and calculate BER [238].

5.2.2 Experimental Results and Discussion

In our real-time system demonstration, we use a free-running semiconductor InAs/InP common cavity QD-DW-DFBL presented in Chapter 4. A typical optical spectrum of the QD-DW-DFBL output before optical OC_1 is shown in Fig. 5.3 with two highly correlated
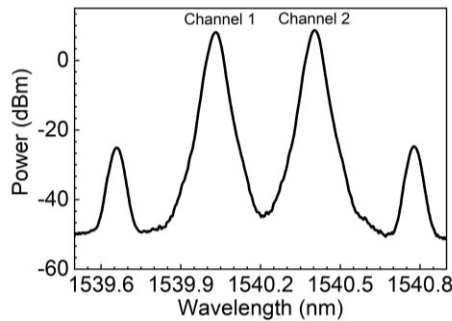
Figure 5.3: Optical spectrum of the QD-DW-DFBL.
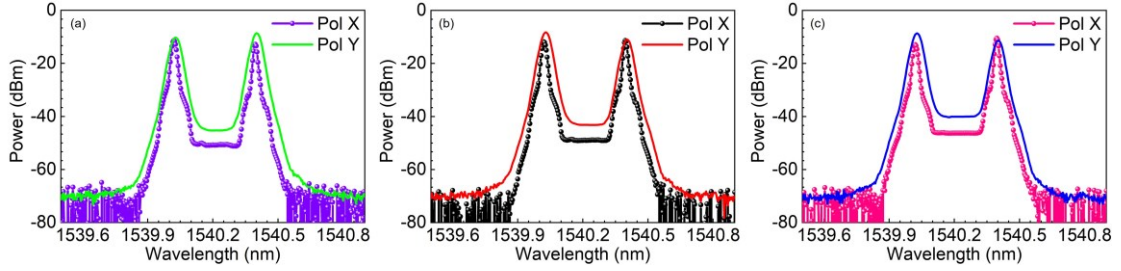
Figure 5.4: Optical spectra of the 2 Gbaud 16 QAM modulated data channel and optical LO channel at X and Y polaization states of the received 2×2 MIMO streams at RRU for (a) BtB, (b) 10 km, and 25 km SMF link configurations.

modes (channel 1 and channel 2) and four-wave mixing (FWM) modes. Each optical channel features very low average relative intensity noise (RIN) < – 150 dB/Hz and low phase noise with spectral linewidth < 30 kHz. The performance of the proposed photonic-assisted single-carrier 2×2 MIMO wireless system based on QD-DW-DFBL is analyzed with a real-time demonstration of 2 Gbaud 16 QAM MMWoF wireless links. Photonic remote heterodyning is used to generate the single-carrier 2×2 MIMO MMW wireless streams at 5G NR FR2 (V-band) of around 47.3 GHz. The links include a 2 m indoor free space wireless channel with BtB, 10 km, and 25 km SMF configurations. The BtB configuration is incorporated for performance comparison. The two wireless streams are parallel in a cross-polarization configuration. The free-space path loss (FSL) for each wireless stream at a frequency of around 47.3 GHz is about 72 dB, which is calculated using Eq. (2.3). Considering an identical gain of around 24 dBi for each pairs of antennas at the transmitter and receiver, the FSL for each wireless stream becomes ~24 dB. The system's transmission is evaluated in terms of EVM, BER, constellation, and eye diagrams. Figure 5.4 (a), Fig. 5.4 (b), and Fig. 5.4 (c) show optical spectra of the received optical signals recorded after the OAts at the RRU for BtB, 10 km, and 25 km SMF, respectively. The optical spectra show both 2Gbaud 16QAM modulated data channel and optical LO for the respective polarization planes, i.e., X and Y polarization, for all three configurations. Note that the slight difference in the spectrum of X and Y polarization is due to different resolutions of two different optical spectrum analyzers used for measurements. The optical channels at X polarization were measured with an optical spectrum analyzer having a resolution of 0.01 nm. In contrast, the optical channels at Y polarization were measured using a spectrum analyzer having a resolution of 0.03 nm.
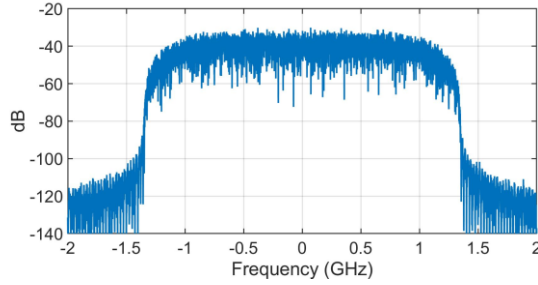
Figure 5.5: Typical electrical spectrum of the 2 Gbaud 16 QAM modulated baseband data signal at the transmitter with 2.7 GHz transmission bandwidth.

On the other hand, Fig. 5.5 depicts the electrical spectrum of the corresponding transmitted 2 Gbaud 16 QAM baseband modulated data signal with 2.7 GHz transmission bandwidth. Moreover, for the three configurations, a typical spectrum of the received 2 Gbaud 16 QAM modulated vector MMW 2×2 MIMO data streams at the UE with 2.7 GHz transmission bandwidth at an IF of around 17.4 GHz after down-conversion can be seen in 5.6 (a), 5.6 (b), and Fig. 5.6 (c), respectively. The corresponding X and Y polarization spectra were measured at the received optical power (ROP) of around -3.5 dBm and -3.3 dBm at the PD1 and PD2, respectively. The uneven envelope of the received modulated data signals towards the high-frequency end is believed to be due to the cut-off operating frequency range of the corresponding PDs, PAs.

Furthermore, Table 5.1, Table 5.2, and Table 5.3 show the constellation diagrams, eye diagrams, EVM, and BER values for the wirelessly received 2×2 MIMO streams over 2 m free space indoor channel at X (POL X) and Y (POL Y) polarization for BtB, 10 km, and 25 km, respectively. Note that POL X and POL Y results were measured at the ROP of
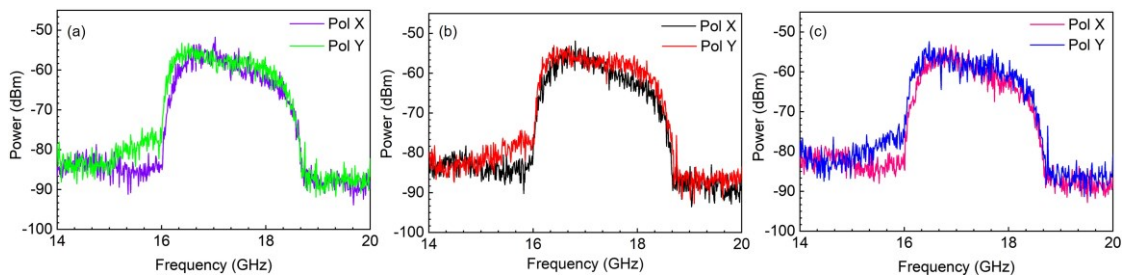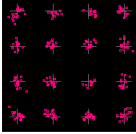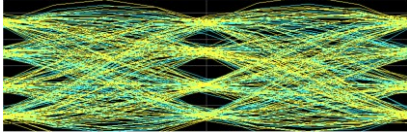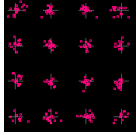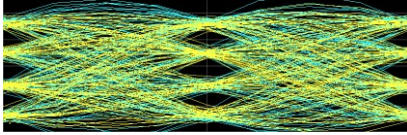
Figure 5.6: Typical spectra of the wirelessly received single-carrier MMW 2×2 MIMO streams at the UE after down-conversion showing the received 2 GBaud I/Q modulated 16-QAM data signals occupying 2.7 GHz transmission bandwidth for (a) BtB, (b) 10 km, and (c) 25 km.

126

Table 5.1: Experimental results for BtB plus 2m MMWoF 2×2 MIMO wireless links.

Stream	Constellation	Eye Diagram	EVM (%)	BER
POL X			6.9	3.0×10^{-11}
POL Y			6.8	1.3×10^{-11}

around -3.5 dBm and -3.3 dBm at the PD1 and PD2, respectively. On average, the fiber length of 10 km and 25 km induce slight performance degradation with EVM penalty of around 0.5/0.4 dB and 0.8/0.7 dB for POL X/Y, respectively, compared to the optical heterodyne MMW wireless transmissions in the BtB configuration. Thanks to the remote optical heterodyning of a single-carrier based baseband modulated correlated o ptical data channel and optical LO of the QD-DW-DFBL for better performance. The single-carrier baseband data transmission over fiber optic link exhibits high tolerance to chromatic dispersion and amplifier non-linearities. Also, the slight EVM improvement for the Y POL streams of the 2×2 MIMO MMWoF links is perceived to be due to the slightly high ROP at the PD compared to POL X. Moreover, the HA_Y is at the V-band (40-60GHz) with a slightly higher gain than HA_X at the Q-band (33-50 GHz). Overall, the results show that BER for all the cases is smaller than the FEC limit, resulting in error-free transmission.

Table 5.2: Experimental results for 10 km SMF plus 2m MMWoF 2×2 MIMO wireless links.
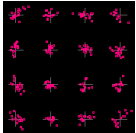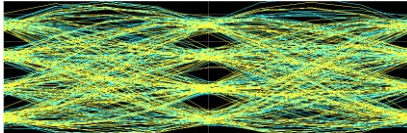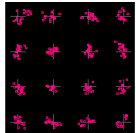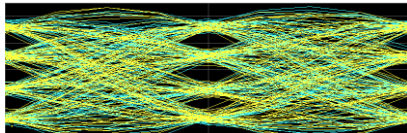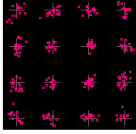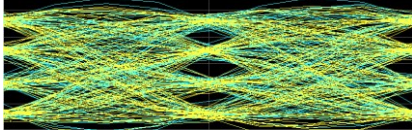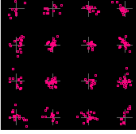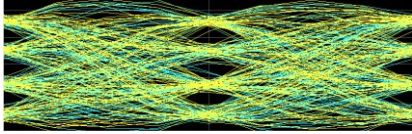
Stream	Constellation	Eye Diagram	EVM (%)	BER
POL X			7.3	3.4×10^{-10}
POL Y			7.1	1.1×10^{-10}

Table 5.3: Experimental results for 25km SMF plus 2m MMWoF 2×2 MIMO wireless links.

Stream	Constellation	Eye Diagram	EVM (%)	BER
POL X			7.6	$1.5×10^{-9}$
POL Y			7.4	$5.7×10^{-10}$

Moreover, the 2 Gbaud 16 QAM corresponds to a bit rate of 8 Gb/s. Therefore, the 2×2 MIMO streams result in an aggregated bit rate of 16 Gb/s, doubling the system data capacity. Thus, using a single optical source, the simultaneous wireless transmission of two MMW modulated data streams with a total data rate of 16 Gb/s is realized. In this way, we can achieve fiber-like broadband wireless connectivity when complemented by photonic MMW MIMO technology using optical heterodyning of a single simple and compact low-noise QD-DW-DFBL, which can significantly increase data capacity, improve system reliability, and reduce system complexity.

5.3 Design and Experimental Demonstration of a Multi-Gb/s Full Duplex Bidirectional Photonic MMWoF Wireless Transmission System Based on QD-DW-DFBL

The schematic of our proposed duplex bidirectional wavelength reused photonic-aided MMWoF wireless transmission with figurative signals along the transmission path is shown in Fig. 5.7. A frequency division duplex (FDD) scenario is emulated where downlink and uplink are at the V-band and Ka-band, respectively. The selected bands correspond to the 5G NR FR2-1 bands of n262 (47GHz) and n261 (28GHz), respectively. In our experiment, a typical 5G C-RAN fronthaul scenario is imitated, which includes BBU in the CO, RRU, and wireless receiver or MMW UE. The BBU is comprised of a photonic MMW transceiver system encompassing the downlink and uplink transmitter and receiver, respectively. On the other hand, the RRU is comprised of a downlink and uplink receiver
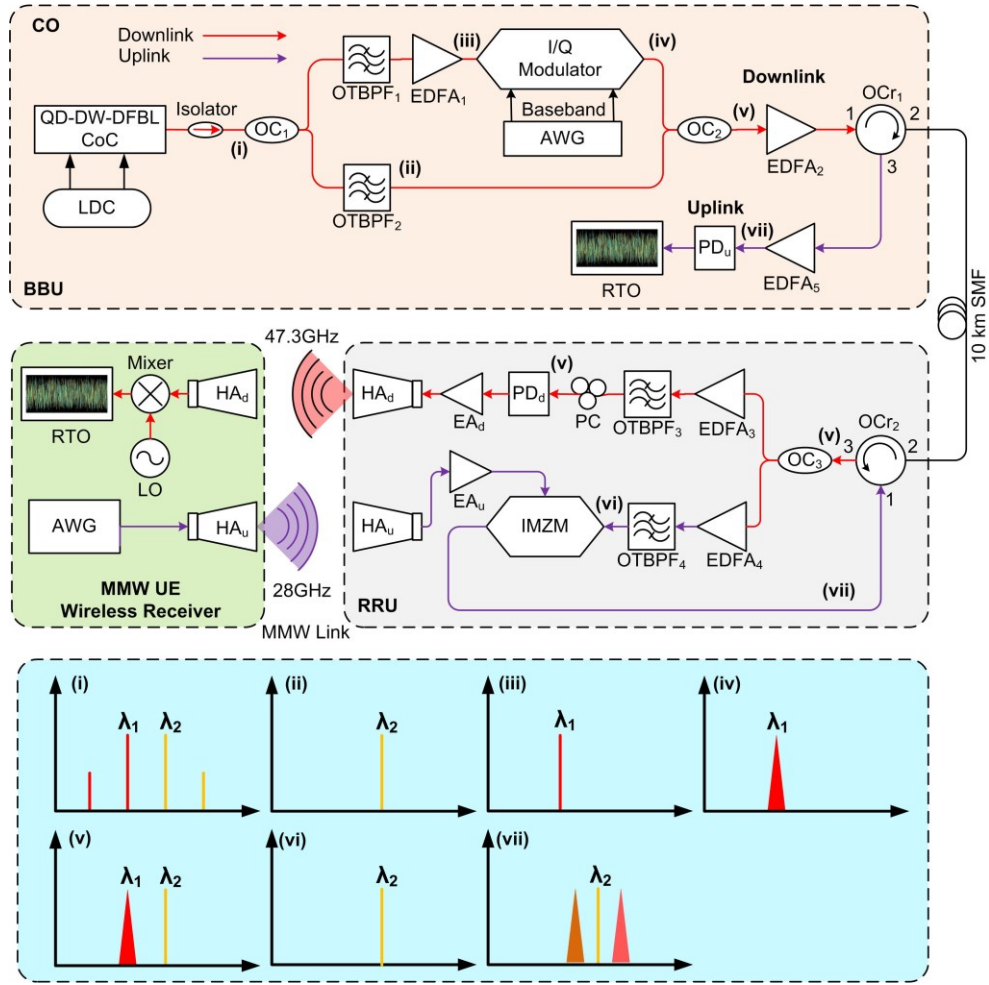
Figure 5.7: Schematic of the experimental setup for the proposed wavelength reused duplex bidirectional photonic MMWoF wireless transmission system based on QD-DW-DFBL, including optical signals' figurative spectra at different points along the transmission path.

and transmitter, respectively. The MMW UE also includes a wireless transciever. In our system, a single QD-DW-DFBL optical source is used to realize the duplex bidirectional links where remote optical heterodyning of two optical channels of the laser up-convert baseband data singles to around 47.3 GHz MMW carrier frequency without using any RF LO. Similarly, one of the downlink wavelengths is reused to transport the uplink 28 GHz data signal. In the CO, a laser diode controller (LDC) is used to control the QD-DW-DFBL CoC and to drive the TEC to maintain the device's temperature at 18 °C. The output light of the laser is coupled from its front facet through a PM lensed fiber attached to a two-stage PM isolator to avoid any back reflections from the system. The optical path is then split into two paths using OC1 with a 10:90 split ratio to select two optical channels, one as an
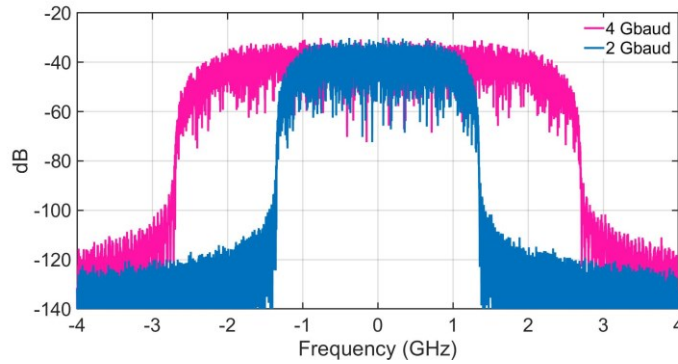
Figure 5.8: Typical electrical spectra of the 2Gbaud and 4Gbaud 16 QAM modulated baseband data signals at the transmitter in BBU before optical modulation.

optical data channel i.e., the shorter wavelength, and another as an optical LO channel, i.e., the longer wavelength, by incorporating $OTBPF_1$ and $OTBPF_2$, respectively. Figure 5.7 (ii) and Fig 5.7 (iii) show the corresponding figurative spectra of the optical LO and optical data channel, respectively. The data channel is used for downlink data transmission, whereas the optical LO channel is used for both the downlink MMW carrier generation and uplink data transmission. The data channel is amplified by an $EDFA_1$ and modulated with the downlink baseband 2Gbaud and 4Gbaud 16QAM signals using an IQ modulator of a DP-QAM optical transmitter system, as depicted in Fig. 5.7 (iv). An AWG is used to generate the corresponding 16QAM baseband data signals with a symbol rate of 2 or 4Gbaud employing a PRBS pattern with a sequence length of 2^{15}-1 bits. For Nyquist pulse shaping, an RRC filter with a roll-off factor of 0.35 is also used. Figure 5.8 shows the electrical spectra of the corresponding 2 and 4Gbaud 16 QAM baseband modulated data signals with 2.7 and 5.4 GHz transmission bandwidth, respectively. The two optical paths are combined in a 50:50 PM OC_2 and the resultant optical signal (depicted in Fig. 5.7 (v)) is amplified by $EDFA_2$ before feeding it to the port one of a PM optical circulator (OCr_1), as shown in Fig. 5.7. The signal is transmitted in the downlink to RRU over a 10 km SMF.

In the RRU, the downlink optical signal is received into port two of an OCr_2 followed by splitting into downlink and uplink paths using a 50:50 PM OC_3 through port three of the OCr_2. The downlink path is amplified by $EDFA_3$, followed by $OBPF_3$ to filter out its ASE noise before feeding it to the downlink PD (New Focus 45 GHz IR PD, Model 1014). A polarization controller (PC) is also added to the path to adjust the polarization direction of
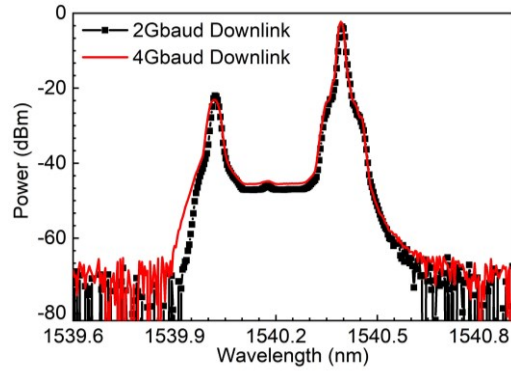
Figure 5.9: Optical spectra of the downlink transmitted 2 and 4Gbaud 16QAM baseband modulated data and optical LO channels measured at the RRU.

the incoming optical signals depending on the condition to ensure maximum output power from the PD. The corresponding 2 Gbaud and 4 Gbaud downlink data channels and optical LOs before the PD are shown in Fig. 5.9. The PD directly attached to a 22-24 dBi HA_d (WR-22) through an electrical power amplifier (EA_d) photonically up-converts the 2 and 4Gbaud baseband data signals to the desired MMW carrier of around 47.3 GHz in the V-band by mixing the optical LO and data channels, which in turn excites the antenna to transmit the signals in free space over 2 m indoor wireless channel. After receiving the signal in the MMW UE wireless receiver by an identical HA_2, it is down-converted to an IF of around 17.3 GHz with an LO before capturing into a RTO for processing. Figure 5.10 shows the electrical spectrum of the corresponding wirelessly received down-converted 2 and 4Gbaud 16QAM modulated IF signals. The received signals are processed and
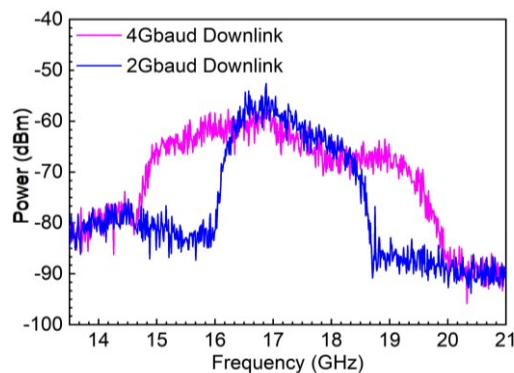
Figure 5.10: Electrical spectrum of the downlink wirelessly received 2 and 4Gbaud 16QAM MMW down-converted signals occupying 2.7 and 5.4GHz transmission bandwidth measured at the MMW UE wireless receiver.

131

demodulated in real-time to measure the system's EVM and calculate the BER [238] performance.

Moreover, the corresponding uplink path is amplified by EDFA$_4$ followed by OTBPF$_4$ to retrieve the optical LO channel for the uplink transmission, as shown in Fig. 5.7 (iv). Figure 5.11 (a) shows the optical spectrum of the filtered, longer wavelength optica channel reused for uplink transmission. This channel is modulated by the uplink 2Gbaud and 4Gbaud 16 QAM modulated signals at 28 GHz in a double sideband (DSB) configuration using an intensity modulator (IMZM). As it is well established that the DSB is highly prone to chromatic dispersion. However, the DSB configuration is used in our experiment due to the unavailability of the required components to achieve a single sideband (SSB). Similar to the downlink, the 2/4Gbaud 16-QAM data signals at 28GHz are generated using an AWG and directly fed to the IMZM without any wireless transmission due to the limited components in the Lab. Before modulating the optical LO, the 2Gbaud and 4Gbaud
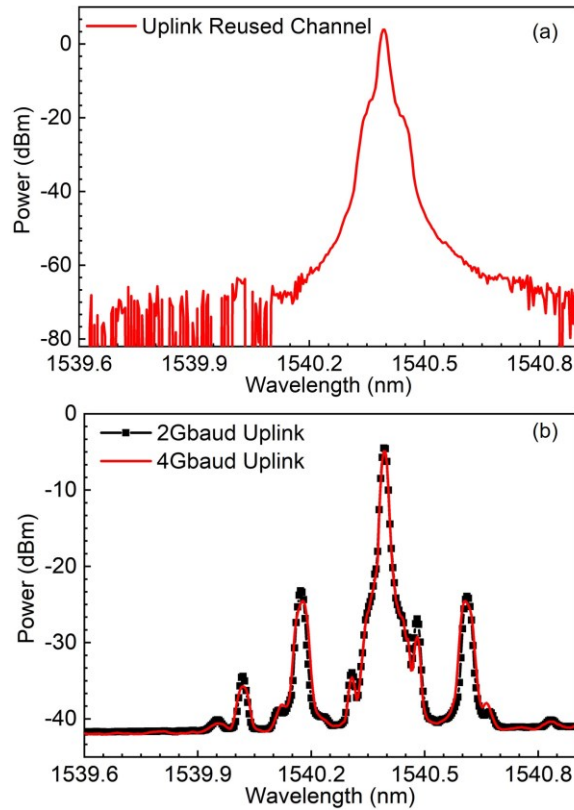
Figure 5.11: Optical spectra of the (a) uplink reused LO at the RRU and (b) uplink received 28 GHz 2 and 4Gbaud 16QAM DSB modulated data signals measured at the BBU.
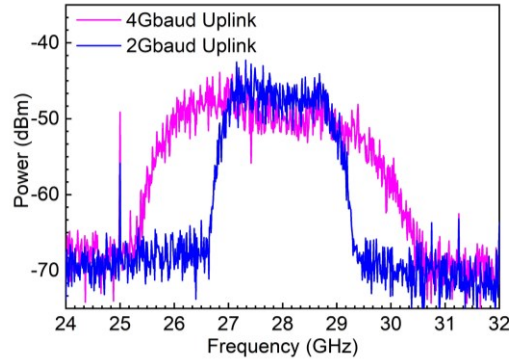
Figure 5.12: Electrical of the uplink received 2 and 4Gbaud 16QAM data signals at 28 GHz occupying 2.7 and 5.4GHz transmission bandwidth measured at the BBU.

modulated 28 GHz signals are amplified by low noise EA_u. The uplink-modulated optical DSB signal is transmitted through port one of the OCr_2 over the same 10 km SMF. The signals are then received in the BBU through port three of OCr_1 and are amplified before shining them on a 35 GHz (New Focus model 1474-A) fiber optic receiver (FOR). Figure 5.11 (b) shows the optical spectra of the corresponding received DSB 2 and 4Gbaud 16QAM signals. After the FOR, the signal is captured in an RTO and processed similarly to the downlink for EVM and BER analysis. Figure 5.12 shows the electrical spectrum of the corresponding captured 2Gbaud and 4Gbaud 16QAM received signals with 2.7GHz and 5.4GHz bandwidth, respectively.

The performance of the proposed duplex bidirectional system is experimentally evaluated in terms of EVM, BER, constellation, and eye diagrams. Table 5.4 and Table 5.5

Table 5.4: Experimental results for 2Gbaud 16QAM bidirectional MMWoF wireless link with 10 km SMF and 2 m wireless distance.
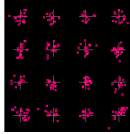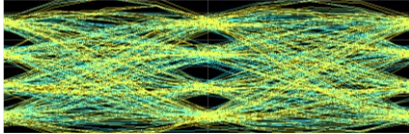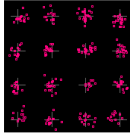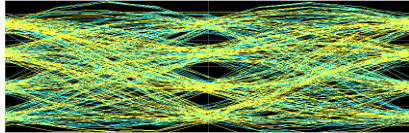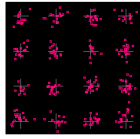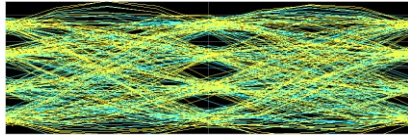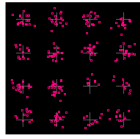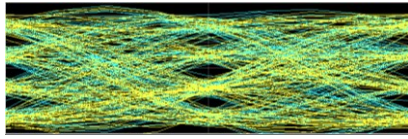
Direction	Constellation	Eye Diagram	EVM (%)	BER
Downlink			8.4	3.8×10^{-8}
Uplink			8.6	7.5×10^{-8}

Table 5.5: Experimental results for 4Gbaud 16QAM bidirectional MMWoF wireless link with 10 km SMF and 2 m wireless distance.

Direction	Constellation	Eye Diagram	EVM (%)	BER
Downlink			9.06	3.0×10^{-7}
Uplink			10.13	3.8×10^{-6}

summarize the corresponding results for the simultaneous transmission of the identical data rates in both directions through the same fiber. The results are measured for the wirelessly received 2Gbaud and 4Gbaud 16QAM signals recorded at the MMW UE in the case of downlink, whereas they are recorded at the BBU in the CO in the case of uplink. Consequently, a single carrier-based 16QAM signals with a baud rate of 2Gbaud and 4Gbaud are used to successfully realize real-time broadband MMW bidirectional links through a single 10 km SMF with a total capacity of 8Gb/s and 16Gb/s, respectively. The results show that EVM and BER are below the standard requirements of 12.5% and 3.8×10^{-3} FEC limit for 16QAM, respectively, at the ROP of around 3 dBm at the PD/FOR in both directions. Thus, error-free simultaneous bidirectional transmission of broadband MMW 16QAM modulated signals with a maximum data throughput of 16 GB/s is achieved. Compared to the downlink, an EVM degradation of about 0.2 dB and 1 dB is observed in the uplink for 2Gbaud and 4Gbaud, respectively. The degradation in the uplink performance compared to the downlink is ascribed to the DSB signals. In addition, the effect of Raleigh backscattering cannot be undermined, considering two identical bidirectional optical channels in a single optical fiber link. Moreover, the wide-band 4Gbaud with a transmission bandwidth of 5.4GHz accumulates relatively more noise compared to 2Gbaud with a tansmission bandwidth of 2.7GHz.

It can be seen from the results that by using two optical channels of a single QD-DW-DFBL, MMWcarrier signals of around 47.3GHz and 28GHz with a maximum bit rate of

16Gb/s are successfully delivered simultaneously through a single 10 km SMF in both downlink and uplink directions, respectively. Thus, the results highlight the potential of low noise monolithic integrated InAs/InP QD-DW-DFBLs for potential deployment in the next-generation multi-Gb/s MMWoF duplex systems.

5.4   Design and Experimental Demonstration of a Duplex Photonic MMWoF Wireless Transmission System Based on PML QD-MWL

Figure 5.13 shows the architecture of the proposed duplex MMWoF system based on a single PML InAs/InP QD-MWL coherent frequency comb (CFC) presented in Chapter 3. The figure also includes a spectrum representation of the signals at different points along the transmission path. Similar to the duplex bidirectional systems based on QD-DW-DFBL presented in Section 5.3, we emulated a typical 5G C-RAN fronthaul architecture. However, an FDD scenario with both downlink and uplink at the Ka-band is realized in this case. At the CO, the CFC is coupled into a lensed PM fiber through a two-stage optical isolator to avoid undesired back reflections into the device cavity. An 85/15 OC1 connected to the output of the optical isolator is used to split the light into two paths, with one (85%) passing through an $OTBPF_1$ to select one comb line. After being amplified by an $EDFA_1$, the comb line is sent into a DP-MZM optical transmitter, where a microwave 16-QAM signal at 3 GHz generated by an AWG modulates the comb line. The DP-MZM optical transmitter is comprised of two branches having thermally stable I/Q Lithium Niobate (LiNbO3) nested MZI structures. In other words, each branch of the DP-MZM optical transmitter includes a MZM integrated in parallel. In one of the two sub-MZIs in each arm, a phase modulator is incorporated. By applying a DC voltage of V_π, where V_π is the halfwave voltage, to the two sub MZIs (to have them operate at the minimum transmission points) and $V_\pi/2$ to the phase modulator to introduce a 90° phase shift, a single-sideband with suppressed carrier (SSB-SC) optical signal is generated. The purpose of using SSB-SC modulation is to eliminate the dispersion-induced power fading effect as well as to improve the spectral efficiency. The second path's light passes through a second $OTBPF_2$ to select a second (adjacent) comb line, which has a wavelength spacing with the first comb line of ~0.2 nm or 25.08 GHz. The modulated signal and the second comb line are
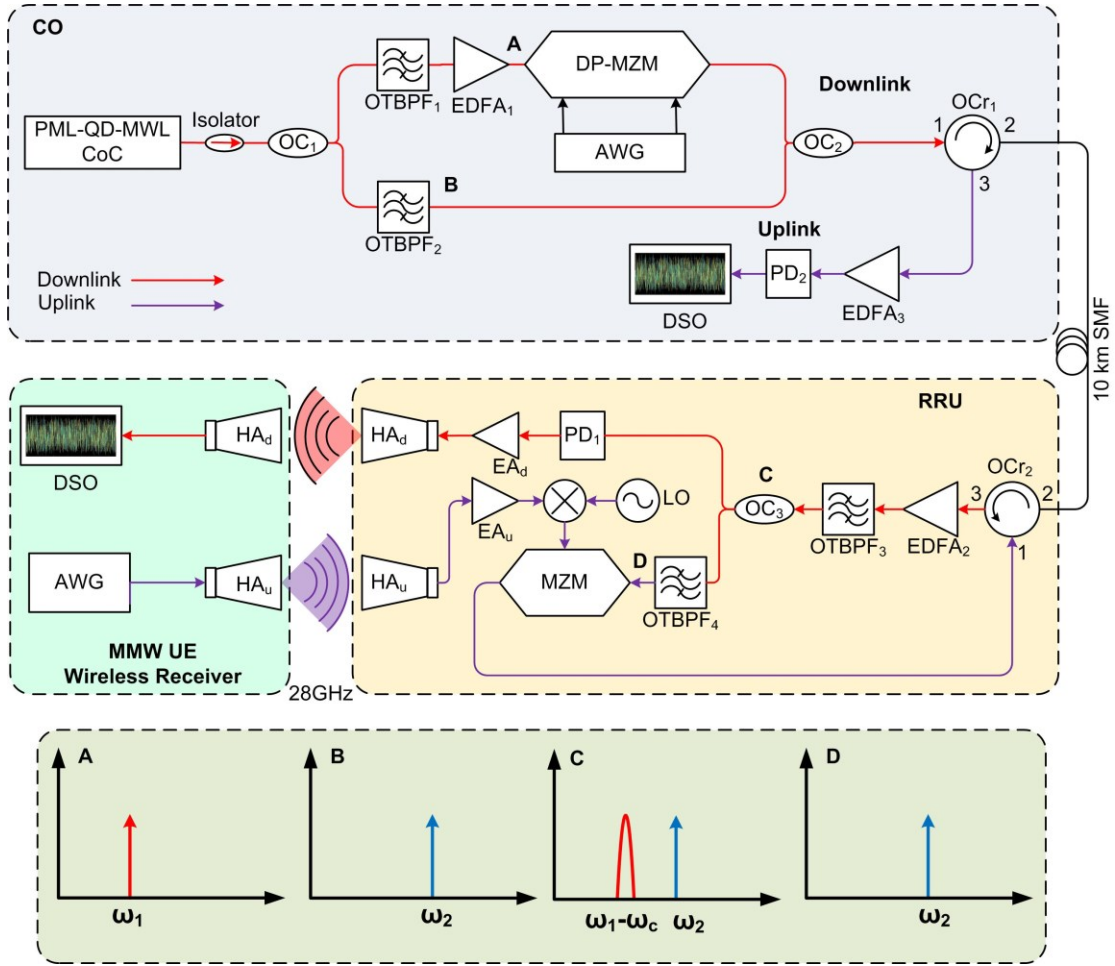
Figure 5.13: Schematic of the duplex bidirectional MMWoF link using an InAs/InP PML QD-MWL. Optical spectra at different locations along the transmission link are shown. PML QD-MWL: passively mode-locked quantum-dash multi-wavelength laser; OC: optical coupler, OTBPF: optical tunable bandpass filter, EDFA: erbium-doped fiber amplifier, DP-MZM: dual-parallel Mach-Zehnder modulator, AWG: arbitrary waveform generator. OCr: optical circulator, SMF: single mode fiber, PD: photodetector, EA: electrical amplifier, MZM: Mach-Zehnder modulator; DSO: digital storage oscilloscope, CO: central office, RRU: remote radio unit.

combined at an optical coupler OC_2 and transmitted in the downlink over a 10 km SMF to the RRU via two optical circulators (OCr_1 and OCr_2).

At the RRU, the downlink received optical signal is amplified by a second $EDFA_2$ and sent to $OTBPF_3$ to remove the ASE noise from $EDFA_1$ and $EDFA_2$ to increase the optical signal-to-noise ratio (OSNR). The optical signal is then detected at a high-speed PD_1 where the modulated optical signal and the second comb line beat to generate an MMW signal with its frequency up-converted to 28.08 GHz. The generated MMW signal is amplified by an EA_d and then radiated and received by a pair of 17-20 dBi WR-34 HAs, i.e., HA_d,

that are separated by 2 m. The received MMW signal is then sent to a digital storage oscilloscope (DSO) for further offline DSP to evaluate the transmission performance. The DSP includes steps, such as IQ components' down-conversion to baseband, low pass filtering, equalization, and symbols detection.

An uplink 16-QAM MMW signal at 28 GHz is realized using an AWG and sent it to the CO over the same fiber link at an IF, achieving duplex bidirectional transmission. For this, part of the downlink signal is taped via an optical coupler OC_3 and filtered by an $OTBPF_4$ to extract the second comb line. Before being modulated on the retrieved optical carrier, the reused comb line from the downlink signal, the uplink signal is realized at an IF of 3 GHz. Therefore, the required bandwidth of an intensity MZM used for uplink transmission can be relatively small. After modulation at the intensity MZM, the uplink modulated optical signal is sent via the same 10 km SMF back to the CO. Note that two optical circulators (OCr_1 and OCr_2) are used to enable duplex transmission using the same SMF. The uplink optical signal at the CO is then converted to an electrical signal using a second PD_2 after being amplified by a third $EDFA_3$. The detected electrical signal is also sampled and stored at a DSO for further offline DSP.

The proposed MMWoF link using the PML QD-MWL for duplex transmission is experimentally demonstrated. The experiment settings are as follows: both the downlink data stream and uplink data stream are 1Gbaud, 16QAM signals; the wireless communication distance is set at 2 m, which was the maximum distance that we could achieve due to the limited lab space during our experiment. To evaluate the performance of the MMWoF link, the EVMs for both the downlink and uplink transmission for different optical power levels at the inputs of the PDs are measured. Based on the EVMs, BERs are estimated [239]. The BERs for BtB and 10 km SMF transmission in a simplex mode are shown in Fig. 5.14(a). As can be seen, when the optical distance is 10 km, the system has a power penalty of about 0.2 dB. The BER for the downlink transmission over 10 km SMF when the link is operating in duplex mode is also shown in Fig. 5.14 (a), which indicates the power penalty when operating in duplex mode is around 2.2 dB. For all cases, when the received optical power is greater than -6.8 dBm, the BERs are smaller than 3.8×10^{-3}, thus error free downlink transmission can be achieved with FEC.
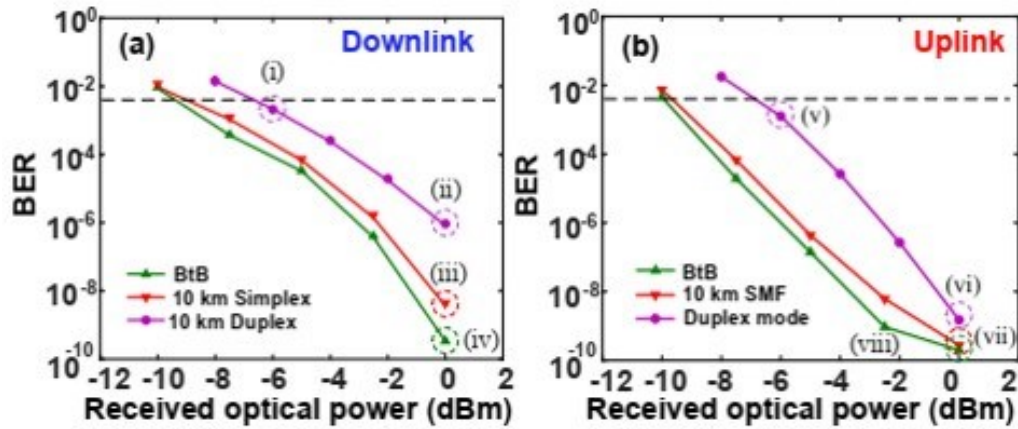
Figure 5.14: (a) BERs versus the received optical power for downlink transmission, blue: BtB, red: 10 km SMF in the simplex mode, and purple: 10 km SMF in the duplex mode. (b) BERs versus the received optical power for uplink transmission, blue: BtB, Red: 10 km SMF in the simplex mode, and purple 10 km SMF in the duplex mode.

Then the BERs of the RoF uplink transmission at different received optical power levels are also investigated. The BERs for BtB and 10 km SMF transmission in the simplex mode are shown in Fig. 5.14 (b). As can be seen, when the optical distance is 10 km, the system has a power penalty of 0.1 dB. When operating in the duplex mode, the BERs for uplink transmission over 10 km SMF are calculated, and the power penalty is 3 dB. For all cases, the BERs are below 3.8×10^{-3} when the received optical power is greater than -7 dBm. Thus the error-free uplink transmission with FEC can be achieved.

The constellation diagrams and the corresponding EVMs for different settings marked in Fig. 5.14 are shown in Fig. 5.15. When comparing the transmission performance for the MMWoF link operating in the downlink and uplink mode, it is found that the uplink transmission performance is better than that for downlink transmission. The reason is believed to be that the MMW carrier for downlink transmission is the beat signal from the two comb lines of a free-running unpackaged bared chip device in an open lab environment. In contrast, the MMW carrier for uplink transmission is generated by highly stable and controlled AWG, and transmitted at an IF. Also, the modulator bias drift could contribute to performance degradation.

The proposed MMWoF link only uses two comb lines of the PML QD-MWL to achieve 4 Gbit/s (1Gbaud×4) transmission in both directions. Considering the same baud rate, with
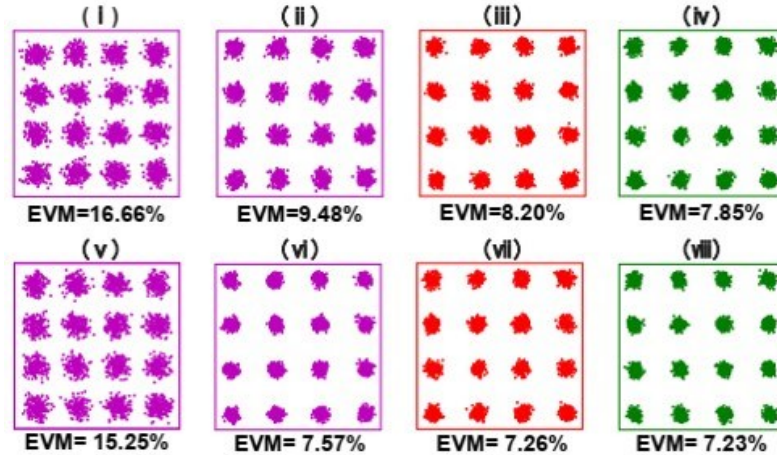
Figure 5.15: Constellations and the corresponding EVMs for the duplex MMWoF link of different settings marked in Fig. 5.14.

the help of the WDM technique, all 47 comb lines of the device can achieve an aggregate 92 Gbit/s downlink and uplink transmission. Nevertheless, this can further be increased by increasing the baud rate of the system. In addition, by employing the PML QD-MWL, MMW carriers in other higher frequency bands can be generated. Moreover, more flexible and scalable MIMO configurations can be achieved by replacing QD-DW-DFBL with PML QD-MWL in the proposed photonic MIMO system presented in Section 5.2.

5.5   Summary

In this chapter, we propose and experimentally demonstrate Multi-Gb/s photonic MMW MIMO and duplex bidirectional systems based on QD-MWLs. This includes an experimental demonstration of a photonic-assisted MMWoF 2×2 MIMO and bidirectional wireless transmission systems at around 47.3 GHz and 28 GHz employing a single low noise InAs/InP quantum dash dual-wavelength DFB laser (QD-DW-DFBL) and InAs/InP passively mode-locked (PML) QD-MWL-based coherent frequency comb (CFC). The 2×2 MIMO structure is realized through optical polarization multiplexing and remote heterodyning of a single optical source together with the cross-polarization configuration of two pairs of antennas to avoid interference at the receiver, reducing system complexity. The demonstration includes real-time error-free transmission and detection of wideband 2GBaud 16QAM MMW wireless signals at V-band in a 2×2 MIMO configuration over a

2m wireless distance through 10km and 25 km SMF. This results in doubling the system data capacity to 16 Gb/s. The system performance is evaluated by exhibiting EVM and bit BER well below the standard requirements, achieving error-free transmission. By replacing QD-DW-DFBL with the PML QD-MWL-based CFC, more flexible and scalable systems with various M×M configurations can be achieved. Moreover, broadband duplex bidirectional systems are proposed and experimentally demonstrated based on QD-DW-DFBL and PML QD-MWL. 8 Gb/s and 16 Gb/s 16 QAM bidirectional MMWoF wireless links with the downlink at around 47.3 GHz and uplink at 28 GHz are realized over a 2m indoor wireless distance through 10 km SMF by employing a single InAs/InP QD-DW-DFBL source. The successful error-free simultaneous transmission of 2Gbaud and 4Gbaud data is achieved over a single SMF in both directions. Similarly, 4Gb/s 16QAM simultaneous duplex bidirectional MMWoF wireless links with the downlink at around 28.08 GHz and uplink at 28 GHz are realized over a 2m indoor wireless distance through 10 km SMF by employing a single InAs/InP PML QD-MWL CFC source. For both downlink and uplink, error-free operation is achieved at the FEC. These QD-MWL-based MMWoF wireless systems' designs and experimental demonstrations could usher in a new era of ultra-high speed broadband multi-Gb/s wireless communications at the MMW frequency bands for next-generation wireless networks.

Chapter 6

High Capacity Spectrally Efficient MIMO and Optical Beamforming Enabled Photonic MMWoF Wireless Transceiver Systems Based on QD-MWLs

6.1 Introduction

THE foreseeable bottleneck in the fronthaul links of next generation wireless communication networks can be alleviated, and the capacity can be increased by incorporating space division multiplexing (SDM) technologies, such as mode division multiplexing (MDM) and multicore fiber (MCF). In the former case, different light propagation paths, also called spatial modes, such as linearly polarized (LP) modes in a single core of few-mode-fiber (FMF) [198] or multimode fiber (MMF) [249], and orbital angular momentum (OAM) spatial modes in RCF [250] and free space optical links [251] are used for simultaneous transmission of multiple RF signals. In addition, linearly polarized vector (LPV) modes in polarization-maintaining elliptical ring core fiber (PM-ERCF) [252] are used for transporting the RF signals. On the other hand, in the latter case, different cores in the same cladding of MCF are used for concurrent transmission of various RF signals using single or multiple optical wavelengths and electrical frequencies [199]. The transmission capacity of RoF links, in particular of 5G and beyond fronthaul networks, can significantly be increased by leveraging additional multiplexing techniques such as WDM and polarization multiplexing (PolM) [11]. Thus motivated by the fact that A-RoF transport solutions with SDM and WDM technologies and photonic MMW signals generation and distribution in the optical domain can achieve high bandwidth, high centralization, low latency and cost-effectiveness, in this chapter, we propose MIMO and optical beamforming (OBF) enabled high capacity all-optical WDM and SDM based MMWoF wireless transciever systems for 5G and beyond wireless networks using QD-MWLs. The proposed system designs provide seamless fiber-wireless integration (optical fiber and RF integration) in the form of RoF with photonic MMW signals generation and distribution in the optical domain using low noise highly coherent, correlated and integrated QD-MWL optical sources with flat spectra comprising multiple equally spaced

optical channels. The optical fiber's inherent characteristics of high bandwidth, low loss, and immunity to electromagnetic interference allow for these high frequency and ultra-broadband MMW wireless signals to be distributed efficiently to long distances. Thus, this integration not only overcomes the problem of high bandwidth requirement, transmission capacity and span limitation of these high frequency signals, but at the same time, it can significantly reduce the system cost and complexity by eliminating expensive RF components such as ADCs/DACs and electrical local oscillators, especially in the case of 5G ultra-dense networks with small cells in centralized cloud radio access network (C-RAN) configuration where a large number of RRHs/RRUs with M-MIMO will be deployed. In addition, fiber-wireless integration for antenna remoting through photonic MMW signals generation with M-MIMO phased array antennas (PAAs) also facilitates remote analog optical beamforming, which is used to overcome the high propagation loss of MMW signals in the wireless channel. Compared with the conventional electrical beamforming, where a dedicated RF chain or phase/amplitude control is required for each radiating antenna element that adds up to the size, complexity and hardware cost in addition to bandwidth limitations, electromagnetic interference and high power consumption, OBF with higher available bandwidth can significantly reduce the complexity, cost and power consumption using photonic true time delay lines (TTDLs). The OBF with photonic TTDLs can also help in alleviating the problem of beam squint in wide-band applications. Since in the case of OBF with TTDLs, the beam pointing direction is a function of the optical delay line where all frequency components have the same delay times, whereas, in the case of beamforming with electrical phase shifters, it is dependent on the signal frequency leading to beam squint in wide-bandwidth applications. Moreover, the existing fronthaul links between the RRHs/RRUs and BBUs are based on digital RoF (D-RoF) with a common public radio interface (CPRI) as the main interface protocol, which poses major challenges in terms of extremely high capacity requirements for 5G and beyond wireless networks, as discussed in chapter 2. Therefore, analog RoF (A-RoF) fronthaul is considered as an alternative to CPRI based D-RoF [11]–[13], [174].

Part of this chapter is based on the published article in [48]. In the following sections, a comprehensive literature review on the recent research trends in A-RoF-based fronthaul with SDM technologies for the next generation of wireless networks is presented in Section

6.2. Section 6.3 presents the basic concept of the proposed transceiver systems' design, framework, and principle operation. The design and different implementation scenarios of the proposed system are discussed in Section 6.4. Section 6.5 briefly discusses the fundamental A-RoF SDM-based technology challenges and potential solutions. Finally, the conclusion is presented in Section 6.6.

6.2 Review of Recent Related Works

As established earlier, the infrastructure of the current mobile fronthaul will not meet the requirements of 5G and beyond; therefore, research efforts are intensely focused on designing novel RoF technologies and systems. Several approaches have been proposed to overcome the limitations of the current D-RoF fronthaul for achieving C-RAN, as discussed in Section 2.4 of Chapter 2. However, A-RoF fronthaul approach has been considered one of the best potential candidates for 5G and beyond C-RAN due to its bandwidth efficiency, low latency, and cost-effectiveness [11]–[13], [174], [176], [182], [183], [198]. Nevertheless, considering the cell densification with a large number of antennas remoting, M-MIMO and beamforming technology and the use of MMW spectrum, the required bandwidth in RoF links, in particular fronthaul links, would scale up to the extent that would exceed the huge bandwidth provided by the single optical fiber link [249], [253]. Therefore, this expected rise in the bandwidth requirements of fronthaul optical links calls for novel multiplexing dimensions of SDM such as mode MDM in FMF in the form of LP modes [198], [249], RCF in the form of OAM modes [250], and MCF [199], [254] tailored with WDM and Pol-Mux. Yet, the concept of MDM application in fronthaul of mobile wireless networks has been recently introduced, and not much research work has been devoted to its investigation. There are few studies available in the literature that demonstrate the use of SDM for fronthaul and evaluate its performance in A-RoF links using LP modes in FMF [198], [253], [255]–[258] and MMF [249], [259], LPV modes in PM-ERCF [252], OAM modes in RCF [250] and free space optical links [251], and SDM in MCF [199], [254], [260]–[262]. Moreover, the feasibility of MDM for implementing RoF distributed antenna system (DAS) architectures was also reported in [263]–[266]. Thus, considering the aforementioned technologies and requirements, the design of an

efficient, flexible and scalable A-RoF fronthaul for 5G and beyond mobile networks is yet to be developed.

In order to realize the use of MDM in FMF for the next generation mobile fronthaul application, a symmetrical bidirectional system based on MDM and wavelength reuse scheme was proposed in [198]. The system was experimentally demonstrated by multiplexing four 25 Gb/s downlink channels and four supplementary carriers for uplink channels using WDM and transmitting them over LP_{01} and LP_{11} modes of 10-km two mode FMF, respectively. In addition, to mitigate the upstream power penalty due to Rayleigh backscattering as a result of upstream and downstream spectrum overlapping, the shifting of downstream frequency is proposed. Likewise, an MDM based RoF link for W-band wireless spectrum (75-110 GHz) was proposed in [255]. The link was experimented with utilizing LP_{01} and $LP_{11a/b,x,y}$ modes of 30-km differential modal group delay compensated FMF. Additionally, to avoid RF power fading due to mode coupling in MDM-RoF links, mode assignment and crosstalk filtering technique was proposed in [256], where RF carrier and signal components are transmitted over different LP modes using different wavelengths. In this way, the unwanted crosstalk can be filtered out before photo-mixing and wireless signal generation. The proposed technique was evaluated by transporting carrier and signal components over LP_{01} and $LP_{11a/b,x,y}$ modes of 30-km FMF, respectively, with successful crosstalk suppression. However, this technique is only suitable for high bandwidth wireless signals such as MMWs (W-band). Moreover, it is shown in [257] that MDM over FMF A-RoF link can further reduce the non-linearity effects (stimulated Brillouin scattering and intermodulation distortion (IMD)) and increase the gain of the link. This is investigated through MDM of two modes, i.e., LP_{01} and LP_{11}, over 10-km four mode FMF, and it was observed that the MDM reduces the third-order IMD and improves the spurious-free dynamic range (SFDR) compared to using only any single mode of FMF or SMF. Similarly, in [249], a fully analog fronthaul was numerically investigated for massive MIMO using MDM and FDM over 10-km MMF with direct detection and all-optical passive Mux/Demux. It is numerally proven that using smart dynamic assignment for the mode-frequency optical resources between the radio antennas and the mode/frequency dimensions allows us to overcome the intermodal crosstalk limitations. On the other hand, the transmission of 4.46 Gb/s 2x2 MIMO orthogonal frequency division

multiplexing (OFDM) with offset QAM was experimentally demonstrated in [253] over two LP modes (LP_{01} and LP_{11a}) of 2-km elliptical three modes FMF along with 0.4 m wireless link. To overcome the problem of differential channel delay among the MIMO channels in the absence of cyclic prefix, which leads to inter-symbol interference and inter-carrier interference, a time-offset crosstalk algorithm was also presented. Additionally, in order to optically power the remote antennas units (RAUs), a system for simultaneous transmission of optical data (A-RoF) and high feed power (power-over-fiber) was designed and demonstrated in [259] over 2-km and 4-km FMF. To mitigate the modal dispersion and feed light crosstalk of the corresponding signals, center-launching and offset-launching techniques were adopted.

Moreover, for the first time in [252], LPV modes in polarization-maintaining elliptical ring core fiber (PM-ERCF) were introduced for RF signals' transmission. The transmission of different RF signals using 2.4 GHz and 3.3 GHz RF carriers over four LPV modes of 900-m PM-ERCF was experimentally demonstrated without using MIMO processing. The four modes include $LPV_{11a,x}$, $LPV_{11b,x,y}$, and $LPV_{21,a,y}$, where two polarization of LPV_{11b}, i.e., $LPV_{11b,x,y}$, are employed to analyze the polarization multiplexing property of modes. The modes are further investigated in terms of the bending property of fiber, observing high loss for $LPV_{21,a,y}$ channel compared to the other three channels.

Furthermore, OAM modes in FMF along with LP modes and RCF were also investigated. In [258], the combination of LP and OAM modes, i.e., LP_{01}, LP_{11a}, LP_{11b}, OAM_{+1}, and OAM_{-1}, in 5-km FMF was used to analyze the performance of analog signals' transmission. It was shown that mode relative losses of different modes influence the analog transmission, and higher order modes suffer from degradation in SFDR due to high loss. However, with the same mode relative loss, all modes show similar performance. Nevertheless, FMF supports only a few lower order OAM modes [267]. It was also reported in [250] that due to the short length and high capacity requirements, OAM modes are suitable for fronthaul links. Since OAM are less prone to inter-modal crosstalk than LP modes due to their distinct propagation constants.

On the other hand, SDM in radio-over-multicore fiber has been proposed to increase the capacity, scalability and flexibility of the analog mobile fronthaul links. To this end, in [199], the simultaneous transmission of LTE-A and worldwide interoperability for microwave access (WiMAX) RF signals was demonstrated over 150-m four core MCF considering both linear and non-linear optical power regimes of fiber. It was shown that by exciting the underlying Kerr non-linearity in MCF, the EVM fluctuations due to random nature of fiber can be reduced [199], [268]. Similarly, MIMO and carrier aggregation over MCF for fronthaul was proposed and evaluated in [260], [269]. Various configurations of single-input-single-output (SISO), MIMO and carrier aggregation were investigated over 15-m of four core MCP utilizing different cores for uplink and downlink transmissions. It was shown that carrier aggregation has no effect on the signal quality provided that the carriers are not overlapped in the spectrum. Besides, it was revealed that existing 3GPP MIMO algorithms could be effectively applied to MCF in fronthaul applications, which increase the data rate multiple times compared to SISO at the expense of merely a few dB of power penalty [260], [269]. To further increase the system capacity and spectral efficiency, a 4 x 4 MIMO radio over four cores of 20-km seven-core MCF system was demonstrated using sparse code multiple access (SCMA) and OFDM/OQAM schemes [261]. Moreover, in [254], the transmission of bidirectional two RF channels of MIMO OFDM/OQAM signals over 20-km seven-core fiber and 0.4-m wireless link was experimentally demonstrated. For the uplink colorless transmission, an optical carrier is sent into the middle core of the seven-core MCF, which is split into two optical carriers at the remote site for the modulation of the corresponding uplink signals. In addition, the simultaneous provision of 2G, 3G and 4G services was demonstrated over a reconfigurable radio-over-multicore fiber fronthaul in [261]. The signals from different standards were fed to the remote antennas through different cores of the MCF using the same frequency band for achieving reconfigurable Ro-FMCF fronthaul. On the other hand, in [262], the radio and power over MCF transmission were also demonstrated.

Moreover, the feasibility of MDM for implementing MIMO RoF DAS was experimentally demonstrated in [263] using MMF. It was reported that the wireless MIMO algorithm is capable of overcoming the distortion and crosstalk in both wireless and low power optical channels. Likewise, it was experimentally demonstrated in [264], [270] that

the distribution of wireless MIMO signals in in-building DAS is feasible through MDM in commercially-available MMF infrastructure, even under a tight fiber conditions. Besides, in [265] the statistical characteristics of RF MIMO signals was studied in MDM using MMF. Similarly, in [266], an MIMO enabled DAS architecture was simulated by employing mode group division multiplexing (MGDM) in combination with WDM in plastic optical fibers (POFs) for MMW communication. It was shown that the generation of MMW 2x2 MIMO signals at the RAUs is feasible using MGDM and WDM in POF.

The state-of-the-art literature review of analog mobile fronthaul systems reveals that A-RoF based fronthaul with SDM technologies for achieving C-RAN and seamless fiber-wireless integration cannot be avoided within the list of high gain, flexible and scalable fronthual system designs for 5G and beyond of wireless networks.

6.3   SDM Based MIMO Enabled All-Optical MMWoF Transceiver System for Next Generation Fronthaul using QD-MWL

A general overview of the fronthaul architecture is shown in Fig. 6.1, where BBUs in the central office are connected to the RRHs/RRUs/RAUs through optical fiber transmission links in various potential configurations. It supports both indoor and outdoor MMW communications along with macro and small cell environments. The schematic of system design, configuration and detailed operation of the proposed wavelength reused symmetric bidirectional A-MMWoF fronthaul system are shown in Fig. 6.2. To achieve a high capacity gain in the fronthaul links, SDM and WDM technologies are employed in the proposed architectural design. As an example, SDM is realized through MDM using LP modes as separating multiple optical channels in a single FMF as an alternative to multiple standard SMFs in the schematic shown in Fig. 6.2. It can also be employed through OAM modes using specialized fibers, such as RCF. Since FMF supports only few lower order OAM modes [267]. It should also be noted that a large number of LP modes usually encounter more crosstalk than OAM modes as they propagate along the fiber. This is because LP modes share common eigenmodes, whereas OAM modes are constructed from distinct eigenmodes [250]. Moreover, SDM through MCF and FM-MCF can also be considered depending on the requirements.
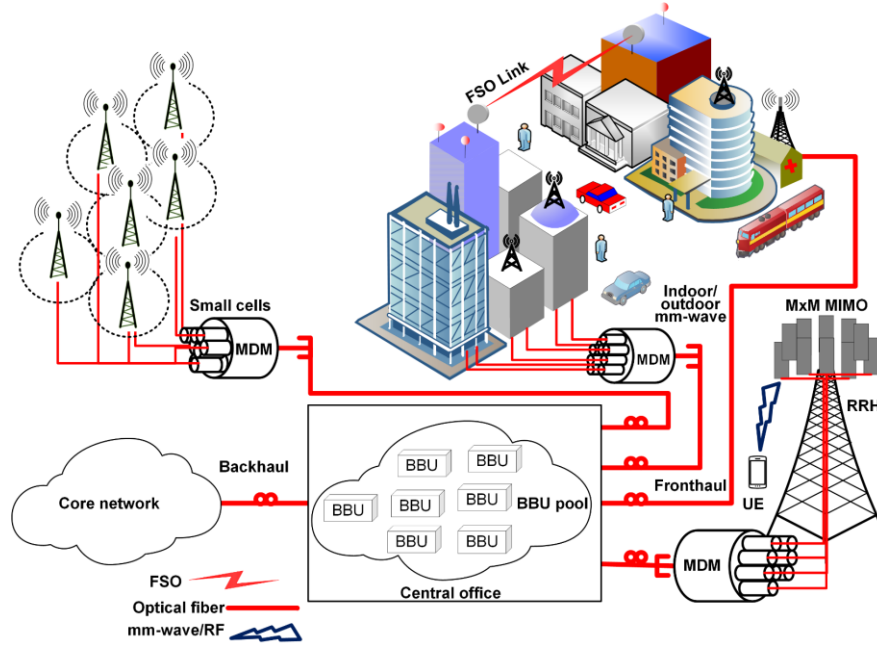
Figure 6.1: A generic SDM based MMWoF fronthaul architecture. UE: user equipment, FSO: free space optical, MDM: mode division multiplexing.

For high capacity multiplexing gain and diversity gain in the wireless domain, MMW M×M MIMO signals are used, which are also realized here and can be adopted according to the system requirements. The MMW signals' generation is realized through optical heterodyne at the RRHs/RRUs/RAUs. Consequently, the corresponding MMW M×M MIMO signals are generated and distributed in the optical domain using SDM. In the proposed design, in the BBUs, one/few (depending on system requirements) of the multiple coherent optical carriers from QD-MWL comb source are used for downlink data transmission of MMW M×M MIMO signals over the spatial modes through SDM, i.e., MDM, in FMF while another optical carrier (s) is transmitted as an auxiliary carrier for use in heterodyne MMW signals generation and uplink transmission in the RRH/RRU/RAU as shown in Fig. 6.2. The design is flexible and scalable, depending on system requirements, multiple optical carriers can be used for both downlink and uplink transmission with different combinations of spatial modes.

In a simple exampalry scenario, its principle operation at the BBU is such that two wavelengths λ_x and λ_y (where $x, y = 1, 2 \ldots n,$ and $x \neq y$) with the required MMW frequency difference are selected from the optical carriers of coherent QD-MWL comb
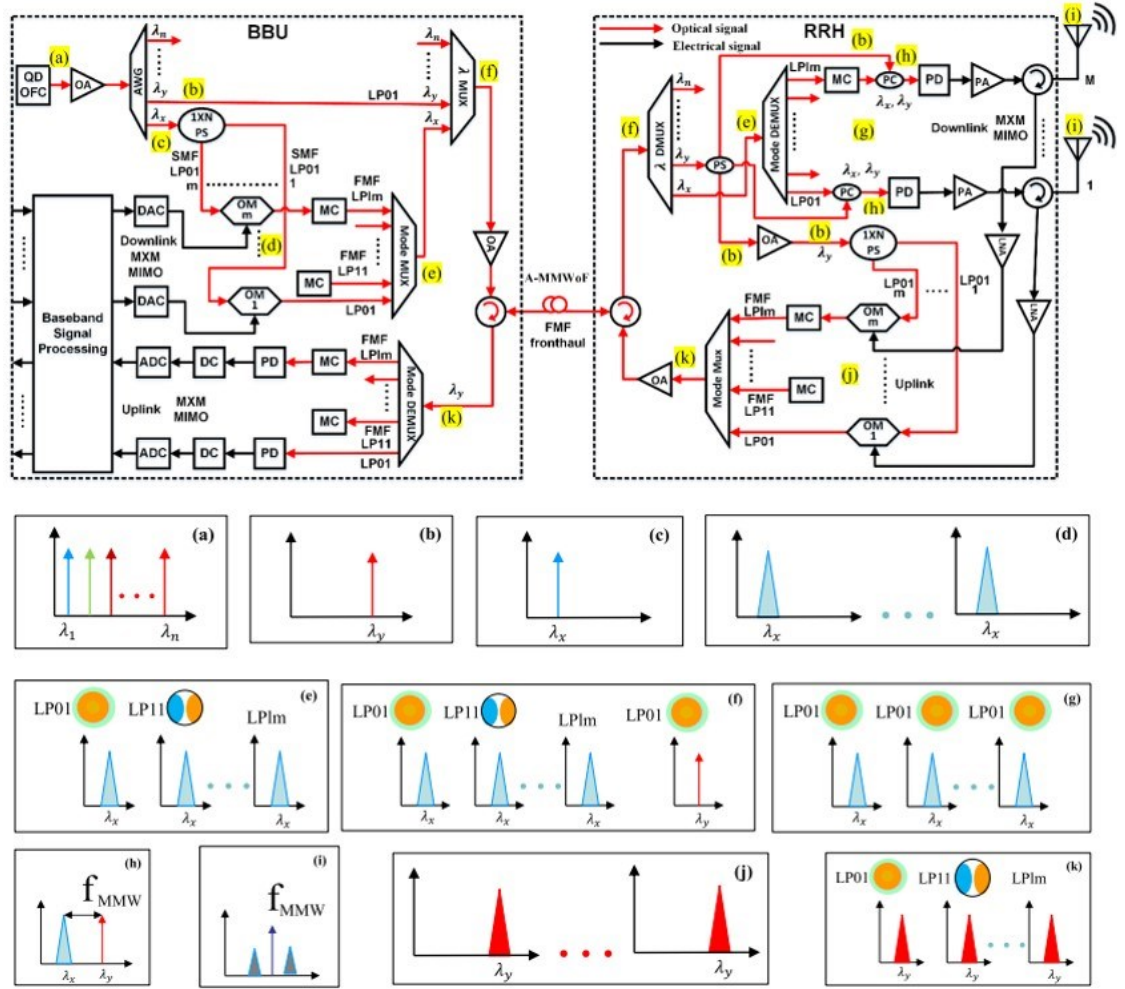
Figure 6.2: Design of symmetric bidirectional MIMO enabled all-optical A-MMWoF fronthaul system using MDM in FMF. Description of (a) - (c) optical spectrum, (d) downlink modulated signals' spectrum, (e) - (g) downlink modulated and unmodulated signals in various modes, (h) beating signals' spectrum, (i) the spectrum of corresponding MMW carrier along, and (j) - (k) uplink modulated signals and their representation in various modes. QD: quantum dot, OFC: optical frequency comb, PS: power splitter, SMF: single mode fiber, FMF: few mode fiber, MUX: multiplexer, DEMUX: de-multiplexer, OM: optical modulator, MC: mode converter, DC: down conversion, DAC: digital to analog converter, PC: power combiner, OA: optical amplifier, PD: photodetector, PA: RF power amplifier, LNA: low noise amplifier, LPlm: linearly polarized modes.

source as shown in Fig. 6.2 (a) – 6.2 (c), respectively. λ_x is intended for carrying downstream data transmission channels while λ_y is set to be used for upstream signals' modulation and heterodyne MMW signal generation at the remote unit. The light of λ_x with fundamental mode LP_{01} is split into *m* paths by a *1-to-m* splitter, which are modulated by potential 5G modulated RF signals using external optical modulators, as depicted in Fig. 6.2. The description of the corresponding modulated signals is shown in Fig. 6.2 (d). The design is transparent to the modulation formats and supports all of the 5G candidate waveforms

149

including simultaneous transmission of different multiple RF signals. In addition, optical beamforming can also be easily employed in the proposed system design, which will be explained in the coming section of this chapter. The corresponding modulated signals are converted from LP_{01} modes to specific LP_{lm} modes of FMF by mode converter (MC) and combined by low crosstalk mode multiplexer (Mode-MUX) as shown in Fig. 6.2 (e). Consequently, these m modulated signals and a supplementary carrier channel are multiplexed using wavelength multiplexer (λ-MUX) on different spatial modes or on different FMF pairs, amplified and transmitted over FMF from BBU to RRH. The spectra of these signals are depicted in Fig. 6.2 (f). In other words, the supplementary carrier will be either wavelength-multiplexed with one of the modulated signals before the mode multiplexer, on a separate spatial mode, or in a separate FMF, depending on the system configuration. Therefore, this is not to be confused with the multiplexing of a wavelength channel with an already-modes multiplexed channel. The wavelength multiplexer (λ-MUX) in the BBU represents multiplexing before MDM takes place or the addition of the supplementary wavelength on a different FMF in the given exemplary scenario. This point will be clarified in the proposed system's three methods presented in the coming section.

At the RRH/RRU/RAU, the optical carriers carrying supplementary channel and data signals are de-multiplexed using a wavelength de-multiplexer (λ-DEMUX) after mode-demultiplexing in the case of WDM into SDM scenario or received on different FMFs. The corresponding data carrying optical carrier λ_x is sent to a low crosstalk mode de-multiplexer (Mode-DEMUX) followed by MCs to extract the modulated individual data signal as shown in Fig. 6.2 (g). Then each of them is sent to the respective photodetector (PD) for MMW signals generation after combing them with the corresponding supplementary optical carrier as depicted in Fig. 6.2 (h). On the other hand, the supplementary optical carrier λ_y is split into different paths where part of them are used in heterodyne generation of the corresponding MMW signals and the rest is amplified and further split into m paths, which are then fed to the respective optical modulators for upstream signals modulation similar to that of downstream as shown in Fig. 6.2 (j). The corresponding generated M×M MIMO MMW signals are sent to the respective antennas for wireless propagation as shown in Fig.6.2 (i).

Similar to the downlink transmission, the corresponding uplink MMW modulated signals are converted onto higher order LP modes using MCs followed by mode multiplexing, amplification and transmission over FMF to the BBU as described in Fig. 6.2 (k). In the BBU, the uplink signals are mode-DEMUXED and down converted to the desired frequency before sending them to based band processing. Although in this example, the use of only two wavelengths are realized, nonetheless, the spectral efficiency and data rate can be further increased by using the combination of more wavelengths and more spatial modes at the expense of merely few dB of power penalties. However, this is cost-effective compared to using multiple parallel SMF. In addition, in this example, we have realized MDM through LP modes, nevertheless, OAM modes can also be used. Thus, with this simple design concept, a flexible M×M MIMO enabled all optical processing based MMWoF fronthaul can be achieved for 5G and beyond of wireless networks. We believe that the proposed design is capable of achieving high speed, high capacity, low latency, and high flexibility and scalability. The following section presents different implementation methods of the proposed system with optical beamforming and M×M MIMO scenarios.

6.4 Design Framework and Implementation Configurations of the Proposed QD-MWL Based MIMO and Optical Beamforming Enabled Photonic MMWoF Transceiver System using WDM and SDM

The proposed novel methods provide photonic MMW signals generation and distribution along with OBF capability for M-MIMO MMWoF systems of 5G and beyond wireless communication networks using QD-MWL technology together with WDM and SDM. These systems employ multi-wavelength channels of QD-MWL-based CFC for photonic MMW signals generation/down-conversion and remote OBF control and SDM along with WDM for transporting MMW MIMO signals in the optical domain. Thus, these novel MMWoF transport solutions with SDM and WDM technologies and photonic MMW signals generation and distribution in the optical domain can efficiently achieve the high bandwidth, high speed, high centralization, low latency and cost-effectiveness requirements of 5G and beyond wireless communication networks. For instance, these methods can be employed in 5G fixed wireless access (FWA) networks, which aim at providing fiber-like connectivity.
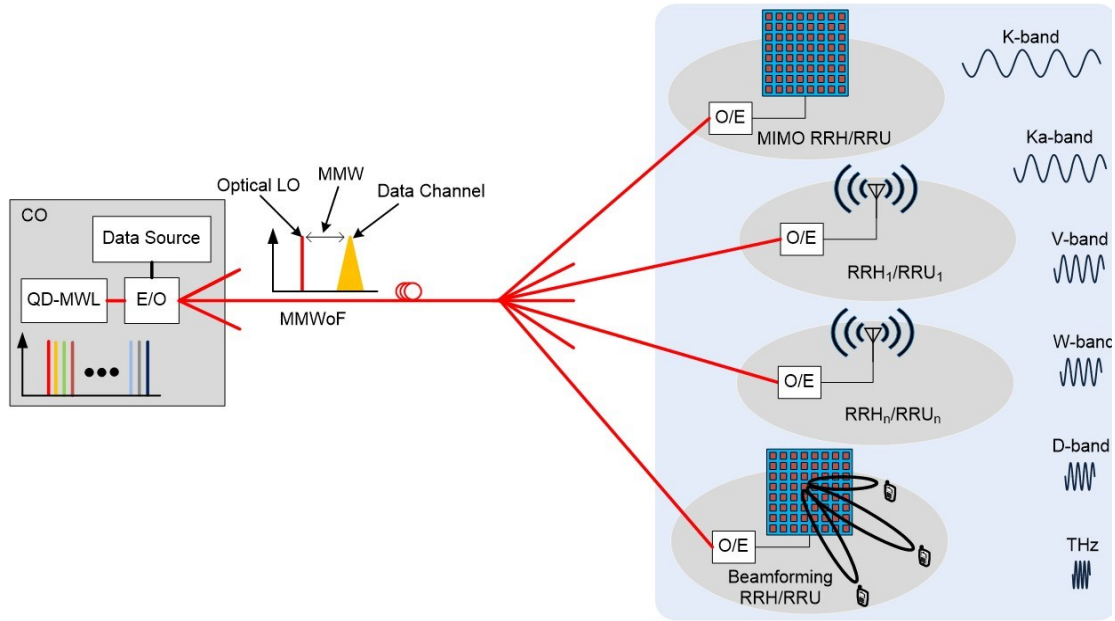
Figure 6.3: Conceptual schematic of the proposed system's architecture.

In these methods, the step of multiplexing comprises at least one of WDM and/or SDM where multiple optical frequency individual or WDM multiplexed signals are transmitted in in different spatial modes of the optical SDM link in both directions. The optical signals are then used to generate RF MMW SISO or M-MIMO, or OBF signals or combination of them at the RRHs/RRUs in various frequency bands with single or multi-beam operation depending on network requirements for wireless transmission to one or more users, as shown in Fig. 6.3. For optical beamforming in the transmission and receiving end, remote optical beamforming control through optical beamforming network (OBFN) is implemented to adjust the relative amplitude and time delays or phase of the transmitted and received signals from the radiating antenna elements of a PAA for the intended shape and direction of the wireless beam.

Figure 6.3 shows a high level overview of an MMWoF wireless system design based on QD-MWL with WDM and SDM. The system comprises a central office (CO) with an electrical to optical conversion system comprising of optical modulators with a single QD-MWL for providing multiple coherent wavelength channels spaced at the desired MMW frequency signals for converting RF wireless data signals from a data source onto the multiple optical signals. The optical signals include data channels and optical local oscillator

(LO) channels spaced at the desired MMW frequency from the data channels. The modulated optical signals and optical LOs may be multiplexed over a long standard single mode fiber (s) (SSFM) or spatial few/multi-mode/core or spatial modes fiber (s) for transmission to remote radio heads/units (RRHs)/(RRUs). The optical signals are separated by a splitter, which may be comprised of one or more multiplexers, wavelength selective switches, routers or photonic devices that can separate and/or combine optical signals at the RRHs/RRUs and are directed over shorter fibers towards the respective RRHs/RRUs, which may be SISO, M-MIMO, beamforming or combinations of RRHs/RRUs depending on network deployment and requirements. The corresponding optical signals are then used to generate MMW SISO or M-MIMO, or OBF signals or combination of them depending on network requirements at RRHs/RRUs for transmission to one or more user equipment (UE). The RRH/RRU is comprised of an optical to electrical converter which may include optical amplifier (s) and photodetector (s) (PD) for converting the multiplexed optical signals to multiple RF frequency bands in the higher microwave and MMW spectrum, such as K-band, Ka-band, V-band, W-band, D-band, and even up to THz by selecting appropriate optical channels. This includes the standard 3GPP 5G NRs FR2 spectrum of 24.25 GHz to 71 GHz. The RRH/RRU may also include individual or PAAs along with electrical amplifiers for achieving SISO or M-MIMO and beamforming signals. In addition, the RRH/RRU include optical modulators for uplink electrical to optical conversion. Accordingly, the QD-MWL is used as a common optical source for different RRHs/RRUs in different cells or M-MIMO RRHs configuration with beamforming capability to provide optical LO and data channels through SDM and WDM optical transport solutions. Thus, a single QD-MWL will be employed instead of many individual laser sources in the CO and RRHs/RRUs.

6.4.1 WDM-Based System Configuration

Figure 6.4 shows a wavelength-reused bidirectional MIMO and OBF enabled MMWoF wireless system design based on QD-MWL with WDM. Generally, in the CO, multiple coherent optical carriers (depending on the system requirements) of the QD-MWL CFC are selected through a wavelength selective switch (WSS) for downlink data channels and optical LOs to optically generate MMW M×M MIMO signals remotely over WDM in a

standard SMF. As discussed earlier, two wavelengths λ_x and λ_y, with the required MMW frequency difference are selected from the optical carriers of the QD-MWL source.

Figure 6.4: Schematic of the proposed high capacity WDM-based photonic MMWoF tranceiver system using QD-MWL.OA: optical amplifier, OC: optical coupler, Mux/Demux: multiplexer/demultiplexer, WSS: wavelength selective switch, DAC/ADC: digital to analog and anolog to digital converter, OBFN: optical beamforming network, PDC: photonic down-conversion module,OM: optical modulator, PD: photodetector, PA: power amplifier, LNA: low noise amplifier, PAA: phased array antenna.

In one example, λ_x is employed for carrying downstream data transmission channels while λ_y is employed for upstream signal modulation and heterodyne MMW signal generation at the RRH/RRU. For transmission beamforming in the RRH/RRU, these channels are passed through the OBFN, as shown in Fig. 6.4(a), before beating them on PDs to generate the corresponding MMW signals and feeding them to the respective radiating elements of a PAA. The OBFN comprises of variable optical attenuators and optical true time delay lines (OTTDLs) for controlling the relative amplitudes and relative time delays of the signals that excite the antenna elements in accordance with the intended beam shape and beam direction, as shown in Fig. 6.4(a). Thus the OBFN adjusts the amplitude and time delay or phase of the signal in order to steer the beam in the desired direction. In the uplink, the optical LOs are single sideband modulated with or without carrier suppression by the upstream MMW signals depending on the implementation scenario. These signals are then down-converted to intermediate/baseband signals at the CO by using the same QD-MWL. The system design of Fig. 6.4 can be used to realize SISO and/or M-MIMO without or with OBF configuration in various frequency bands with single or multi-beam operation with few or large numbers of RRHs/RRUs depending on the network requirements.

More specifically, Fig. 6.4 shows an exemplary implementation of a bidirectional system for a potential 5G network. For example, in the CO, a single QD-MWL source generates an optical signal comprising multiple wavelengths amplified by an optical amplifier (OA). The amplified signal is received by an optical coupler or optical splitter (OC/OS), which splits the signal into two parts, with one part destined for a downlink WSS and another part of the signal sent to an uplink WSS. The WSS is used to select individual channels. For example, two channels, λ_1 and λ_2 can be selected based on the desired MMW frequency at the RRU)/(RRH. For instance, if the desire is to generate a 60 GHz frequency signal, then λ_1 and λ_2 are selected for this frequency spacing. λ_1 can be selected as a data channel and modulated with an RF data signal, e.g., a 5G signal from the BBU by an optical modulator (OM), whereas λ_2 is selected as an optical LO signal. In this particular example, the same process is repeated for λ_n and λ_{n-1}, in which λ_{n-1} is selected as a modulated data channel and λ_n as an optical LO signal. Figure 6.4 (i) shows the optical spectra at different points in the transmission link. This spectrum is for one example implementation scenario.

The selection of the optical channels is flexible, which are dynamically selected based on the system requirement. Fewer optical LO modes may be selected for up-converting multiple channels at the RRU/RRH. In some scenarios, for instance, OBF or MIMO, a single optical modulator can be used to modulate all of the required optical channels from λ_1 to λ_{n-1} by a single RF data signal. λ_1, λ_2, λ_n, and λ_{n-1} are then multiplexed with other channels by a flexible grid wavelength multiplexer and downlink transmitted via a standard SMF between an optical circulator (OCr) of the CO and an OCr at the RRH/RRU. The standard SMF can be 5 - 25km in length.

At the RRH/RRU, the received signal is amplified by an OA and received at an OC/OS, which splits the signal into two parts, with one part of the signal destined for a flexible grid wavelength demultiplexer and another part of the signal sent to an uplink WSS. The demultiplexer separates the channels λ_1, λ_2, λ_{n-1}, λ_n, and then the two channels λ_1, λ_2, which were selected in the CO with the 60GHz spacing, are fed into the OBFN in the case of OBF operation scenario where the amplitude and time delay or phase of the signals are adjusted in accordance with the intended direction of the beam steering. Then the two channels λ_1, λ_2 are mixed on an array of PDs. Next, the MMW signal generated after the PDs is amplified by an array of power amplifiers (PAs) before it is received by the individual antenna (s) or PAA via front-end circulator for SISO or M×M MIMO operation with beamforming. The corresponding downlink MMW signals are transmitted over the air interface for wireless propagation. On the other hand, a percentage of the optical LO signal is reused to modulate the uplink transmission channels. In the case of OBF, the MMW signal beam from an N×M PAA is directed to a specific user or location. The exact process is repeated for λ_n and λ_{n-1} channels.

For the uplink, RF MMW signals from the PAA or individual antennas with SISO or M×M MIMO configuration or beamforming signals from each antenna element are amplified by an array of low-noise amplifiers (LNAs). The reused optical LOs are directed to an uplink WSS to extract the desired channel from λ_2 to λ_n, for uplink transmission. In one example, λ_2 is selected as an optical carrier for uplink and modulated with an RF MMW data signal from the LNAs using, for example single sideband (SSB) or carrier-suppressed single-sideband modulation (CS-SSB) by employing an OM. The channels λ_2 to λ_n are then

multiplexed together by a multiplexer and uplink transmitted via the standard SMF between OCr at the RRH/RRU and the OCr of the CO.

At the CO, the received signals are sent to a demultiplexer which separates the channels and sends them to a photonic down-conversion (PDC) module, where these optical signals are mixed with the signals from WSS obtained from the same QD-MWL source to generate a lower frequency band signal (s), which is ultimately received by ADC. The digital signal is subsequently sent to the digital signal processing (DSP) module of the BBU for baseband signal processing. The PDC module can have different configurations depending on the system implementation and network scenario. In one example with a simple SISO or MIMO implementation with a large number of RRHs/RRUs, the PDC can include an array of PD along with other components such as OCs etc., to down-convert the received SISO or MIMO signals, as shown in Fig. 6.4(b). In another example with OBF scenario where the received optical signals from the PAA elements in the RRH/RRU are passed through a received OBFN for time delay or phase and amplitude adjustments, as shown in Fig. 6.4(c), such that the converted electrical signals are at low frequency and can be added up to construct the final receiving beam in the direction the receiving wireless signals. This signal processing operation can be performed either in analog form or in digital form by sending the corresponding electrical signals to the BBU. On the other hand, if the converted electrical wireless signals after the OBFN operation are still in the MMW frequency band, for instance, if the uplink wireless signals are SSB modulated at the RRH/RRU and then detected at the CO after adjusting the time delay or phase and amplitude through OBFN, then the received wireless beam is down-converted to an IF or baseband before sending it to the BBU for DSP, as shown in Fig. 6.4 (d). This down-conversion at the CO can either be realized optically using the multiple channels of the same QD-MWL or electrically by using an RF local oscillator.

6.4.1.1 System Simulation

As a proof-of-concept, the proposed WDM-based system is simulated in a simple configuration with 4×4 MIMO bidirectional MMW carrier streams without data using OptiSystem design simulation software. A single optical source with equally spaced optical channels is used to remotely synthesize four MMW carriers in the downlink without modulated data and transmit and down-convert the uplink unmodulated MMW 4×4 MIMO signals in the Ka-band (28 GHz) to a 900 MHz IF signals based on the system design in Fig. 6.4. The K and Ka bands have emerged the most important 5G spectrum bands for potential initial deployments. The 5G NR FR2-1 band n257 with 3-GHz bandwidth (26.5 to 29.5 GHz) in the Ka-band is particularly important. Therefore, in our proof-of-concept system's simulation, we consider the 28 GHz spectrum as an example. In the simulation, a PML QD-MWL-based CFC with a channel spacing of 28.9 GHz, as shown in Fig. 6.5, is imitated through an array of CW laser sources with equally spaced emission of eight frequencies in the C-band. In the CO, 50% of the eight optical channels, including four optical data channels (without data) and four optical LOs, as shown in Fig. 6.6, are selected for the generation and transmission of downlink 4×4 MIMO MMW wireless streams. Four optical channels of the remaining 50% of the spectrum are used for photonic down-conversion of the uplink received MMW signals in the PDC module at the CO. The optical LOs are used for the photonic generation of 4×4 MIMO MMW carriers in the downlink
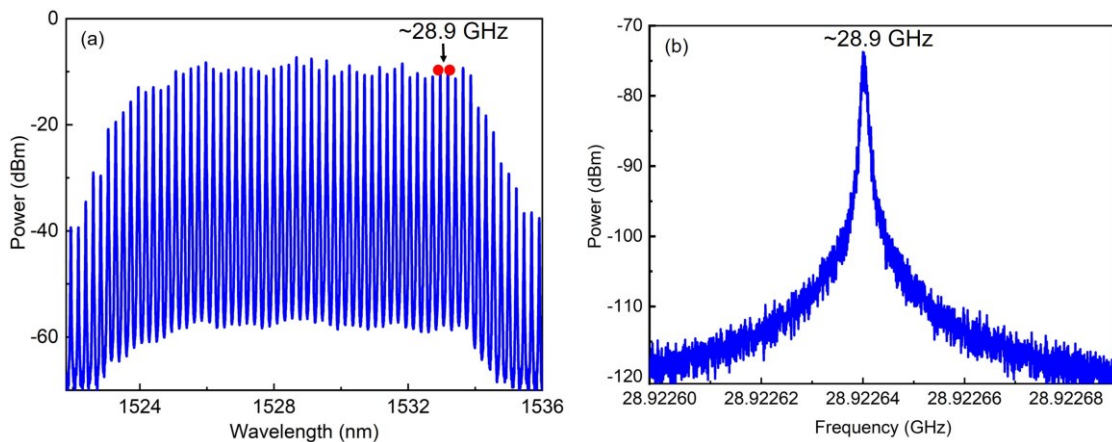
Figure 6.5: Experimentally measured optical spectrum of (a) a 28.9 GHz BH PML QD-MWL and (b) its RF beating frequency spectrum between any two adjacent channels.
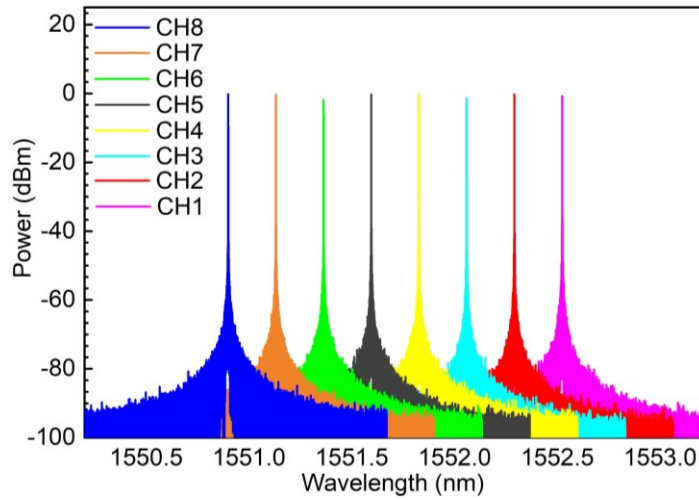
Figure 6.6: Optical spectrum of the selected equally spaced eight channels at 28.9 GHz from the optical source imitating QD-MWL-based CFC for realizing bidirectional 4×4 MIMO streams. CH: channel

and uplink transmission of the received MMW signals at the RRU/RRH. The eight optical channels are multiplexed and transmitted over a 20 km SMF to the RRU. Figure 6.7 (a) and Fig 6.7 (b) show the optical spectrum of the multiplexed signal at the CO and the RRU after amplification, respectively. After demultiplexing, Fig. 6.8 (a)-(d) shows spectra of the optical data and LO channels at the RRU for the downlink 4×4 MIMO streams. On the other hand, Fig. 6.8 (e)-(h) shows spectra of the corresponding four generated MMW carriers at 28.9 GHz. Moreover, Fig. 6.9 shows spectrum of the four extracted optical LOs for reuse in the uplink transmission.
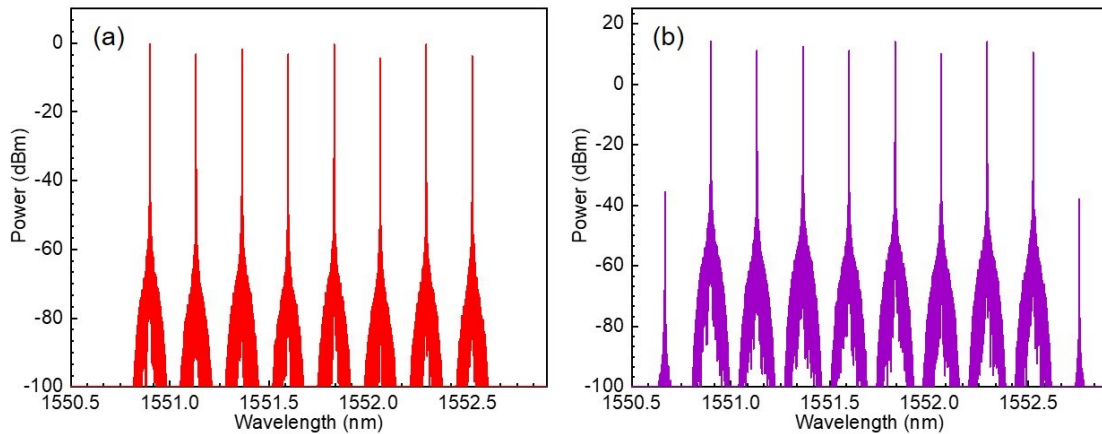
Figure 6.7: Optical spectra of (a) the eight multiplexed channels at the CO and (b) at the RRU/RRH after transmission through 20 km of SMF and amplification.
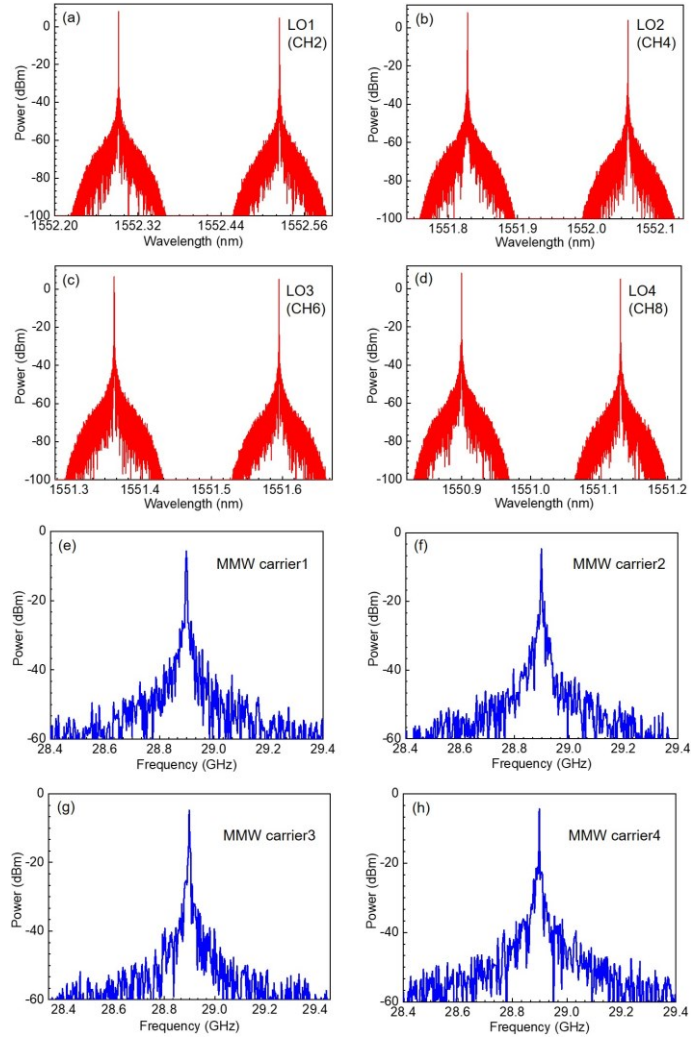
Figure 6.9: Optical spectra of data and LO channels for downlink MMW 4×4 MIMO streams: (a) stream 1, (b) stream 2, (c) stream 3, and (d) stream 4. Electrical spectra of the four generated MMW carriers at 28.9 GHz: (e) MMW carrier 1, (f) MMW carrier 2, (g) MMW carrier 3, and (h) MMW carrier 4.
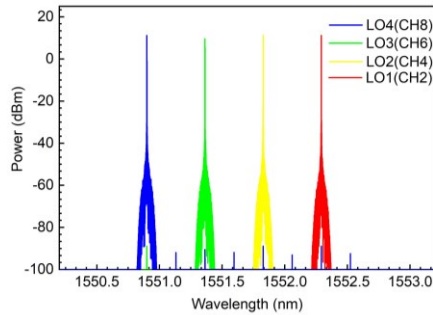
Figure 6.8: Optical spectrum of the four reused optical LOs extracted from the downlink optical signal at the RRU for uplink transmission.

In the RRU/RRH, four 28 GHz MMW uplink signals are generated without any

modulated data, as shown in Fig. 6.10 (a)-(d). Using the retrieved four optical LOs, the

four MMW carrier signals drive four dual-drive MZMs to achieve carrier-suppressed
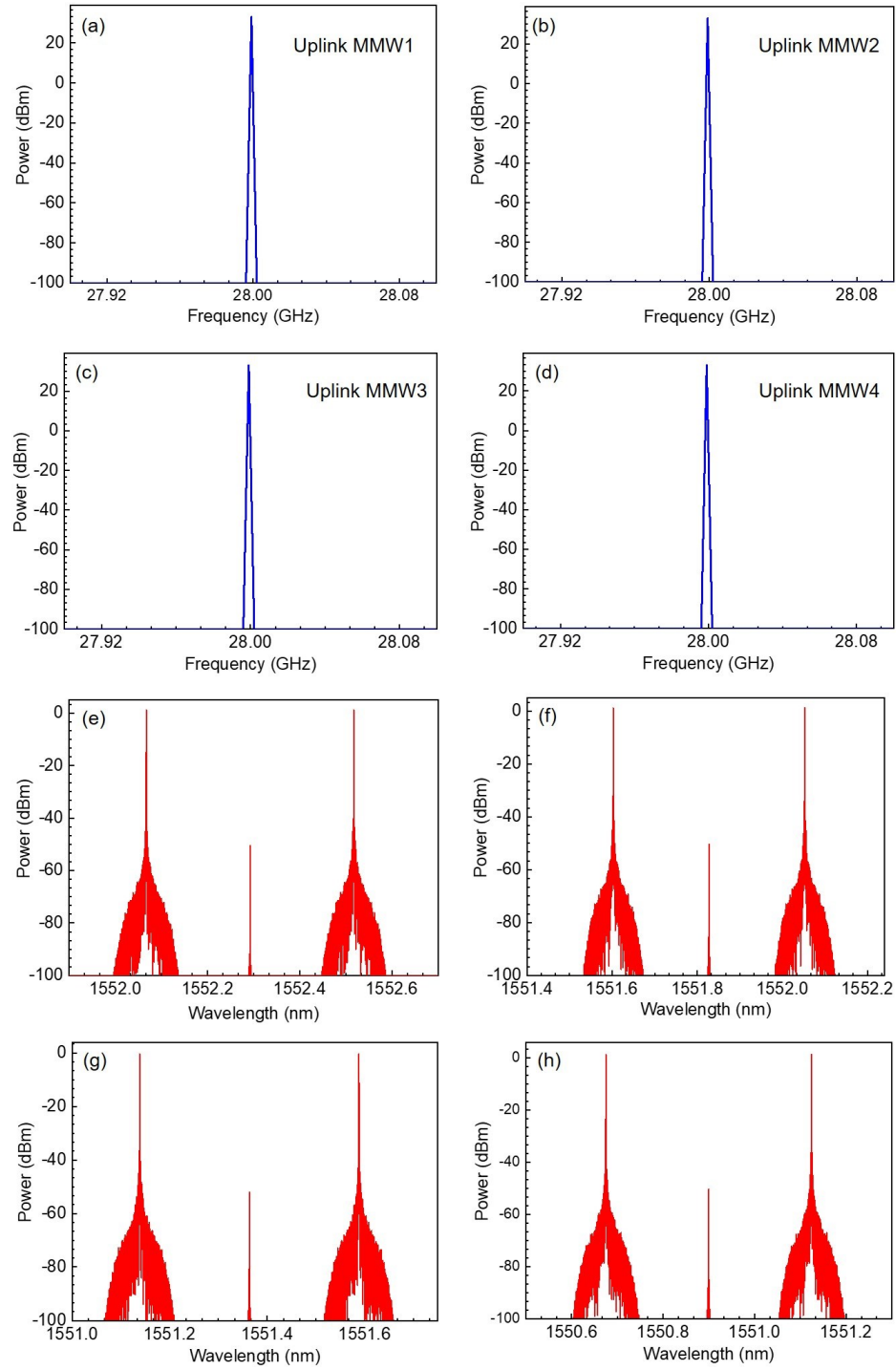
Figure 6.10: (a)-(d) MMW spectra of the received 28 GHz 4×4 MIMO MMW uplink signals and (e)-(h) optical spectra of their modulation in CS-DSB configuration using the four optical LOs at the RRU/RRH.
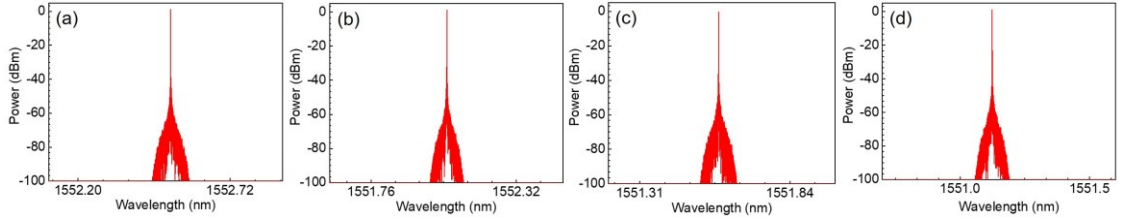
Figure 6.11: (a)-(d) Four CS-SSB modulated channels at the RRU/RRH.

double sideband optical modulation (CS-DSB), as shown in Fig. 6.10 (e)-(h). These four optical CS-DSB modulated channels are then passed through four OBPFs to realize CS-SSB optical modulated channels. The spectra of CS-SSB modulated channels are shown in Fig. 6.11 (a)-(d). The resultant four uplink CS-SSB modulated optical channels are multiplexed and transmitted over a separate 20 km SMF to the CO. Figures 6.12 (a) and 6.12 (b) show the transmitted and received four MUXED optical channels, respectively. In the CO, the received optical channels are de-multiplexed. To realize photonic down-conversion in the PDC module of our proposed system shown in Fig. 6.4, 50% of four optical channels from the same optical source spacing at 28.9 GHz are combined with the received four CS-SSB channels, which are used as optical LOs, imitating the QD-MWL's LO channels. Figure 6.13 (a)-(d) shows the optical spectra of the corresponding CS-SSB signals combined with optical LOs. Each optical channel having MMW CS-SSB modulated signal and optical LO is mixed in individual PDs to down-convert the corresponding 28 GHz 4×4 MIMO signals to 900 IF signals. The electrical spectra of the
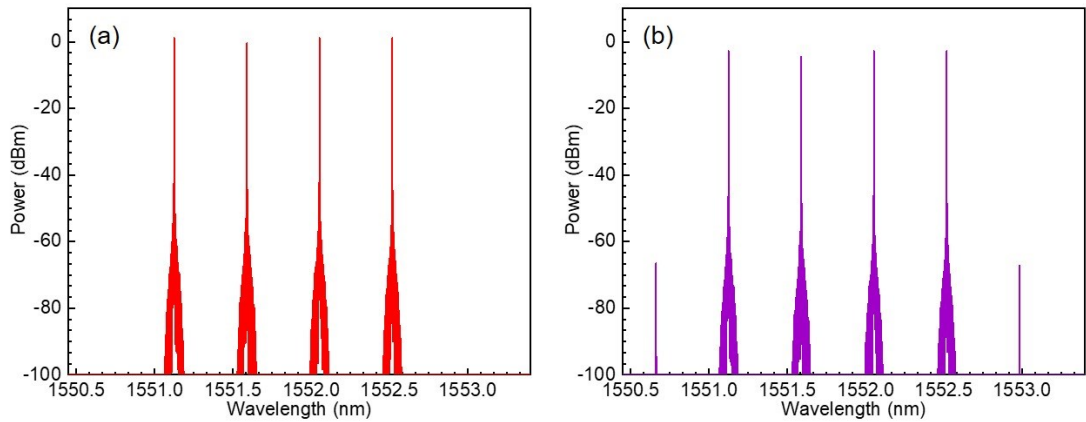
Figure 6.12: Optical spectra of the four multiplexed channels (each carrying uplink CS-SSB modulated MMW signal) (a) at the RRU/RRH and (b) at the CO after transmission through 20 km SMF.

162

corresponding down-converted IF signals at 900 MHz are shown in Fig. 6.13 (e)-(h). In this way, all four 28 GHz uplink signals are photonically down-converted to the desired IF signals of 900 MHz. Thus, it is shown through the 4×4 MIMO example that M×M MIMO MMW carrier signals can be efficiently synthesized remotely and down-converted to IF/baseband signals using only a single optical source without any electrical RF LO, and QD-MWL makes the system much simpler.
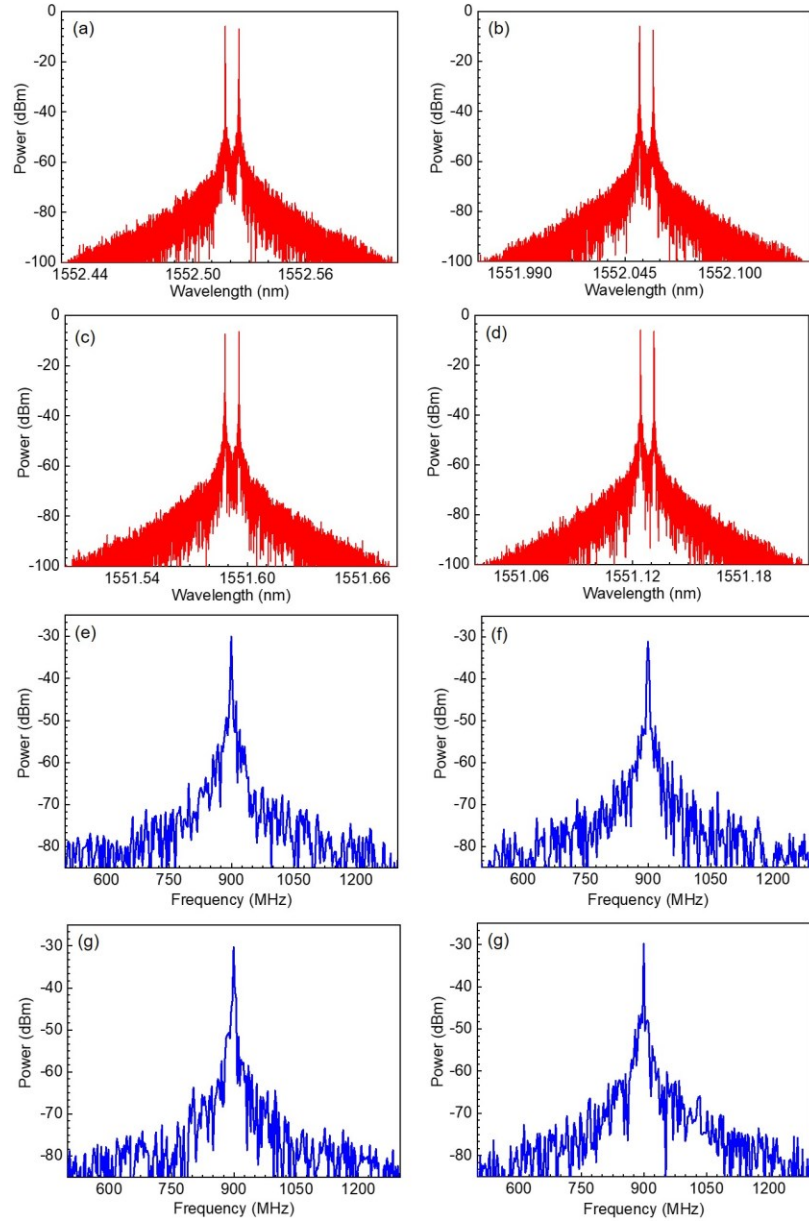
Figure 6.13: Optical spectra of (a)-(d) four received CS-SSB modulated channels combined with the four optical LO at the CO. (e)-(h) RF spectra of the down-converted IF at 900 MHz for the corresponding four uplink received signals at the CO.

6.4.2 SDM-Based System Configuration

Figure 6.14 shows an SDM-based bidirectional system design for photonic MMW signals generation, OBF and MIMO configuration. The system design is similar to the system shown in Fig. 6.4. However, this system design is based on SDM by employing MDM.
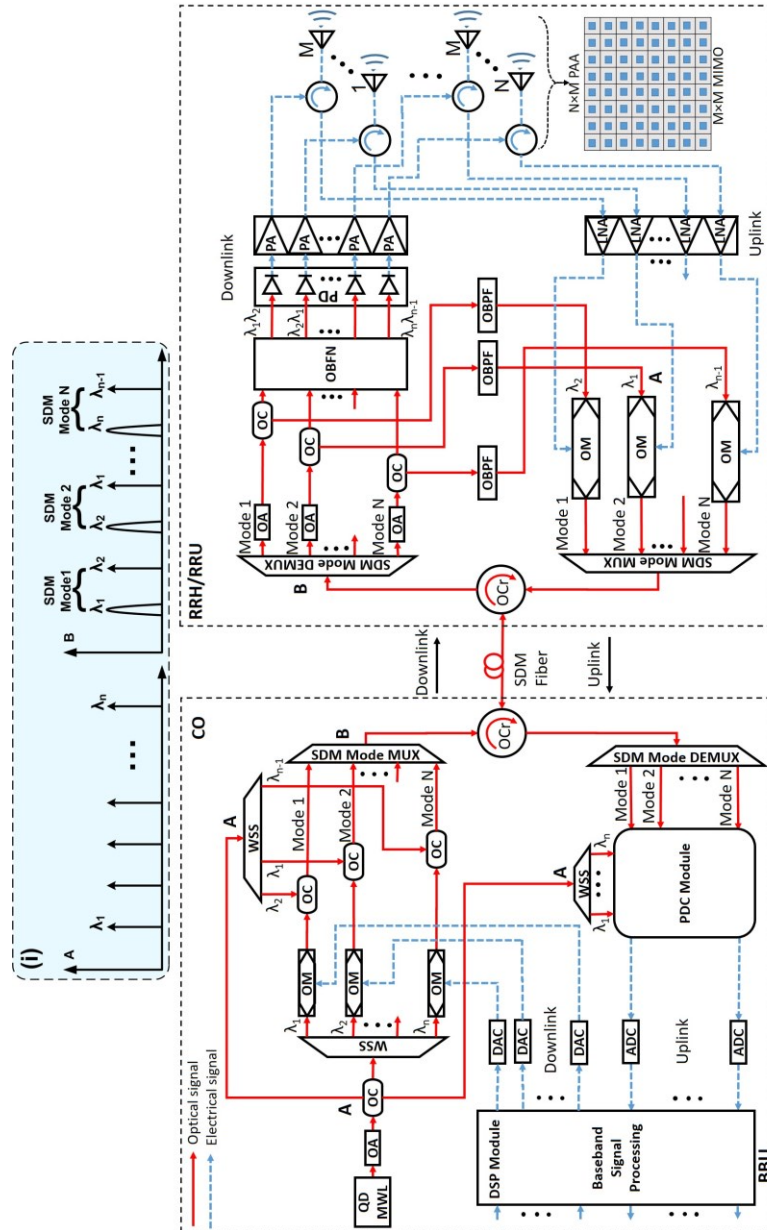
Figure 6.14: Schematic of the proposed high capacity SDM-based photonic MMWoF transceiver system using QD-MWL. OA: optical amplifier, OC: optical coupler, Mux/Demux: multiplexer/demultiplexer, WSS: wavelength selective switch, DAC/ADC: digital to analog and anolog to digital converter, OBFN: optical beamforming network, PDC: photonic down-conversion module, OM: optical modulator, PD: photodetector, PA: power amplifier, LNA: low noise amplifier, PAA: phased array antenna.

Because in this implementation, all the optical channels of QD-MWL can be employed simultaneously both for data channels and optical LO, thereby substantially increasing the spectrum efficiency and capacity. In this system's architectural design, the CO is communicatively coupled to RRH/RRU over an SDM fiber.

The principal operation of this system is such that in the CO, the QD-MWL provides multiple coherent optical channels, which are amplified by an OA, and split by OC/SP. These different splits are sent to two WSSs in the downlink path and one in the uplink path, as shown in Fig. 6.14. One of the two WSSs in the downlink path provides multiple channels of differing wavelengths from which individual channels λ_1, λ_2 …λ_n can be selected. For example, two channels can be selected based on the desired MMW frequency at RRU/RRH. For instance, multiple channels, i.e., λ_1 to λ_n, are chosen as a data channel and are modulated with an RF data signal, e.g., a 5G signals, from the BBU by OMs. In the case of MIMO with beamforming, a single OM can be used to modulate multiple optical channels with the RF data signal. Correspondingly, a second WSS provides multiple optical LO channels of differing wavelengths from which individual channels λ_1, λ_2 …λ_{n-1} can be selected. The different optical data channels and optical LO at the desired MMW frequencies are combined by OCs, i.e., $\lambda_1\lambda_2$, $\lambda_2\lambda_1$….λ_n λ_{n-1}. Figure 6.14 (i) shows the corresponding spectra of this example at different locations. As mentioned earlier, a variety combination of optical LO and data channels can be adopted based on the system requirements and implementation scenario. The combined signals from the OCs are then mode multiplexed by an SDM-MDM multiplexer over different spatial modes. The multiplexed channels are downlink transmitted via SDM fiber between an OCr of the CO and an OCr at the RRH/RRU.

In the RRU/RRH, the spatially multiplexed channels are received by SDM demultiplexer, which separates the channels, and the separated channels are amplified by an OA before splitting into downlink and uplink channels. In certain cases, to decouple the spatial modes, MIMO DSP may be required, which can be implemented in the form of application specific integrated circuit (ASIC). Next, a downlink portion of the split signal from OCs is received by OBFN in the case of an OBF scenario to adjust the time delay or phase and amplitude of the signals for the intended beam direction, and then the

corresponding pair of channels, i.e., $\lambda_1\lambda_2$, $\lambda_2\lambda_1$...$\lambda_n\lambda_{n-1}$, are mixed on an array of PDs to generate the MMW signals for wireless propagation. The MMW signals generated after the PDs are amplified by an array of PAs before being received by the respective radiating elements of the PAA or individual antennas for M×M MIMO or SISO operation depending on the implementation scenario and mode of operation. The uplink portion of the split signal from OCs is received by optical bandpass filters (OBPFs), and the downlink LOs' output, i.e., λ_2, λ_1,... λ_{n-1}, are extracted and received by uplink OMs. These optical carriers are modulated by the uplink MMW signals in SSB or CS-SSB modulation configuration and the corresponding optical signals at different wavelengths are then spatially multiplexed on different spatial modes by an SDM multiplexer, as shown in Fig. 6.14.

For the uplink, RF MMW signals from the PPA elements of M×M MIMO system are sent to an array of LNAs for amplification. At the OMs, λ_2, λ_1 and λ_{n-1} are selected as uplink optical carriers, respectively, for uplink transmission of the MMW wireless signals received from PAA elements in the case of MIMO with beamforming. The selected optical channels are then SSB or CS-SSB modulated with the corresponding RF MMW data signal from the LNAs. The modulated channels are then multiplexed on different combinations of sub-sets of spatial modes by an SDM multiplexer and uplink transmitted via the SDM fiber to the CO.

At the CO, the received signals at the OCr are sent to an SDM demultiplexer which separates the channels. MIMO DSP may be required to separate the corresponding spatial channels. These channels are then combined with the outputs selected from the uplink WSS in the PDC module. The PDC module mixes the signals from the SDM demultiplexer and WSS, depending on the implementation scenario, to generate lower frequency band signals which are received by ADCs. The corresponding digital signals are sent to the DSP module for signal processing. The PDC module can have different configurations depending on the system implementation and network scenario as discussed earlier with reference to the system design in Fig.6.4. Thus, this design brings more flexibility and scalability in the transport network, which can be used to realize SISO and/or M-MIMO without or with OBF configuration in various frequency bands with single or multi-beam operation with few or large numbers of multiple RRHs/RRUs depending on the network requirements.

6.4.3 WDM-SDM-Based System Configuration

In another implementation, as shown in Fig. 6.15, a comprehensive system design of the proposed wavelength-reused bidirectional photonic MMW signals generation and
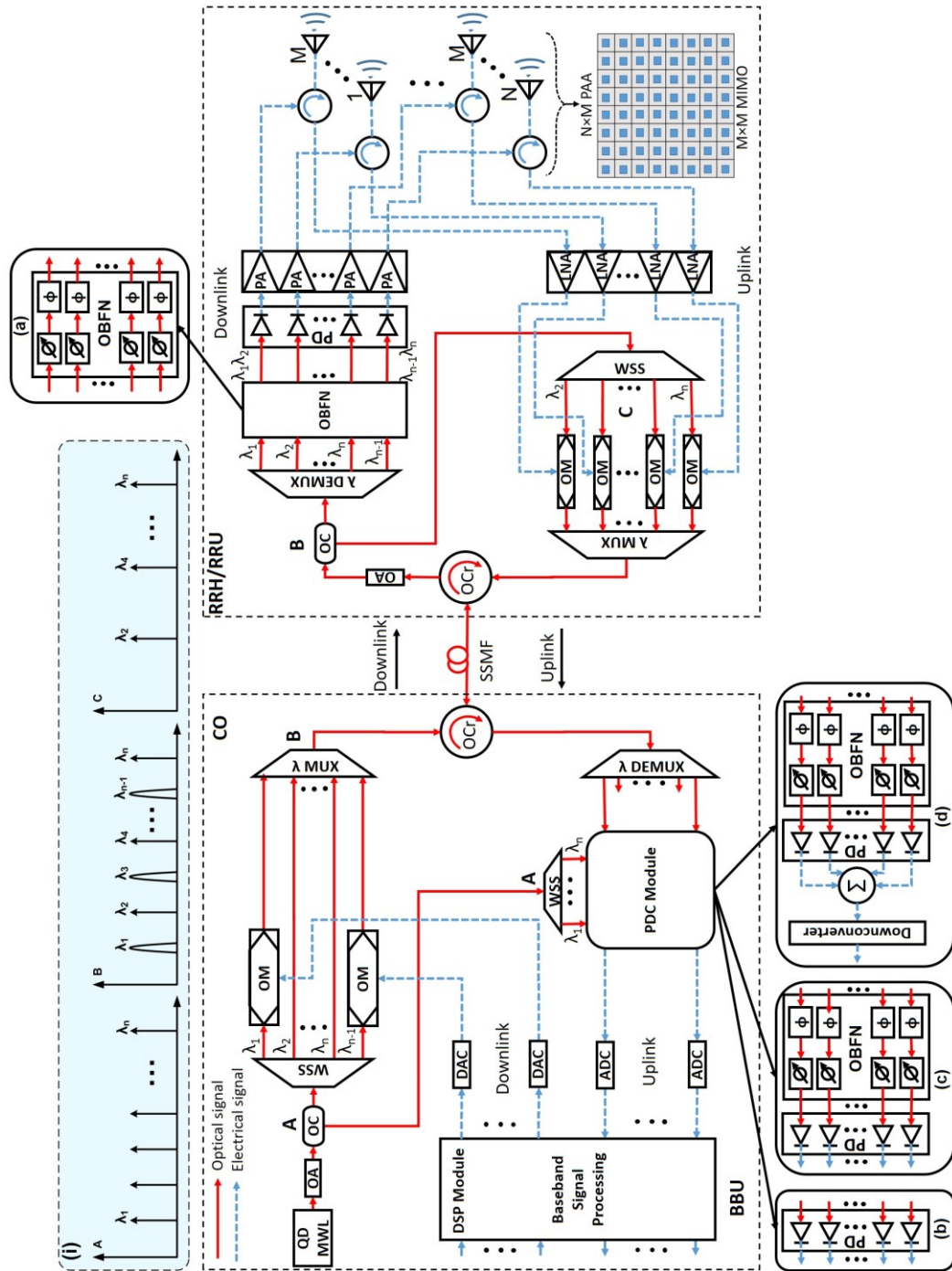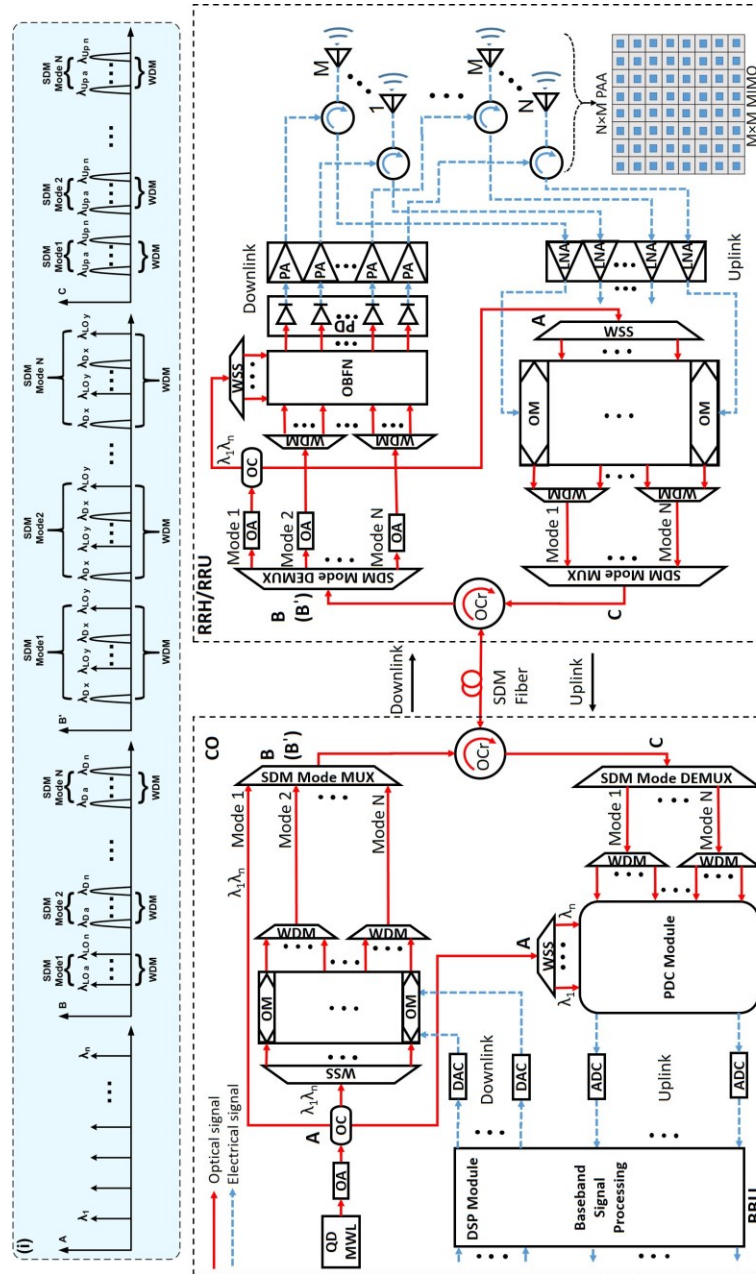

Figure 6.15: Schematic of the proposed QD-MWL-based high capacity WDM-SDM-based photonic MMWoF tranceiver system. OA: optical amplifier, OC: optical coupler, Mux/Demux: multiplexer/demultiplexer, WSS: wavelength selective switch, DAC/ADC: digital to analog/anolog to digital converter, OBFN: optical beamforming network, PDC: photonic down-conversion module, OM: optical modulator, PD: photodetector, PA: power amplifier, LNA: low noise amplifier, PAA: phased array antenna.

distribution with OBF and MIMO capabilities. The QD-MWL spectrum is simultaneously used as a data channel and optical LOs for M×M MIMO configuration or SISO scenarios with up-conversion at the RRH/RRU and down-conversion at the CO. This is achieved through WDM of a multiple optical channels into different spatial modes of SDM (WDM-SDM) through MDM where one sub-set of different spatial modes is used to transport the QD-MWL based WDM multiplexed data channels and a combination of another spatial mode (s) is used to transport the corresponding multiplexed (wavelength MUX) optical LOs in both directions. The data and optical LO signals can also be transported together in various WDM multiplexed channels on different spatial modes of the SDM link in both directions, as shown in Fig. 6.15 (i). However, to alleviate interaction and crosstalk between the optical signals in the link, different combination of wavelengths (frequencies) and spatial modes are selected in both directions. This process can be nested into further modes by using the same CFC laser source or a different QD-MWL CFC source depending on the network requirements. Accordingly, this makes the design tremendously flexible and scalable. Depending on system requirements, multiple optical carriers can be used for both downlink and uplink transmission with different combinations of optical frequencies and spatial modes. The principal implementation of this system and OBF of MIMO N×M-PPAs in this method are similar to those in the systems shown in Fig. 6.4 and Fig. 6.14. In this system design, various combination of optical signals from QD-MWL can be multiplexed to transport RF MMW wireless data signals in different combination of spatial modes in both directions for SISO, M-MIMO and OBF links depending on the network scenario and system requirements, as depicted in Fig. 6.15 (i).

6.5   Challenges and Potential Solutions

The key challenges in designing fronthaul architecture for the next generation of wireless networks are to avoid the capacity bottleneck and to achieve low latency and high centralization. A-RoF technology is introduced as an enabler to overcome the capacity limitations and to simplify the fronthaul design by achieving C-RAN as highlighted in the literature review. Moreover, the A-RoF fronthaul will become more scalable and flexible when tailored with SDM technology, which can be achieved by leveraging MDM in FMF, MCF, RCF or the combination of them. This increases the capacity and reduces the latency,

168

cost and complexity. SDM and WDM technologies are employed in the proposed systems in order to achieve a high-capacity gain in the fronthaul links. SDM can be realized through MDM using LP modes by separating multiple optical channels in a single FMF as an alternative to multiple standard SMFs. It can also be employed through OAM modes using specialized fibers, such as RCF. Furthermore, SDM through MCF and FM-MCF can also be considered depending on the requirements. The MMW signals generation/distribution and down-conversion is realized through remote optical heterodyne of QD MWL at the RRHs/RRUs and CO, respectively. Consequently, the corresponding MMW M×M MIMO signals are generated and distributed in the optical domain using SDM and WDM. In addition, OBF can be performed on all channels by incorporating remote OBFN of TTDLs with N×M PAAs. Nevertheless, SDM links are prone to inter-modal crosstalk due to the interaction and power leakage between the different spatial modes, especially when multiple optical signals are multiplexed onto a single SDM link, which may reduce the transmission performance. In addition, inter-modal dispersion due to differential mode delay and other mode dependent losses due fiber bending etc., which limit the spurious-free dynamic range of the links. Consequently, this limits the transmission distance as well as the full special multiplexing capability. These impairments can be overcome by designing optimized components and specialized optical fibers, and using DSP algorithms, dispersion compensation component, and optimized combinations of modes in MDM. Different combinations of optical signals and different sub-sets of spatial modes in both uplink and downlink directions can alleviate the crosstalk. For example, one sub-set of spatial modes can be used for transporting the RF MMW signals in the downlink direction and a different second sub-set of spatial modes for transporting the signals in the uplink direction. Similarly, various combinations of optical signals at different wavelengths (frequencies) can be employed in the uplink and downlink directions. Besides, the crosstalk may be reduced using multiple SDM or WDM links on separate fibers where permitted. In addition, MIMO DSP may be required to decouple the spatial modes at the receiving end, which can be achieved through incorporating MIMO DSP ASICs in the system, depending on the implementation and system requirements. Besides, novel optical components, such as mode converters, Mux/DeMux, modes-specific optical amplifiers and specialized fibers,

are required for both LP and OAM modes. Moreover, A-RoF fronthaul is prone to various impairments discussed in Section 2.5.

6.6   Summary

In this chapter, high capacity spectrally efficient MIMO and OBF enabled photonic MMWoF wireless transceiver system design and methods are proposed for 5G and beyond wireless networks based on QD-MWLs with WDM and SDM. Different potential implementation scenarios of the proposed system's design are discussed in detail. As a proof-of-concept, the proposed WDM-based photonic MMW RoF wireless transmission system is also simulated in a simple bidirectional 4×4 MIMO configuration. A single QD MWL source in the CO is comprehended to generate multiple optical data signals and optical LOs for both downlink and uplink transmission. The transmission of enormous optical signals is realized in WDM channels, SDM channels or WDM channels multiplexed on different spatial modes of the SDM in both directions. The optical data and LO signals remotely generate MMW carrier signals in SISO or MIMO, or OBF configuration, or a combination of them at the RRUs in various frequency bands with single or multi-beam operation, depending on requirements, for wireless transmission to the users. For OBF in the transmission and receiving end, remote OBF control through OBFN is realized to adjust the relative amplitude and time delay or phase of the transmitted and received signals to/from the radiating antenna elements of a PAA according to the shape and direction of the wireless beam. Thus, these system designs are flexible and scalable, achieving high spectral efficiency, high capacity, high speed, and low latency photonic MMWoF wireless links. Moreover, the proposed systems are supported by a comprehensive state-of-the-art literature review. In addition, the fundamental challenges of SDM-based A-RoF fronthaul are explored, and the corresponding potential solutions are highlighted.

Chapter 7

Conclusion and Future Work

THIS chapter summarizes and discusses the conclusions of the thesis. It also provides directions for future work.

7.1 Conclusion

The key challenges in designing the next-generation wireless networks are to avoid the capacity bottleneck and to achieve high-speed, low latency and high centralization for efficient resource management. Photonic MMW with A-RoF technology is introduced as an alternative enabler solution. Photonic MMW RoF technology integrates high capacity, reliable and transparent optical networks with the flexible, mobile and pervasive wireless network, which can achieve fiber-like broadband wireless connectivity with high capacity, low latency and high centralization when complemented by MIMO and beamforming technologies. However, photonic MMW RoF technology requires low noise and cost-effective optical sources. To this end, well-designed quantum-confined nanostructures such as semiconductor QD-MWLs offer great potential due to the inherent properties of QD materials. This thises aims to cover both aspects of the mentioned technologies with the focus on the experimental investigation of QD-MWLs, including a single-section semiconductor BH InAs/InP PML QD-MWL-based CFC and a novel BH InAs/InP QD-DW-DFBL for photonic MMW signals generation in the 5G NR bands and multi-Gb/s MMWoF wireless links, specifically for cost-effective and sustainable 5G fronthaul transmission systems and high-speed wireless access networks. Multi-Gb/s photonic-aided MMWoF system designs are proposed and experimentally demonstrate using QD-MWLs with photonic generation, wireless transmission and detection of broadband multi-Gb/s modulated RF MMW wireless signals at 5G NR (FR2) in the K-band, Ka-band and V-band in simplex, duplex and MIMO configurations. These frequency bands in this research work are considered for the sake of prototype implementation of RF MMW A-RoF wireless links. Nonetheless, a single QD-MWL can be used to generate RF signals in multiple higher frequency bands of MMW spectrum and even THz range depending on the optical channels spacing of the device. Thus, the thesis expands upon the state-of-the-art MMW

fiber-wireless integrated technology and QD-MWLs for multi-Gb/s MMW signals generation, transmission and detection, showing their potential for high capacity and high-speed MMW RoF wireless communications networks of 5G and beyond fronthaul, and wireless access networks – hopefully, this brings the technology one step closer to the commercial deployment.

In chapter two, a comprehensive background, a thorough literature review, and fundamental concepts about the work in this thesis are presented. This includes discussion on semiconductor lasers in general and QD-MWLs in particular, key challenges and potential solutions of MMW wireless communications, the notion of photonic MMW signals generation and transmission and classification of the state-of-the-art photonic MMW signals generation techniques, introduction to radio access and fronthaul networks and next generation fronthaul challenges and key solutions, and introduction to RoF and key enabling technologies. Finally, a comprehensive related literature review on the state-of-the-art QD-MWL-based RoF systems is presented.

In chapter three, a highly coherent low-noise and monolithically integrated semiconductor BH PML InAs/InP QD-MWL-based CFC is presented for broadband fiber-wireless integrated RoF-based 5G NR fronthaul systems. The CFC features low threshold current, high output power, and flat broadband spectrum with a 6-dB bandwidth of around 9 nm having ~47 equally spaced highly coherent and low noise optical channels. The device is experimentally characterized. The noise performance of each filtered individual channel of the device exhibit an optical phase noise of less than 466.5 kHz and an integrated average RIN of typically less than -130 dB/Hz over the frequency range from 10MHz to 20GHz. Its RF beat note linewidth between two adjacent channels is measured to be ≤ 3 kHz with a calculated time jitter of ≤ 5.53 fs. Furthermore, using the CFC, a successful demonstration of photonic generation, transmission, and detection of broadband wireless RF signals at around 25 GHz over 0.5m to 2-m free space indoor wireless links through a total of 25.22 km SSMF with a data rate of 16 Gb/s is presented. The demonstrated RoF wireless links achieve EVM and BER well below the standard requirements. The results indicate that the InAs/InP BH QD-MWL-based CFC has the potential to synthesize LO-free radio signals at frequencies of up to 1.15 THz with multi-Gb/s wireless signals delivery

172

featuring low noise and cost-efficient solution for broadband RoF-based fronthaul systems of next generation wireless communication networks.

In chapter four, a novel monolithic semiconductor buried heterostructure InAs/InP QD-DW-DFBL as a compact optical source for MMW. The device uses a common gain medium in a single cavity structure for simultaneous correlated and stable dual-mode lasing from within the same cavity of the device due to the distributed feedback provided by a novel synthesized aperiodic non-uniform diffraction grating. The integrated RIN and optical linewidth for each mode are measured to be typically less than -150 dB/Hz in the frequency range from 10 MHz to 20 GHz and 30 kHz in free-running operation. This subsequently results in a beat signal with a 3dB linewidth typically ≤ 40 kHz. The device can be tuned between 46 and 48 GHz by controlling the drive current and temperature. Nevertheless, the RF beat note of the device can be adjusted from the GHz to the THz range by modifying the design of the synthesized aperiodic grating of the device for the desired spectrum. Moreover, we successfully demonstrate various real-time broadband photonic MMWoF wireless links featuring multi-Gb/s data rates with a maximum data rate of 36 Gb/s having EVM and BER below the standard 7% overhead FEC limit of 3.8 x 10^{-3} using the QD-DW-DFBL in free running condition. We experimentally demonstrate real-time broadband multi-Gb/s electrical RF synthesizer-free MMW signals generation and wireless transmission at the 5G NR frequency band of 47 GHz. One laser mode is encoded using 4-/6-Gbaud M-QAM (16-/32-/64-QAM) baseband data signals; the other lasing mode is used as an optical local oscillator for optical-heterodyne remote up-conversion to an MMW carrier of 47.27 GHz. Consequently, optical baseband modulated data signals with data capacity up to 36 Gb/s are transmitted through back-to-back (BtB) and 25-/50-km of standard single mode fiber (SSMF) before the MMW carrier is optically synthesized remotely for free space wireless data transmission and detection over up to 9-m. The results indicate that the optical heterodyning of two highly correlated and low-noise optical signals is an efficient method for transporting and distributing high-frequency MMW data signals in the optical domain over long distances. After long-reach transmission of these basebands data modulated optical signals, the desired MMW modulated carrier signal can be optically synthesized remotely through photonic up-conversion in the MMW RoF systems for free space wireless data transmission. This significantly simplifies the overall system by

173

preserving any modulated data format on the optical signals and translating it to the corresponding MMW carrier signal. This eliminates expensive front-end components, such as electrical LOs and ADCs/DACs at the RRU.

In chapter five, we propose and experimentally demonstrate Multi-Gb/s photonic MMW MIMO and duplex bidirectional systems based on QD-MWLs. This includes an experimental demonstration of a photonic-assisted MMWoF 2×2 MIMO and bidirectional wireless transmission systems at around 47.3 GHz and 28 GHz employing a single low noise InAs/InP quantum dash dual-wavelength DFB laser (QD-DW-DFBL) and InAs/InP PML QD-MWL-based CFC. The 2×2 MIMO structure is realized through optical polarization multiplexing and remote heterodyning of a single optical source together with the cross-polarization configuration of two pairs of antennas to avoid interference at the receiver, reducing system complexity. The demonstration includes real-time error-free transmission and detection of wideband 2GBaud 16QAM MMW wireless signals at V-band in a 2×2 MIMO configuration over a 2m wireless distance through 10km and 25 km SMF. This results in doubling the system data capacity to 16 Gb/s. The system performance is evaluated by exhibiting EVM and bit BER well below the standard requirements, achieving error-free transmission. By replacing QD-DW-DFBL with the PML QD-MWL-based CFC, more flexible and scalable systems with various M×M configurations can be achieved. Moreover, broadband duplex bidirectional systems are proposed and experimentally demonstrated based on QD-DW-DFBL and PML QD-MWL. 8 Gb/s and 16 Gb/s 16 QAM bidirectional MMWoF wireless links with the downlink at around 47.3 GHz and uplink at 28 GHz are realized over a 2m indoor wireless distance through 10 km SMF by employing a single InAs/InP QD-DW-DFBL source. The successful error-free simultaneous transmission of 2Gbaud and 4Gbaud data is achieved over a single SMF in both directions. Similarly, 4Gb/s 16QAM simultaneous duplex bidirectional MMWoF wireless links with the downlink at around 28.08 GHz and uplink at 28 GHz are realized over a 2m indoor wireless distance through 10 km SMF by employing a single InAs/InP PML QD-MWL CFC source. The error-free operation is achieved at the FEC for both downlink and uplink.

Finally, in chapter six, high capacity spectrally efficient MIMO and OBF enabled photonic MMWoF wireless transceiver system design and methods are proposed for 5G and beyond wireless networks based on QD-MWLs with WDM and SDM. Different potential implementation scenarios of the proposed system's design are discussed in detail, and accordingly, a proof-of-concept system is simulated in a basic 4×4 MIMO configuration. The proposed system designs are flexible and scalable, achieving high spectral efficiency, high capacity, high speed, and low latency photonic MMWoF wireless links.

7.2   Future Work

This thesis covers most of the device and system implementation aspects of the QDM-WL technology for photonic MMW signals generation and transmission. For future work, this study could be extended in the following potential research directions:

- A reconfigurable photonic integrated system for tunable multiband MMW signals generation can be developed using QD-MWL-based CFC. The system can be designed based on a programmable specialized wavelength selective switch, arrayed waveguide gratings and/or tunable filters along with optical couplers and an array of photodetectors depending on the system configuration. The system can be dynamically configured through software control where a pair of optical channels of the QD-MWL will be selected, amplified and outputted as an optical heterodyne signal to a photodetector for desired MMW frequency. The device will allow simultaneous tunning of multiple MMW frequency bands. A flowchart
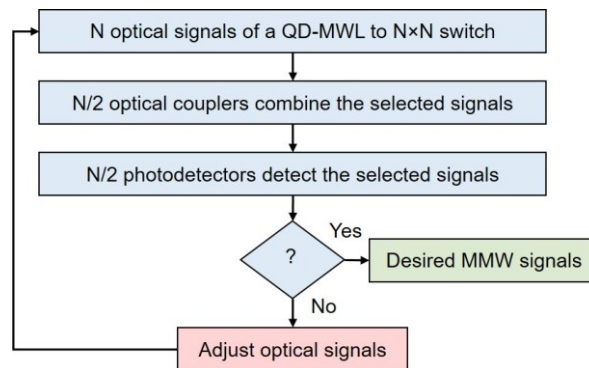
Figure 7.1: Flowchart showing the operating process of a QD-MWL-based MMW system.

in Fig. 7.1 describes an abstract-level process of the device generating MMW frequency tones based on optical signals from a single PML QD-MWL.

- In this work, off-the-shelf components are used to demonstrate our proof-of-concept broadband multi-Gb/s MMWoF system. Nevertheless, these components could be heterogeneously integrated on a single chip. For instance, the integration of QD-MWL with optical modulators, photodetectors, antennas and other passive components can be investigated. For this, different integration platforms can be explored, such as Si, InP etc.

- Optical beamforming with M-MIMO configurations can be experimentally investigated based on QD-MWL-based CFCs. In addition, multicarrier-modulated signals can be explored to further investigate the noise performance of the QD-MWLs.

- The effect of chromatic dispersion on the QD-MWLs' performance, both from within the device cavity and external to the cavity, can be investigated/calculated, and the cavity design can be improved accordingly. Morever, the coherence of the PML QD-MWLs can be studied for different path lengths. Besides, the temperature stability of the presented devices and systems can be investigated, and appropriate control mechanisms can be established. Similarly, optical/electrical injection locking mechanisms can be studied on the presented QD-MWLs, especially the QD-DW-DFB laser.

- The application of SDM technology in fronthaul links is promising, particularly considering the multi-wavelength coherent channels of the QD-MWLs; however, not much research is devoted to it. SDM links are prone to inter-modal crosstalk due to the interaction and power leakage between the different spatial modes, especially when multiple optical signals are multiplexed onto a single SDM link, which may reduce the transmission performance. In addition, inter-modal dispersion due to differential mode delay and other mode-dependent losses due to fiber bending etc., limit the spurious-free dynamic range of the links. Consequently, this limits the transmission distance and the full special multiplexing capability. These impairments can be overcome by designing optimized components and specialized optical fibers and using DSP algorithms, dispersion compensation components, and optimized combinations of modes in MDM. Besides, novel optical components, such as mode converters, Mux/DeMux, modes-specific optical amplifiers and specialized fibers, can be designed for both LP and OAM modes.

176

Bibliography

[1] T. S. Rappaport *et al.*, "Millimeter Wave Mobile Communications for 5G Cellular: It Will Work!," *IEEE Access*, vol. 1, pp. 335–349, 2013, doi: 10.1109/ACCESS.2013.2260813.

[2] P. Jonsson et al., "Ericsson Mobility Report," Ericsson, Stockholm, Sweden, Jun. 2022. [Online]. Available: https://bit.ly/3SJjh7l

[3] C. Amon, "How mission critical connectivity has helped the world adapt to COVID-19–and prepare for the next crisis," *on the agenda of World Economic Forum,* Apr. 2020. https://bit.ly/3W7obhh

[4] "IMT Vision—Framework and overall objectives of the future development of IMT for 2020 and beyond," ITU-R, Recommendation M.2083-0, Sep. 2015. [Online]. Available: https://bit.ly/3FjIIJy

[5] H. -Y. Wang, C. -H. Cheng, B. Su, and G. -R. Lin, "QAM-GFDM of Dual-Mode VCSEL Mixed 28-GHz MMW Carrier for Fiber-Wireless Link," *J. Light. Technol.*, vol. 39, no. 19, pp. 6076–6084, Oct. 2021, doi: 10.1109/JLT.2021.3096246.

[6] "User equipment (UE) radio transmission and reception; Part 2: Range 2 standalone (Release 15)," 3GPP, Tech. Spec. 38.101–2 V15.1.0, Mar. 2018. [Online]. Available: https://bit.ly/3gOwiza

[7] "Summary of Rel-17 Work Items (Release 17)," 3GPP, Tech. Rep. 21.917 V1.0.0, Sep. 2022. [Online]. Available: https://bit.ly/3D6YGUE

[8] Z. Jia, J. Yu, G. Ellinas, and G. -K. Chang, "Key Enabling Technologies for Optical–Wireless Networks: Optical Millimeter-Wave Generation, Wavelength Reuse, and Architecture," *J. Light. Technol.*, vol. 25, no. 11, pp. 3452–3471, Nov. 2007, doi: 10.1109/JLT.2007.909201.

[9] J. Yao, "Microwave Photonics," *J. Light. Technol.*, vol. 27, no. 3, pp. 314–335, Feb. 2009, doi: 10.1109/JLT.2008.2009551.

[10] J. Yu, "Photonics-Assisted Millimeter-Wave Wireless Communication," *IEEE J. Quantum Electron.*, vol. 53, no. 6, pp. 1–17, Dec. 2017, doi: 10.1109/JQE.2017.2765742.

[11] I. A. Alimi, A. L. Teixeira, and P. P. Monteiro, "Toward an Efficient C-RAN Optical Fronthaul for the Future Networks: A Tutorial on Technologies, Requirements, Challenges, and Solutions," *IEEE Commun. Surv. Tutor.*, vol. 20, no. 1, pp. 708–769, Firstquarter 2018, doi: 10.1109/COMST.2017.2773462.

[12] M. Sung, S. -H. Cho, J. Kim, J. K. Lee, J. H. Lee, and H. S. Chung, "Demonstration of IFoF-Based Mobile Fronthaul in 5G Prototype With 28-GHz Millimeter wave," *J. Light. Technol.*, vol. 36, no. 2, pp. 601–609, Jan. 2018, doi: 10.1109/JLT.2017.2763156.

[13] R. Muñoz *et al.*, "Experimental Demonstration of Dynamic Optical Beamforming for Beyond 5G Spatially Multiplexed Fronthaul Networks," *IEEE J. Sel. Top. Quantum Electron.*, vol. 27, no. 6, pp. 1–16, Dec. 2021, doi: 10.1109/JSTQE.2021.3079726.

[14] U. Gliese, T. N. Nielsen, S. Norskov, and K. E. Stubkjaer, "Multifunctional fiber-optic microwave links based on remote heterodyne detection," *IEEE Trans. Microw. Theory Tech.*, vol. 46, no. 5, pp. 458–468, May 1998, doi: 10.1109/22.668642.

[15] J. Yu, X. Li, and W. Zhou, "Tutorial: Broadband fiber-wireless integration for 5G+ communication," *APL Photonics*, vol. 3, no. 11, p. 111101, Nov. 2018, doi: 10.1063/1.5042364.

[16] A. Delmade *et al.*, "Optical Heterodyne Analog Radio-Over-Fiber Link for Millimeter-Wave Wireless Systems," *J. Light. Technol.*, vol. 39, no. 2, pp. 465–474, Jan. 2021, doi: 10.1109/JLT.2020.3032923.

[17] C. Lim and A. Nirmalathas, "Radio-Over-Fiber Technology: Present and Future," *J. Light. Technol.*, vol. 39, no. 4, pp. 881–888, Feb. 2021, doi: 10.1109/JLT.2020.3024916.

[18] C. Browning *et al.*, "Gain-Switched Optical Frequency Combs for Future Mobile Radio-Over-Fiber Millimeter-Wave Systems," *J. Light. Technol.*, vol. 36, no. 19, pp. 4602–4610, Oct. 2018, doi: 10.1109/JLT.2018.2841365.

[19] X. Li *et al.*, "1-Tb/s Millimeter-Wave Signal Wireless Delivery at D-Band," *J. Light. Technol.*, vol. 37, no. 1, pp. 196–204, Jan. 2019, doi: 10.1109/JLT.2018.2871472.

[20] J. L. Li, F. Zhao, and J. Yu, "D-band Millimeter Wave Generation and Transmission Though Radio-Over-Fiber System," *IEEE Photonics J.*, vol. 12, no. 2, pp. 1–8, Apr. 2020, doi: 10.1109/JPHOT.2020.2976505.

[21] X. Pan *et al.*, "Photonic vector mm-wave signal generation by optical dual-SSB modulation and a single push-pull MZM," *Opt Lett*, vol. 44, no. 14, pp. 3570–3573, Jul. 2019, doi: 10.1364/OL.44.003570.

[22] G. K. M. Hasanuzzaman, H. Shams, C. C. Renaud, J. Mitchell, A. J. Seeds, and S. Iezekiel, "Tunable THz Signal Generation and Radio-Over-Fiber Link Based on an Optoelectronic Oscillator-Driven Optical Frequency Comb," *J. Light. Technol.*, vol. 38, no. 19, pp. 5240–5247, Oct. 2020, doi: 10.1109/JLT.2019.2953070.

[23] G. K. M. Hasanuzzaman, A. Kanno, P. T. Dat, and S. Iezekiel, "Self-Oscillating Optical Frequency Comb: Application to Low Phase Noise Millimeter Wave Generation and Radio-Over-Fiber Link," *J. Light. Technol.*, vol. 36, no. 19, pp. 4535–4542, Oct. 2018, doi: 10.1109/JLT.2018.2844344.

[24] K. Mallick *et al.*, "Bidirectional OFDM-MMWOF transport system based on mixed QAM modulation format using dual mode colorless laser diode and RSOA for next generation 5-G based network," *Opt. Fiber Technol.*, vol. 64, p. 102562, Jul. 2021, doi: 10.1016/j.yofte.2021.102562.

[25] C. -T. Tsai *et al.*, "Incoherent Laser Heterodyned Long-Reach 60-GHz MMWoF Link With Volterra Filtered 16-QAM OFDM Beyond 13 Gbps," *IEEE J. Sel. Top. Quantum Electron.*, vol. 27, no. 2, pp. 1–11, Apr. 2021, doi: 10.1109/JSTQE.2020.2991736.

[26] G. Carpintero *et al.*, "Microwave Photonic Integrated Circuits for Millimeter-Wave Wireless Communications," *J. Light. Technol.*, vol. 32, no. 20, pp. 3495–3501, Oct. 2014, doi: 10.1109/JLT.2014.2321573.

[27] S. E. Alavi, M. R. K. Soltanian, I. S. Amiri, M. Khalily, A. S. M. Supa'at, and H. Ahmad, "Towards 5G: A Photonic Based Millimeter Wave Signal Generation for Applying in 5G Access Fronthaul," *Sci. Rep.*, vol. 6, no. 1, p. 19891, Jan. 2016, doi: 10.1038/srep19891.

[28] L. Fan, G. Xia, J. Chen, X. Tang, Q. Liang, and Z. Wu, "High-purity 60GHz band millimeter-wave generation based on optically injected semiconductor laser under subharmonic microwave modulation," *Opt. Express*, vol. 24, no. 16, pp. 18252–18265, Aug. 2016, doi: 10.1364/OE.24.018252.

[29] K. Balakier, M. J. Fice, L. Ponnampalam, A. J. Seeds, and C. C. Renaud, "Monolithically Integrated Optical Phase Lock Loop for Microwave Photonics," *J. Light. Technol.*, vol. 32, no. 20, pp. 3893–3900, Oct. 2014, doi: 10.1109/JLT.2014.2317941.

[30] L. A. Johansson and A. J. Seeds, "Generation and transmission of millimeter-wave data-modulated optical signals using an optical injection phase-lock loop," *J. Light. Technol.*, vol. 21, no. 2, pp. 511–520, Feb. 2003, doi: 10.1109/JLT.2003.808747.

[31] Q. Tareq, A. M. Ragheb, E. Alkhazraji, M. A. Esmail, S. Alshebeili, and M. Z. M. Khan, "Hybrid 28 GHz MMW over fiber-wireless QPSK transmission system based on mid L-band external injection-locked quantum-dash laser comb source," *Opt. Fiber Technol.*, vol. 64, p. 102553, Jul. 2021, doi: 10.1016/j.yofte.2021.102553.

[32] M. Z. M. Khan, Q. Tareq, A. M. Ragheb, M. A. Esmail, and S. A. Alshebeili, "Bidirectional MMWoF-wireless convergence system based on a 1610 nm L-band quantum-dash laser," *Opt Express*, vol. 29, no. 17, pp. 27493–27507, Aug. 2021, doi: 10.1364/OE.433414.

178

[33] K. Mallick, P. Mandal, R. Mukherjee, G. C. Mandal, B. Das, and A. S. Patra, "Generation of 40 GHz/80 GHz OFDM based MMW source and the OFDM-FSO transport system based on special fine tracking technology," *Opt. Fiber Technol.*, vol. 54, p. 102130, Jan. 2020, doi: 10.1016/j.yofte.2019.102130.

[34] A. M. Ragheb, Q. Tareq, E. Alkhazraji, M. A. Esmail, S. Alshebeili, and M. Z. Khan, "Extended L-Band InAs/InP Quantum-Dash Laser in Millimeter-Wave Applications," *Photonics*, vol. 8, no. 5, 2021, doi: 10.3390/photonics8050167.

[35] H. Zhang *et al.*, "Quantum Dot Coherent Comb Laser Source for Converged Optical-Wireless Access Networks," *IEEE Photonics J.*, vol. 13, no. 3, pp. 1–9, Jun. 2021, doi: 10.1109/JPHOT.2021.3081060.

[36] M. J. Fice *et al.*, "146-GHz millimeter-wave radio-over-fiber photonic wireless transmission system," *Opt. Express*, vol. 20, no. 2, pp. 1769–1774, Jan. 2012, doi: 10.1364/OE.20.001769.

[37] P. Mandal, K. Mallick, S. Santra, B. Kuiri, B. Dutta, and A. S. Patra, "A bidirectional hybrid WDM-OFDM network for multiservice communication employing self-injection locked Qdash laser source based on elimination of Rayleigh backscattering noise technique," *Opt. Quantum Electron.*, vol. 53, no. 5, p. 263, Apr. 2021, doi: 10.1007/s11082-021-02948-2.

[38] K. Mallick *et al.*, "Bidirectional OFDM Based MMW/THzW Over Fiber System for Next Generation Communication," *IEEE Photonics J.*, vol. 13, no. 4, pp. 1–7, Aug. 2021, doi: 10.1109/JPHOT.2021.3104943.

[39] Z. Lu *et al.*, "InAs/InP Quantum Dash Semiconductor Coherent Comb Lasers and their Applications in Optical Networks," *J. Light. Technol.*, vol. 39, no. 12, pp. 3751–3760, Jun. 2021, doi: 10.1109/JLT.2020.3043284.

[40] R. Rosales *et al.*, "High performance mode locking characteristics of single section quantum dash lasers," *Opt. Express*, vol. 20, no. 8, pp. 8649–8657, Apr. 2012, doi: 10.1364/OE.20.008649.

[41] F. Lelarge *et al.*, "Recent Advances on InAs/InP Quantum Dash Based Semiconductor Lasers and Optical Amplifiers Operating at 1.55 μm," *IEEE J. Sel. Top. Quantum Electron.*, vol. 13, no. 1, pp. 111–124, Feb. 2007, doi: 10.1109/JSTQE.2006.887154.

[42] Z. G. Lu, J. R. Liu, P. J. Poole, C. Y. Song, and S. D. Chang, "Ultra-narrow linewidth quantum dot coherent comb lasers with self-injection feedback locking," *Opt. Express*, vol. 26, no. 9, pp. 11909–11914, Apr. 2018, doi: 10.1364/OE.26.011909.

[43] K. Merghem, V. Panapakkam, Q. Gaimard, F. Lelarge, and A. Ramdane, "Narrow Linewidth Frequency Comb Source based on Self-injected Quantum-Dash Passively Mode-Locked Laser," in *Conference on Lasers and Electro-Optics*, in OSA Technical Digest (online). San Jose, California: Optica Publishing Group, May 2017, p. SW1C.5. doi: 10.1364/CLEO_SI.2017.SW1C.5.

[44] K. Zeb *et al.*, "InAs/InP quantum dash buried heterostructure mode-locked laser for high capacity fiber-wireless integrated 5G new radio fronthaul systems," *Opt. Express*, vol. 29, no. 11, pp. 16164–16174, May 2021, doi: 10.1364/OE.424504.

[45] Y. Mao *et al.*, "High Performance InAs/InP Quantum Dash Frequency Comb Laser for High Capacity RoF Wireless Networks," *Sens. Transducers*, vol. 255, no. 1, pp. 24–34, 2022.

[46] K. Zeb *et al.*, "Broadband Optical Heterodyne Millimeter-Wave-over-Fiber Wireless Links Based on a Quantum Dash Dual-Wavelength DFB Laser," *J. Light. Technol.*, vol. 40, no. 12, pp. 3698–3708, Jun. 2022, doi: 10.1109/JLT.2022.3154652.

[47] M. Rahim *et al.*, "Monolithic InAs/InP quantum dash dual-wavelength DFB laser with ultra-low noise common cavity modes for millimeter-wave applications," *Opt. Express*, vol. 27, no. 24, pp. 35368–35375, Nov. 2019, doi: 10.1364/OE.27.035368.

[48] K. Zeb, X. Zhang, and Z. Lu, "High Capacity Mode Division Multiplexing Based MIMO Enabled All-Optical Analog Millimeter-Wave Over Fiber Fronthaul Architecture for 5G and Beyond," *IEEE Access*, vol. 7, pp. 89522–89533, 2019, doi: 10.1109/ACCESS.2019.2926276.

[49] R. N. Hall, G. E. Fenner, J. D. Kingsley, T. J. Soltys, and R. O. Carlson, "Coherent Light Emission From GaAs Junctions," *Phys Rev Lett*, vol. 9, no. 9, pp. 366–368, Nov. 1962, doi: 10.1103/PhysRevLett.9.366.

[50] Z. I. Alferov and R. F. Kazarinov, "Semiconductor laser with electric pumping," Inventor's Certificate No. 181737 [in Russian], Application No. 950840, Mar. 1963

[51] I. Hayashi, M. B. Panish, P. W. Foy, and S. Sumski, "JUNCTION LASERS WHICH OPERATE CONTINUOUSLY AT ROOM TEMPERATURE," *Appl. Phys. Lett.*, vol. 17, no. 3, pp. 109–111, Aug. 1970, doi: 10.1063/1.1653326.

[52] J. P. van der Ziel, R. Dingle, R. C. Miller, W. Wiegmann, and W. A. Nordland, "Laser oscillation from quantum states in very thin GaAs−Al0.2Ga0.8As multilayer structures," *Appl. Phys. Lett.*, vol. 26, no. 8, pp. 463–465, Apr. 1975, doi: 10.1063/1.88211.

[53] R. D. Dupuis, P. D. Dapkus, N. Holonyak, E. A. Rezek, and R. Chin, "Room-temperature laser operation of quantum-well Ga(1−x)AlxAs-GaAs laser diodes grown by metalorganic chemical vapor deposition," *Appl. Phys. Lett.*, vol. 32, no. 5, pp. 295–297, Mar. 1978, doi: 10.1063/1.90026.

[54] R. Dingle and C. H. Henry, *Quantum effects in heterostructure lasers*. Google Patents, 1976.

[55] A. Y. Cho, "Film Deposition by Molecular-Beam Techniques," *J. Vac. Sci. Technol.*, vol. 8, no. 5, pp. S31–S38, Sep. 1971, doi: 10.1116/1.1316387.

[56] Y. Arakawa and H. Sakaki, "Multidimensional quantum well laser and temperature dependence of its threshold current," *Appl. Phys. Lett.*, vol. 40, no. 11, pp. 939–941, Jun. 1982, doi: 10.1063/1.92959.

[57] P. M. Petroff, A. C. Gossard, R. A. Logan, and W. Wiegmann, "Toward quantum well wires: Fabrication and optical properties," *Appl. Phys. Lett.*, vol. 41, no. 7, pp. 635–638, Oct. 1982, doi: 10.1063/1.93610.

[58] H. Hirayama, K. Matsunaga, M. Asada, and Y. Suematsu, "Lasing action of $Ga_{0.67}In_{0.33}As$/GaInAsP/InP tensile-strained quantum-box laser," *Electron. Lett.*, vol. 30, no. 2, pp. 142–143, Jan. 1994.

[59] N. Kirstaedter *et al.*, "Low threshold, large T_o injection laser emission from (InGa)As quantum dots," *Electron. Lett.*, vol. 30, no. 17, pp. 1416–1417, Aug. 1994.

[60] P. Poole, "Chapter 11 - InP-Based Quantum Dot Lasers," in *Semiconductors and Semimetals*, J. J. Coleman, A. C. Bryce, and C. Jagadish, Eds., Elsevier, 2012, pp. 419–453. doi: 10.1016/B978-0-12-391066-0.00011-3.

[61] D. G. Deppe, K. Shavritranuruk, G. Ozgur, H. Chen, and S. Freisem, "Quantum dot laser diode with low threshold and low internal loss," *Electron. Lett.*, vol. 45, no. 1, pp. 54–56, Jan. 2009.

[62] J. Wu, S. Chen, A. Seeds, and H. Liu, "Quantum dot optoelectronic devices: lasers, photodetectors and solar cells," *J. Phys. Appl. Phys.*, vol. 48, no. 36, p. 363001, Aug. 2015, doi: 10.1088/0022-3727/48/36/363001.

[63] J. Oshinowo, M. Nishioka, S. Ishida, and Y. Arakawa, "Highly uniform InGaAs/GaAs quantum dots (∼15 nm) by metalorganic chemical vapor deposition," *Appl. Phys. Lett.*, vol. 65, no. 11, pp. 1421–1423, Sep. 1994, doi: 10.1063/1.112070.

[64] P. B. Joyce, T. J. Krzyzewski, P. H. Steans, G. R. Bell, J. H. Neave, and T. S. Jones, "Variations in critical coverage for InAs/GaAs quantum dot formation in bilayer structures," *J. Cryst. Growth*, vol. 244, no. 1, pp. 39–48, Sep. 2002, doi: 10.1016/S0022-0248(02)01607-X.

[65] F. Y. Chang, C. C. Wu, and H. H. Lin, "Effect of InGaAs capping layer on the properties of InAs/InGaAs quantum dots and lasers," *Appl. Phys. Lett.*, vol. 82, no. 25, pp. 4477–4479, Jun. 2003, doi: 10.1063/1.1585125.

[66] P. J. Poole, K. Kaminska, P. Barrios, Z. Lu, and J. Liu, "Growth of InAs/InP-based quantum dots for 1.55µm laser applications," *J. Cryst. Growth*, vol. 311, no. 6, pp. 1482–1486, Mar. 2009, doi: 10.1016/j.jcrysgro.2009.01.129.

[67] H. Huang, "Optical nonlinearities in quantum dot lasers for high-speed communications," Paris, ENST, 2017.

[68] D. Bimberg, M. Grundmann, and N. N. Ledentsov, *Quantum dot heterostructures*. John Wiley & Sons, 1999.

[69] T. C. Newell, D. J. Bossert, A. Stintz, B. Fuchs, K. J. Malloy, and L. F. Lester, "Gain and linewidth enhancement factor in InAs quantum-dot laser diodes," *IEEE Photonics Technol. Lett.*, vol. 11, no. 12, pp. 1527–1529, Dec. 1999, doi: 10.1109/68.806834.

[70] D. Nielsen and S. L. Chuang, "Four-wave mixing and wavelength conversion in quantum dots," *Phys Rev B*, vol. 81, no. 3, p. 035305, Jan. 2010, doi: 10.1103/PhysRevB.81.035305.

[71] S. S. Mikhrin *et al.*, "High power temperature-insensitive 1.3 µm InAs/InGaAs/GaAs quantum dot lasers," *Semicond. Sci. Technol.*, vol. 20, no. 5, p. 340, Feb. 2005, doi: 10.1088/0268-1242/20/5/002.

[72] M. Z. M. Khan, T. K. Ng, and B. S. Ooi, "Self-assembled InAs/InP quantum dots and quantum dashes: Material structures and devices," *Prog. Quantum Electron.*, vol. 38, no. 6, pp. 237–313, Nov. 2014, doi: 10.1016/j.pquantelec.2014.11.001.

[73] Zhenguo Lu, "Quantum-dot coherent comb lasers for terabit optical networking systems," presented at the Proc.SPIE, Mar. 2019, p. 109210N. doi: 10.1117/12.2507274.

[74] Z. Mi, J. Yang, P. Bhattacharya, G. Qin, and Z. Ma, "High-Performance Quantum Dot Lasers and Integrated Optoelectronics on Si," *Proc. IEEE*, vol. 97, no. 7, pp. 1239–1249, Jul. 2009, doi: 10.1109/JPROC.2009.2014780.

[75] D. L. Huffaker, G. Park, Z. Zou, O. B. Shchekin, and D. G. Deppe, "1.3 µm room-temperature GaAs-based quantum-dot laser," *Appl. Phys. Lett.*, vol. 73, no. 18, pp. 2564–2566, Nov. 1998, doi: 10.1063/1.122534.

[76] V. M. Ustinov *et al.*, "Low-threshold quantum-dot injection heterolaser emitting at 1.84 µm," *Tech. Phys. Lett.*, vol. 24, no. 1, pp. 22–23, Jan. 1998, doi: 10.1134/1.1261977.

[77] K. Nishi, M. Yamada, T. Anan, A. Gomyo, and S. Sugou, "Long-wavelength lasing from InAs self-assembled quantum dots on (311) B InP," *Appl. Phys. Lett.*, vol. 73, no. 4, pp. 526–528, Jul. 1998, doi: 10.1063/1.121922.

[78] R. H. Wang *et al.*, "Room-temperature operation of InAs quantum-dash lasers on InP [001]," *IEEE Photonics Technol. Lett.*, vol. 13, no. 8, pp. 767–769, Aug. 2001, doi: 10.1109/68.935797.

[79] T. Utzmeier, P. A. Postigo, J. Tamayo, R. García, and F. Briones, "Transition from self-organized InSb quantum-dots to quantum dashes," *Appl. Phys. Lett.*, vol. 69, no. 18, pp. 2674–2676, Oct. 1996, doi: 10.1063/1.117674.

[80] S. P. Guo, H. Ohno, A. Shen, F. Matsukura, and Y. Ohno, "InAs self-organized quantum dashes grown on GaAs (211)B," *Appl. Phys. Lett.*, vol. 70, no. 20, pp. 2738–2740, May 1997, doi: 10.1063/1.119007.

[81] W. Rudno-Rudziński *et al.*, "Carrier delocalization in InAs/InGaAlAs/InP quantum-dash-based tunnel injection system for 1.55 µm emission," *AIP Adv.*, vol. 7, no. 1, p. 015117, Jan. 2017, doi: 10.1063/1.4975634.

[82] G. -H. Duan *et al.*, "High performance InP-based quantum dash semiconductor mode-locked lasers for optical communications," *Bell Labs Tech. J.*, vol. 14, no. 3, pp. 63–84, Fall 2009, doi: 10.1002/bltj.20388.

[83] W. Kaiser *et al.*, "Static and dynamic properties of laterally coupled DFB lasers based on InAs/InP QDash structures," *Electron. Lett.*, vol. 41, no. 14, pp. 808–810, Jul. 2005.

[84] M. Faugeron *et al.*, "High Peak Power, Narrow RF Linewidth Asymmetrical Cladding Quantum-Dash Mode-Locked Lasers," *IEEE J. Sel. Top. Quantum Electron.*, vol. 19, no. 4, pp. 1101008–1101008, Aug. 2013, doi: 10.1109/JSTQE.2013.2241025.

[85] R. Rosales *et al.*, "InAs/InP Quantum-Dot Passively Mode-Locked Lasers for 1.55-µ m Applications," *IEEE J. Sel. Top. Quantum Electron.*, vol. 17, no. 5, pp. 1292–1301, Oct. 2011, doi: 10.1109/JSTQE.2011.2116772.

[86] P. J. Poole, Z. Lu, J. Liu, P. Barrios, Y. Mao, and G. Liu, "A Performance Comparison Between Quantum Dash and Quantum Well Fabry-Pérot Lasers," *IEEE J. Quantum Electron.*, vol. 57, no. 6, pp. 1–7, Dec. 2021, doi: 10.1109/JQE.2021.3107850.

[87] Y. Mao, Z. Lu, J. Liu, P. J. Poole, and G. Liu, "Pulse Timing Jitter Estimated From Optical Phase Noise in Mode-Locked Semiconductor Quantum Dash Lasers," *J. Light. Technol.*, vol. 38, no. 17, pp. 4787–4793, Sep. 2020, doi: 10.1109/JLT.2020.2996424.

[88] Y. Mao, J. Liu, Z. Lu, C. Song, and P. J. Poole, "Ultra-Low Timing Jitter of Quantum Dash Semiconductor Comb Lasers With Self-Injection Feedback Locking," *IEEE J. Sel. Top. Quantum Electron.*, vol. 25, no. 6, pp. 1–7, Dec. 2019, doi: 10.1109/JSTQE.2019.2916840.

[89] C. Weber *et al.*, "Quantum dash frequency comb laser stabilisation by optical self-injection provided by an all-fibre based delay-controlled passive external cavity," *Electron. Lett.*, vol. 55, no. 18, pp. 1006–1009, 2019, doi: https://doi.org/10.1049/el.2019.2016.

[90] L. F. Lester, N. A. Naderi, F. Grillot, R. Raghunathan, and V. Kovanis, "Strong optical injection and the differential gain in a quantum dash laser," *Opt Express*, vol. 22, no. 6, pp. 7222–7228, Mar. 2014, doi: 10.1364/OE.22.007222.

[91] F. van Dijk, A. Accard, A. Enard, O. Drisse, D. Make, and F. Lelarge, "Monolithic dual wavelength DFB lasers for narrow linewidth heterodyne beat-note generation," in *2011 International Topical Meeting on Microwave Photonics jointly held with the 2011 Asia-Pacific Microwave Photonics Conference*, Oct. 2011, pp. 73–76. doi: 10.1109/MWP.2011.6088672.

[92] Z. G. Lu, J. R. Liu, S. Raymond, P. J. Poole, P. J. Barrios, and D. Poitras, "312-fs pulse generation from a passive C-band InAs/InP quantum dot mode-locked laser," *Opt. Express*, vol. 16, no. 14, pp. 10835–10840, Jul. 2008, doi: 10.1364/OE.16.010835.

[93] Z. G. Lu *et al.*, "Ultra-high repetition rate InAs/InP quantum dot mode-locked lasers," *Opt. Commun.*, vol. 284, no. 9, pp. 2323–2326, May 2011, doi: 10.1016/j.optcom.2010.11.083.

[94] E. U. Rafailov, M. A. Cataluna, and W. Sibbett, "Mode-locked quantum-dot lasers," *Nat. Photonics*, vol. 1, no. 7, pp. 395–401, Jul. 2007, doi: 10.1038/nphoton.2007.120.

[95] G. Girault *et al.*, "Quantum dash actively modelocked Fabry-Perot laser module demonstrated as part of wavelength tunable RZ transmitter," *Electron. Lett.*, vol. 44, no. 14, pp. 873–875, Jul. 2008.

[96] X. Huang, A. Stintz, H. Li, L. F. Lester, J. Cheng, and K. J. Malloy, "Passive mode-locking in 1.3 µm two-section InAs quantum dot lasers," *Appl. Phys. Lett.*, vol. 78, no. 19, pp. 2825–2827, May 2001, doi: 10.1063/1.1371244.

[97] M. J. R. Heck *et al.*, "Observation of Q-switching and mode-locking in two-section InAs/InP (100) quantum dot lasers around 1.55 µm," *Opt. Express*, vol. 15, no. 25, pp. 16292–16301, Dec. 2007, doi: 10.1364/OE.15.016292.

[98] M. J. R. Heck *et al.*, "Analysis of hybrid mode-locking of two-section quantum dot lasers operating at 1.5 μm," *Opt. Express*, vol. 17, no. 20, pp. 18063–18075, Sep. 2009, doi: 10.1364/OE.17.018063.

[99] C. Gosset *et al.*, "Subpicosecond pulse generation at 134GHz using a quantum-dash-based Fabry-Perot laser emitting at 1.56μm," *Appl. Phys. Lett.*, vol. 88, no. 24, p. 241105, Jun. 2006, doi: 10.1063/1.2213007.

[100] C.-Y. Lin, Y.-C. Xin, Y. Li, F. L. Chiragh, and L. F. Lester, "Cavity design and characteristics of monolithic long-wavelength InAs/InP quantum dash passively mode-locked lasers," *Opt. Express*, vol. 17, no. 22, pp. 19739–19748, Oct. 2009, doi: 10.1364/OE.17.019739.

[101] J. Renaudier *et al.*, "45 GHz self-pulsation with narrow linewidth in quantum dot Fabry-Perot semiconductor lasers at 1.5 μm," *Electron. Lett.*, vol. 41, no. 18, pp. 1007–1008, Sep. 2005.

[102] J. P. Tourrenc *et al.*, "Experimental investigation of the timing jitter in self-pulsating quantum-dash lasers operating at 1.55 μm," *Opt. Express*, vol. 16, no. 22, pp. 17706–17713, Oct. 2008, doi: 10.1364/OE.16.017706.

[103] Y. Mao *et al.*, "Ultralow Noise and Timing Jitter Semiconductor Quantum-Dot Passively Mode-Locked Laser for Terabit/s Optical Networks," *Photonics*, vol. 9, no. 10, 2022, doi: 10.3390/photonics9100695.

[104] Z. Jiao *et al.*, "Tunable Terahertz Beat Signal Generation From an InAs/InP Quantum-Dot Mode-Locked Laser Combined With External-Cavity," *IEEE Photonics Technol. Lett.*, vol. 24, no. 6, pp. 518–520, Mar. 2012, doi: 10.1109/LPT.2011.2182642.

[105] Z. G. Lu *et al.*, "An L-band monolithic InAs/InP quantum dot mode-locked laser with femtosecond pulses," *Opt. Express*, vol. 17, no. 16, pp. 13609–13614, Aug. 2009, doi: 10.1364/OE.17.013609.

[106] Z. G. Lu *et al.*, "High performance InAs/InP quantum dot 34.462-GHz C-band coherent comb laser module," *Opt. Express*, vol. 26, no. 2, pp. 2160–2167, Jan. 2018, doi: 10.1364/OE.26.002160.

[107] D. T. Emerson, "The work of Jagadis Chandra Bose: 100 years of millimeter-wave research," *IEEE Trans. Microw. Theory Tech.*, vol. 45, no. 12, pp. 2267–2273, Dec. 1997, doi: 10.1109/22.643830.

[108] M. Xiao *et al.*, "Millimeter Wave Communications for Future Mobile Networks," *IEEE J. Sel. Areas Commun.*, vol. 35, no. 9, pp. 1909–1935, Sep. 2017, doi: 10.1109/JSAC.2017.2719924.

[109] Z. Pi and F. Khan, "An introduction to millimeter-wave mobile broadband systems," *IEEE Commun. Mag.*, vol. 49, no. 6, pp. 101–107, Jun. 2011, doi: 10.1109/MCOM.2011.5783993.

[110] S. Rangan, T. S. Rappaport, and E. Erkip, "Millimeter-Wave Cellular Wireless Networks: Potentials and Challenges," *Proc. IEEE*, vol. 102, no. 3, pp. 366–385, Mar. 2014, doi: 10.1109/JPROC.2014.2299397.

[111] T. S. Rappaport, J. N. Murdock, and F. Gutierrez, "State of the Art in 60-GHz Integrated Circuits and Systems for Wireless Communications," *Proc. IEEE*, vol. 99, no. 8, pp. 1390–1436, Aug. 2011, doi: 10.1109/JPROC.2011.2143650.

[112] J. E. Smee, "5 key technology inventions in 5G NR Release 17," Qualcomm Technologies, Apr. 2022. [Online]. Available: https://bit.ly/3gcYk7F

[113] "Technical Feasibility of IMT in Bands above 6 GHz," International Telecommunication Union, document ITUR M.2376-0, ITU-R, 2015. [Online]. Available: https://bit.ly/3Vk6l9L

[114] M. Marcus and B. Pattan, "Millimeter wave propagation: spectrum management implications," *IEEE Microw. Mag.*, vol. 6, no. 2, pp. 54–62, Jun. 2005, doi: 10.1109/MMW.2005.1491267.

[115] A. Hilt, "Availability and Fade Margin Calculations for 5G Microwave and Millimeter-Wave Anyhaul Links," *Appl. Sci.*, vol. 9, no. 23, 2019, doi: 10.3390/app9235240.

[116] K. Nakamura, N. Iwasawa, K. Kawasaki, S. Yoshida, and M. Takahashi, "The attenuation characteristics of millimeter-wave by snow accretion," *IEICE Commun. Express*, vol. 9, no. 12, pp. 674–678, 2020, doi: 10.1587/comex.2020XBL0128.

[117] H. Zhao *et al.*, "28 GHz millimeter wave cellular communication measurements for reflection and penetration loss in and around buildings in New York city," in *2013 IEEE International Conference on Communications (ICC)*, Jun. 2013, pp. 5163–5167. doi: 10.1109/ICC.2013.6655403.

[118] E. J. Violette, R. H. Espeland, R. O. DeBolt, and F. K. Schwering, "Millimeter-wave propagation at street level in an urban environment," *IEEE Trans. Geosci. Remote Sens.*, vol. 26, no. 3, pp. 368–380, May 1988, doi: 10.1109/36.3038.

[119] Y. Niu, Y. Li, D. Jin, L. Su, and A. V. Vasilakos, "A Survey of Millimeter Wave Communications (MmWave) for 5G: Opportunities and Challenges," *Wirel Netw*, vol. 21, no. 8, pp. 2657–2676, Nov. 2015, doi: 10.1007/s11276-015-0942-z.

[120] C. -C. Chen, C. -C. Li, B. -J. Huang, K. -Y. Lin, H. -W. Tsao, and H. Wang, "Ring-Based Triple-Push VCOs With Wide Continuous Tuning Ranges," *IEEE Trans. Microw. Theory Tech.*, vol. 57, no. 9, pp. 2173–2183, Sep. 2009, doi: 10.1109/TMTT.2009.2027073.

[121] Z. Li, G. Cheng, T. Han, Z. Li, and M. Tian, "A 23–36.8-GHz Low-Noise Frequency Synthesizer With a Fundamental Colpitts VCO Array in SiGe BiCMOS for 5G Applications," *IEEE Trans. Very Large Scale Integr. VLSI Syst.*, vol. 28, no. 11, pp. 2243–2256, Nov. 2020, doi: 10.1109/TVLSI.2020.3014962.

[122] A. Chung, A. M. Darwish, E. Viveiros, H. A. Hung, P. Mitran, and S. Boumaiza, "Analysis and Compensation of Nonidealities in Frequency Multiplier-Based High-Frequency Vector Signal Generators," *IEEE Trans. Microw. Theory Tech.*, vol. 67, no. 6, pp. 2270–2283, Jun. 2019, doi: 10.1109/TMTT.2019.2909901.

[123] C. -Y. Lin *et al.*, "Millimeter-Wave Carrier Embedded Dual-Color Laser Diode for 5G MMW oF Link," *J. Light. Technol.*, vol. 35, no. 12, pp. 2409–2420, Jun. 2017, doi: 10.1109/JLT.2016.2646743.

[124] T. Nagatsuma, "Photonic generation of millimeter waves and its applications," in *OFC/NFOEC*, Mar. 2012, pp. 1–3.

[125] X. Li, J. Yu, and G. -K. Chang, "Photonics-Assisted Technologies for Extreme Broadband 5G Wireless Communications," *J. Light. Technol.*, vol. 37, no. 12, pp. 2851–2865, Jun. 2019, doi: 10.1109/JLT.2019.2906498.

[126] G. Grosskopf *et al.*, "Optical millimeter-wave generation and wireless data transmission using a dual-mode laser," *IEEE Photonics Technol. Lett.*, vol. 12, no. 12, pp. 1692–1694, Dec. 2000, doi: 10.1109/68.896351.

[127] W. -J. Jiang *et al.*, "Simple 14-Gb/s Short-Range Radio-Over-Fiber System Employing a Single-Electrode MZM for 60-GHz Wireless Applications," *J. Light. Technol.*, vol. 28, no. 16, pp. 2238–2246, Aug. 2010, doi: 10.1109/JLT.2010.2045341.

[128] M. G. Larrode, A. M. J. Koonen, J. J. V. Olmos, and A. Ng'Oma, "Bidirectional radio-over-fiber link employing optical frequency multiplication," *IEEE Photonics Technol. Lett.*, vol. 18, no. 1, pp. 241–243, Jan. 2006, doi: 10.1109/LPT.2005.862011.

[129] S. Liu, P. -C. Peng, M. Xu, D. Guidotti, H. Tian, and G. -K. Chang, "A Long-Distance Millimeter-Wave RoF System With a Low-Cost Directly Modulated Laser," *IEEE Photonics Technol. Lett.*, vol. 30, no. 15, pp. 1396–1399, Aug. 2018, doi: 10.1109/LPT.2018.2850705.

[130] R. . -P. Braun, G. Grosskopf, D. Rohde, and F. Schmidt, "Low-phase-noise millimeter-wave generation at 64 GHz and data transmission using optical sideband injection locking," *IEEE Photonics Technol. Lett.*, vol. 10, no. 5, pp. 728–730, May 1998, doi: 10.1109/68.669405.

[131] D. W. Grund, G. A. Ejzak, G. J. Schneider, J. Murakowski, and D. W. Prather, "A Widely Tunable Narrow Linewidth RF Source Integrated in a Heterogeneous Photonic Module," *J. Light. Technol.*, vol. 32, no. 7, pp. 1363–1369, Apr. 2014, doi: 10.1109/JLT.2014.2302138.

[132] H.-Y. Chen, Y.-C. Chi, and G.-R. Lin, "Remote heterodyne millimeter-wave over fiber based OFDM-PON with master-to-slave injected dual-mode colorless FPLD pair," *Opt. Express*, vol. 23, no. 17, pp. 22691–22705, Aug. 2015, doi: 10.1364/OE.23.022691.

[133] H. Wen, L. Chen, C. Huang, and S. Wen, "A full-duplex radio-over-fiber system using direct modulation laser to generate optical millimeter-wave and wavelength reuse for uplink connection," *Opt. Commun.*, vol. 281, no. 8, pp. 2083–2088, Apr. 2008, doi: 10.1016/j.optcom.2007.12.058.

[134] A. Ng'oma *et al.*, "Performance of a Multi-Gb/s 60 GHz Radio Over Fiber System Employing a Directly Modulated Optically Injection-Locked VCSEL," *J. Light. Technol.*, vol. 28, no. 16, pp. 2436–2444, Aug. 2010, doi: 10.1109/JLT.2010.2046623.

[135] A. Delmade, E. Martin, C. Browning, and L. P. Barry, "5G Millimeter-Wave Analog RoF System employing Optical Injection Locking and Direct Modulation of DFB Laser," in *2022 Optical Fiber Communications Conference and Exhibition (OFC)*, Mar. 2022, pp. 1–3.

[136] Y. Wang *et al.*, "QAM Vector mm-Wave Signal Generation Based on Optical Orthogonal Polarization SSB Scheme By a Single Modulator," *J. Light. Technol.*, vol. 39, no. 24, pp. 7628–7635, Dec. 2021, doi: 10.1109/JLT.2021.3068742.

[137] Y. -D. Chung, K. -S. Choi, J. -S. Sim, H. -K. Yu, and J. Kim, "A 60-GHz-Band Analog Optical System-on-Package Transmitter for Fiber-Radio Communications," *J. Light. Technol.*, vol. 25, no. 11, pp. 3407–3412, Nov. 2007, doi: 10.1109/JLT.2007.906816.

[138] W. Li and J. Yao, "Investigation of Photonically Assisted Microwave Frequency Multiplication Based on External Modulation," *IEEE Trans. Microw. Theory Tech.*, vol. 58, no. 11, pp. 3259–3268, Nov. 2010, doi: 10.1109/TMTT.2010.2075671.

[139] T. Wang, M. Chen, H. Chen, and S. Xie, "Millimetre-wave signal generation using FWM effect in SOA," *Electron. Lett.*, vol. 43, no. 1, pp. 36-38(2), Jan. 2007.

[140] H. Zhou, C. Fei, Y. Zeng, Y. Tan, and M. Chen, "A ROF system based on 18-tuple frequency millimeter wave generation using external modulator and SOA," *Opt. Fiber Technol.*, vol. 61, p. 102402, Jan. 2021, doi: 10.1016/j.yofte.2020.102402.

[141] C. Zhang, L. Wang, and K. Qiu, "Proposal for all-optical generation of multiple-frequency millimeter-wave signals for RoF system with multiple base stations using FWM in SOA," *Opt. Express*, vol. 19, no. 15, pp. 13957–13962, Jul. 2011, doi: 10.1364/OE.19.013957.

[142] A. Wiberg, P. Perez-Millan, M. V. Andres, and P. O. Hedekvist, "Microwave-photonic frequency multiplication utilizing optical four-wave mixing and fiber Bragg gratings," *J. Light. Technol.*, vol. 24, no. 1, pp. 329–334, Jan. 2006, doi: 10.1109/JLT.2005.860164.

[143] D.-H. Kim, J.-Y. Lee, H.-J. Choi, and J.-I. Song, "All-optical single-sideband frequency upconversion utilizing the XPM effect in an SOA-MZI," *Opt. Express*, vol. 24, no. 18, pp. 20309–20317, Sep. 2016, doi: 10.1364/OE.24.020309.

[144] H.-J. Kim and J.-I. Song, "All-optical single-sideband upconversion with an optical interleaver and a semiconductor optical amplifier for radio-over-fiber applications," *Opt. Express*, vol. 17, no. 12, pp. 9810–9817, Jun. 2009, doi: 10.1364/OE.17.009810.

[145] W. Li, W. H. Sun, W. T. Wang, and N. H. Zhu, "All-optical frequency upconversion for radio-over-fiber applications based on cross-gain modulation and cross-polarization modulation in a semiconductor optical amplifier," *Opt. Lett.*, vol. 39, no. 9, pp. 2672–2675, May 2014, doi: 10.1364/OL.39.002672.

[146] T. Schneider, M. Junker, and D. Hannover, "Generation of millimetre-wave signals by stimulated Brillouin scattering for radio over fibre systems," *Electron. Lett.*, vol. 40, no. 23, pp. 1500–1502, Nov. 2004.

[147] C. Du *et al.*, "Photonic millimeter-wave ultrawideband signal generation using frequency upconversion based on the stimulated Brillouin scattering effect," *Opt. Lett.*, vol. 43, no. 20, pp. 4915–4918, Oct. 2018, doi: 10.1364/OL.43.004915.

[148] S. H. Han, C. S. Park, S. Hann, S. R. Lee, and C.-S. Park, "Millimeter-wave carrier generation by optical frequency multiplication using stimulated Brillouin scattering and four-wave mixing," *Microw. Opt. Technol. Lett.*, vol. 53, no. 9, pp. 2185–2189, 2011, doi: https://doi.org/10.1002/mop.26204.

[149] R. Karembera, C. Censur, and T. Gibbon, "Sub-60-GHz power-efficient fronthaul system of up to 16-Gbps using RF carriers generated from a gain-switched VCSEL," *OSA Contin.*, vol. 3, no. 12, pp. 3482–3496, Dec. 2020, doi: 10.1364/OSAC.404883.

[150] M. Wang and J. Yao, "Tunable Optical Frequency Comb Generation Based on an Optoelectronic Oscillator," *IEEE Photonics Technol. Lett.*, vol. 25, no. 21, pp. 2035–2038, Nov. 2013, doi: 10.1109/LPT.2013.2280666.

[151] L. Liu, Y. Liu, X.-Z. Gao, and X. Zhang, "Flexible Ultra-Wide Electro-Optic Frequency Combs for a High-Capacity Tunable 5G+ Millimeter-Wave Frequency Synthesizer," *Appl. Sci.*, vol. 11, no. 22, 2021, doi: 10.3390/app112210742.

[152] E. S. Lima, R. M. Borges, N. Andriolli, E. Conforti, G. Contestabile, and A. C. Sodré, "Integrated optical frequency comb for 5G NR Xhauls," *Sci. Rep.*, vol. 12, no. 1, p. 16421, Sep. 2022, doi: 10.1038/s41598-022-20553-5.

[153] Q. Yuan, X. Yin, X. Xin, C. Yu, Y. Chen, and B. Liu, "A millimeter-wave WDM-ROF system based on supercontinuum technique," *Optoelectron. Lett.*, vol. 7, no. 6, pp. 440–442, Nov. 2011, doi: 10.1007/s11801-011-1081-0.

[154] L. Zhang, X. Xin, B. Liu, Y. Wang, J. Yu, and C. Yu, "OFDM Modulated WDM-ROF System based on PCF-Supercontinuum," *Opt. Express*, vol. 18, no. 14, pp. 15003–15008, Jul. 2010, doi: 10.1364/OE.18.015003.

[155] A. Stöhr *et al.*, "60 GHz radio-over-fiber technologies for broadband wireless services [Invited]," *J. Opt. Netw.*, vol. 8, no. 5, pp. 471–487, May 2009, doi: 10.1364/JON.8.000471.

[156] A. Stöhr *et al.*, "Millimeter-Wave Photonic Components for Broadband Wireless Systems," *IEEE Trans. Microw. Theory Tech.*, vol. 58, no. 11, pp. 3071–3082, Nov. 2010, doi: 10.1109/TMTT.2010.2077470.

[157] D. Wake, C. R. Lima, and P. A. Davies, "Optical generation of millimeter-wave signals for fiber-radio systems using a dual-mode DFB semiconductor laser," *IEEE Trans. Microw. Theory Tech.*, vol. 43, no. 9, pp. 2270–2276, Sep. 1995, doi: 10.1109/22.414575.

[158] F. Pozzi, R. M. De La Rue, and M. Sorel, "Dual-Wavelength InAlGaAs–InP Laterally Coupled Distributed Feedback Laser," *IEEE Photonics Technol. Lett.*, vol. 18, no. 24, pp. 2563–2565, Dec. 2006, doi: 10.1109/LPT.2006.887205.

[159] N. Kim *et al.*, "Monolithic dual-mode distributed feedback semiconductor laser for tunable continuous-wave terahertz generation," *Opt. Express*, vol. 17, no. 16, pp. 13851–13859, Aug. 2009, doi: 10.1364/OE.17.013851.

[160] L. Hou, M. Haji, I. Eddie, H. Zhu, and J. H. Marsh, "Laterally coupled dual-grating distributed feedback lasers for generating mode-beat terahertz signals," *Opt. Lett.*, vol. 40, no. 2, pp. 182–185, Jan. 2015, doi: 10.1364/OL.40.000182.

[161] R. Paquet *et al.*, "Coherent continuous-wave dual-frequency high-Q external-cavity semiconductor laser for GHz–THz applications," *Opt. Lett.*, vol. 41, no. 16, pp. 3751–3754, Aug. 2016, doi: 10.1364/OL.41.003751.

[162] T. Uusitalo, H. Virtanen, J. Viheriälä, and M. Dumitrescu, "Dual-mode DFB laser diodes with apodized surface gratings," *Opt. Express*, vol. 26, no. 13, pp. 16303–16314, Jun. 2018, doi: 10.1364/OE.26.016303.

[163] Q. Tang *et al.*, "25 Gb/s Directly Modulated Widely Tunable 1.3 μm Dual Wavelength DFB Laser for THz Communication," *IEEE Photonics Technol. Lett.*, vol. 32, no. 7, pp. 410–413, Apr. 2020, doi: 10.1109/LPT.2020.2976569.

[164] H. J. Kbashi, V. Sharma, and S. Sergeyev, "Dual-wavelength fiber-laser-based transmission of millimeter waves for 5G-supported Radio-over-Fiber (RoF) links," *Opt. Fiber Technol.*, vol. 65, p. 102588, Sep. 2021, doi: 10.1016/j.yofte.2021.102588.

[165] Y. Li, A. Rolland, K. Iwamoto, N. Kuse, M. Fermann, and T. Nagatsuma, "Low-noise millimeter-wave synthesis from a dual-wavelength fiber Brillouin cavity," *Opt. Lett.*, vol. 44, no. 2, pp. 359–362, Jan. 2019, doi: 10.1364/OL.44.000359.

[166] R. Khayatzadeh, J. Poette, and B. Cabon, "Impact of Phase Noise in 60-GHz Radio-Over-Fiber Communication System Based on Passively Mode-Locked Laser," *J. Light. Technol.*, vol. 32, no. 20, pp. 3529–3535, Oct. 2014, doi: 10.1109/JLT.2014.2322254.

[167] N. Kuse and M. E. Fermann, "A photonic frequency discriminator based on a two wavelength delayed self-heterodyne interferometer for low phase noise tunable micro/mm wave synthesis," *Sci. Rep.*, vol. 8, no. 1, p. 13719, Sep. 2018, doi: 10.1038/s41598-018-31712-y.

[168] H. H. Elwan, R. Khayatzadeh, J. Poette, and B. Cabon, "Impact of Relative Intensity Noise on 60-GHz Radio-Over-Fiber Wireless Transmission Systems," *J. Light. Technol.*, vol. 34, no. 20, pp. 4751–4757, Oct. 2016, doi: 10.1109/JLT.2016.2544106.

[169] V. Vujicic *et al.*, "Quantum Dash Mode-Locked Lasers for Data Centre Applications," *IEEE J. Sel. Top. Quantum Electron.*, vol. 21, no. 6, pp. 53–60, Dec. 2015, doi: 10.1109/JSTQE.2015.2487884.

[170] G. Carpintero, M. G. Thompson, K. Yvind, R. V. Penty, and I. H. White, "Comparison of the noise performance of 10 GHz repetition rate quantum-dot and quantum well monolithic mode-locked semiconductor lasers," *IET Optoelectron.*, vol. 5, no. 5, pp. 195–201, Oct. 2011.

[171] A. Checko *et al.*, "Cloud RAN for Mobile Networks—A Technology Overview," *IEEE Commun. Surv. Tutor.*, vol. 17, no. 1, pp. 405–426, Firstquarter 2015, doi: 10.1109/COMST.2014.2355255.

[172] A. Pizzinat, P. Chanclou, F. Saliou, and T. Diallo, "Things You Should Know About Fronthaul," *J. Light. Technol.*, vol. 33, no. 5, pp. 1077–1083, Mar. 2015, doi: 10.1109/JLT.2014.2382872.

[173] C. Sexton, N. J. Kaminski, J. M. Marquez-Barja, N. Marchetti, and L. A. DaSilva, "5G: Adaptable Networks Enabled by Versatile Radio Access Technologies," *IEEE Commun. Surv. Tutor.*, vol. 19, no. 2, pp. 688–720, Secondquarter 2017, doi: 10.1109/COMST.2017.2652495.

[174] P. T. Dat, A. Kanno, N. Yamamoto, and T. Kawanishi, "Radio-over-Fiber-based Seamless Fiber-Wireless Convergence for Small Cell and Linear Cell Networks," in *2018 Optical Fiber Communications Conference and Exposition (OFC)*, Mar. 2018, pp. 1–3.

[175] B. G. Kim, H. Kim, and Y. C. Chung, "Impact of Multipath Interference on the Performance of RoF-Based Mobile Fronthaul Network Implemented by Using DML," *J. Light. Technol.*, vol. 35, no. 2, pp. 145–151, Jan. 2017, doi: 10.1109/JLT.2016.2629667.

[176] S. Papaioannou *et al.*, "5G small-cell networks leveraging optical technologies with mm-wave massive MIMO and MT-MAC protocols," presented at the Proc.SPIE, Jan. 2018, p. 105590B. doi: 10.1117/12.2297276.

[177] S. Nanba and A. Agata, "A new IQ data compression scheme for front-haul link in Centralized RAN," in *2013 IEEE 24th International Symposium on Personal, Indoor and Mobile Radio Communications (PIMRC Workshops)*, Sep. 2013, pp. 210–214. doi: 10.1109/PIMRCW.2013.6707866.

[178] S. Zhou, X. Liu, F. Effenberger, and J. Chao, "Low-latency high-efficiency mobile fronthaul with TDM-PON (mobile-PON)," *J. Opt. Commun. Netw.*, vol. 10, no. 1, pp. A20–A26, Jan. 2018, doi: 10.1364/JOCN.10.000A20.

[179] J. Bartelt, P. Rost, D. Wubben, J. Lessmann, B. Melis, and G. Fettweis, "Fronthaul and backhaul requirements of flexibly centralized radio access networks," *IEEE Wirel. Commun.*, vol. 22, no. 5, pp. 105–111, Oct. 2015, doi: 10.1109/MWC.2015.7306544.

[180] U. Dötsch, M. Doll, H. Mayer, F. Schaich, J. Segel, and P. Sehier, "Quantitative analysis of split base station processing and determination of advantageous architectures for LTE," *Bell Labs Tech. J.*, vol. 18, no. 1, pp. 105–128, Jun. 2013, doi: 10.1002/bltj.21595.

[181] "IEEE Standard for Radio over Ethernet Encapsulations and Mappings," IEEE, P1914.3-2018, 2018. [Online]. Available: https://bit.ly/3WjNMmz

[182] Z. Zhang, J. Ma, Q. Zhang, and S. Huang, "An analog mobile fronthaul based on low and high frequency hybrid network for next generation mobile system," *Opt. Fiber Technol.*, vol. 38, pp. 123–129, Nov. 2017, doi: 10.1016/j.yofte.2017.09.007.

[183] P. L. Carro, Á. Hernández-Solana, and A. V. Bardají, "Evaluation of Radio Resource Management Impact on RoF Signal Transmission for Downlink LTE," *J. Light. Technol.*, vol. 36, no. 9, pp. 1591–1600, May 2018, doi: 10.1109/JLT.2017.2784622.

[184] "Study on new radio access technology: Radio access architecture and interfaces (Release 14)," 3GPP, Tech. Rep38.801 V1.0.0, Dec. 2016. [Online]. Available: https://bit.ly/3Wcidvn

[185] "eCPRI Interface Specification V2.0," CPRI, May 2019. [Online]. Available: https://bit.ly/3YhpMSK

[186] "IEEE Standard for Local and metropolitan area networks — Time-Sensitive Networking for Fronthaul," IEEE, P802.1CM – 2018, Mar. 2018. [Online]. Available: https://bit.ly/3iQ3Xt8

[187] "IEEE Standard for Packet-based Fronthaul Transport Networks," *IEEE Std 19141-2019*, pp. 1–94, Apr. 2020, doi: 10.1109/IEEESTD.2020.9079731.

[188] E. Grass *et al.*, "Dynamically reconfigurable optical-wireless backhaul/fronthaul with cognitive control plane for small cells and cloud-RANs," *5G-Xhaul EuCNC Oulu Finl. Proj. ID*, vol. 671551, 2015.

[189] X. Costa-Perez *et al.*, "5G-crosshaul: An SDN/NFV integrated fronthaul/backhaul transport network architecture," *IEEE Wirel. Commun.*, vol. 24, no. 1, pp. 38–45, 2017.

[190] S. González *et al.*, "5G-Crosshaul: An SDN/NFV control and data plane architecture for the 5G integrated Fronthaul/Backhaul," *Trans. Emerg. Telecommun. Technol.*, vol. 27, no. 9, pp. 1196–1205, 2016, doi: https://doi.org/10.1002/ett.3066.

[191] A. Aijaz, H. Aghvami, and M. Amani, "A survey on mobile data offloading: technical and business perspectives," *IEEE Wirel. Commun.*, vol. 20, no. 2, pp. 104–112, Apr. 2013, doi: 10.1109/MWC.2013.6507401.

[192] X. Xie and X. Zhang, "Pre-filtered and post-filtered 1-bit delta sigma modulator for fronthaul downlinks," *Opt. Commun.*, vol. 510, p. 127908, May 2022, doi: 10.1016/j.optcom.2022.127908.

[193] H. Li *et al.*, "Real-Time 100-GS/s Sigma-Delta Modulator for All-Digital Radio-Over-Fiber Transmission," *J. Light. Technol.*, vol. 38, no. 2, pp. 386–393, Jan. 2020, doi: 10.1109/JLT.2019.2931549.

[194] L. Zhong *et al.*, "An SNR-improved Transmitter of Delta-sigma Modulation Supported Ultra-High-Order QAM Signal for Fronthaul/WiFi Applications," *J. Light. Technol.*, vol. 40, no. 9, pp. 2780–2790, May 2022, doi: 10.1109/JLT.2022.3147059.

[195] K. Bai *et al.*, "Digital Mobile Fronthaul Based on Performance Enhanced Multi-Stage Noise-Shaping Delta-Sigma Modulator," *J. Light. Technol.*, vol. 39, no. 2, pp. 439–447, Jan. 2021, doi: 10.1109/JLT.2020.3027911.

[196] W. Hao, G. Sun, J. Zhang, P. Xiao, and L. Hanzo, "Secure Millimeter Wave Cloud Radio Access Networks Relying on Microwave Multicast Fronthaul," *IEEE Trans. Commun.*, vol. 68, no. 5, pp. 3079–3095, May 2020, doi: 10.1109/TCOMM.2020.2974743.

[197] R. G. Stephen and R. Zhang, "Joint Millimeter-Wave Fronthaul and OFDMA Resource Allocation in Ultra-Dense CRAN," *IEEE Trans. Commun.*, vol. 65, no. 3, pp. 1411–1423, Mar. 2017, doi: 10.1109/TCOMM.2017.2649519.

[198] Y. Chen *et al.*, "Cost effective wavelength reused MDM system for bidirectional mobile fronthaul," *Opt. Express*, vol. 24, no. 20, pp. 22413–22422, Oct. 2016, doi: 10.1364/OE.24.022413.

[199] A. Macho, M. Morant, and R. Llorente, "Next-Generation Optical Fronthaul Systems Using Multicore Fiber Media," *J. Light. Technol.*, vol. 34, no. 20, pp. 4819–4827, Oct. 2016, doi: 10.1109/JLT.2016.2573038.

[200] E. Ruggeri *et al.*, "A 5G Fiber Wireless 4Gb/s WDM Fronthaul for Flexible 360° Coverage in V-Band massive MIMO Small Cells," *J. Light. Technol.*, vol. 39, no. 4, pp. 1081–1088, Feb. 2021, doi: 10.1109/JLT.2020.3029608.

[201] F. J. Effenberger and D. Zhang, "WDM-PON for 5G Wireless Fronthaul," *IEEE Wirel. Commun.*, vol. 29, no. 2, pp. 94–99, Apr. 2022, doi: 10.1109/MWC.001.2100420.

[202] Y. Nakayama and D. Hisano, "Wavelength and Bandwidth Allocation for Mobile Fronthaul in TWDM-PON," *IEEE Trans. Commun.*, vol. 67, no. 11, pp. 7642–7655, Nov. 2019, doi: 10.1109/TCOMM.2019.2939319.

[203] J. Kim, S. H. Chang, and J. K. Lee, "Comparative study for evaluating the cost efficiency of 5G Ethernet mobile fronthaul networks," *J. Opt. Commun. Netw.*, vol. 14, no. 12, pp. 960–969, Dec. 2022, doi: 10.1364/JOCN.471194.

[204] A. S. Gowda, A. R. Dhaini, L. G. Kazovsky, H. Yang, S. T. Abraha, and A. Ng'oma, "Towards Green Optical/Wireless In-Building Networks: Radio-Over-Fiber," *J. Light. Technol.*, vol. 32, no. 20, pp. 3545–3556, Oct. 2014, doi: 10.1109/JLT.2014.2315960.

[205] C. Lim, Y. Yang, and A. Nirmalathas, "Transport Schemes for Fiber-Wireless Technology: Transmission Performance and Energy Efficiency," *Photonics*, vol. 1, no. 2, pp. 67–82, 2014, doi: 10.3390/photonics1020067.

[206] A. Udalcovs *et al.*, "Total Cost of Ownership of Digital vs. Analog Radio-Over-Fiber Architectures for 5G Fronthauling," *IEEE Access*, vol. 8, pp. 223562–223573, 2020, doi: 10.1109/ACCESS.2020.3044396.

[207] A. Nirmalathas, P. A. Gamage, C. Lim, D. Novak, and R. Waterhouse, "Digitized Radio-Over-Fiber Technologies for Converged Optical Wireless Access Network," *J. Light. Technol.*, vol. 28, no. 16, pp. 2366–2375, Aug. 2010, doi: 10.1109/JLT.2010.2051017.

[208] D. M. Akos, M. Stockmaster, J. B. Y. Tsui, and J. Caschera, "Direct bandpass sampling of multiple distinct RF signals," *IEEE Trans. Commun.*, vol. 47, no. 7, pp. 983–988, Jul. 1999, doi: 10.1109/26.774848.

[209] C. Lim, A. Nirmalathas, K. -L. Lee, D. Novak, and R. Waterhouse, "Intermodulation Distortion Improvement for Fiber–Radio Applications Incorporating OSSB+C Modulation in an Optical

Integrated-Access Environment," *J. Light. Technol.*, vol. 25, no. 6, pp. 1602–1612, Jun. 2007, doi: 10.1109/JLT.2007.896814.

[210] Z. Zakrzewski, "D-RoF and A-RoF Interfaces in an All-Optical Fronthaul of 5G Mobile Systems," *Appl. Sci.*, vol. 10, no. 4, 2020, doi: 10.3390/app10041212.

[211] X. Liu, H. Zeng, N. Chand, and F. Effenberger, "Efficient Mobile Fronthaul via DSP-Based Channel Aggregation," *J. Light. Technol.*, vol. 34, no. 6, pp. 1556–1564, Mar. 2016, doi: 10.1109/JLT.2015.2508451.

[212] H. Zeng, X. Liu, S. Megeed, N. Chand, and F. Effenberger, "Real-Time Demonstration of CPRI-Compatible Efficient Mobile Fronthaul Using FPGA," *J. Light. Technol.*, vol. 35, no. 6, pp. 1241–1247, Mar. 2017, doi: 10.1109/JLT.2017.2660484.

[213] H. Li *et al.*, "Digital Code-Division Multiplexing Channel Aggregation for Mobile Fronthaul Architecture With Low Complexity," *IEEE Photonics J.*, vol. 10, no. 2, pp. 1–10, Apr. 2018, doi: 10.1109/JPHOT.2017.2751538.

[214] F. Lecoche *et al.*, "60 GHz bidirectional optical signal distribution system at 3 Gbps for wireless home network," in *2009 International Topical Meeting on Microwave Photonics*, Oct. 2009, pp. 1–3.

[215] E. Alkhazraji *et al.*, "Hybrid dual-injection locked 1610 nm quantum-dash laser for MMW and THz applications," *Opt. Commun.*, vol. 452, pp. 355–359, Dec. 2019, doi: 10.1016/j.optcom.2019.07.062.

[216] Q. Tareq, A. Ragheb, M. Esmail, S. Alshebeili, and M. Z. M. Khan, "Demonstration of MMW over Fiber-FSO-Wireless 5G QPSK Transmission in Mid L-band Wavelength Region," in *26th Optoelectronics and Communications Conference*, Optica Publishing Group, 2021, p. S4B.3. doi: 10.1364/OECC.2021.S4B.3.

[217] Q. Tareq, A. M. Ragheb, M. A. Esmail, S. A. Alshebeili, and M. Z. M. Khan, "Performance of Injection-Locked Quantum-Dash MMW Source Under Clear and Dusty Weather Conditions," *IEEE Photonics J.*, vol. 13, no. 3, pp. 1–9, Jun. 2021, doi: 10.1109/JPHOT.2021.3074425.

[218] Q. Tareq *et al.*, "Wireless Transmission of Millimeter Waves Generated by L-band InAs/InP Quantum-dash Laser," in *2020 IEEE Photonics Conference (IPC)*, Oct. 2020, pp. 1–2. doi: 10.1109/IPC47351.2020.9252531.

[219] F. van Dijk *et al.*, "Quantum dash mode-locked lasers for millimeter wave signal generation and transmission," in *2010 23rd Annual Meeting of the IEEE Photonics Society*, Nov. 2010, pp. 187–188. doi: 10.1109/PHOTONICS.2010.5698821.

[220] A. Delmade *et al.*, "Quantum Dash Passively Mode Locked Laser for Optical Heterodyne Millimeter-Wave Analog Radio-over-Fiber Fronthaul Systems," in *2020 Optical Fiber Communications Conference and Exhibition (OFC)*, Mar. 2020, pp. 1–3.

[221] G. C. Mandal, R. Mukherjee, B. Das, and A. S. Patra, "A full-duplex WDM hybrid fiber-wired/fiber-wireless/fiber-VLC/fiber-IVLC transmission system based on a self-injection locked quantum dash laser and a RSOA," *Opt. Commun.*, vol. 427, pp. 202–208, Nov. 2018, doi: 10.1016/j.optcom.2018.06.048.

[222] J. Liu *et al.*, "Photonic microwave generation in the X- and K-band using integrated soliton microcombs," *Nat. Photonics*, vol. 14, no. 8, pp. 486–491, Aug. 2020, doi: 10.1038/s41566-020-0617-x.

[223] D. Marpaung, J. Yao, and J. Capmany, "Integrated microwave photonics," *Nat. Photonics*, vol. 13, no. 2, pp. 80–90, Feb. 2019, doi: 10.1038/s41566-018-0310-5.

[224] E. Lucas, P. Brochard, R. Bouchand, S. Schilt, T. Südmeyer, and T. J. Kippenberg, "Ultralow-noise photonic microwave synthesis using a soliton microcomb-based transfer oscillator," *Nat. Commun.*, vol. 11, no. 1, p. 374, Jan. 2020, doi: 10.1038/s41467-019-14059-4.

[225] Zhenguo Lu *et al.*, "Quantum dot semiconductor lasers for 5G and beyond wireless networks," presented at the Proc.SPIE, Mar. 2021, p. 116900N. doi: 10.1117/12.2577084.

[226] M. Z. M. Khan *et al.*, "Injection-Locked Quantum-Dash Laser in Far L-Band 192 Gbit/s DWDM Transmission," *IEEE Photonics J.*, vol. 12, no. 5, pp. 1–11, Oct. 2020, doi: 10.1109/JPHOT.2020.3029026.

[227] E. Alkhazraji, M. S. Alias, K. K. Qureshi, and M. Z. M. Khan, "Monolithic Tunable InAs/InP Broadband Quantum-Dash Laser," *IEEE Access*, vol. 8, pp. 39046–39055, 2020, doi: 10.1109/ACCESS.2020.2975632.

[228] Khan Zeb *et al.*, "A quantum dash mode-locked laser-based photonic aided broadband multi-Gb/s wireless signal delivery system at 5G NR," presented at the Proc.SPIE, Mar. 2021, p. 117110I. doi: 10.1117/12.2583066.

[229] Yuichi Takushima, Hideyuki Sotobayashi, Matthew E. Grein, Erich P. Ippen, and Hermann A. Haus, "Linewidth of mode combs of passively and actively mode-locked semiconductor laser diodes," presented at the Proc.SPIE, Oct. 2004, pp. 213–227. doi: 10.1117/12.580046.

[230] T. Habruseva, S. O'Donoghue, N. Rebrova, F. Kéfélian, S. P. Hegarty, and G. Huyet, "Optical linewidth of a passively mode-locked semiconductor laser," *Opt Lett*, vol. 34, no. 21, pp. 3307–3309, Nov. 2009, doi: 10.1364/OL.34.003307.

[231] F. X. Kärtner *et al.*, "Few-Cycle Pulses Directly from a Laser," in *Few-Cycle Laser Pulse Generation and Its Applications*, F. X. Kärtner, Ed., Berlin, Heidelberg: Springer Berlin Heidelberg, 2004, pp. 73–136. doi: 10.1007/978-3-540-39849-3_2.

[232] R. Rosales, K. Merghem, A. Martinez, F. Lelarge, A. Accard, and A. Ramdane, "Timing jitter from the optical spectrum in semiconductor passively mode locked lasers," *Opt Express*, vol. 20, no. 8, pp. 9151–9160, Apr. 2012, doi: 10.1364/OE.20.009151.

[233] D. von der Linde, "Characterization of the noise in continuously operating mode-locked lasers," *Appl. Phys. B*, vol. 39, no. 4, pp. 201–217, Apr. 1986, doi: 10.1007/BF00697487.

[234] F. Kefelian, S. O'Donoghue, M. T. Todaro, J. G. McInerney, and G. Huyet, "RF Linewidth in Monolithic Passively Mode-Locked Semiconductor Laser," *IEEE Photonics Technol. Lett.*, vol. 20, no. 16, pp. 1405–1407, Aug. 2008, doi: 10.1109/LPT.2008.926834.

[235] L. Drzewietzki, S. Breuer, and W. Elsäßer, "Timing jitter reduction of passively mode-locked semiconductor lasers by self- and external-injection: Numerical description and experiments," *Opt Express*, vol. 21, no. 13, pp. 16142–16161, Jul. 2013, doi: 10.1364/OE.21.016142.

[236] S. Latkowski, "Radio frequency and terahertz signals generated by passively mode-locked semiconductor lasers," Dublin City University, 2010.

[237] Y. Ben M'Sallem *et al.*, "Quantum-Dash Mode-Locked Laser as a Source for 56-Gb/s DQPSK Modulation in WDM Multicast Applications," *IEEE Photonics Technol. Lett.*, vol. 23, no. 7, pp. 453–455, Apr. 2011, doi: 10.1109/LPT.2011.2106116.

[238] R. A. Shafik, M. S. Rahman, and A. R. Islam, "On the Extended Relationships Among EVM, BER and SNR as Performance Metrics," in *2006 International Conference on Electrical and Computer Engineering*, Dec. 2006, pp. 408–411. doi: 10.1109/ICECE.2006.355657.

[239] R. Schmogrow *et al.*, "Error Vector Magnitude as a Performance Measure for Advanced Modulation Formats," *IEEE Photonics Technol. Lett.*, vol. 24, no. 1, pp. 61–63, Jan. 2012, doi: 10.1109/LPT.2011.2172405.

[240] Y. -S. Juan and F. -Y. Lin, "Photonic Generation of Broadly Tunable Microwave Signals Utilizing a Dual-Beam Optically Injected Semiconductor Laser," *IEEE Photonics J.*, vol. 3, no. 4, pp. 644–650, Aug. 2011, doi: 10.1109/JPHOT.2011.2158413.

[241] Q. Li *et al.*, "InAs/GaAs Quantum Dot Dual-Mode Distributed Feedback Laser Towards Large Tuning Range Continuous-Wave Terahertz Application," *Nanoscale Res. Lett.*, vol. 13, no. 1, p. 267, Sep. 2018, doi: 10.1186/s11671-018-2674-3.

[242] K. Zeb *et al.*, "A Quantum-Dash Dual-Wavelength DFB Laser for Optical Millimeter-Wave Radio-over-Fiber Systems," in *2021 Optical Fiber Communications Conference and Exhibition (OFC)*, Jun. 2021, pp. 1–3.

[243] K. Zeb *et al.*, "Photonic Generation of Spectrally Pure Millimeter-Wave Signals for 5G Applications," in *2019 International Topical Meeting on Microwave Photonics (MWP)*, Oct. 2019, pp. 1–4. doi: 10.1109/MWP.2019.8892197.

[244] K. Zeb *et al.*, "Ultra-Low Intensity and Phase Noise Quantum-Dash Dual-Wavelength DFB Laser for 5G Millimeter-Wave Signals," in *Laser Congress 2020 (ASSL, LAC)*, Optica Publishing Group, 2020, p. JTu5A.13. [Online]. Available: https://opg.optica.org/abstract.cfm?URI=LAC-2020-JTu5A.13

[245] W. H. Press, S. A. Teukolsky, W. T. Vetterling, and B. P. Flannery, *Numerical Recipes in C (2nd Ed.): The Art of Scientific Computing*. USA: Cambridge University Press, 1992.

[246] A. Kanno *et al.*, "Optical and radio seamless MIMO transmission with 20-Gbaud QPSK," in *2012 38th European Conference and Exhibition on Optical Communications*, Sep. 2012, pp. 1–3. doi: 10.1364/ECEOC.2012.We.3.B.2.

[247] K. Zeb *et al.*, "Photonic Millimeter-Wave-over-Fiber MIMO Wireless System Based on a QDash Laser," in *2022 Photonics North (PN)*, May 2022, pp. 1–1. doi: 10.1109/PN56061.2022.9908363.

[248] Y. Huang *et al.*, "Duplex Millimeter-Wave Over Fiber Link Using an InAs/InP Quantum-Dash Mode-Locked Laser," in *2022 IEEE International Topical Meeting on Microwave Photonics (MWP)*, Oct. 2022, pp. 1–4. doi: 10.1109/MWP54208.2022.9997655.

[249] L. Combi, A. Matera, A. Gatto, P. Parolari, P. Boffi, and U. Spagnolini, "Radio-over-modes for C-RAN architecture with smart optical resources assignment," in *2017 IEEE International Conference on Communications (ICC)*, May 2017, pp. 1–6. doi: 10.1109/ICC.2017.7997215.

[250] L. A. Rusch, M. Rad, K. Allahverdyan, I. Fazal, and E. Bernier, "Carrying Data on the Orbital Angular Momentum of Light," *IEEE Commun. Mag.*, vol. 56, no. 2, pp. 219–224, Feb. 2018, doi: 10.1109/MCOM.2018.1700058.

[251] M. Li, "On Performance of Optical Wireless Communication With Spatial Multiplexing Towards 5-G," *IEEE Access*, vol. 6, pp. 28108–28113, 2018, doi: 10.1109/ACCESS.2018.2837145.

[252] R. M. Nejad, F. Tavakoli, L. Wang, X. Guan, S. LaRochelle, and L. A. Rusch, "RoF Data Transmission Using Four Linearly Polarized Vector Modes of a Polarization Maintaining Elliptical Ring Core Fiber," *J. Light. Technol.*, vol. 36, no. 17, pp. 3794–3801, Sep. 2018, doi: 10.1109/JLT.2018.2851613.

[253] Q. Mo *et al.*, "2 × 2 MIMO OFDM/OQAM radio signals over an elliptical core few-mode fiber," *Opt. Lett.*, vol. 41, no. 19, pp. 4546–4549, Oct. 2016, doi: 10.1364/OL.41.004546.

[254] J. He *et al.*, "Experimental Demonstration of Bidirectional OFDM/OQAM-MIMO Signal Over a Multicore Fiber System," *IEEE Photonics J.*, vol. 8, no. 5, pp. 1–8, Oct. 2016, doi: 10.1109/JPHOT.2016.2607203.

[255] N. P. Diamantopoulos *et al.*, "Mode-division multiplexed W-Band RoF transmission for higher-order spatial multiplexing," in *2015 Optical Fiber Communications Conference and Exhibition (OFC)*, Mar. 2015, pp. 1–3. doi: 10.1364/OFC.2015.W4G.2.

[256] N. P. Diamantopoulos *et al.*, "Mitigation of Modal Crosstalk-induced Power Fading in Mode Division Multiplexed W-Band RoF links," in *Optical Fiber Communication Conference*, Optica Publishing Group, 2016, p. Th4A.1. doi: 10.1364/OFC.2016.Th4A.1.

[257] C. Xu *et al.*, "Experimental Demonstration of Analog Transmission using Mode Division Multiplexing," in *2018 Optical Fiber Communications Conference and Exposition (OFC)*, Mar. 2018, pp. 1–3.

[258] J. Du, D. Xie, C. Yang, and J. Wang, "Demonstration of analog links using spatial modes in km-scale few mode fiber," *Opt Express*, vol. 25, no. 4, pp. 3613–3620, Feb. 2017, doi: 10.1364/OE.25.003613.

[259] H. Kuboki and M. Matsuura, "Modal Dispersion and Feed Light Crosstalk Mitigations by Using Center- and Offset-Launching for Optically-Powered Radio-over-Multimode Fiber Systems," in *2018 Optical Fiber Communications Conference and Exposition (OFC)*, Mar. 2018, pp. 1–3.

[260] M. Morant and R. Llorente, "Performance Analysis of Carrier-Aggregated Multiantenna 4 × 4 MIMO LTE-A Fronthaul by Spatial Multiplexing on Multicore Fiber," *J. Light. Technol.*, vol. 36, no. 2, pp. 594–600, Jan. 2018, doi: 10.1109/JLT.2017.2786582.

[261] C. Liu *et al.*, "Experimental demonstration of high spectral efficient 4 × 4 MIMO SCMA-OFDM/OQAM radio over multi-core fiber system," *Opt. Express*, vol. 25, no. 15, pp. 18431–18441, Jul. 2017, doi: 10.1364/OE.25.018431.

[262] T. Umezawa, P. T. Dat, K. Kashima, A. Kanno, N. Yamamoto, and T. Kawanishi, "100-GHz Radio and Power Over Fiber Transmission Through Multicore Fiber Using Optical-to-Radio Converter," *J. Light. Technol.*, vol. 36, no. 2, pp. 617–623, Jan. 2018, doi: 10.1109/JLT.2017.2731991.

[263] G. S. D. Gordon, M. J. Crisp, R. V. Penty, T. D. Wilkinson, and I. H. White, "Feasibility Demonstration of a Mode-Division Multiplexed MIMO-Enabled Radio-Over-Fiber Distributed Antenna System," *J. Light. Technol.*, vol. 32, no. 20, pp. 3521–3528, Oct. 2014, doi: 10.1109/JLT.2014.2313649.

[264] Y. Lei *et al.*, "Feasibility of Space-Division-Multiplexed Transmission of IEEE 802.11 n/ac-Compliant Wireless MIMO Signals Over OM3 Multimode Fiber," *J. Light. Technol.*, vol. 36, no. 11, pp. 2076–2082, Jun. 2018, doi: 10.1109/JLT.2018.2802441.

[265] Y. Lei *et al.*, "Experimental study on the statistic characteristics of a 3x3 RF MIMO channel over a single conventional multimode fiber," *Opt. Lett.*, vol. 42, no. 11, pp. 2217–2220, Jun. 2017, doi: 10.1364/OL.42.002217.

[266] A. Raza, S. Ghafoor, and M. F. U. Butt, "MIMO-enabled integrated MGDM–WDM distributed antenna system architecture based on plastic optical fibers for millimeter-wave communication," *Photonic Netw. Commun.*, vol. 35, no. 2, pp. 265–273, Apr. 2018, doi: 10.1007/s11107-017-0741-9.

[267] S. Chen and J. Wang, "Theoretical analyses on orbital angular momentum modes in conventional graded-index multimode fibre," *Sci. Rep.*, vol. 7, no. 1, p. 3990, Jun. 2017, doi: 10.1038/s41598-017-04380-7.

[268] A. Macho, M. Morant, and R. Llorente, "Experimental evaluation of nonlinear crosstalk in multi-core fiber," *Opt. Express*, vol. 23, no. 14, pp. 18712–18720, Jul. 2015, doi: 10.1364/OE.23.018712.

[269] M. Morant, A. Macho, and R. Llorente, "On the Suitability of Multicore Fiber for LTE–Advanced MIMO Optical Fronthaul Systems," *J. Light. Technol.*, vol. 34, no. 2, pp. 676–682, Jan. 2016, doi: 10.1109/JLT.2015.2507137.

[270] Y. Lei *et al.*, "Space-division-multiplexed transmission of 3x3 multiple-input multiple-output wireless signals over conventional graded-index multimode fiber," *Opt. Express*, vol. 24, no. 25, pp. 28372–28382, Dec. 2016, doi: 10.1364/OE.24.028372.